STUDY OF SINGLE CRYSTAL DIAMOND SCHOTTKY BARRIER DIODES FOR POWER ELECTRONICS APPLICATIONS

ARIE NAWAWI

SCHOOL OF ELECTRICAL AND ELECTRONIC ENGINEERING

2014

STUDY OF SINGLE CRYSTAL DIAMOND SCHOTTKY BARRIER DIODES FOR POWER ELECTRONICS APPLICATIONS

ARIE NAWAWI

School of Electrical and Electronic Engineering

A thesis submitted to the Nanyang Technological University
in partial fulfilment of the requirement for the degree of
Doctor of Philosophy

2014

ACKNOWLEDGEMENTS

Throughout the past few years of my Ph.D. study, I have received guidance, assistance, and support from many people, both directly and indirectly. I am happy to have the opportunity to express my gratitude to all of them.

First, I would like to thank my supervisor Dr. Tseng King Jet for his constant guidance, valuable advices, and support during this research. Dr. Tseng's enthusiasm, professionalism, and pleasant personality have made deep impression on me. Without his help, this thesis would have never come to reality. I am really indebted to him. Thank you Prof Tseng!

I would like also to thank Dr. Rusli and Prof. Gehan Amaratunga for their encouragement, constructive suggestions, and productive discussions. It has been a pleasure and an honour working with them.

I want to express my gratitude to National Institute of Advanced Industrial Science and Technology (AIST), Japan for the fruitful collaboration, in particular Dr. Shinichi Shikata and Dr. Hitoshi Umezawa from Diamond Research Laboratory. I have been benefited from their professional experiences and skills during our discussions.

I am really thankful to all the staffs in Power Electronics Research Laboratory, Nanyang Technological University for their continuous support during this research, especially Ms. Lee-Loh Chin Khim. She is a kind person who is always ready to give assistance.

Many thanks also go out to my fellow colleagues and friends for creating pleasant research environment. Especially I wish to thank Dr. Tan Yen Kheng who always guides me during the ups and downs in my Ph.D. study.

I really appreciate the support given by Mr. Mohamed Faizal Bin Osman and all my housemates. They all have been my close and caring friends in Singapore.

I would like to express sincere acknowledgments to Dra. Dharmawati Utomo Ang, MM and Ms. Misliaty Lee for their motivations, kind words of advices, and unending support all this time.

I feel deep sense of gratitude to my parents for everything they have given to me. Their love and dedications has been source of my inspirations all these years. I am always grateful to be their son. Thank you Mom and Dad!

Special thanks also go out to my big-family members, especially my grandparents, my sister, and her husband who keep on cheering me up all this time.

The research scholarship and research fund granted by Nanyang Technological University is gratefully acknowledged.

TABLE OF CONTENTS

ACKNOWLEDGEMENTS i

TABLE OF CONTENTS iii

SUMMARY vii

LIST OF FIGURES ix

LIST OF TABLES xvii

LIST OF ABBREVIATIONS xix

LIST OF SYMBOLS xxii

1 INTRODUCTION 1

1.1 Background and motivations 1

1.2 Objectives and contributions of the thesis 2

1.3 Organization of thesis 4

2 LITERATURE REVIEW 6

2.1 Introduction 6

2.1.1 Brief history on development of power devices and their applications 7

2.1.2 Wide band gap materials and their properties 8

2.1.3 Fundamental properties relevant to power semiconductor devices 11

2.1.4 Role of wide band gap devices 15

2.2 Diamond diode 17

2.2.1 Classification of diamond crystals 17

2.2.2 Type of diamond diode 19

2.2.3 Unipolar p-type diamond Schottky barrier diode 23

2.3 Conclusions 24

3 MODELLING OF SINGLE CRYSTAL DIAMOND FOR IMPLEMENTATION IN NUMERICAL SIMULATIONS 26

3.1 Introduction 26

3.2 Incomplete ionization model 27

3.3 Mobility model 31

3.3.1 Low field mobility 31

3.3.2 High field saturation 35

3.4 Impact ionization model 39

3.5 Conclusions 43

4 STATIC AND TRANSIENT CHARACTERISTICS OF DIAMOND SCHOTTKY BARRIER DIODE 45

4.1 Introduction 45

4.2 Devices under investigation 46

4.3 Device Modelling for implementation in numerical simulations 47

4.4 Static characteristics 48

4.4.1 Diamond metal-intrinsic-p+ diode 48

4.4.2 Diamond Schottky barrier diode 60

4.5 Transient characteristics 64

4.5.1 Diamond Schottky barrier diode 65

4.5.2 Diamond metal-intrinsic-p+ diode 74

4.6 Conclusions 81

5 CHARACTERIZATIONS OF VERTICAL MO/DIAMOND SCHOTTKY BARRIER DIODE FROM NON-IDEAL *I*-*V* AND *C*-*V* MEASUREMENTS BASED ON THE MIS MODEL 82

5.1 Introduction 82

5.2 Investigated vertical Mo/diamond Schottky barrier diodes 83

5.2.1 Fabrication process 83

5.2.2 Experimental results and discussions 86

5.3 Theoretical background of the MIS model 97

5.3.1 Expression of barrier height and surface potential 97

5.3.2 Current- voltage ($I-V$) characteristics 100

5.3.3 Capacitance- voltage ($C-V$) characteristics 102

5.4 Characterizations from *I-V* and *C-V* measurements 103

5.5 Conclusions 110

6 MODELLING AND SIMULATIONS OF NON-IDEAL CHARACTERISTICS OF VERTICAL MO/DIAMOND SCHOTTKY BARRIER DIODE BASED ON THE MIS MODEL 112

6.1 Introduction 112

6.2 Diode under investigation 113

6.3 Experiment results and characterizations 114

6.4 Modelling and simulations 119

6.5 Effects of the interfacial layer and interface states charges on diamond Schottky barrier diode 129

6.6 Conclusions 132

7 TERMINATION STRUCTURES FOR DIAMOND SCHOTTKY BARRIER DIODE 134

7.1 Introduction 134

7.2 Termination structures for diamond Schottky barrier diode 134

7.3 Performances comparisons- Simulation studies 137

7.4 Conclusions 145

8 CONCLUSIONS AND RECOMMENDATIONS 146

8.1 Conclusions 146

8.2 Recommendations 148

LIST OF PUBLICATIONS 150

BIBLIOGRAPHY 152

APPENDICES 161

APPENDIX A: TCAD SENTAURUS SIMULATION SOFTWARE 161
APPENDIX B: PARAMETER FILE IN TCAD SENTAURUS DEVICE SIMULATIONS.. 163
APPENDIX C: COMMAND FILES FOR SIMULATIONS OF TRANSIENT CHARACTERISTICS OF DIAMOND SBD IN TCAD SENTAURUS SOFTWARE 169
APPENDIX D: COMMAND FILES FOR SIMULATIONS OF DIAMOND SBD WITH INTERFACIAL LAYER IN TCAD SENTAURUS SOFTWARE 179
APPENDIX E: COMMAND FILES FOR SIMULATIONS OF DIAMOND SBD WITH EDGE TERMINATION STRUCTURE IN TCAD SENTAURUS SOFTWARE.. 186

SUMMARY

Continuous growth of technology has pushed the requirements of power electronics devices beyond the limits possible with Silicon material. Some of the current and near future applications require high efficiency devices to perform at high temperature and high frequency with high current density and high voltage ratings. This has prompted researches in devices based on the wide band gap materials which have superior electronics properties compared to Silicon. Among the wide band gap semiconductors, diamond is regarded as one of the ultimate materials with extreme mechanical and electrical properties such as high breakdown electric field of 10-20 MV/cm (due to large band gap of 5.47 eV), high electron and hole mobility of 4500 $cm^2.V^{-1}.s^{-1}$ and 3800 $cm^2.V^{-1}.s^{-1}$, high saturation velocity of $2.7x10^7$ cm/s, and high thermal conductivity of 22-24 W/cm.K. Calculations of different figure of merit (FOM) also show huge potential of diamond compared to the other materials. Recent progress in the fabrication technology of high quality single crystal diamond has enabled laboratory fabrication of diamond Schottky barrier diode with high blocking voltage and high temperature operation. Despite of these, diamond is still in the early research stage and there are still many challenges to overcome.

This thesis focuses on the development, characterizations, analysis, modeling and simulations, and design optimizations of diamond Schottky barrier diode (SBD) for power electronics applications. Throughout the study, several p-type vertical diamond SBDs with Molybdenum Schottky contact and different specifications have been fabricated and measured. Various physics models and parameters suitable for numerical simulations of single crystal diamond material were reviewed and adapted for implementation in the finite element physics based Technology Computer Aided Design (TCAD) Sentaurus software. Static and transient characteristics of the diamond SBDs at different temperatures were investigated based on the experimental results, numerical simulations, and theoretical considerations.

Measurements results of the experimental Mo/diamond SBDs show increase in the Schottky barrier height (and turn-on voltage) that indicates Fermi level

pinning and excess current which cannot be explained with pure thermionic emission and Schottky barrier lowering theory. To accurately simulate these non-ideal behaviours, we present modeling and analysis of the SBDs based on the metal-interfacial layer-semiconductor (MIS) structure. Characterizations and parameter extractions of the experimental SBD were carried out using their $I-V$ and $C-V$ measurements results. Extensive numerical simulations based on the MIS model result in good correlation with the SBD's measured forward and reverse bias $I-V$ characteristics simultaneously at different temperature.

Furthermore, we propose planar mesa termination to replace the conventional field plate termination for the edge termination structure of a diamond power SBD with the aim to increase the trade-off between the forward and the reverse bias capability. Design and optimizations for both structures to find optimal device's geometry were performed. Finite element numerical simulation studies indicate that the proposed structure has the potential to yield higher blocking voltage and higher current carrying capability if the choice of suitable high k materials for the field oxide is carefully addressed.

LIST OF FIGURES

Figure 2-1: Present applications of power devices based on the voltage and current ratings [8]. 6
Figure 2-2: Present applications of power devices based on the frequency and power ratings [8]. 7
Figure 2-3: Maximum breakdown voltage of a power device at the same doping density normalized to Si [3]. 13
Figure 2-4: Required width of the drift region for different breakdown voltage ratings for different materials [3]. 13
Figure 2-5: Vertical diode structure 21
Figure 2-6: Lateral/ Planar diode structure 21
Figure 2-7: Pseudo-vertical diode structure 22
Figure 3-1: Variations of resistivity of Boron doped diamond at 300 K with respect to the Boron doping concentrations [70]. 27
Figure 3-2: Variations of Boron activation energy with Boron concentration. 28
Figure 3-3: Intrinsic concentration in diamond as function of temperature. 30
Figure 3-4: Hole concentration against Boron concentration in diamond for negligible compensation ($N_D \leq 1\text{x}10^{10}$ cm^{-3}). 31
Figure 3-5: Hole mobility versus Boron concentration in single crystal CVD diamond at temperature of 300 K, 400 K, and 500 K. 34
Figure 3-6: The calculated conductivity of Boron doped diamond at temperature range of 200K to 600K for different Boron doping concentration. 34
Figure 3-7: Variation of velocity saturation with temperature for $v_{sat,0}$= 2x10^{7} cm/s and different values of $v_{sat,\exp}$ 36
Figure 3-8: Calculated drift velocity versus electric field in diamond for Boron concentration of 10^{11} cm^{-3} at 300 K with different values of β_0 (Beta0). 37
Figure 3-9: Calculated drift velocity versus electric field in diamond for different Boron doping concentration of 10^{11}, 10^{15}, 10^{17} cm^{-3} at 300 K. 37
Figure 3-10: Calculated drift velocity versus electric field in diamond with Boron doping concentration of 10^{11} cm^{-3} at 300 K, 400 K, and 500 K. 38
Figure 3-11: Ideal parallel plate diamond Schottky barrier diode structure. 40

Figure 3-12: The simulated reverse breakdown characteristics in ideal parallel plate diamond Schottky barrier diode structure.. 41
Figure 3-13: Simulated electric field profile at breakdown in ideal parallel plate diamond Schottky barrier diode structure.. 42
Figure 4-1: Structure of a vertical diamond SBD without edge termination.......... 45
Figure 4-2: The packaged diamond m-i-p+ diode [14]... 46
Figure 4-3: Top view of the investigated diamond SBD [54]. 47
Figure 4-4: Miniaturized diamond SBD structure employed in the simulation with the meshes used for the finite element calculations.. 48
Figure 4-5: Forward $I-V$ characteristics of the diamond m-i-p+ diode with small and large Au Schottky contact. 49
Figure 4-6: SEM image of the surface of diamond drift layer [77]. 49
Figure 4-7: Simulation results and experimental data of static forward $I-V$ characteristics of diamond m-i-p+ diodes with Au and Al Schottky contact and various drift length at 300K. 50
Figure 4-8: Simulation results and experimental data of static forward $I-V$ characteristics of diamond m-i-p+ diodes with Au Schottky contact and 10 μm drift length at 300 K, 400 K, and 507 K. 51
Figure 4-9: Energy band diagram for the diamond m-i-p+ diode with Al Schottky contact at 300 K at equilibrium condition (0 V). 53
Figure 4-10: The distribution of hole density in the diamond m-i-p+ diode at thermal equilibrium and under different bias conditions. 53
Figure 4-11: Energy band diagram for the diamond m-i-p+ diode with Al Schottky contact at 300 K under forward bias V_f of 0.4 V. 55
Figure 4-12: Energy band diagram for the diamond m-i-p+ diode with Al Schottky contact at 300 K under forward bias V_f of 4.86 V. 56
Figure 4-13: Energy band diagram for the diamond m-i-p+ diode with Al Schottky contact at 300 K under reverse bias V_r of 10 V. 57
Figure 4-14: Simulated electric field distribution profiles in the diamond m-i-p+ diode with Au Schottky contact at breakdown for drift length of 10 μm, 12 μm, and 16 μm. 58
Figure 4-15: Measured reverse bias $I-V$ characteristics of Au diamond m-i-p+ diodes gold point contact in the liquid dielectric [14, 84]. 59

Figure 4-16: Simulation results and experimental data of static forward $I-V$ characteristics of the investigated diamond SBD at 298 K, 398 K, and 523 K. The simulation result using ideal metal work function at 298 K (298K_Ideal_WF curve) is also shown. 60
Figure 4-17: Energy band diagram for the diamond SBD at 298 K at equilibrium condition (0V). 62
Figure 4-18: Energy band diagram for the diamond SBD 298 K under forward bias V_f of 1 V. 62
Figure 4-19: Energy band diagram for the diamond SBD 298 K under forward bias V_f of 2.108 V. 63
Figure 4-20: The distribution of hole density in the diamond SBD at thermal equilibrium (298 K) and under different bias conditions 63
Figure 4-21: The distribution of hole density in the diamond SBD under forward bias of 4 V at different temperatures 64
Figure 4-22: Circuit diagram of the double-pulse test-circuit to study the transient characteristics of the diode 65
Figure 4-23: Measured turn-off transient characteristics of the investigated SBD at 298 K with 0.5 A forward current and 100 V reverse voltage under different di/dt. 66
Figure 4-24: Measured turn-off transient characteristics of the investigated SBD with 0.4 A forward current and 50 V reverse voltage at temperature of 298 K and 523 K. 67
Figure 4-25: Simulated double-pulse test circuit with MOSFET switch and circuit parasitic components. 67
Figure 4-26: Sub-circuit SPICE model of the power NMOS implemented in the simulations. 68
Figure 4-27: Simulated transfer characteristics ($Id-Vgs$) of the power NMOS for different drain-source voltage. 69
Figure 4-28: Simulated output characteristics ($Id-Vds$) of the power NMOS for different gate-source voltage. 69
Figure 4-29: Simulation results and measurement data of the turn-off transient characteristics of the investigated SBD at 298 K with 0.5 A forward current, 100 V reverse voltage, and $di/dt =$ 30 A/μs. Variation of diode voltage with different

values of MOSFET gate-drain capacitance CGD are shown. The diode's forward voltage drop at 0.5 A forward current is 3 V. 71
Figure 4-30: Simulated turn-on transient characteristics of the MOSFET at 298 K when the diamond SBD is turned-off with di/dt = 30 A/μs. 71
Figure 4-31: Simulation results and measurement data of the turn-off transient characteristics of the investigated SBD at 298 K with 0.5 A forward current, 100 V reverse voltage, and di/dt = 50 A/μs. 72
Figure 4-32: Simulation results and measurement data of the turn-off transient characteristics of the investigated SBD at 298 K with 0.4 A forward current and 50 V reverse voltage. 73
Figure 4-33: Simulation results and measurement data of the turn-off transient characteristics of the investigated SBD at 523 K with 0.4 A forward current and 50 V reverse voltage. 74
Figure 4-34: The simulated voltage in node 1 and 2 during the turn-off transient simulation of the investigated SBD at 523 K with 0.4 A forward current and 50 V reverse voltage. 74
Figure 4-35: Simulated turn-off transient characteristics of Al diamond m-i-p+ diode with different forward current under reverse voltage of 50 V at 300 K. 76
Figure 4-36: Simulated turn-off transient characteristics of Al diamond m-i-p+ diode with 0.1 A forward current under different reverse voltage at 300 K. 77
Figure 4-37: Simulated turn-off transient characteristics of Au diamond m-i-p+ diode with forward current of 0.1 A under reverse voltage of 50 V at 300 K, 400 K, and 507 K. 78
Figure 4-38: Simulation results of the turn-off transient characteristics of the investigated diamond m-i-p+ diode with Al Schottky contact (area of 0.0097 cm^2) at 298 K with 0.5 A forward current, 100 V reverse voltage. The diode's forward voltage drop at 0.5 A forward current is 8.5 V. 80
Figure 5-1: Structure of the experimental vertical Mo/diamond SBD with field plate termination structure. 83
Figure 5-2: The top view of R100230-03 die with SBDs of different sizes and field plate lengths. 85
Figure 5-3: The top view of R100230-17 die with SBDs of different sizes and field plate lengths. 85

Figure 5-4: The measured forward bias $I-V$ characteristics of the Mo/diamond SBDs on R100230-03 wafer at 298 K in terms of: (a) total current and (b) current density. 87
Figure 5-5: The measured forward bias $I-V$ characteristics of the Mo/diamond SBDs on R100230-03 wafer at 423 K in terms of: (a) total current and (b) current density. 88
Figure 5-6: The measured forward bias $I-V$ characteristics of the Mo/diamond SBDs on R100230-03 wafer at 523 K in terms of: (a) total current and (b) current density. 89
Figure 5-7: The measured reverse bias $I-V$ characteristics of the Mo/diamond SBDs on R100230-03 wafer at 298 K. 90
Figure 5-8: The measured reverse bias $I-V$ characteristics of the Mo/diamond SBDs on R100230-03 wafer at 423 K. 90
Figure 5-9: The measured reverse bias $I-V$ characteristics of the Mo/diamond SBDs on R100230-03 wafer at 523 K. 91
Figure 5-10: The measured forward bias $I-V$ characteristics of the Mo/diamond SBDs on R100230-17 wafer at 298 K in terms of: (a) total current and (b) current density. 93
Figure 5-11: The measured forward bias $I-V$ characteristics of the Mo/diamond SBDs on R100230-17 wafer at 423 K in terms of: (a) total current and (b) current density. 94
Figure 5-12: The measured forward bias $I-V$ characteristics of the Mo/diamond SBDs on R100230-17 wafer at 523 K in terms of: (a) total current and (b) current density. 95
Figure 5-13: The measured reverse bias $I-V$ characteristics of the Mo/diamond SBDs on R100230-17 wafer at 298 K. 96
Figure 5-14: The measured reverse bias $I-V$ characteristics of the Mo/diamond SBDs on R100230-17 wafer at 423 K. 96
Figure 5-15: The measured reverse bias $I-V$ characteristics of the Mo/diamond SBDs on R100230-17 wafer at 523 K. 97
Figure 5-16: Energy band diagram of the metal-interfacial layer-semiconductor (MIS) structure under zero bias (a) and under applied forward bias (b). 98

Figure 5-17: Measured forward bias $I-V$ characteristics of the experimental Mo/diamond SBD 12B200 on wafer R100230-17 at different temperatures. 104
Figure 5-18: The experimental and fitting curves of $d(V)/d(\ln I) vs I$ plots in (a) and $H(I) vs I$ plots in (b) of the experimental Mo/diamond SBD 12B200 on wafer R100230-17 at different temperatures. 105
Figure 5-19: The reverse bias $C-V$ characteristics of the experimental Mo/diamond SBD 12B200 on wafer R100230-17 measured at 50 kHz at 298 K. 106
Figure 5-20: The measured reverse bias $C^{-2}-V$ characteristics the experimental Mo/diamond SBD 12B200 on wafer R100230-17 and the linear fitting curve measured at 50 kHz at 298 K. 107
Figure 5-21: Variation of depletion layer width with forward bias of the experimental Mo/diamond SBD 12B200 on wafer R100230-17 at 298 K. 109
Figure 5-22: Energy distribution of the interface state density of the experimental Mo/diamond SBD 12B200 on wafer R100230-17 at 298 K. 110
Figure 6-1: Comparison of measured forward bias $I-V$ characteristics of SBDs 11F30 fabricated on wafer R100230-03 and R100230-17 with simulation results of SBD 11F30 on R100230-03 using intimate contact diode model. 113
Figure 6-2: Measured $I-V$ characteristics of the experimental Mo/diamond SBD 11F30 on wafer R100230-03 at different temperatures: (a) forward bias and (b) reverse bias. 114
Figure 6-3: Fitting of $V-\log I$ curve at temperature of 298 K in MATLAB Curve Fitting Toolbox with 95% confidence bounds. 115
Figure 6-4: Fitting of $V-\log I$ curve at temperature of 423 K in MATLAB Curve Fitting Toolbox with 95% confidence bounds. 115
Figure 6-5: Fitting of $V-\log I$ curve at temperature of 523 K in MATLAB Curve Fitting Toolbox with 95% confidence bounds. 116
Figure 6-6: Energy distribution profile of the interface states density of the experimental Mo/diamond SBD 11F30 on wafer R100230-03 at different temperatures. 118
Figure 6-7: The simulated two dimensional MIS device structure implemented in TCAD Sentaurus software. 119

Figure 6-8: Variations in the simulated forward $I-V$ characteristics with respect to changes in parameters for Nonlocal tunnelling and interfacial layer in linear (a) and log scale (b). 122
Figure 6-9: Variations in the simulated reverse $I-V$ characteristics with respect to changes in parameters for Nonlocal tunnelling and interfacial layer. 123
Figure 6-10: Simulation and experiment results of (a) forward bias and (b) reverse bias $I-V$ characteristics of the experimental Mo/diamond SBD 11F30 on wafer R100230-03 at different temperatures. 124
Figure 6-11: Energy band diagram for the investigated SBD based on MIS model at 298 K at equilibrium condition (0V). The zoom-in figure at the metal-diamond interface is given in (b). 126
Figure 6-12: Energy band diagram for the investigated SBD based on MIS model at 298 K under forward bias V_f 3 V. The zoom-in figure at the metal-diamond interface is given in (b). 127
Figure 6-13: Energy band diagram for the investigated SBD based on MIS model at 298 K under forward bias V_f 5 V. The zoom-in figure at the metal-diamond interface is given in (b). 127
Figure 6-14: Energy band diagram for the investigated SBD based on MIS model at 298 K under reverse bias V_r 4 V. The zoom-in figure at the metal-diamond interface is given in (b). 128
Figure 6-15: Simulated distribution of hole density in the MIS structure at thermal equilibrium and under different bias condition.. 128
Figure 6-16: Comparison between simulated forward bias $I-V$ characteristics of the SBD with ideal intimate Schottky contact and experiment results....................... 130
Figure 6-17: Distribution of simulated electric field in the investigated Mo/diamond SBD with interfacial layer and interface state charges (MIS model) at reverse bias of 1300 V at 298 K... 131
Figure 6-18: Simulated electric field distribution in MIS diode structure and intimate contact SBD structure at reverse bias of 1300 V and at 298 K along the horizontal line y= 0 µm (a) and vertical line x= 0 µm (b). 132
Figure 7-1: Schottky barrier diode structure without termination structure. 135
Figure 7-2: Schottky barrier diode with field plate type of termination structure. 135

Figure 7-3: Schottky barrier diode with planar mesa type of termination structure. 136
Figure 7-4: Process flow for fabrication of planar mesa termination for diamond SBD. (a) Masking of p- region at center area for Schottky contact. (b) Selective ICP etching to create diamond mesa structure. (c) Oxide deposition to fill in the trench region for termination purposes. (d) Schottky contact metallization. 136
Figure 7-5: Distribution of electric field in the non-terminated diamond SBD at reverse bias of 250 V: (a) In the half of symmetrical device and (b) along the metal-diamond interface. 138
Figure 7-6: (a) Variations of simulated breakdown voltage for different field plate length L_F and oxide thickness T_{OX} for field plate terminated diamond SBD. (b) Distribution of reverse current density in the field plate terminated diamond SBD at 1480 V. 139
Figure 7-7: Distribution of electric field in the field plate terminated diamond SBD at 1480 V: (a) In the half of symmetrical device and (b) along the line y= 0 µm (oxide- diamond) and y= -1 µm (metal- oxide). 140
Figure 7-8: (a) Variations of simulated breakdown voltage for different field plate length L_F and oxide thickness T_{OX} for planar mesa terminated diamond SBD. (b) Distribution of reverse current density in the planar mesa terminated diamond SBD at 1751 V. 141
Figure 7-9: Distribution of electric field in the planar mesa terminated SBD: (a) At 1751 V in the half of the symmetrical device. (b) At 1751 V and at 1440 V along the line y= 0 µm. 142
Figure 7-10: Top view schematic diagram of optimum field plate terminated SBD and planar mesa terminated SBD occupying the same total device's area (diameter of 230 µm). L_S and L_F are the diameter of Schottky contact and length of metal plate extension in the corresponding structures. 142
Figure 7-11: Simulated forward $I-V$ characteristics of the field plate terminated (FP) and planar mesa terminated (PM) diamond SBD with the same total device's area (diameter of 230 µm): (a) Comparison of forward current density. (b) Comparison of total forward current. 143

LIST OF TABLES

Table 2-1: Properties of wide band gap materials in comparison with Silicon and Gallium Arsenide. 9
Table 2-2: Main Figure of Merits (FOM) of wide band gap materials in comparison with Silicon and Gallium Arsenide* [3]. 10
Table 2-3: Classification of diamond crystal 17
Table 3-1: Parameters' values for hole mobility in diamond based on University of Bologna bulk mobility model. 33
Table 3-2: Impact ionization coefficients reported in the literature with the simulated breakdown voltage and maximum electric field in ideal parallel plate SBD structure. 40
Table 4-1: Modified values of parameters used in the simulations of the investigated diamond m-i-p+ diode 52
Table 4-2: Modified values of parameters used in the simulations of the investigated diamond SBD. 61
Table 4-3: Values of parameters used in the transient simulations of diamond SBD at 298 K with 0.5 A forward current and 100 V reverse voltage. 70
Table 4-4: Values of parameters used in the transient simulations of diamond SBD with 0.4 A forward current and 50 V reverse voltage for elevated temperature set-up 73
Table 4-5: Diodes' characteristics implemented in the transient simulations. 75
Table 5-1: Specifications of the fabricated diamond wafers. 84
Table 5-2: Specifications of the diamond SBDs fabricated on each wafers. 84
Table 5-3: Temperature dependent values of various parameters extracted from forward I-V characteristics of the experimental Mo/diamond SBD 12B200 on wafer R100230-17 104
Table 6-1: Temperature dependent values of various parameters extracted from forward bias $I-V$ characteristics of the experimental Mo/diamond SBD 11F30 on wafer R100230-03. 116

Table 6-2: Calculated temperature dependent values of degeneracy factor, Fermi level, and ionized acceptor concentration. 117
Table 6-3: Values of temperature dependent parameters used in the simulations. 125
Table 7-1: Performances comparisons between optimum field plate and planar mesa termination structure for diamond Schottky barrier diode.................................... 143

LIST OF ABBREVIATIONS

AC	Alternative Current
AIST	National Institute of Advanced Industrial Science and Technology
Al	Aluminium
AlN	Aluminium Nitride
Au	Gold
B	Boron
BFM	Baliga's Figure of Merit
BJT	Bipolar Junction Transistor
BP	Bond-Polarization
BPFM	Bipolar Power-Handling-Capacity Figure of Merit
BSFM	Bipolar Switching Speed Figure of Merit
BTFM	Bipolar Power-Switching Product
cBN	Cubic Boron Nitride
CMOS	Complementary Metal Oxide Semiconductor
CVD	Chemical Vapour Deposition
CTE	Coefficient of Thermal Expansion
DIGS	Defect-Induced-Gap-States
FEM	Finite Element Method
FOM	Figure of Merit
FPFM	FET Power-Handling-Capacity Figure of Merit
FSFM	FET Switching Speed Figure of Merit
FTFM	FET Power-Switching Product
GaAs	Gallium Arsenide
GaN	Gallium Nitride
GaP	Gallium Phosphide
GTO	Gate Turn-off Thyristor
GUI	Graphical User Interface
HEMT	High Electron Mobility Transistor
HEV	Hybrid Electric Vehicle
HVDC	High Voltage Direct Current
HPHT	High Pressure High Temperature

ICP	Inductively Coupled Plasma
IGBT	Insulated Gate Bipolar Transistor
InP	Indium Phosphate
JBS	Junction Barrier Schottky
JFET	Junction Field Effect Transistor
JFM	Johnson's Figure of Merit
k	Dielectric Constant
m-i-p+	Metal-Intrinsic-p+
MESFET	Metal-Semiconductor Field Effect Transistor
MIGS	Metal-Induced-Gap-States
MIS	Metal-Interfacial layer-Semiconductor
MISFET	Metal-Insulator-Semiconductor Field Effect Transistor
Mo	Molybdenum
MOS	Metal-Oxide-Semiconductor
MOSFET	Metal-Oxide-Semiconductor Field Effect Transistor
MPCVD	Microwave Plasma Chemical Vapour Deposition
MPS	Merged p-i-n Schottky
N	Nitrogen
Pt	Platinum
RF	Radio Frequency
SBD	Schottky Barrier Diode
SCL	Space Charge Limited
SDevice	Sentaurus Device
SSE	Sentaurus Structure Editor
Si	Silicon
SiC	Silicon Carbide
SIMS	Secondary Ion Mass Spectrometry
SMPS	Switch Mode Power Supply
SNPD	Schottky p-n Junction Diode
TMB	Trimethylboron
TCAD	Technology Computer Aided Design
Ti	Titanium
TMBS	Trench MOS Barrier Schottky
TSBS	Trench Schottky Barrier Controlled Schottky

UNCD	Ultra-Nano-Crystalline Diamond
UV	Ultraviolet
WBG	Wide Band Gap
WKB	Wentzel-Kramers-Brillouin

LIST OF SYMBOLS

A	Area of a diode's Schottky contact
A^*	Effective Richardson constant
a_n , b_n	Impact ionization coefficients for electron
a_p , b_p	Impact ionization coefficients for hole
α	Scaling factor for concentration dependent ionization energy
α_v	Parameter of high field mobility model
α_n	Ionization rate for electron
α_p	Ionization rate for hole
β	Temperature dependent factor of high field mobility model
β_n	Dependence of effective barrier height on bias voltage
β_0	Value of β at 300 K
$\beta_{\exp}$	Temperature dependent exponent factor of β
χ	Electron affinity
c_2	Interfacial layer's parameter of MIS diode
$C-V$	Capacitance-Voltage
C_0	Measured zero bias capacitance
CDS	MOSFET drain-source capacitance
CGD	MOSFET gate-drain capacitance
CGS	MOSFET gate-source capacitance
C_{HF}	High frequency capacitance of a MIS diode
C_i	Interfacial layer capacitance
C_{it}	Interface state capacitance
C_{LF}	Low frequency capacitance of a MIS diode
C_{max}	Maximum capacitance
C_{sc}	Space charge capacitance
D_{it}	Density of acceptor like interface states

δ	Thickness of the interfacial layer
Δ	Potential drop across interfacial layer
Δ_{ga}	Temperature dependent factor of degeneracy factor
E_A	Acceptor ionization energy
E_{A0}	Low concentration acceptor ionization energy
E_C	Semiconductor's conduction band
E_{Crit}	Critical/ maximum breakdown electric field
E_F	Fermi level
E_{FM}	Fermi level in metal
E_{Fp}	Quasi-Fermi level for holes
E_f	Electric field
E_g	Semiconductor band gap
E_{gi}	Band gap of the interfacial layer
ε_i	Permittivity of the interfacial layer
ε_0	Permittivity in vacuum ($8.854187817 \times 10^{-14}$ F/cm)
ε_S	Permittivity of semiconductor
E_{SS}	Interface states energy level
E_V	Semiconductor's valence band
E_{vac}	Vacuum energy level
g_A	Degeneracy factor for the acceptor impurity levels
g_c	Dimensionless scaling factor for electron in Nonlocal tunneling model
g_v	Dimensionless scaling factor for holde in Nonlocal tunneling model
G^{ii}	Electron- hole pair generation rate through impact ionization process
γ	Temperature dependent factor of ionization rates
h	Planck constant ($6.62606957 \times 10^{-34}$ J.s)
H	A function used in Cheung and Cheung method for extraction of Schottky barrier diode's parameters

I	Current
$I-V$	Current-Voltage
I_F	Diode's forward current
I_0	Saturation current
I_{Rpeak}	Diode's peak reverse current
J	Current density
J_F	Forward current density
J_S	Saturation current density
k	Boltzmann constant (1.3806488 x 10^{-23} J/K)
L	Load inductor of the double-pulse test circuit
L_σ	Stray inductance of the double-pulse test circuit
L_i	Length of the intrinsic region
L_S	Width of Schottky contact
L_F	Length of metal plate extension for the edge termination structure
m_c	Electron tunneling mass in Nonlocal tunneling model
m_e	Electron rest mass (9.10938291 $\times$ 10^{-31} kg)
$m_{e,dos}$	Density of states effective mass for electron
m_v	Electron tunneling mass in Nonlocal tunneling model
$m_{h,dos}$	Density of states effective mass for hole
n	Electron concentration or diode's ideality factor (depend on the context)
N_f	Density of positive fixed surface charge
n_i	Intrinsic carrier concentrations
N_A	Acceptor doping concentration
N_A^-	Concentration of ionized acceptor
$N_{A,crit}$	Critical acceptor concentration above which acceptor is assumed to be completely ionized
N_C	Effective density of states in the conduction band

N_D	Concentration of compensating donor or donor doping
N_D^+	Concentration of ionized compensating donor
n_i	Intrinsic carrier concentration
N_V	Effective density of states in the valence band
p	Hole concentration
ϕ_B	Effective Schottky barrier height
ϕ_{B0}	Mean Schottky barrier height at zero bias
ϕ_m	Metal work-function
ϕ_0	Neutrality level of the interface states
ψ_S	Surface or diffusion potential
q	Elementary charge (1.602176565 × 10^{-19} C)
Q_f	Positive fixed surface charge on semiconductor surface
Q_{it}	Interface state charge density in semiconductor interface
Q_{sc}	Space charge density in the semiconductor depletion layer
RG	MOSFET gate resistance
$R_{on,sp}$	Specific on-resistance
R_{p-}	Resistance of the p- region
$R_{parasitic}$	Simulated total parasitic resistance of the substrates and contacts (Ω.µm)
R_S	Series resistance
R_{series}	Simulated absolute series resistance (Ω)
T	Temperature
T_{OX}	Field oxide thickness used in the edge termination structure
μ_{dop}	Temperature dependence and doping concentration dependence mobility model
μ_{low}	Mobility of carriers under low electric field
μ_{high}	Mobility of carriers under high electric field

μ_n	Electron mobility
μ_p	Hole mobility
v	Drift velocity of carrier
V	Voltage
V_0	Intercept voltage
V_2	Correction factor due to transition region
V_{Br}	Breakdown voltage
V_{drive}	Switch's drive voltage of the double-pulse test circuit
Vds	MOSFET drain-source voltage
V_f	Forward voltage
VG	MOSFET gate voltage
V_i	Built-in potential
V_{in}	Input voltage of the double-pulse test circuit
V_r	Reverse voltage
v_n	Electron velocity
v_p	Hole velocity
V_p	Potential difference between Fermi level and the valence band level
v_{sat}	Carrier saturation velocity
$v_{sat,0}$	Carrier saturation velocity at 300 K
$v_{sat,\exp}$	Temperature dependent exponent factor of saturation velocity model
V_{TO}	Diode's turn-on voltage
W	Semiconductor depletion layer width

1 INTRODUCTION

1.1 Background and motivations

Throughout recent centuries, history has recorded huge advancement of technology due to electronics revolution. In the 20th century, Silicon based electronics as the first generation of semiconductor started the integrated circuit revolution. Gallium Arsenide (GaAs) and Indium Phosphate (InP) based electronics that contributed to wireless and information revolution around the turn of 21st century can be regarded as the 2nd generation semiconductor [1].

While silicon is well established semiconductor technology, continuous improvements and optimizations in device designs and production processes have reached a saturation point, approaching ideal theoretical limit of silicon materials. On the other hand, continuous growth of technology demands devices' performances that exceed the limit of Si materials. This is very true especially in the power electronics devices area. Current and near future applications require high power, high voltage, and high frequency devices to operate under wide ranges of temperature with high efficiency. For example, the estimated blocking voltage required for future electric warship applications is up to 40 kV [2]. Fulfilling these levels of requirements by using Si devices connected in series and parallel will not yield high efficiency in terms of devices' performances, reliability, and cost.

These have prompted research and development of wide band gap (WBG) semiconductor technology with superior electronics properties compared to Si, such as Silicon Carbide (SiC), Gallium Nitride (GaN), and diamond. Among them, diamond is regarded as one of the ultimate materials with extreme electrical and mechanical properties such as high critical electric field of 10-20 MV/cm (due to large band gap of 5.47 eV), high carrier mobility (3800 $cm^2.V^{-1}.s^{-1}$ for hole and 4500 $cm^2.V^{-1}.s^{-1}$ for electron), high saturation velocity of $2.7x10^7$ cm/s, and high thermal conductivity (22-24 W/(cm.K)) [3-6]. Calculations of different figure of merit (FOM) also show huge potential of diamond for high performance power semiconductor devices. Due to its radiation hard property, diamond based devices

are potential candidate for military and space applications where devices are subjected to extreme/harsh environmental conditions.

However, diamond is still in the early research stage and there are still many challenges to overcome, such as the fabrication process (growth process, large area substrate, defects, etc.), contact technology (reliability, metal-diamond interface, etc.), device designs and optimizations (device structure, edge termination, etc.), up-scaling of the devices, etc.

Difficulties in fabricating single crystal diamond for electronics purposes have caused development of diamond devices to fall behind SiC and GaN. Currently SiC devices such as SiC Schottky diode, Junction Field Effect Transistor (JFET), and Metal-Oxide-Semiconductor Field Effect Transistor (MOSFET) have made their entrance into commercial market, followed by GaN devices. Therefore, SiC and GaN based technology might be considered as the 3rd generation semiconductor, while diamond may be considered as future generation semiconductor [1].

Considering the potential of diamond materials and accompanied by the lack of diamond technology developments creates the motivation for exciting and worthy research undertakings. The scope of this research is mainly on the diamond Schottky barrier diode (SBD) for power electronics applications. We focus on the development, characterizations, analysis, modelling and simulations, and design optimizations of diamond power SBD.

1.2 Objectives and contributions of the thesis

Improvements of the semiconductor device characteristics often are the key factor in improving overall system performances in terms of size, efficiency, and weight. Theoretical calculations of diamond based power devices estimate huge improvements in performances compared to silicon devices or any other wide band gap materials based devices. Therefore advancement in diamond based power devices technology is important to cope with definite requirements of high ratings devices for future applications.

As diamond is still in the early research stage, we focus our research on the diamond power SBD. Among all devices, it has simplest structure consisting of metal-semiconductor junctions (ohmic and Schottky contact) which are the building blocks for more complicated devices such as JFET, MESFET, and HEMT.

Understanding of the diode's characteristics is important in analysing and realizing more advanced devices.

The objectives of this research are to review the current status of diamond power SBD, to study and investigate the characteristics of experimental diamond SBDs for power electronics applications, to develop accurate modelling and simulations approaches for device's design, analysis, and optimizations, and to develop optimal device design of high voltage diamond SBD.

The original contributions of this thesis can be summarized as follows:

- Performances of diamond m-i-p+ diode and diamond SBD were compared and studied by means of experiment data and numerical simulation results. Turn-off transient characteristics of the diodes at different temperatures were investigated using transient simulations in mixed-mode environment in TCAD Sentaurus software for the first time.
- Measurements and characterizations results of the fabricated vertical diamond SBDs with various dimensions of Molybdenum Schottky contact, field plate termination structure with high k dielectric Al_2O_3, and different Boron doping concentrations were presented.
- The non-ideal behaviours of the experimental Mo/diamond SBD were analysed based on metal-interfacial layer-semiconductor (MIS) model for the first time. Parameters extractions and determination of interface states charges density from current-voltage ($I-V$) and capacitance- voltage ($C-V$) measurements were presented.
- Rigorous modelling and simulations of non-ideal characteristics of the experimental Mo/diamond SBD were carried out in TCAD Sentaurus software by using MIS model. Parameter extractions and extensive simulations were conducted to best fit the measured forward and reverse bias $I-V$ characteristics simultaneously at different temperatures. Impacts of the interfacial layer and interface states charges at the metal-diamond interface to the forward and reverse bias performance of the diamond SBD were investigated by numerical simulations.

- Planar mesa structure with high k dielectric Al_2O_3 was proposed and investigated for the edge termination of the diamond power SBD for the first time. Design and optimization of the power SBD were carried out using numerical simulations in TCAD Sentaurus software. Forward and reverse bias performances of the planar mesa terminated SBD were evaluated and compared to those of conventional field plate terminated SBD.

1.3 Organization of thesis

The thesis is organized into eight chapters. Chapter 1 describes the background and motivations for this research, objectives and contributions, and organization of the thesis.

Literature review in Chapter 2 provides the properties of diamond material in comparison with other wide band gap materials like SiC and GaN and elaborates how these properties affect the potential performances of power devices. Global benefits of implementing wide band gap devices in terms of efficiency improvements and potential savings are discussed. Subsequently, we present different types of diamond diode and focus on the current status of unipolar p-type diamond Schottky barrier diode.

In Chapter 3, we introduce the numerical simulation software that was used to simulate the diamond devices in our study, i.e. finite element physics based TCAD Sentaurus software from Synopsys. Important physics models and parameters suitable for simulations of single crystal diamond devices are elaborated and discussed.

Next, analysis and investigations of the characteristics of diamond m-i-p+ diode and typical p-type diamond SBD are presented in Chapter 4 by means of experimental data and numerical simulation results. Transient simulations studies for both diodes at different temperatures are presented for the first time using TCAD Sentaurus software in mixed-mode environment.

Chapter 5 presents the experimental results of the vertical diamond SBDs with different size of Molybdenum Schottky contact and field plate termination structure using Al_2O_3 field oxide that were fabricated on different diamond wafers (p- and p+ layer stack). The non-ideal behaviours of the experimental Mo/diamond SBD were

analysed using MIS model to account for the Fermi level pinning at the Schottky metal-diamond interface. We then present characterization and parameters extraction of the diode including the determination of the interfacial layer thickness and interface states charges density from the measured current-voltage ($I-V$) and capacitance-voltage ($C-V$) characteristics.

Using these characterization and extraction methods based on the MIS model, we demonstrate rigorous approach to the modelling and simulations of non-ideal characteristics of the experimental Mo/diamond SBD in Chapter 6. The applied MIS model and parameters are able to fit simultaneously the measured forward and reverse bias $I-V$ characteristics of the investigated diamond SBD at different temperatures. In addition, the significance of the interfacial layer and interface states charges on the performances of the diamond SBD were examined by means of numerical simulations.

In Chapter 7, we propose planar mesa structure with high k dielectric Al_2O_3 for the edge termination of high voltage diamond power SBD. The forward and reverse bias performance of the planar mesa terminated SBD were evaluated and compared with those of conventional field plate terminated SBD through numerical simulations studies in TCAD Sentaurus software. The electric field distributions and effects of electric field crowding in the devices were analysed and taken into considerations for the design and optimization of the diodes.

Finally, Chapter 8 concludes and summarizes the thesis. Recommendations for future works are also included.

2 LITERATURE REVIEW

2.1 Introduction

Advancement in technology has driven the development of modern power devices for various applications. Recent demand on the power devices for transportation applications (electric vehicles, warships, and fighter planes), utility applications (power electronics converters for transmission systems, etc.), industry applications (high power motor drives, space exploration) requires power devices with higher blocking voltage, higher power, higher frequency, and high temperature capability which are beyond the theoretical limit of Silicon devices [2-4, 7]. These factors have prompted the development of power devices based on the wide band gap materials with superior properties.

Present applications of power devices can be found over broad range of current, voltage, and frequency ratings as shown in Figure 2-1 and Figure 2-2 [8]. To satisfy these broad ranges of applications, different power devices were developed over the time to suit certain applications.

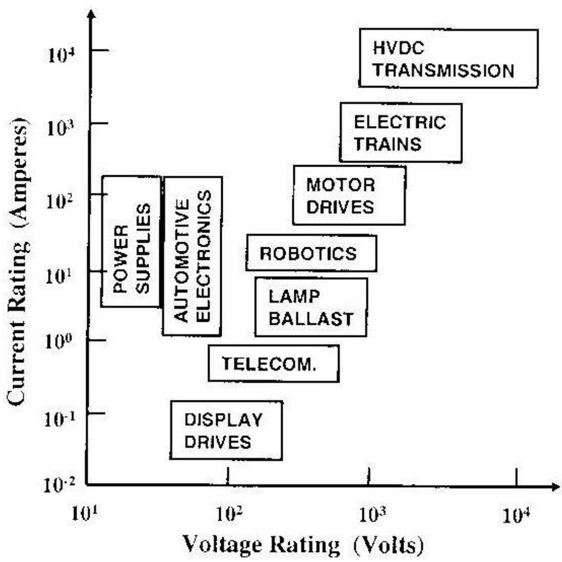

Figure 2-1: Present applications of power devices based on the voltage and current ratings [8].

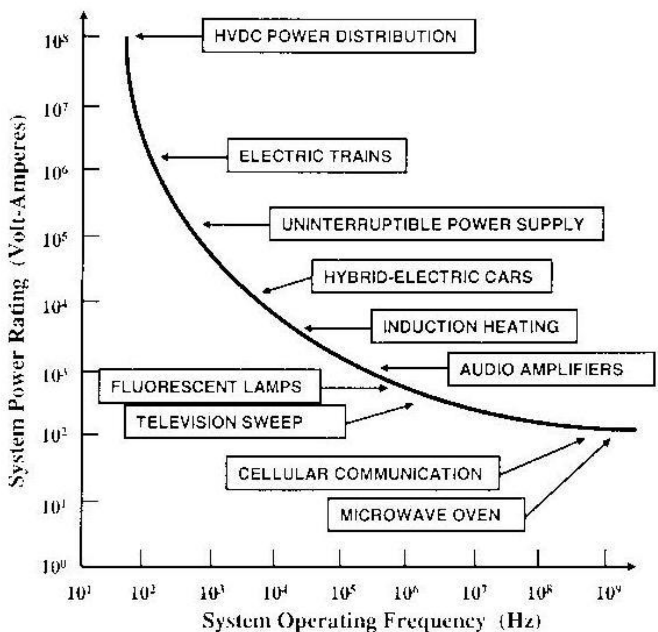

Figure 2-2: Present applications of power devices based on the frequency and power ratings [8].

2.1.1 Brief history on development of power devices and their applications

History of modern solid state power devices started in the 1950s, when vacuum tube devices were replaced with solid state devices, i.e. power bipolar junction transistor (BJT) for medium power applications and gate turn-off thyristor (GTO) for high power applications [8]. In 1970s, silicon power MOSFET was invented and used extensively for high frequency and low voltage (<100Volts) applications. In 1980s, invention of Insulated Gate Bipolar Transistor (IGBT) as a combination of Metal-Oxide-Semiconductor (MOS) and BJT technology made a successful breakthrough in most of medium and high power applications. Current power switching devices market is still dominated by Silicon devices:

- Thyristor for low frequency and high power applications, such as High Voltage Direct Current (HVDC) power distribution and locomotive drives. Individually, it can handle voltage over 6000 V and current of 2000 A.
- IGBT for medium frequency, medium and high power applications, best for voltage range of 300V to 3000V with high current handling capability.

- Power MOSFET for high frequency and low power applications (operating voltage less than 100 V), such as automotive electronics and switch mode power supply (SMPS).

The first solid state power rectifier introduced commercially was Silicon p-i-n diode in the 1950's. Later on, different designs of rectifiers were developed to suit different ratings requirements such as Si Schottky diode, Si Junction Barrier Schottky (JBS) diode, Si Trench MOS Barrier Schottky (TMBS) diode, Si Trench Schottky Barrier Controlled Schottky (TSBS) diode, Si Merged p-i-n Schottky (MPS) diode, etc. Reviews on different structures of power rectifiers and power switches for different applications can be found in [9, 10].

In year 2001, SiC Schottky diode was the first SiC devices made available commercially [11]. In the recent years, tremendous achievements have been made with introduction of commercial SiC power switches such as SiC JFET and SiC MOSFET [7, 12].

2.1.2 Wide band gap materials and their properties

Wide band gap materials refer to semiconductor material with large band gap (more than 1.7 eV, 2 eV, or even 2.5 eV). They include diamond (C), IV-IV-compound semiconductor SiC, III-V compound semiconductor GaN, Aluminium Nitride (AlN), Gallium Phosphide (GaP), or even II-VI compound semiconductors [11, 13]. Out of these materials, only SiC, GaN, and diamond are considered suitable material for power devices. They have comparable or higher thermal conductivity and carrier mobility compared to values in Silicon. Among these semiconductors, diamond has superior electrical properties which are ideal for power devices, i.e. highest band gap, breakdown electric field, electron and hole mobility, saturation velocity, and thermal conductivity. However, in terms of maturity of technological process, SiC and GaN are far more advanced. Based on the thermal expansion coefficient, SiC and GaN are also well match to the typical packaging materials [13].

Table 2-1 lists the important properties of SiC, GaN, diamond in comparison with Si and GaAs. Among these semiconductors, diamond has superior electrical

properties which are ideal for power devices, i.e. highest band gap, breakdown electric field, electron and hole mobility, saturation velocity, and thermal conductivity. However, in terms of maturity of technological process, SiC and GaN are far more advanced. Based on the thermal expansion coefficient, SiC and GaN are also well match to the typical packaging materials [13].

Table 2-1: Properties of wide band gap materials in comparison with Silicon and Gallium Arsenide.

Property	Si	GaAs	4H-SiC	GaN	Diamond
Band Gap (eV) [14]	1.12	1.424	3.26	3.295	5.47
Relative Dielectric Constant [14]	11.7	12.9	10	5.35	5.7
Breakdown Electric Field (MV/cm) [14]	0.41	0.48	2.4	5	20
Electron Mobility ($cm^2.V^{-1}.s^{-1}$) [14]	1450	8600	900	2000	4500
Hole Mobility ($cm^2.V^{-1}.s^{-1}$) [14]	480	130	120	200	3800
Saturation Velocity x10^7 (cm/s) [14]	0.86	0.72	2	2.5	2.7
Thermal Conductivity ($W.m^{-1}.K^{-1}$) [11, 13]	130	55	380	110	600-2000
Coefficient of Thermal Expansion (ppm/K) [13]	2.6	5.73	5.12	5.4- 7.2	0.8
Melting Point (^{0}C) [15]	1420	1240	2830	2500	4000
Direct/ Indirect Band Gap [13]	Indirect	Direct	Indirect	Direct	Indirect

GaN is suitable for unipolar devices due to its high electron to hole mobility ratio. High frequency performance and direct band gap of GaN make it suitable for optoelectronics and radio frequency applications [3]. However, usage of GaN as power rectifiers (Schottky barrier diode) and power switches (MOSFET and HEMT) have also been demonstrated in recent years [3, 16]. While SiC has poorer electrical properties compared to GaN, it has high thermal conductivity that makes it suitable for high temperature and high power devices. At this moment, SiC is

used in the most commercially available wide band gap devices [17]. Performance comparisons solely based on materials' properties for these semiconductors can be seen from their Figures of Merit (FOM) in Table 2-2 for SiC, GaN, diamond, GaAs and Si [3].

Table 2-2: Main Figure of Merits (FOM) of wide band gap materials in comparison with Silicon and Gallium Arsenide* [3].

Figures of Merit	Si	GaAs	4H-SiC	GaN	Diamond
JFM	1.0	1.8	215.1	215.1	81000
BFM	1.0	14.8	223.1	186.7	25106
FSFM	1.0	11.4	61.2	65.0	3595
BSFM	1.0	1.6	12.9	52.5	2402
FPFM	1.0	3.6	56.0	30.4	1476
FTFM	1.0	40.7	3424.8	1973.6	5304459
BPFM	1.0	0.9	35.4	10.7	594
BTFM	1.0	1.4	458.1	560.5	1426711

*All values are normalized with respect to Si.

*Explanations of the FOMs are [3]:

- JFM: Johnson's figure of merit, a measure of the ultimate high-frequency capability of the material
- BFM: Baliga's figure of merit, a measure of the specific on-resistance of the drift region of a vertical FET
- FSFM: FET switching speed figure of merit
- BSFM: Bipolar switching speed figure of merit
- FPFM: FET power-handling-capacity figure of merit
- FTFM: FET power-switching product
- BPFM: Bipolar power-handling-capacity figure of merit
- BTFM: Bipolar power-switching product

Relationship between the semiconductor's properties and performances of the devices are discussed in the following section.

2.1.3 Fundamental properties relevant to power semiconductor devices

Ideal power semiconductor device incurs zero conduction loss and switching loss. The device should be able to conduct any amount of current with zero voltage drop and block any applied reverse voltage with zero leakage current. It should also turn-on and turn-off instantaneously. While such ideal device does not exist in reality, device designers constantly strive to achieve the best trade-off for those device's behaviours.

Wide band gap materials such as SiC, GaN, and diamond are chosen for power devices due to their superior properties compared to Silicon. These superior properties affect the performance of power semiconductor devices.

1. Leakage current and device operating temperature

Due to the large energy band gap of wide band gap materials, their intrinsic carrier concentrations n_i are much lower compared to that of Si at the same temperature. Diamond has the largest band gap and therefore the lowest n_i (in the order of 10^{-27}cm^{-3} in intrinsic diamond at room temperature) compared to other wide band gap materials [18]. As a result, generation of carrier in the depletion region is smaller, and consequently, leakage current (usually proportional to n_i or n_i^2) is smaller. On the reality, other issues such as defects, dislocation, and traps may lead to higher leakage.

In small band gap device, when temperature is high, thermal excitation of carriers creates high number of n_i that is comparable to the doping concentration, thus affecting the device's performances (uncontrolled conduction). On the other hand, with larger band gap, it is possible to have low enough n_i even at a high temperature. It means that materials with large band gap can have more stable operation at high temperature, without negative effect of thermal generation.

2. Breakdown voltage, thickness, and on-resistance loss

In power device applications, breakdown voltage capability is a very important aspect. The breakdown voltage is the voltage that can be supported by the device just before breakdown. The maximum electric field that can be supported before breakdown is called breakdown/ critical electric field. Due to the large band gap of wide band gap materials, they have larger breakdown electric field compared to Si. As a result, they can withstand higher voltage across them which effectively increase the breakdown voltage capability.

Using a single device with high breakdown capability, instead of using several of devices with low breakdown voltage ratings that are connected in series and parallel, will increase the overall efficiency, reduce synchronization problems, and remove the unnecessary protection devices, anti-parallel diodes, etc., which ultimately reduce the cost of the system and improve the reliability.

Effect of high breakdown electric field value to breakdown voltage can be shown, for example from analysis of breakdown voltage of an abrupt p+ n junction where depletion region is fully supported in the n- region. Assuming complete ionization, the breakdown voltage V_{Br} of abrupt p+ n junction can be related to critical/ maximum breakdown electric field E_{Crit} by Eq. (2.1) [3].

$$V_{Br} = \frac{\varepsilon_S E_{Crit}^2}{2qN_D} \tag{2.1}$$

q is the charge of an electron, ε_S is the permittivity of semiconductor, and N_D is the donor doping concentration of uniformly doped n- region. From Eq. (2.1), we can make a simple comparison of the breakdown voltage of abrupt p+ n junction made of different materials. For the same N_D, the V_{Br} ratio is given by the ratio of their $\varepsilon_S E_{Crit}^2$. Therefore, V_{Br} of wide band gap materials are much larger due to their larger E_{Crit} as shown in Figure 2-3. As expected, theoretical breakdown voltage of the diamond is the highest (around 514 times of Si).

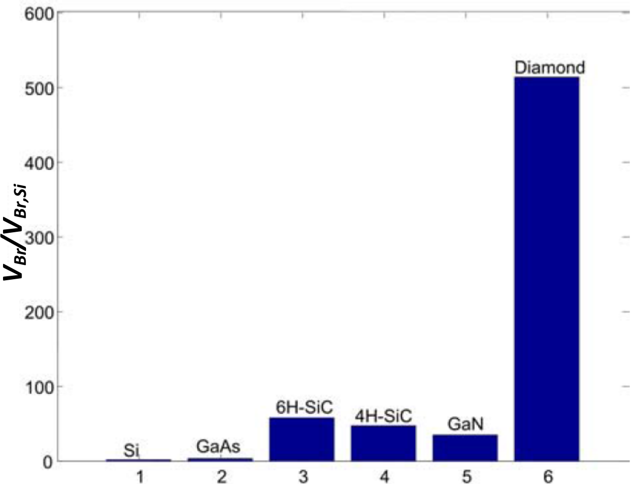

Figure 2-3: Maximum breakdown voltage of a power device at the same doping density normalized to Si [3].

In addition, high breakdown electric field also has positive impact on the thickness of the device. Breakdown voltage can be related to drift region (depletion region) thickness w by Eq. (2.2) [3, 8].

$$V_{Br} = \int E.dx = \frac{WE_{Crit}}{2} \tag{2.2}$$

For the same device's breakdown voltage rating, wide band gap devices require thinner drift region compared to Silicon devices. Figure 2-4 shows comparisons of required w for different breakdown voltage computed for different materials [3].

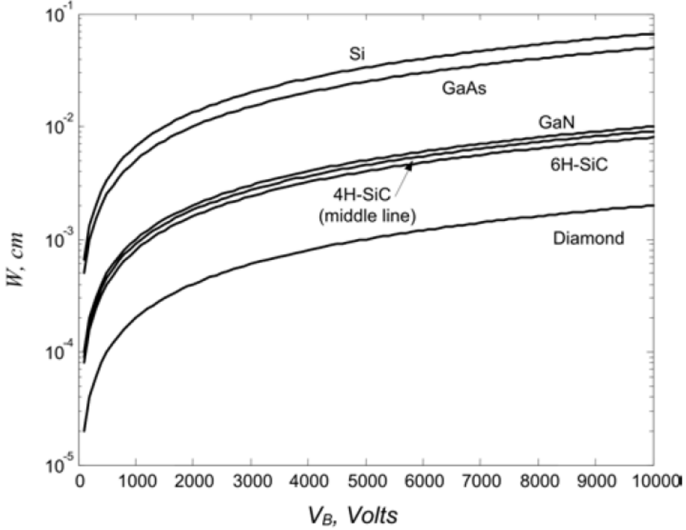

Figure 2-4: Required width of the drift region for different breakdown voltage ratings for different materials [3].

As the width of drift region is decreased, doping concentration N_D needs to be increased to maintain the same charge [11]. From Poisson's equation, W is related to N_D and E_{Crit} by Eq. (2.3), assuming complete ionization of dopants [3, 8, 11].

$$qN_D = \frac{\varepsilon_S E_{Crit}}{W} \tag{2.3}$$

Larger N_D would mean huge decrease in the resistance of the drift region. Furthermore, the specific on-resistance $R_{on,sp}$ of the drift region related to V_{Br} and E_{Crit} is given in Eq. (2.4) for unipolar power devices [3, 8] with μ_n as the electron mobility

$$R_{on,sp} = \frac{4{V_{Br}}^2}{\varepsilon_S \mu_n E_{Crit}^3} \tag{2.4}$$

Based on Eq. (2.4), diamond should have the lowest specific on-resistance in the drift region for a given V_{Br}, mainly due to the high critical electric field and carrier mobility.

3. Frequency/ speed of the device

Wide band gap devices are suitable for high speed/frequency applications because of their high drift saturation velocity. Materials like SiC, GaN, and diamond have saturation velocity more than twice of value in Si such that they can be switched at higher frequency. With high drift velocity, diode made of wide band gap materials is expected to have faster removal of charges in depletion region, smaller reverse recovery current, and faster recovery time [3].

4. Thermal conductivity

In the power devices, thermal conductivity for heat dissipation is important parameter. Higher thermal conductivity means better conduction of heat that allows higher power density in a device, more stable operation at higher temperature, reduction of thermal management requirements (cooling system, etc.), and therefore reduction of the cost, size, and weight of overall system [19]. Diamond has the

highest thermal conductivity, followed by SiC. As SiC has higher thermal conductivity compared to GaN, SiC is preferred for power device applications [3].

5. Radiation hard

Other than thermal energy, radiation energy can also excite electron to the conduction band and promote uncontrolled conduction. Wide band gap materials are more radiation hard because of their larger band gap (larger radiation energy is needed to excite electron). Suitable applications for example are diamond detectors for radiation monitoring, ultraviolet (UV) photolithography, etc. [20, 21].

6. Compatibility to packaging materials

To be of practical use, device (chip) needs to be packaged to protect it chemically and physically from environmental impurities. Thus, it is important to consider the package compatibility to the device. In order to minimize the thermal stress on device and package, it is important to have small Coefficient of Thermal Expansion (CTE) mismatch between the device/chip and the package. CTE of different packaging materials are listed in [13]. SiC and GaN have better compatibility (smaller CTE mismatch) to the existing packaging materials compared to Si. On the other hand, CTE of diamond is very low compared to the currently available packaging materials. However, this should not be a reason of not pursuing diamond device because after all, diamond is the future semiconductor materials, and there is future possibility of better matched packaging materials.

2.1.4 Role of wide band gap devices

Throughout the years, power electronics has played important roles in the development of many utilities, ranging from the power transmission and distribution, submarine, automobile, aerospace, industry, consumer electronics, etc. Nowadays, it is hard to find an application that is totally free of power electronics. Global market for power semiconductor devices is estimated to be around 10 billion and it is growing by 8%- 10% per year [22].

The main contribution of wide band gap devices is ultimately higher efficiency of the system for energy distribution and consumption. As electric energy is generated and distributed to end users, it goes through a number of conversions in power electronic converters for various purposes (e.g. power supplies for computer, servers, telecom systems, motor drives, etc.). Currently, these conversions are highly inefficient such that approximately only 20% of the generated energy reaches the end users [17]. Most of the losses are dissipated in the power semiconductor devices which are based on Silicon devices. Therefore, usage of wide band gap devices with superior performances compared to conventional Silicon devices will allow higher efficiency of electric energy distribution and transformation.

As power electronics devices have widespread usage across applications, improved efficiencies of wide band gap power electronics devices has significant impact on the efficient use of electricity. Worldwide electric energy consumption can be broken down by applications to approximately 51% for motion control, 16% for heating and cooling, 14% for information technology, and 19% for lighting [23]. Usage of SiC devices with variable speed drives can increase the system efficiency for motion control (applications such as washing machines, industrial motor, pumps, and robotics) and heating and cooling area (mainly compressor and fans). In the information technology area, efficiency can be improved by implementation of SiC devices for switch mode power supplies (SMPS) and GaN devices in radio frequency (RF) applications (wireless broadcast). Usage of SiC devices in the solid state ballast for fluorescent lighting and potential solid state lighting using GaN emitters can further increase the efficiency. Therefore, widespread applications of SiC devices for SMPS and motor drives (variable speed drives) and GaN HEMT for RF applications offer estimated potential savings of $30 billion/year, which is estimated only for electricity usage [23].

Recent trends in green technologies as parts of effort to face global warming have also increased the impact of energy efficient power electronics even more. Worries about increasing oil prices and diminishing oil resources has made more and more industries to introduce electric or hybrid electric vehicle (HEV) to replace traditional gasoline and diesel engines. Military is ready to go for all electric warships and electric fighter planes [2]. Thus, global impacts of energy efficient WBG power electronics devices are becoming more important than ever before.

2.2 Diamond diode

Even though diamond electronic devices technology is still in its infancy, many diamond devices have already been demonstrated. Various types of diodes such as p-n diodes, p-i-n diodes, Schottky diodes, radiation detectors, etc. and various types of transistors like MISFETs, MESFETs, and JFETs have been reported in the literature [22]. Among these devices, Schottky barrier diode has the simplest structure and it is the foundation/ building block for many other devices. It is simple to fabricate (compared to other devices) and understanding of its characteristics is essential in designing more complex devices.

2.2.1 Classification of diamond crystals

First of all, it is important to understand the type of diamond crystal as various diamond devices are built on them. Diamond crystals are classified based on the impurities concentration of Nitrogen (N) and Boron (B) atoms measured by infrared (IR) spectrometer and their arrangement in the diamond crystal lattice. Diamond can be classified into several types as indicated in Table 2-3 [14, 24, 25]. This classification is not restricted to natural diamond only, but also synthetically grown diamond by high-pressure high-temperature (HPHT) or chemical vapour deposition (CVD).

Table 2-3: Classification of diamond crystal

Diamond classification	Specifications
Type I:	-Has enough concentration of N (0.3-0.5% N concentration) to be measured by IR spectrometry.
• Type Ia:	-N atoms that replace the C atoms (substitutional N atoms) aggregate together and in close proximity to each other.
− Type IaA	-Pair of N atoms occupies neighbouring substitutional lattice site. -Usually known as A aggregates or A centers.

	C — C — C — C C — C — N — N C — C — C — C N — N — C — C
– Type IaB	- Cluster of 4 substitutional N atoms that symmetrically surround a vacancy (V) in diamond crystal lattice. - Usually known as B aggregates or B centers. C — C — C — C C — C — N — C C — N — V — N C — C — N — C
• Type Ib	- N atoms that replace the C atoms are isolated from each other. - Usually known as isolated N, single substitutional N, or C centers. - Mostly synthetic HPHT diamond crystals are of this type. C — C — C — N N — C — C — C C — C — N — C C — C — C — C
Type II:	- Has very low N concentration $< 10^{17}$ cm^{-3} below IR detection limit.
• Type IIa	- Has a very low N and B impurity which makes it the

	purest form of diamond crystal. - Very low defects results in colourless and transparent crystal. - Mostly gemstone diamond crystal. C — C — C — C C — C — C — C C — C — C — C C — C — C — C
• Type IIb	- Has B concentration higher than N concentration which results in p-type semiconducting properties. - Rare in nature. C — C — C — B C — C — C — C C — B — C — C C — C — C — C
• Type IIc	- Has high concentration of chemically bonded Hydrogen with IR absorptions at 2915 cm^{-1}, 2840 cm^{-1}, and possibly 1465 cm^{-1}.

2.2.2 Type of diamond diode

We categorized diamond diodes based on the material, structure, and type of conduction. They are summarized as follow:

Based on the material

- **Single crystal diamond diode**

Single crystal diamond is the most widely used materials for diamond diode, especially for high voltage high power device. Low defects density and uniform crystal orientation yield high carrier mobility and high breakdown electric field. Single crystal p-type diamond Schottky diode with breakdown voltage up to 10 kV and breakdown electric field up to 7- 9.5 MV/cm have already been demonstrated [26, 27].

- **Polycrystalline diamond diode**

Before the development of single crystal diamond growth technology, polycrystalline diamond was the popular diamond film used. Compared to single crystal diamond, it is cheaper and can be easily grown on large Si wafer [28]. However, large defects density, grain boundaries, and surface roughness degrade the superior electronic properties of diamond.

- **Hetero-junction diode**

Due to unavailability of shallow donor in diamond, more practical n-type materials with shallow donor are used to form p-n junction with p-type diamond, thus forming hetero-junction device. Several attempts to make such device have been reported in the literature:

  - n-type Silicon doped AlN film & p-type single crystal diamond [29]
  - n-type Nitrogen doped ultra-nano-crystalline diamond (UNCD) & p-type single crystal diamond [30, 31]
  - n-type Silicon & p-type polycrystalline diamond [32]
  - n-type Silicon doped cubic Boron Nitride (cBN) bulk crystal & p-type Boron doped diamond [33, 34]

Based on the structure

- **Vertical structure**

Vertical structure is preferred for high voltage devices because of several reasons [35]. It allows lower series resistance and more uniform electric field distribution in device (therefore higher blocking ability). Since it is grown on free

standing sample with ohmic back contact, it allows maximum wafer cross-sectional area to be utilized for the contact (therefore increasing current carrying capability). Figure 2-5 shows the structure of vertical diode without edge termination.

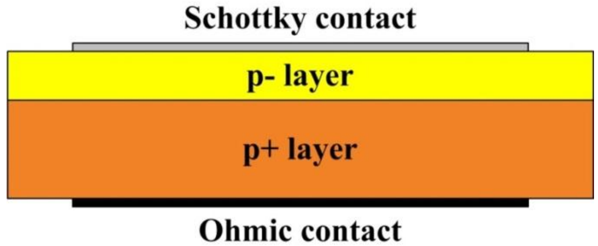

Figure 2-5: Vertical diode structure

- **Lateral/ planar structure**

Even though vertical structure device is usually used in high power device, low resistivity substrates with back contact layer are very limited in terms of the size and resistance and they are not available commercially at this moment [36]. Thus, many diamond devices are fabricated in lateral structure where ohmic contact and Schottky contact are at the same side of the chip, as shown in the Figure 2-6 [37]. Lateral structure is not suitable for high voltage devices due to non-uniform distribution of electric field and electric field crowding in the device which might cause device's premature breakdown. Furthermore, this structure exhibits large on-resistance due to poor ohmic contacts and non-optimum device geometry.

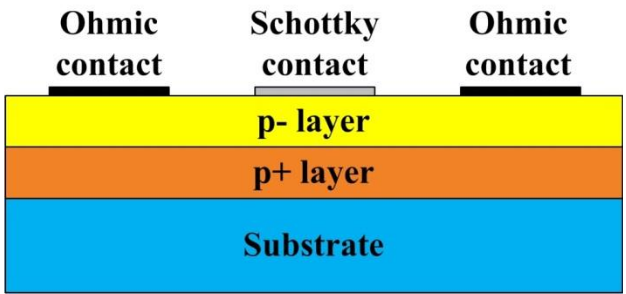

Figure 2-6: Lateral/ Planar diode structure

- **Pseudo-vertical structure**

Pseudo-vertical structure was developed due to difficulties in getting high quality free standing substrate and the drawbacks of lateral diode structure [36]. While low density of defects (such as edge or mixed threading dislocations) can be achieved with high quality semi-insulating wafer (HPHT Ib substrate), fabrication

of ohmic contact in pseudo-vertical structure is more complicated [38]. Furthermore, large wafer area is needed to accommodate both Schottky and ohmic contact and the on-resistance is limited by the parasitic resistance of the p+ layer [39]. Structure of a pseudo-vertical device is shown in Figure 2-7.

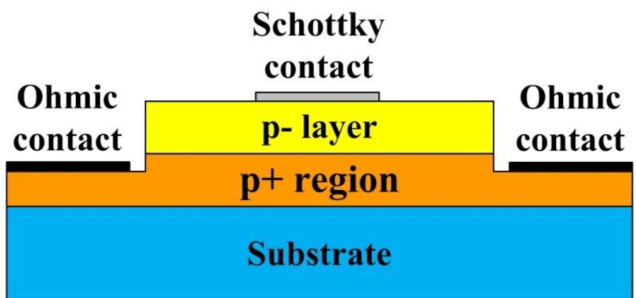

Figure 2-7: Pseudo-vertical diode structure

Up to this date, pseudo-vertical Schottky barrier diode with low leakage and high breakdown field up to 3.1 MV/cm has been reported in the literature [40].

<u>Based on the type of conduction</u>

Based on the carriers involved in the conduction, diamond diodes can be categorized into unipolar and bipolar diode.

- **Unipolar**

  In the unipolar device, there is only one type of carrier involved in the conduction, i.e. electrons or holes. Several unipolar devices that are reported in the literature are:

  - p-type Schottky barrier diode and diamond m-i-p+ diode [39, 41]
  - n-type Schottky barrier diode [42, 43]
  - Schottky p-n junction diode (SPND) [44]
  - Diamond merged diode [45]

- **Bipolar**

  There are big challenges to realize bipolar devices due to unavailability of shallow n-type dopant in diamond. Many attempts were carried out by using different donor dopant for diamond and likewise by utilizing n-type semiconductor

that is not diamond material (hetero-junction device). Several bipolar devices have been reported in the literature:

- p-i-n diode [46]
- p-n diode [47, 48]

2.2.3 Unipolar p-type diamond Schottky barrier diode

Because of high ionization energy of n-type dopant in diamond (the shallowest is 0.57 eV by Phosphorous dopant), the most investigated diamond diode is unipolar p-type based diamond SBD. In the literature, p-type diamond SBD with high blocking voltage (6.5kV, 7.5 kV, and 10 kV), high breakdown electric field (7-9.5 MV/cm), and high operating temperature (up to 1000^0C) have been demonstrated [26, 27, 49-51]. Switching characteristics of diamond SBDs have also been measured even at elevated temperature [52-54].

Despite of these, diamond device technology is still in infancy and there are many issues and challenges to be solved. The nature of metal-diamond interface is still poorly understood. Schottky barrier height dependence on metal work function is unclear and highly dependent on the fabrication process, especially surface treatment. Main issues related to contact technology are contact adhesion, Fermi level pinning, stability at high temperature, and resistance. Recent works on Ru/diamond SBDs have revealed stability over long time and high temperature condition [55].

Most of the fabricated SBDs up to this date yield breakdown electric field less than 4 MV/cm [56], far from the normally quoted value of 10- 20 MV/cm for diamond material. In addition, large leakage current is also observed during reverse bias operation. Explanations using thermionic field emission current transport, contact inhomogeneity, and tunnelling through defects have been proposed [37, 57, 58].

To increase the breakdown capability of the SBDs, quality of the synthetic diamond must be improved. Furthermore, design and optimization of termination structure is crucial to reduce electric field crowding in the device. Several termination structures have been proposed in the literature such as field plate termination structure and ramp oxide termination structure utilizing high k dielectric oxide, etc.

In the design of diamond SBDs, high breakdown voltage and low forward loss (low on-resistance) is desired. However, trade-off must be made between these forward and reverse bias properties in terms of the choice of doping concentration and thickness of the drift/ depletion region. High breakdown voltage requires thick drift region with low doping concentration which will increase on-resistance. Moreover, incomplete ionization due to high ionization energy of the dopant causes low hole concentration and thus higher on-resistance in the drift region. To go around these problems, new device concepts such as m-i-p+ diode, diamond merge diode, and delta-doped Schottky diode have been proposed in the literature [45, 59].

To achieve high power device with high current carrying capability, device with larger cross-sectional area need to be realized. Several works on device scaling based on pseudo-vertical SBD structure have been reported [56, 60]. In these studies, degradation in the device performance such as multiple barrier formation and increased leakage current were noticed due to incorporation of defects in diamond. In addition, larger size diodes also exhibit smaller breakdown electric field [39, 60, 61].

To sum up, there are several key factors for a device to be considered for commercialization, i.e. device performances and cost factor. Device's performances and reliabilities must be good enough compared to its alternative/ competitor devices for reasonable cost. For a commercialization purpose, technology for device's mass production must be available to bring the cost down. Thus availability of good quality substrate wafer with reasonable area for mass production is crucial. Diamond power device is still in the early research stage and there is still long way to go for commercialization of diamond devices.

2.3 Conclusions

In this chapter, we have highlighted ever increasing demands for high ratings devices, especially in power electronics applications and the limitation of Si material to fulfil those demands. The solutions might lie on the devices based on wide band gap materials with superior properties compared to Si, such as SiC, GaN, and diamond. While diamond can be considered as the ultimate material among them, SiC and GaN technologies are much more mature, especially with the commercialization of SiC devices such as SiC Schottky diode, JFET, and MOSFET.

Applications of WBG devices like SiC and GaN devices are expected to increase overall system efficiency and incur huge potential savings.

Furthermore, state of the art of diamond diode technology is elaborated and different types of diamond diode are revealed. Because of the high ionization energy of donor dopant in diamond, development of diamond diode mostly focuses on the p-type unipolar Schottky barrier diode. Up to this date, diamond SBDs with high voltage ratings up to 10 kV and high breakdown electric field of 7- 9.5 MV/cm have been demonstrated. High temperature operations of diamond SBD up to 1000^0C have also been reported in the literature.

However, diamond technology is still in early research stage and there are many challenges to overcome to realize high-power high-voltage high-frequency devices. Fabrication processes need to be improved to produce consistently large area high quality synthetic single crystal diamond with low defects density. Further studies on contact properties, reliabilities, and the effects of surface treatments are required. Moreover, design and optimization of the diode accompanied with efficient edge termination structure is crucial to improve the performances of diamond Schottky barrier diode.

3 MODELLING OF SINGLE CRYSTAL DIAMOND FOR IMPLEMENTATION IN NUMERICAL SIMULATIONS

3.1 Introduction

Diamond is still in the early research stage and there are still many challenges to overcome such as the growth and fabrication process, the quality of synthetic diamond crystal, the properties of the contact, and the design and optimizations of the device's structure. Unavailability of shallow dopant (especially donor dopant) prompted the development of different device concepts and structures such as delta doped devices, metal-intrinsic-p+ (m-i-p+) diode [21], hydrogen induced surface channel FET [62], ramp oxide termination structures [63], etc. Additionally, difficulties in fabricating diamond devices in terms of cost, effort, and time points out the importance of modelling and simulation tools as a low-cost and effective method to study, analyse, design, and optimize diamond devices.

Although several works on the simulation of diamond power devices have been reported in the literature [52, 64-67], accurate modelling and simulations remain challenging at this moment because of many unknown parameters of diamond materials. Therefore, modelling of diamond power device is susceptible to approximations at this stage.

Throughout this study, modelling and simulations have been carried out using finite element method (FEM) in two dimensions in TCAD Sentaurus software from Synopsys. Drift-diffusion transport model is implemented. Emphasis is given to the simulations of unipolar Boron doped single crystal CVD diamond devices which are the most developed devices up to this date. Various physics models and parameters suitable for diamond materials are implemented. Among them, some of the very important models: incomplete ionization model, mobility model, and impact ionization model are discussed in this chapter.

Appendix A gives a brief introduction on the TCAD Sentaurus software. Other fundamental parameters such as the band gap and dielectric constant of diamond are presented in Appendix B in this thesis. Command and parameter files for SSE and SDevice implemented in our simulation work on diamond devices are also presented in the appendixes.

3.2 Incomplete ionization model

Incomplete ionization can occur in diamond because of the wide band gap of diamond material (5.47 eV) and unavailability of shallow dopant in diamond. The smallest known ionization energies are 0.57 eV for Phosphorous donor (n-type dopant) and 0.37 eV for Boron acceptor (p-type dopant) [22]. These high activation energies result in low carrier activation at room temperature.

We simulate this phenomenon in TCAD Sentaurus for Boron acceptor in diamond by implementing incomplete ionization model given by Eq. (3.1) [68, 69] for Boron concentration less than $N_{A,crit}$ of 3x10^{19} cm^{-3}. For Boron concentration higher than $N_{A,crit}$, hopping conduction starts to occur, activation energy starts to decrease rapidly, and conduction increases rapidly towards metallic type conduction at concentration of 3x10^{20} cm^{-3} [14, 22]. Therefore, we assume complete ionization for Boron concentration higher than $N_{A,crit}$. These effects can be observed from the variations of diamond resistivity with Boron concentrations as shown in Figure 3-1 [70].

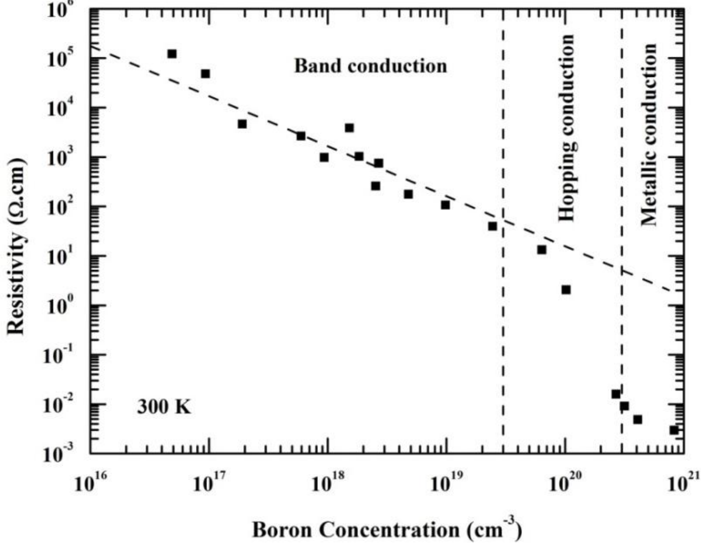

Figure 3-1: Variations of resistivity of Boron doped diamond at 300 K with respect to the Boron doping concentrations [70].

$$N_A^- = \frac{N_A}{1 + g_A exp\left(\frac{E_A - E_F}{kT}\right)} \tag{3.1}$$

In Eq. (3.1), N_A^- is the number of ionized acceptor, N_A is the acceptor doping concentration, E_F is the Fermi level, and E_A is the acceptor ionization energy. For Boron concentration less than 10^{25} cm^{-3} (Experimental evidence showed that the solubility limit of Boron in diamond is ≥ $1.4x10^{22}$ cm^{-3} [22]), E_A can be approximated as temperature independent function with dependence on concentration as given by

$$E_A = E_{A0} - \alpha\left(N_A - N_D\right)^{1/3} \tag{3.2}$$

with N_D as the concentration of compensating donor, E_{A0} = 0.37 eV, and α = $4.1x10^{-8}$ eV.cm [71]. Variation of Boron activation energy with Boron concentration in diamond, assuming negligible compensation ($N_D \approx 0$) is shown Figure 3-2.

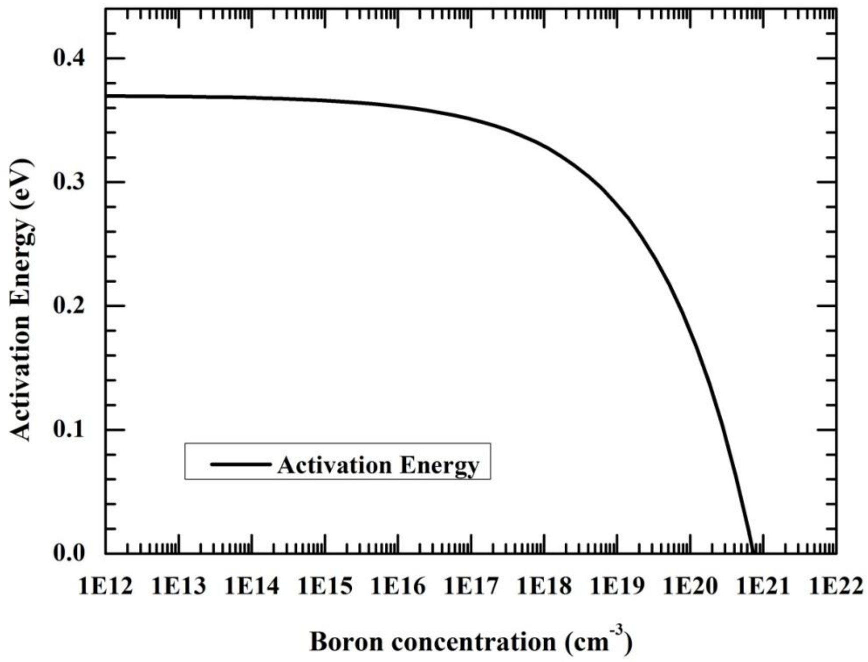

Figure 3-2: Variations of Boron activation energy with Boron concentration.

g_A in Eq. (3.1) is temperature dependent degeneracy factor for acceptor level given by Eq. (3.3) with Δ_{ga} = 6 meV [72].

$$g_a = 4 + 2\exp\left(\frac{-\Delta_{ga}}{kT}\right) \tag{3.3}$$

For non-degenerate semiconductor under thermal equilibrium conditions, electron and hole concentration can be described by Eq. (3.4) and (3.5) shown below.

$$n = N_C exp\left[\frac{-(E_C - E_F)}{kT}\right] \tag{3.4}$$

$$p = N_V exp\left[\frac{-(E_F - E_V)}{kT}\right] \tag{3.5}$$

N_C and N_V are effective density of states in the conduction band and in the valence band. They are given by

$$N_C = 2\left[\frac{2\pi m_{e,dos} kT}{h^2}\right]^{3/2} \tag{3.6}$$

$$N_V = 2\left[\frac{2\pi m_{h,dos} kT}{h^2}\right]^{3/2} \tag{3.7}$$

where h is Planck constant, $m_{e,dos}$ and $m_{h,dos}$ are density of states effective mass for electron and hole. In diamond, $m_{e,dos}$ = 0.56 m_e and $m_{h,dos}$ = 0.8 m_e [22]. The intrinsic carrier concentration n_i can be related to p and n as follows

$$n_i^2 = pn = N_C N_V \exp\left(\frac{-E_g}{kT}\right) \tag{3.8}$$

where E_g is the band gap of diamond (5.47 eV). Due to the wide band gap of the diamond, the intrinsic carrier concentration is very low at room temperature, as shown in Figure 3-3.

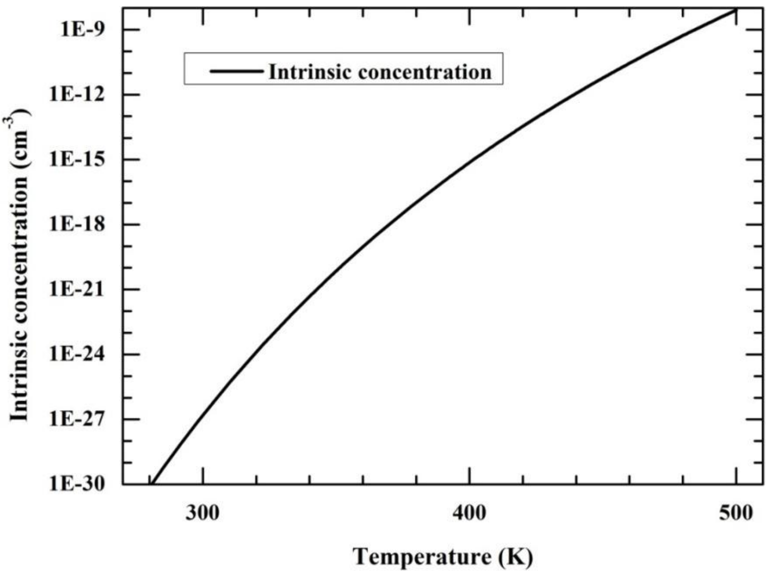

Figure 3-3: Intrinsic concentration in diamond as function of temperature.

Another expression of ionized acceptor concentration can be achieved by substituting Eq. (3.5) to (3.1), and taking $E_V = 0$ as reference level.

$$\mathrm{N}_A^- = \frac{N_A}{1 + g_A \dfrac{p}{N_V \exp\left(\dfrac{-E_A}{kT}\right)}} \tag{3.9}$$

Hole concentration in diamond under thermal equilibrium can be evaluated by considering charge neutrality condition given in Eq. (3.10), where N_A^- and N_D^+ are the number of ionized acceptor and the concentration of ionized compensating donor.

$$p + N_D^+ = n + N_A^- \tag{3.10}$$

By solving Eq. (3.8), (3.9), (3.10), and assuming complete ionization of compensating donor ($N_D = N_D^+$), hole concentration in Boron doped diamond can be evaluated as

$$\frac{p(p+N_D) - n_i^2}{N_A - N_D - p - \dfrac{n_i^2}{p}} = \frac{N_V}{g_A} \exp\left(\frac{-E_A}{kT}\right) \tag{3.11}$$

The degree of Boron ionization at different range of temperature based on Eq. (3.11) for concentration less than $3\text{x}10^{19}$ cm^{-3} is shown in Figure 3-4 for the case of negligible compensation ($N_D \leq 1\text{x}10^{10}$ cm^{-3}). For Boron doping of 10^{16} cm^{-3} at

room temperature (300K), it can be observed that the not all dopants are ionized and the yielded hole concentration is only around 10^{14} cm^{-3}.

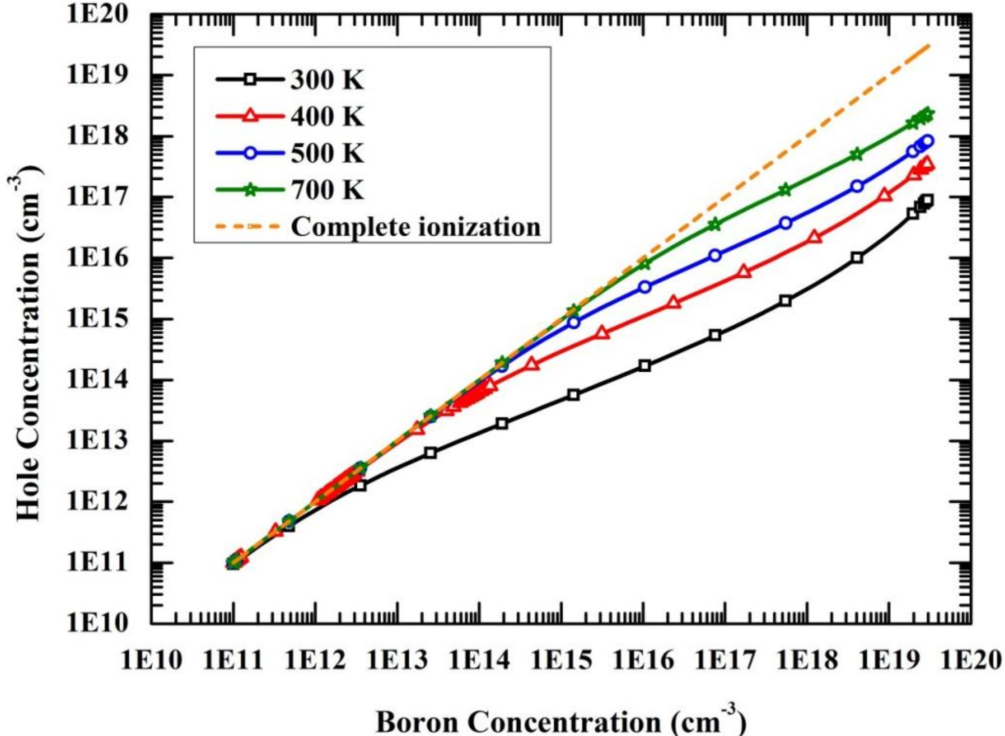

Figure 3-4: Hole concentration against Boron concentration in diamond for negligible compensation ($N_D \leq 1 \times 10^{10}$ cm^{-3}).

3.3 Mobility model

3.3.1 Low field mobility

The low field mobility model describes mobility of carriers under low electric field, where mobility μ_{low} is independent of electric field. In this case, carrier's drift velocity v is proportional to the electric field E_f .

$$v = \mu_{low} E_f \tag{3.12}$$

In the simulations, the low field mobility is modelled by University of Bologna bulk mobility model to take into account temperature dependence and doping concentration dependence. This mobility model is expressed in Eq. (3.13) [68].

$$\mu_{dop}(N_D,N_A,T)=\mu_0(N_D,N_A,T)+\frac{\mu_L(T)-\mu_0(N_D,N_A,T)}{1+\left(\frac{N_D}{C_{r1}(T)}\right)^{\alpha}+\left(\frac{N_A}{C_{r2}(T)}\right)^{\beta}}-\frac{\mu_1(N_D,N_A,T)}{1+\left(\frac{N_D}{C_{s1}(T)}+\frac{N_A}{C_{s2}}\right)^{-2}}$$

(3.13)

$\mu_L(T)$ is the temperature dependent lattice mobility model given by

$$\mu_L(T)=\mu_{\max}\left(\frac{T}{300K}\right)^{-\gamma+c\left(\frac{T}{300K}\right)} \tag{3.14}$$

with $\mu_{\max}$ as the lattice mobility at room temperature. $\mu_0(N_D,N_A,T)$ and $\mu_1(N_D,N_A,T)$ are given by Eq. (3.15) and (3.16) below.

$$\mu_0(N_D,N_A,T)=\frac{\mu_{0d}(T)N_D+\mu_{0a}(T)N_A}{N_A+N_D} \tag{3.15}$$

$$\mu_1(N_D,N_A,T)=\frac{\mu_{1d}(T)N_D+\mu_{1a}(T)N_A}{N_A+N_D} \tag{3.16}$$

The temperature dependency of parameters $C_{r1}(T)$, $C_{r2}(T)$, $C_{s1}(T)$ can be described with relationship given by

$$Par(T)=Par_0\left(\frac{T}{300K}\right)^{\gamma_{par}} \tag{3.17}$$

where $Par(T)$, Par_0, and γ_{par} are the temperature dependent parameter's value, parameter's value at 300 K, and exponential values for temperature dependence. For example: $C_{r2}(T)=C_{r2}\left(\frac{T}{300}\right)^{\gamma_{r2}}$. Parameters $\mu_{0d}(T)$, $\mu_{0a}(T)$, $\mu_{1d}(T)$, $\mu_{1a}(T)$ have the same form of temperature dependency, except that the exponent γ_{par} is negative. For example: $\mu_{0a}(T)=\mu_{0a}\left(\frac{T}{300}\right)^{-\gamma_{0a}}$.

The implemented parameters' values in our simulation are shown in Table 3-1 [52]. They are derived based on the hole mobility model proposed in [14, 64] for temperature below 600K. For the parameters not shown in Table 3-1, their values are 0.

Table 3-1: Parameters' values for hole mobility in diamond based on University of Bologna bulk mobility model.

Parameter	Parameter's Value	
	$T \leq 325K$	$325K < T < 600K$
$\mu_{\max}$	3445	4100
γ	1.5	3.2
μ_{0a}	55	70
γ_{0a}	-2.5	
$C_{r1} = C_{s1} = C_{s2}$	10^{30}	
C_{r2}	$1.12\text{x}10^{14}$	
γ_{r2}	2.589	
α	1	
β	0.589	

Figure 3-5 shows the variation of hole mobility with temperature and concentration in single crystal Boron doped CVD diamond based on the implemented mobility model and parameters. We can see different temperatures dependence of hole mobility for different Boron doping concentration. For low Boron doping concentration, acoustic phonon scattering is the dominant mechanism [14, 73]. In this case, the hole mobility is governed mostly by $\mu_L(T)$ which is decreasing with increasing temperature (based on γ factor). For high Boron doping concentration, ionized impurity scattering is dominant. In this case, hole mobility is increasing with increasing temperature (based on $\mu_{0a}(T)$ with temperature dependence γ_{0a} factor) [14, 74, 75]. However, it is important to note that the carrier mobility values in diamond crystal might vary depending on many factors such as the quality of synthetic diamond crystal, defects density, etc.

Furthermore, it can be observed that the hole mobility value drops very fast for Boron doping concentration larger than 10^{13} cm^{-3} up to small value of 57.73 cm^{2}.V^{-1}.s^{-1} at 2x10^{19} cm^{-3} at 300K. Although hole mobility value decreases with increasing Boron concentration, the conductivity is actually increases due to larger increase in the hole concentration. This can be seen in Figure 3-6, where the conductivity σ_p of Boron doped diamond is calculated based on Eq. (3.18).

$$\sigma_p = q\mu_{dop}(N_D, N_A, T)p \tag{3.18}$$

where $\mu_{dop}(N_D, N_A, T)$ and p is the temperature and concentration dependent hole mobility and hole concentration.

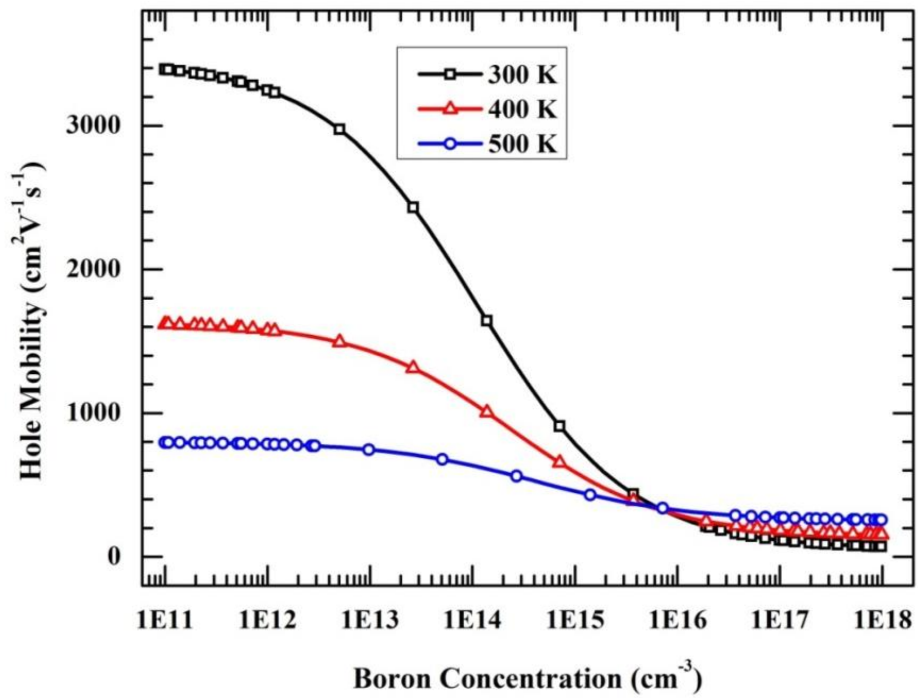

Figure 3-5: Hole mobility versus Boron concentration in single crystal CVD diamond at temperature of 300 K, 400 K, and 500 K.

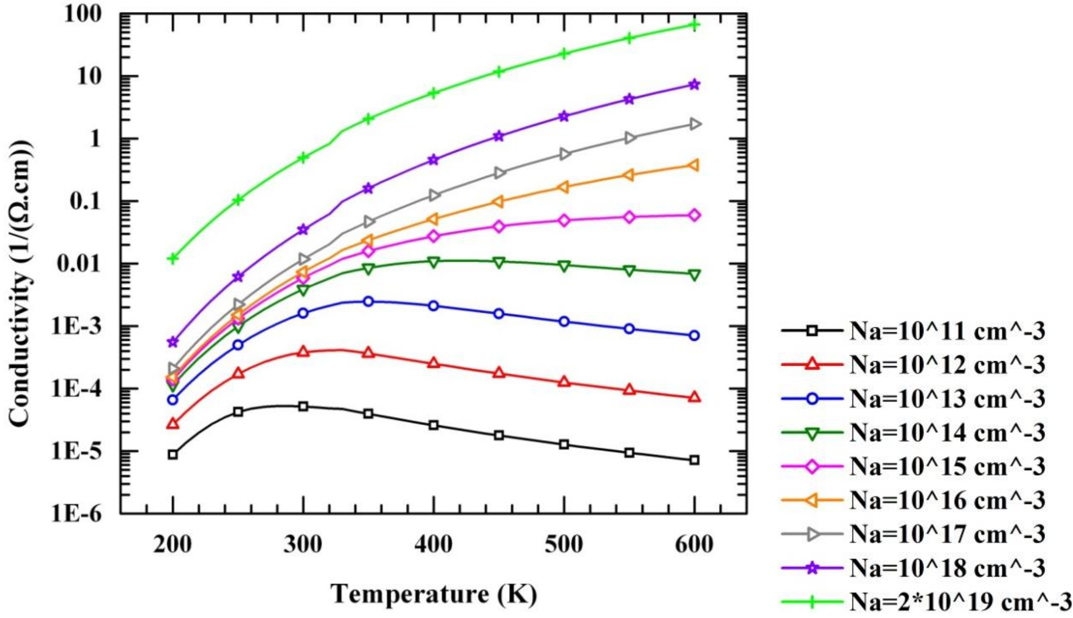

Figure 3-6: The calculated conductivity of Boron doped diamond at temperature range of 200K to 600K for different Boron doping concentration.

For Boron concentration ≤ 10^{14} cm^{-3}, the conductivity curve contains a maximum point, below which, σ_p increases with increasing temperature, and above which, σ_p decreases with increasing temperature. Understanding of these curves' properties is important in designing the temperature coefficient of resistance of the power devices.

3.3.2 High field saturation

Under high electric field E_f, carrier's drift velocity v saturates to some maximum velocity (v_{sat}) and v is no longer proportional to E_f. In the simulation, Extended Canali model based on Caughey-Thomas formula is activated [68]. Carrrier's drift velocity $v(E_f)$ is given by

$$v(E_f) = \mu_{high}(E_f)E_f = \frac{(\alpha_v + 1)\mu_{low}E_f}{\alpha_v + \left[1 + \left(\frac{(\alpha_v + 1)\mu_{low}E_f}{v_{sat}}\right)^{\beta}\right]^{\frac{1}{\beta}}} \tag{3.19}$$

where μ_{low} is the low field mobility modelled by University of Bologna bulk mobility model. The exponent β is temperature dependent value given by

$$\beta = \beta_0 \left(\frac{T}{300K}\right)^{\beta_{\exp}} \tag{3.20}$$

The saturation velocity v_{sat} is temperature dependent parameters given by

$$v_{sat} = v_{sat,0} \left(\frac{T}{300K}\right)^{v_{sat,\exp}} \tag{3.21}$$

where $v_{sat,0}$ is the value of saturation velocity at 300 K.

In the literature, values of saturation velocity for electron and hole in diamond have been determined by means of theoretical calculations, Monte-Carlo simulations, and experimental measurements on both natural diamond and CVD diamond for fields up to 6×10^4 V/cm. Their values exhibit some variations from 0.96×10^7 cm/s to 2.3×10^7 cm/s [22]. Moreover, drift velocity in diamond has been modelled by assuming $\alpha_v = 0$ and $\beta = 0.75$- 2 [22, 76, 77].

In our simulations, the implemented parameters are based on the recent work of M. Brezeanu on the numerical simulation of single crystal diamond device, i.e. $\alpha_v = 0$, $\beta_0 = 2$, $\beta_{\exp} = 0$, and $v_{sat,0} = 2\text{x}10^7$ cm/s, and $v_{sat,\exp} = 0.5$ for both electron and hole [77]. Figure 3-7 shows the calculated values of saturation velocity versus temperature for $v_{sat,0} = 2\text{x}10^7$ cm/s and different values of $v_{sat,\exp}$.

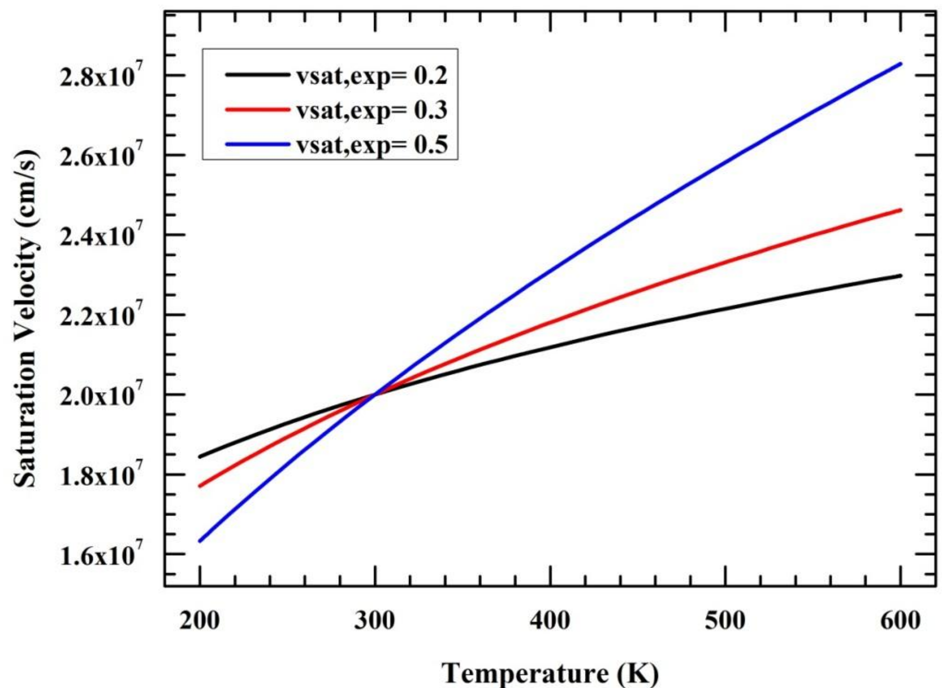

Figure 3-7: Variation of velocity saturation with temperature for $v_{sat,0} = 2\text{x}10^7$ cm/s and different values of $v_{sat,\exp}$.

Figure 3-8 shows the variations of drift velocity in diamond with Boron doping concentration of 10^{11} cm^{-3} at 300 K (using $\beta_{\exp} = 0$, and $v_{sat,0} = 2\text{x}10^7$ cm/s, and $v_{sat,\exp} = 0.5$) for different values of β_0. The value of β_0 affects the transition region from low field transport regime to saturation regime.

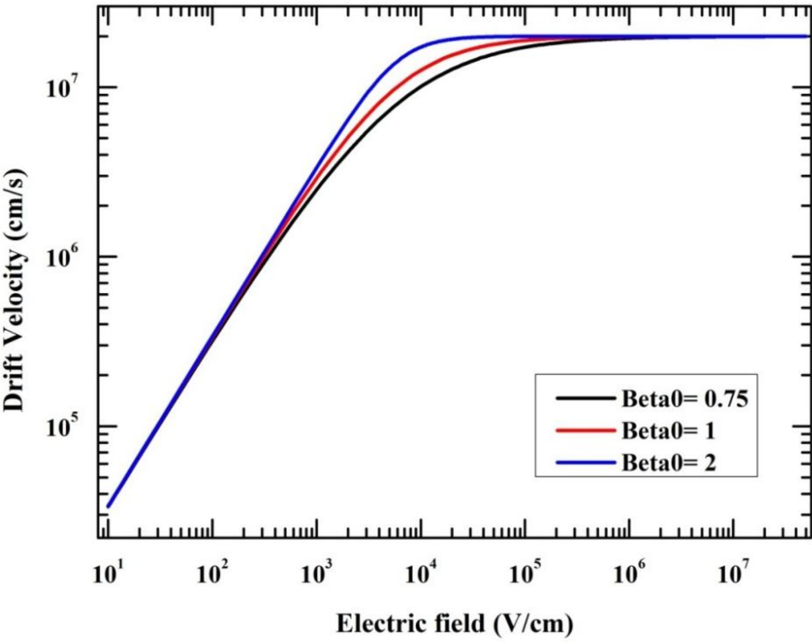

Figure 3-8: Calculated drift velocity versus electric field in diamond for Boron concentration of 10^{11} cm^{-3} at 300 K with different values of β_0 (Beta0).

Figure 3-9 shows the variation of drift velocity for different Boron doping concentration of 10^{11}, 10^{15}, 10^{17} cm^{-3} at 300 K (using $v_{sat,0}$ = 2x10^7 cm/s, $v_{sat,\exp}$ = 0.5, β_0 = 1, and $\beta_{\exp}$ = 0). The drift velocity in the low field transport regime is lower at higher Boron concentration. This is expected as low field mobility value drops at higher acceptor concentration as shown in Figure 3-5.

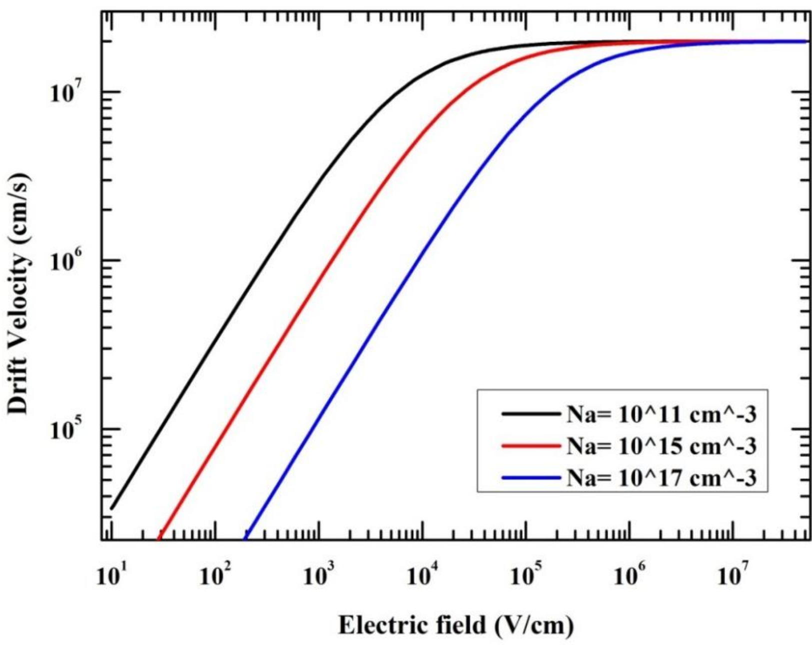

Figure 3-9: Calculated drift velocity versus electric field in diamond for different Boron doping concentration of 10^{11}, 10^{15}, 10^{17} cm^{-3} at 300 K.

Temperature dependence of drift velocity in diamond for Boron doping concentration of 10^{11} is also shown in Figure 3-10 for using $v_{sat,0} = 2\text{x}10^7$ cm/s, $v_{sat,\exp} = 0.5$, $\beta_0 = 1$, and $\beta_{\exp} = 0$. The drift velocity in the low field transport regime is lower at higher temperature because of drops in hole mobility values (refer to Figure 3-5). With $v_{sat,\exp} = 0.5$, increase of saturation velocity at high temperature can be observed.

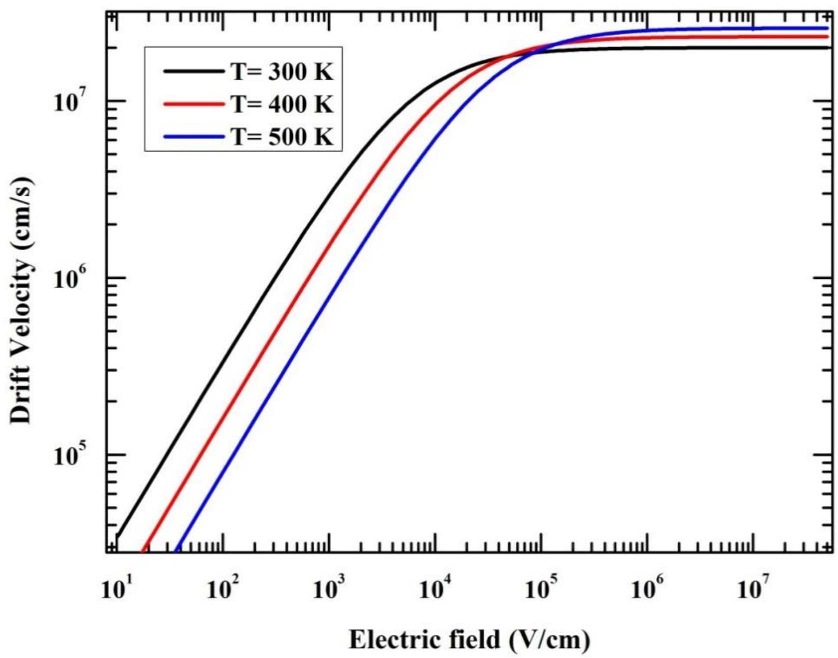

Figure 3-10: Calculated drift velocity versus electric field in diamond with Boron doping concentration of 10^{11} cm^{-3} at 300 K, 400 K, and 500 K.

Since value of saturation velocity v_{sat} has significant effect to the transient characteristics of the device, v_{sat} needs to be adjusted appropriately for dynamic simulations in order to match experiment results.

3.4 Impact ionization model

Impact ionization model is important in simulating breakdown phenomena in the device. It governs the rate of electron- hole pairs generated through impact ionization at high electric field. The electron- hole pair generation rate G^{ii} is given by [68, 69]

$$G^{ii} = \alpha_n n v_n + \alpha_p p v_p \tag{3.22}$$

v_n (v_p) is the electron (hole) velocity and α_n (α_p) is the ionization rate for electron (hole), i.e. the number of electron- hole pairs generated by electron (hole) accelerated along the direction of electric field per unit distance. When G^{ii} goes to a large number, avalanche breakdown occurs. The model implemented in our simulations is van Overstraeten- de Man model [68] given in Eq. (3.23) with E_f as the electric field, $a_{n(p)}$ and $b_{n(p)}$ as the impact ionization coefficients for electron (hole), and γ as temperature dependent factor. At this moment, we do not consider temperature dependent ionization rates in our simulations and the value of γ is set to 1.

$$\alpha_{n(p)}(E_f) = \gamma a_{n(p)} \exp\left(-\frac{\gamma b_{n(p)}}{E_f} \right) \tag{3.23}$$

Up to this date, there is no accurate measurement on the values of impact ionization coefficients in diamond. Several values have been proposed by some authors in the literature. R. J. Trew et al. proposed impact ionization coefficients based on measurement in natural diamond [6]. S. J. Rashid et al. obtained the coefficients values by extrapolating values in Si and SiC to diamond based on their band gap [64]. On the other hand, J. Isberg et al. reported values based on measurements in single crystal CVD diamond. However, no reliable coefficients values can be determined because of low signal to noise ratio in the experiments [78]. These impact ionization coefficients are summarized in Table 3-2.

Table 3-2: Impact ionization coefficients reported in the literature with the simulated breakdown voltage and maximum electric field in ideal parallel plate SBD structure.

	a_n (cm^{-1})	a_p (cm^{-1})	b_n (V.cm^{-1})	b_p (V.cm^{-1})	Breakdown voltage (V)	Maximum electrical field (MV/cm)
R. J. Trew et al.	1.935x10^{8}	1.935x10^{8}	7.749x10^{6}	7.749x10^{6}	222.5	0.846
S. J. Rashid et al.	1.89x10^{5}	5.48x10^{6}	1.7x10^{7}	1.42x10^{7}	1755	2.55
J. Isberg et al.*	-	0.6x10^{6}	-	0.8x10^{7}	2320	3.11
J. Isberg et al.**	-	4x10^{6}	-	1.1x10^{7}	1940	2.73

* and ** refer to two sets of impact ionization coefficients presented by J. Isberg et al. in [78]

To investigate the effects of different impact ionization coefficients on breakdown characteristics, we conducted reverse breakdown simulation of ideal parallel plate diamond Schottky barrier diode structure shown in Figure 3-11. This ideal structure exhibits no electric field crowding such that breakdown is largely dependent on the values of impact ionization coefficients.

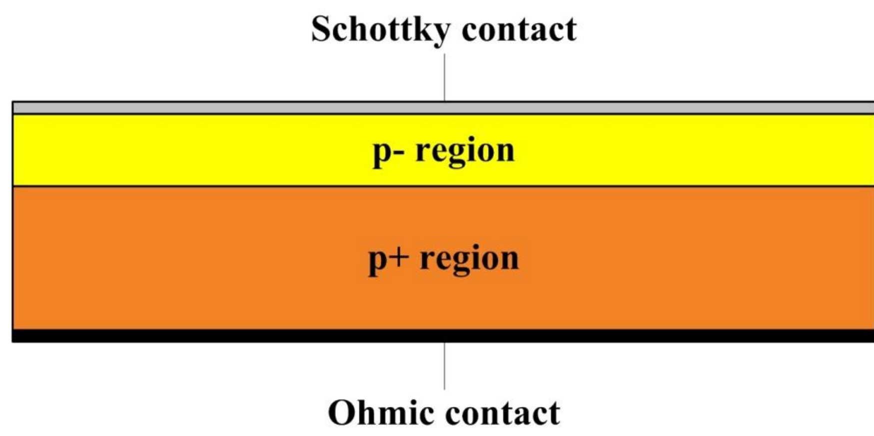

Figure 3-11: Ideal parallel plate diamond Schottky barrier diode structure.

The p+ region is highly Boron doped region (1x10^{20} cm^{-3}) with 20 µm thickness. The p- drift region has Boron doping of 5x10^{15} cm^{-3} and thickness of 10 µm. These doping concentrations can be easily achieved in experimental fabrication using current technology. The diamond surface is Oxygen terminated and has

electron affinity of 1.3 eV. The Schottky metal work-function is set at 4.27 eV to yield Schottky barrier height of 2.5 eV.

To achieve automatic switching from a voltage-controlled pre-breakdown regime to a current controlled post-breakdown regime, external resistor with large resistance value is attached to the ohmic contact [68]. At large reverse voltage, after the onset of impact ionization, most of the voltage drop occurs in the external resistor, thus limiting the reverse current. In the simulations, the breakdown voltage can be extracted as the maximum voltage that can be applied to the contact (shown in Table 3-2) [79] or as the voltage when the reverse current density reaches certain value (e.g. 1×10^{-4} A/cm^2 [66]).

Figure 3-12 and Figure 3-13 show the simulated reverse breakdown characteristics and the distributions of electric field in the device along y- axis for different applied impact ionization coefficients. We can see that different applied impact ionization coefficients yield different breakdown voltage and different maximum electric field E_{Crit} at breakdown, as summarized in Table 3-2. The slope of electric field along the y-axis dE/dy can be calculated based on the Poisson's equation ($dE/dy = -qN_A/\varepsilon_S$) to be -1.587 x10^9 V/cm^2. The depletion width W at breakdown can then be calculated based on Eq. (3.24).

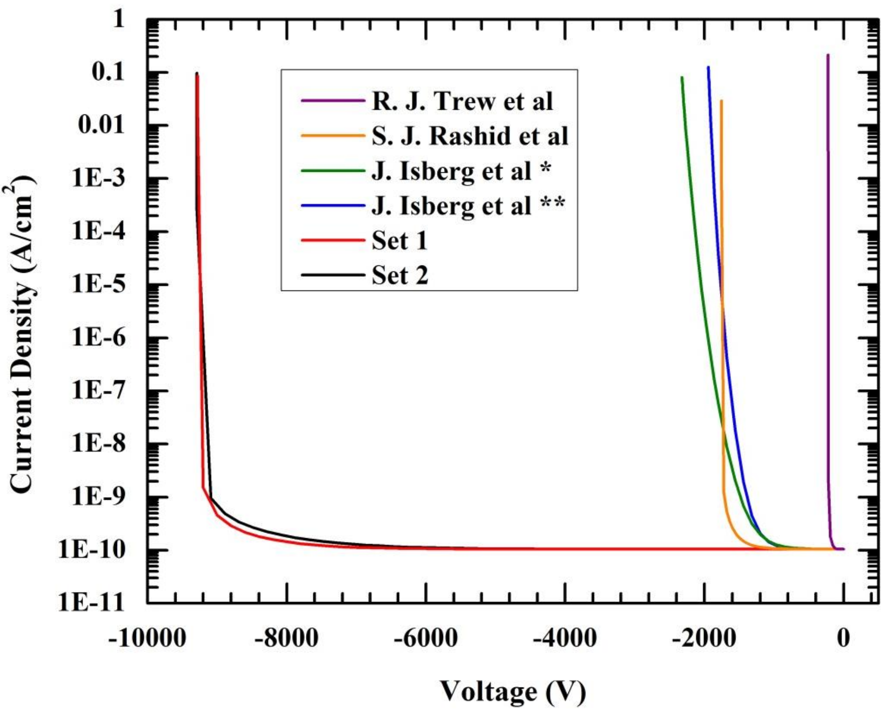

Figure 3-12: The simulated reverse breakdown characteristics in ideal parallel plate diamond Schottky barrier diode structure

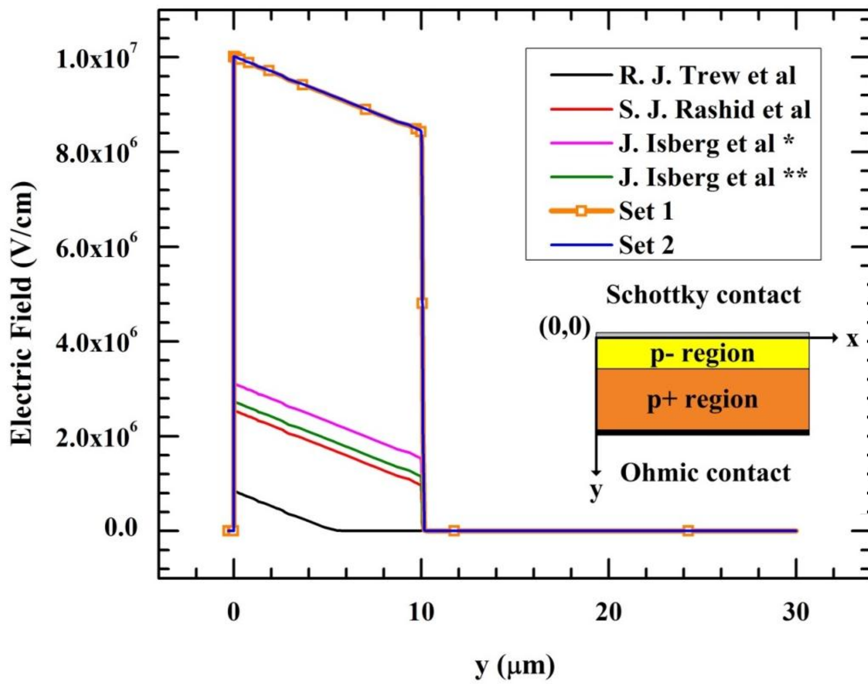

Figure 3-13: Simulated electric field profile at breakdown in ideal parallel plate diamond Schottky barrier diode structure.

$$\frac{dE}{dy} = \frac{E_{Crit}}{W} \tag{3.24}$$

As value of E_{Crit} varies for different applied impact ionization coefficients, so does the value of W. When W is larger than the thickness of drift region (10 μm in this case), the diode is called punch through diode. Else it is called non-punch through diode; e. g. Using E_{Crit} = 0.846 MV/cm (based on impact ionization coefficients proposed by R. J. Trew et al.), the calculated W is 5.33 μm, which is less than the drift thickness of 10 μm.

From Table 3-2, we can see that that the E_{Crit} (at Schottky metal-diamond interface) achieved in single crystal CVD diamond based on these impact ionization coefficients is less than ~4 MV/cm. While this range is commonly demonstrated in most of the fabricated diamond SBDs recently [40, 56, 80], it is much lower compared to the usually cited breakdown electric field of 10- 20 MV/cm for diamond [3, 4, 6, 81, 82].

Furthermore, P. N. Volpe et al. claimed to have achieved diamond SBD with breakdown electric field of approximately 7- 9.5 MV/cm [27]. These lead to a conclusion that the currently available impact ionization coefficients underestimate the real capability of diamond material. This is in agreement with [83].

Through simulations, wide range of impact ionization coefficients can be set to achieve certain value of simulated maximum electric field at breakdown. For example, both Set 1: $\alpha_n = \alpha_p = 5.48\text{x}10^6 exp\left(-8\text{x}10^7 / E_f\right)$ and Set 2 : $\alpha_n = \alpha_p = 0.22\text{x}10^6\, exp\left(-5\text{x}10^7 / E_f\right)$ can be applied in the simulations to achieve simulated breakdown electric field of ~10 MV/cm for ideal parallel plate diamond SBD structure, as shown in Figure 3-12 and Figure 3-13. Therefore, there are no unique and accurate impact ionization coefficients for diamond that can be deduced through simulations. More accurate measurements on impact ionization coefficients in high quality single crystal CVD diamond are needed.

Due to uncertainty in the impact ionization coefficients, reverse bias and breakdown simulations of diamond devices are challenging and somewhat approximate. Some authors simulates breakdown phenomena by stopping the simulation and extracting the breakdown voltage when the electric field in the device reaches the breakdown electric field value of diamond [65].

3.5 Conclusions

In this chapter, we have presented modelling of single crystal diamond (especially Boron doped diamond) for implementation in finite element TCAD Sentaurus software. Important physics models and their parameters are elaborated and discussed. In the incomplete ionization model for Boron acceptor, concentration dependent activation energy and temperature dependent degeneracy factor are incorporated.

To account for concentration and temperature dependent hole mobility in diamond, we applied University of Bologna bulk mobility model with suitable parameters. Carrier transport under high electric field is implemented with Caughey-Thomas high field saturation model with appropriate saturation velocity.

For reverse bias and breakdown simulations, we utilized impact ionization model for avalanche generation. Our investigation on different impact ionization

coefficients reported in the literature using numerical simulations in TCAD Sentaurus software resulted in maximum breakdown electric field less than~ 4 MV/cm. This indicates that the reported coefficients values might not be accurate and underestimate the potential of diamond material (10- 20 MV/cm).

4 STATIC AND TRANSIENT CHARACTERISTICS OF DIAMOND SCHOTTKY BARRIER DIODE

4.1 Introduction

Structure of a vertical diamond SBD without edge termination structure is shown in Figure 4-1. It consists of drift layer and p+ layer stack, with metal contacts at the opposite sides of the device. The p+ layer serves as the carrier injecting region while the drift layer serves to support applied reverse voltage. In typical SBD, the drift layer is lowly doped layer (p- layer). However, high ionization energy of dopants in diamond leads to low carrier concentration available for the conduction (refer to Figure 3-4) and consequently high resistivity, especially at low temperature operation. To overcome this problem, a new type of diamond SBD namely diamond metal-intrinsic-p+ (m-i-p+) diode was introduced [64, 84]. In the m-i-p+ diode, extremely lowly doped, ideally intrinsic region (i- region) is employed as the drift layer instead of p- region to exploit the high carrier mobility in intrinsic diamond, thus compensating the low carrier concentration.

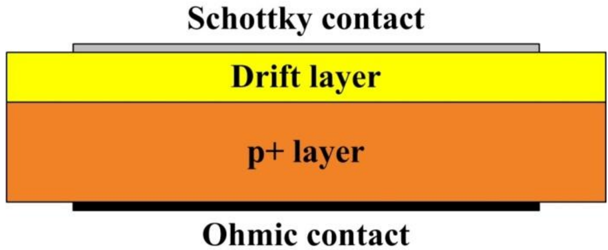

Figure 4-1: Structure of a vertical diamond SBD without edge termination.

Up to this date, several diamond m-i-p+ diodes have been fabricated and their static characteristics have been measured [64, 84]. Moreover, no study on switching characteristics of diamond m-i-p+ diode has been reported, while only limited measurements on switching characteristics of diamond SBD have been reported in the literature [53, 54, 85].

In this study, we investigated and compared the characteristics of diamond m-i-p+ diode and typical p-type diamond SBD by means of experimental data and numerical simulations in TCAD Sentaurus software. The transient characteristics of the diodes are then analysed and simulated in the mixed-mode environment based on the established diodes' models and parameters at different temperatures.

4.2 Devices under investigation

Diamond m-i-p+ diode

The investigated diamond m-i-p+ diodes were fabricated using MPCVD (Microwave Plasma Chemical Vapour Deposition) method and experimentally measured by S.J. Rashid et al. [64, 84]. The 5 mm x 5 mm dies consist of i- layer drift region (ideally intrinsic) of 10-18 µm thickness, grown on highly doped p+ diamond substrate with thickness of 300-600 µm and Boron concentration of ~ $2x10^{19}$ cm^{-3} (refer to Figure 4-1). Ti/Al (Titanium/Aluminium) was used as the ohmic contact, while Al or Au (gold) with different work function of 4.28 eV and 5.1 eV respectively was used for the Schottky metal. The diamond surface was Oxygen terminated by using Oxygen plasma treatment to yield electron affinity χ of 1.3 eV. No edge termination structure was implemented in the investigated diode. More details on the fabrication process can be found in [14]. Top view of the packaged diamond m-i-p+ diode is shown in Figure 4-2 [14].

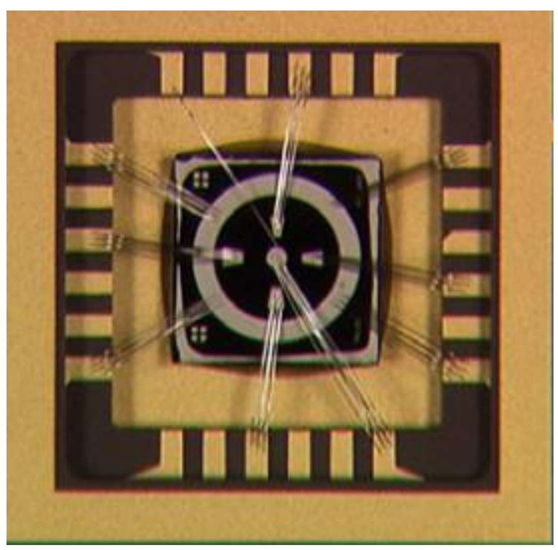

Figure 4-2: The packaged diamond m-i-p+ diode [14].

Diamond p-/p+ SBD

On the other hand, the investigated diamond SBD was fabricated recently by Diamond Research Laboratory, National Institute of Advanced Industrial Science and Technology (AIST), Japan. Its static $I-V$ and turn-off transient characteristics have been experimentally measured and reported [54]. The diamond SBD has Oxygen terminated p- drift layer with thickness of 12 µm and low Boron doping of 10^{16} cm^{-3}. The p+ layer is a highly doped diamond HPHT substrate with Ti (30 nm)/Pt (30 nm)/Au (100 nm) ohmic contact. Mo (30 nm)/Au (200 nm) Schottky contact with square shape and rounded corner was fabricated on the Oxygen terminated p- layer. The active area of the diamond SBD is 0.0097 cm^2. Figure 4-3 shows the top view of the investigated diamond SBD.

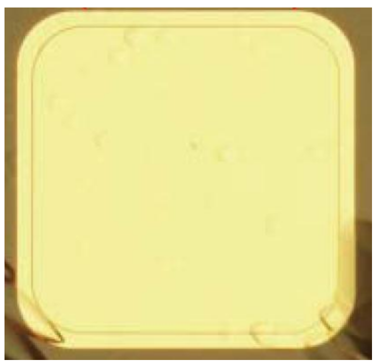

Figure 4-3: Top view of the investigated diamond SBD [54].

4.3 Device Modelling for implementation in numerical simulations

In this numerical simulation studies, the investigated diodes were simulated with a miniaturized intimate contact diode structure, such as shown in Figure 4-4. The diode's cross-sectional area and p+ region thickness were reduced in order to cut the computational time. Parallel plate structure without edge termination was chosen in the simulations to increase convergence during transient simulations. Moreover, the resistance of the thick p+ region (which is modelled much thinner than the real one) and the parasitic resistance were combined in series with the resistance of ohmic contact and modelled as total ohmic contact resistance. This parameter is adjusted accordingly to match the experiment results. In the simulations, various physics based models and parameters described in Chapter 3 were implemented.

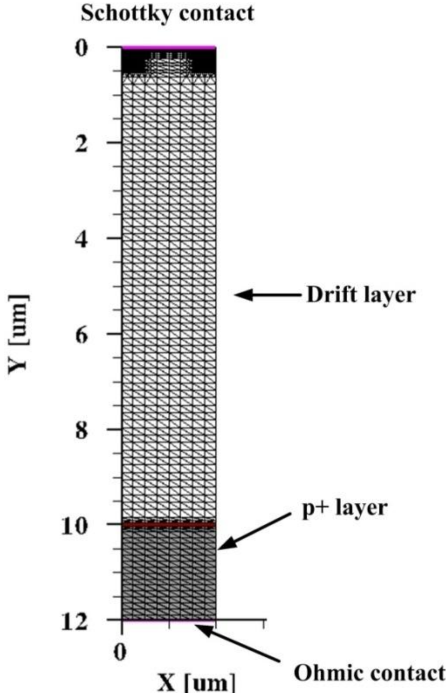

Figure 4-4: Miniaturized diamond SBD structure employed in the simulation with the meshes used for the finite element calculations.

4.4 Static characteristics

4.4.1 Diamond metal-intrinsic-p+ diode

Measurements of the diamond m-i-p+ diodes show wide variations in the $I-V$ characteristics for different Schottky contact size on the same wafer as shown in Figure 4-5 for small contact (approximately 10^{-5} cm^2) and large contact (0.03 cm^2) [77]. Contrary to the small contact diode, degradation in the forward current density in the large contact diode can be noticed. At 5 V forward voltage, the current density of large contact diode reaches only 33 A/cm2, as compared to $100 A/cm^2$ current density in small contact diode.

Brezeanu suggested that non-uniformities of the diamond drift layer surface (as shown in Figure 4-6) reduce the actual interface area of the large Schottky contact significantly. Deformation of large area contact (bending due to stress) might also further reduce the active contact area. The total leakage current for diode with small and large contact area can be calculated to be ~10^{-7} A and ~10^{-10} A. However, it is unclear why the leakage current of the small contact diode presented in [77] is much higher. It is most likely caused by limitation of measurements

equipment and measurements error (inclusion of defects & dislocations on small Schottky contact is less likely to occur).

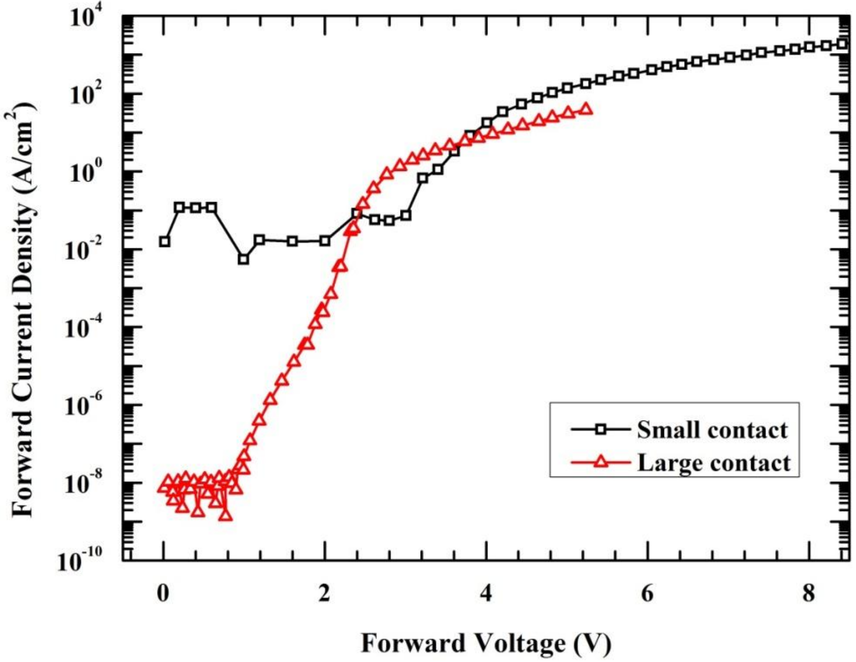

Figure 4-5: Forward $I-V$ characteristics of the diamond m-i-p+ diode with small and large Au Schottky contact.

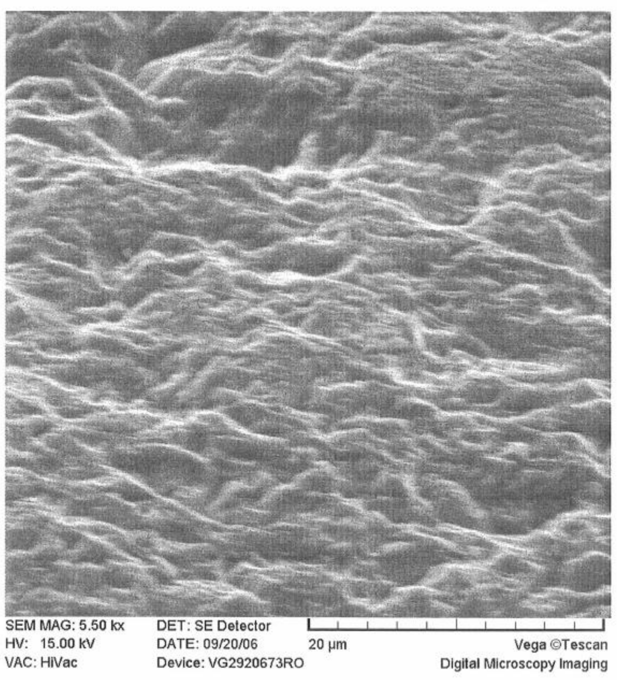

Figure 4-6: SEM image of the surface of diamond drift layer [77].

Figure 4-7 shows our forward bias $I-V$ simulation results and measurements data [64, 84] for diamond m-i-p+ diode with Au and Al Schottky contact with

different drift length (10 μm, 12 μm, 16 μm) at 300K. Measurements and simulation results of forward $I-V$ characteristics of the diode with Au Schottky contact and 10 μm drift length at higher temperature are shown in Figure 4-8. In both figures, the measurements data is shown as scatter plots, while the numerical simulation results are shown as line plots. Good correlations between simulation results and experiment data were found, especially at voltage drop around 2 V above the turn-on voltage (V_{TO}), around which the diodes are expected to operate. Poorer match is noticed for forward $I-V$ characteristics of Au diode at temperature of 400 K.

From Figure 4-7, we can also observe the effect of different drift length to diode's on-resistance (slope of $I-V$ curve). Longer drift length results in higher on-resistance and thus smaller slope of $I-V$ curve. Furthermore, diamond m-i-p+ diode shows positive temperature coefficient of resistance, i.e. its on-resistance increases with increasing temperature (as seen in Figure 4-8). This is reasonable since the forward current is dominantly drift current which is proportional to mobility and hole concentration ($J = q\mu_p pE_f$). As temperature increases, carrier mobility in the intrinsic region drops sharply while there is no addition to the carrier concentration, thus effectively increases the on-resistance.

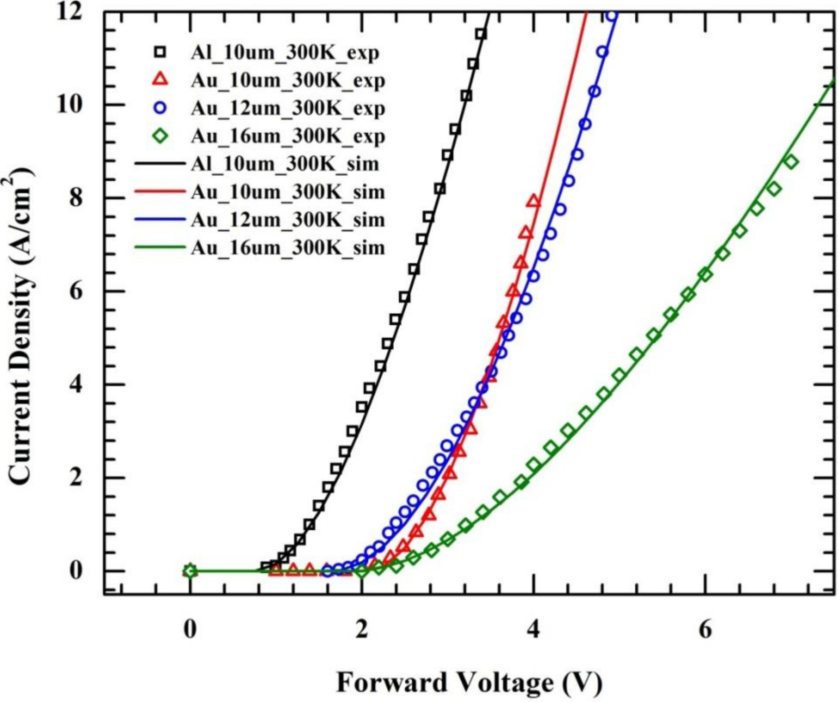

Figure 4-7: Simulation results and experimental data of static forward $I-V$ characteristics of diamond m-i-p+ diodes with Au and Al Schottky contact and various drift length at 300K.

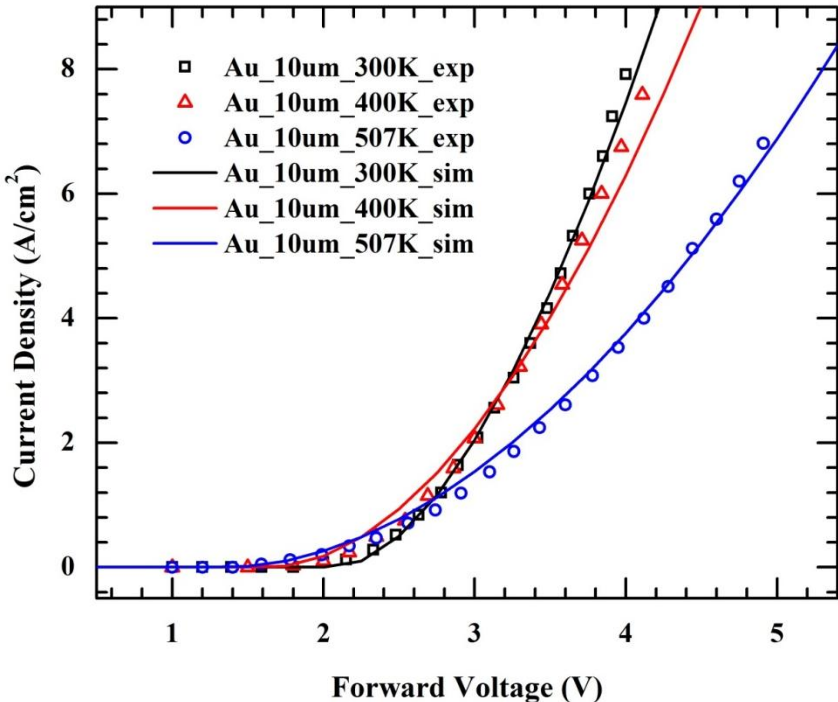

Figure 4-8: Simulation results and experimental data of static forward $I-V$ characteristics of diamond m-i-p+ diodes with Au Schottky contact and 10 μm drift length at 300 K, 400 K, and 507 K.

In the simulations, the work function $q\phi_m$ of Au and Al and the total ohmic resistance were modified to values indicated in Table 4-1 (area factor= 1) to match the experimental data, i.e. the turn-on voltage V_{TO} and the slope of $I-V$ curves at high forward bias. For the intimate contact structure, the Schottky barrier height for holes can be calculated as $q\phi_B = E_g + \chi - q\phi_m$. Using the modified $q\phi_m$ values, it can be observed that the experimental $q\phi_B$ of the Al contact has decreased from the ideal value of 2.49 eV to ~1.27 eV. On the other hand, the experimental $q\phi_B$ of the Au contact has increased from the ideal value of 1.67 eV to ~2.57 eV at 300 K.

The need of modifying metal work function to match the experimentally obtained V_{TO} indicates imperfect metal-diamond interface, such as existence of Fermi level pinning, defects, and interface states charges. These phenomena are not captured in the applied intimate contact diode model. Adjustment in the total ohmic resistance is needed to take into account the resistance of the thick p+ layer in reality and the diamond resistivity variations for this sample (the resistivity might

varies from the implemented models depending on the quality of the fabricated diamond crystal).

Table 4-1: Modified values of parameters used in the simulations of the investigated diamond m-i-p+ diode.

Schottky contact	Metal work function (eV)	Drift length (μm)	Temp (K)	Modified metal work function (eV)	Total ohmic resistance (Ω.μm)
Al	4.28 [14]	10	300	5.5 [10]	$17\text{x}10^5$
Au	5.1 [14]	10	300	4.2 [10]	$10\ \text{x}10^5$
			400	4.45	$1\ \text{x}10^4$
			507	4.55	$2\ \text{x}10^5$
		12	300	4.6	$10\ \text{x}10^5$
		16	300	4.35	$50\ \text{x}10^5$

Simulated energy band diagram for the diamond m-i-p+ diode with Al Schottky contact at 300 K at thermal equilibrium is shown in Figure 4-9. In the figure, the Schottky contact is located at y= 0 μm while the ohmic contact is located at y= 12 μm corresponding to Figure 4-4. As calculated, the Schottky barrier height for holes for the intimate contact structure is found to be 1.27 eV. From the simulation results, $E_F - E_V$ is deduced to be ~0.16 eV and the built-in potential V_i can be calculated to be 1.11 V. The slanted energy band in the drift region indicates that the depletion region extends from the Schottky contact into the whole of drift region due to the low doping (intrinsic) in the drift region.

The distribution of hole density in the diode at thermal equilibrium is shown in Figure 4-10, along with distributions under different bias conditions. Approaching p+ region (y= 10 μm), hole density increases due to the holes diffusion from p+ region into the drift region. This diffusion current is offset by holes drift towards the p+ region along the slanted valence band, therefore resulting in zero net current.

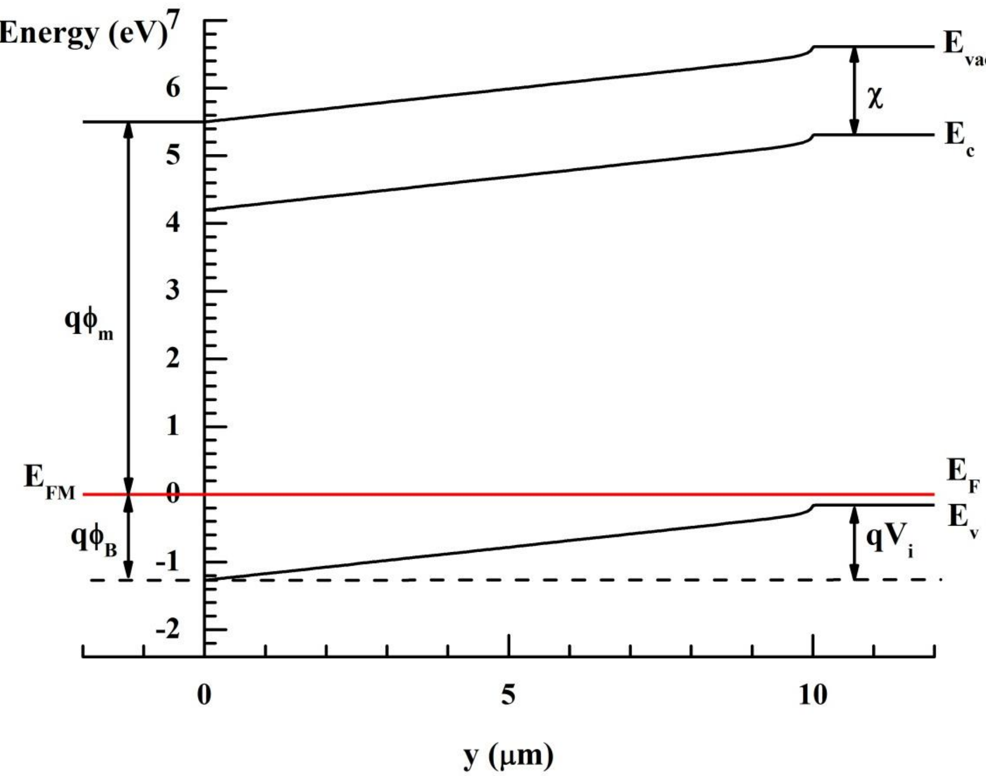

Figure 4-9: Energy band diagram for the diamond m-i-p+ diode with Al Schottky contact at 300 K at equilibrium condition (0 V).

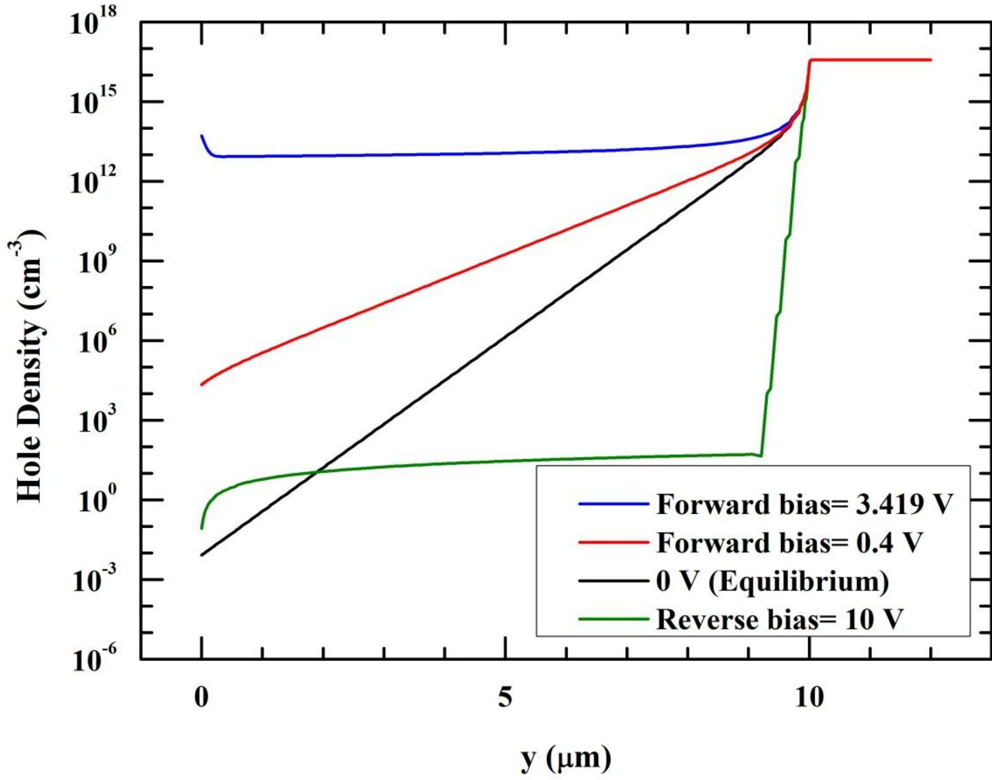

Figure 4-10: The distribution of hole density in the diamond m-i-p+ diode at thermal equilibrium and under different bias conditions.

Furthermore, analysis of forward $I-V$ characteristics of diamond m-i-p+ diode reveals 3 main conduction regimes [41] corresponding to the magnitude of the applied forward voltage:

- **Small forward bias (before and around V_{TO})**

Under small forward bias, the number of holes injected into the drift region starts to increase as shown in Figure 4-10. These holes need to overcome the Schottky barrier in their journey to the Schottky contact as shown in Figure 4-11. Conduction in this regime is dominated by thermionic emission of holes across the Schottky barrier given by Eq. (4.1) and (4.2), where n is the ideality factor and ϕ_{B0} is the Schottky barrier height.

$$J_F = J_S exp\left(\frac{qV_f}{nkT}\right) \tag{4.1}$$

$$J_S = A^*T^2\exp\left(-\frac{q\phi_{B0}}{kT}\right) \tag{4.2}$$

From the measured forward $I-V$ characteristics, the extracted V_{TO} of the Al and Au diamond m-i-p+ diode are approximately 1 V and 2 V respectively. V_{TO} of Au diode with drift length of 12 µm is slightly lower than Au diode with drift length of 10 µm and 16 µm (refer to Figure 4-7). This variation of Schottky barrier height indicates non-uniformity in the formation of Schottky contact (Au/diamond interface).

From Figure 4-8, we can also observe that V_{TO} decreases at higher temperature. This is expected because there is more thermal energy available for the carrier to overcome the Schottky barrier.

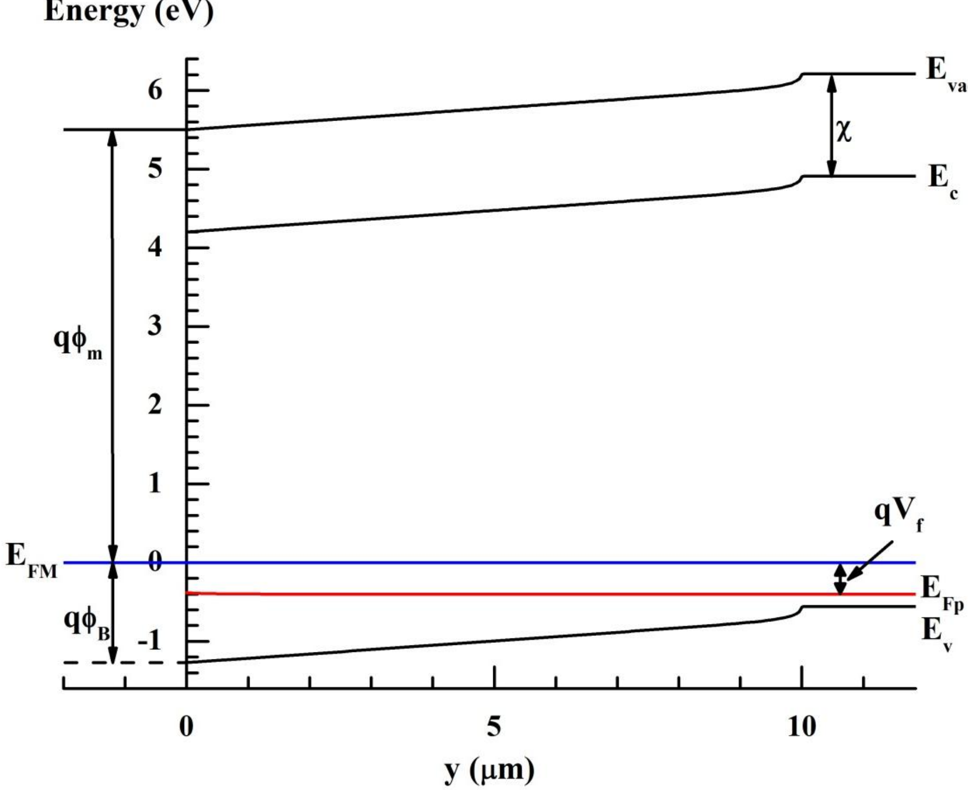

Figure 4-11: Energy band diagram for the diamond m-i-p+ diode with Al Schottky contact at 300 K under forward bias V_f of 0.4 V.

- **Medium forward bias**

The energy band diagram of diamond m-i-p+ diode under larger forward bias V_f is shown in Figure 4-12. Under this condition, more holes are injected into the drift region (refer to Figure 4-10) while Schottky barrier height decreases. When the number of injected holes exceeds the thermal charge concentration, charge balance cannot be supported anymore, and consequently space charge limited (SCL) current conduction dominates. Ideal SCL current is governed by Mott-Gurney law given by Eq. (4.3), where A is the device's cross sectional area, ε_S is the semiconductor permittivity, μ_p is the hole mobility, and L_i is length/ thickness of the intrinsic region. However, SCL current in the practical device does not follow this equation strictly due to existence of traps, defects, carrier diffusion, etc.

$$I = \frac{9}{8} A \varepsilon_S \mu_p \left(\frac{V^2}{L_i^3} \right) \tag{4.3}$$

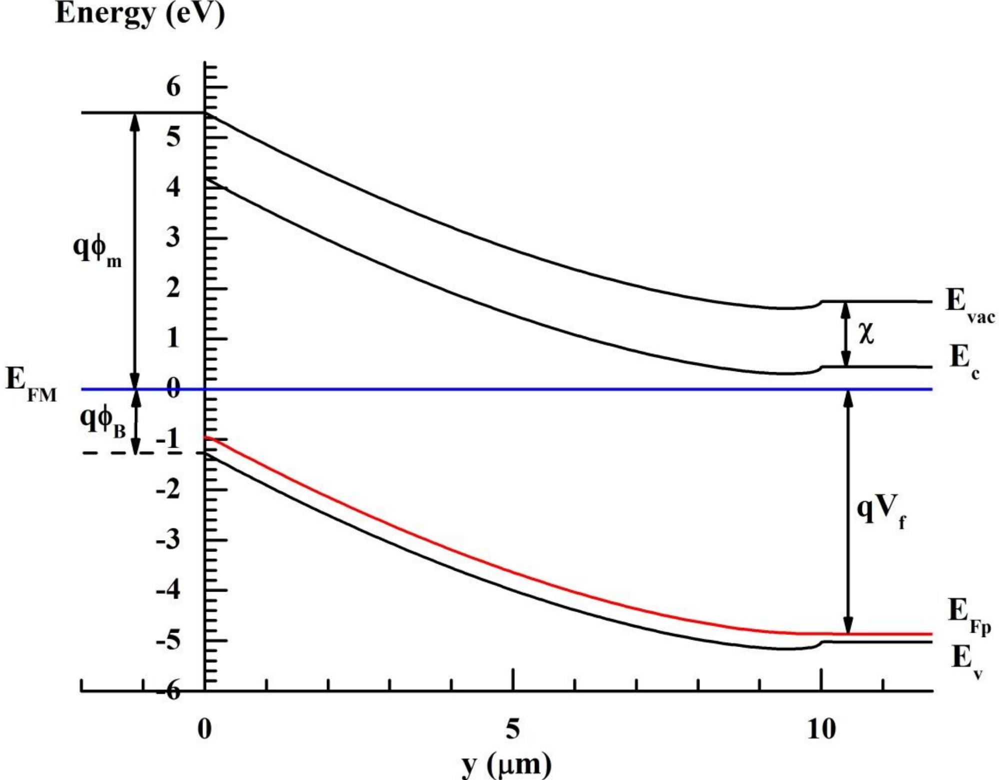

Figure 4-12: Energy band diagram for the diamond m-i-p+ diode with Al Schottky contact at 300 K under forward bias V_f of 4.86 V.

- **Large forward bias**

Under large forward bias, current transport is dominated by ohmic conduction, where voltage drop across series parasitic resistance (substrate and contact resistance) becomes large. Current conduction is governed by Eq. (4.4) which consists of SCL conduction in the first term and ohmic conduction in the second term.

$$V = \sqrt{\frac{8L_i^3}{9A\varepsilon_S\mu_p}I} + R_S I \tag{4.4}$$

At small current, voltage drop across R_S can be ignored and Eq. (4.4) reduces to Eq. (4.3). However, at large current, the second term becomes significant and hence ohmic conduction dominates.

In contrast with forward bias operation, the hole density during reverse bias operation is much lower as shown in Figure 4-10. The simulated energy band

diagram is shown in Figure 4-13 where most of the reverse voltage is sustained in the drift region.

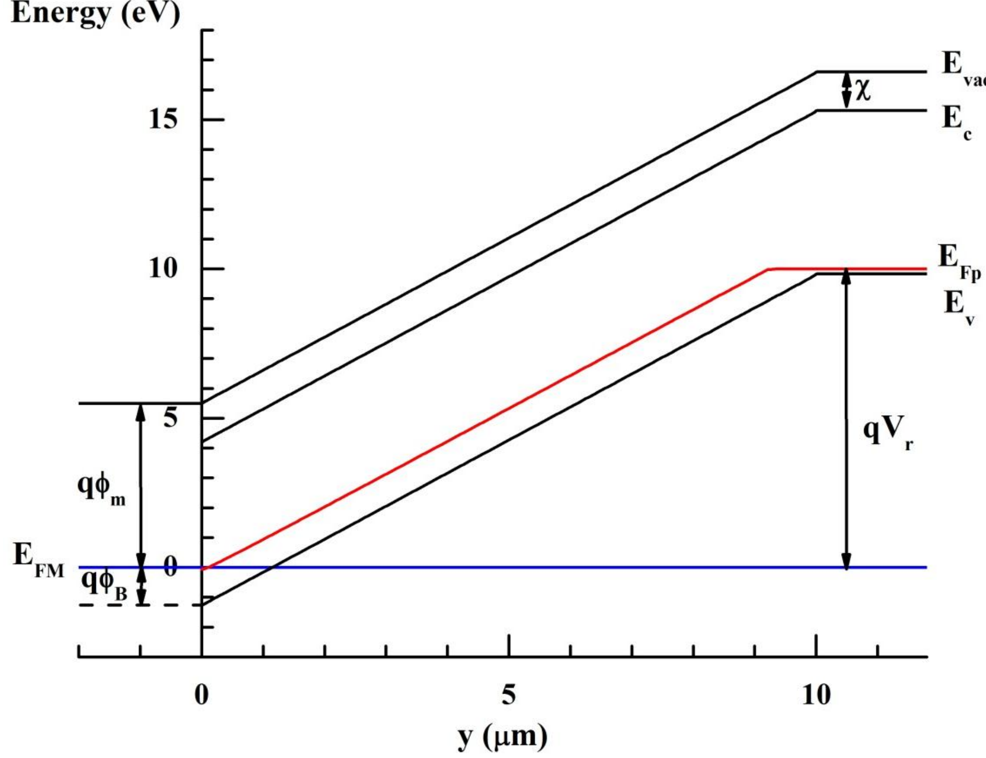

Figure 4-13: Energy band diagram for the diamond m-i-p+ diode with Al Schottky contact at 300 K under reverse bias V_r of 10 V.

By applying the impact ionization coefficients values suggested by S. J. Rashid et al. [64] in Table 3-2 and the established models and parameters in Table 4-1, the extracted breakdown voltage of diamond m-i-p+ diodes with Au Schottky contact for different drift lengths of 10 μm, 12 μm, and 16 μm are approximately 2 kV, 2.3 kV, and 3 kV. The respective simulated electric field profiles in the diodes are shown in Figure 4-14. As concluded in previous Chapter, the simulated breakdown electric field of ~2 MV/cm suggests that the applied impact ionization coefficients underestimate the real potential of diamond material (10- 20 MV/cm).

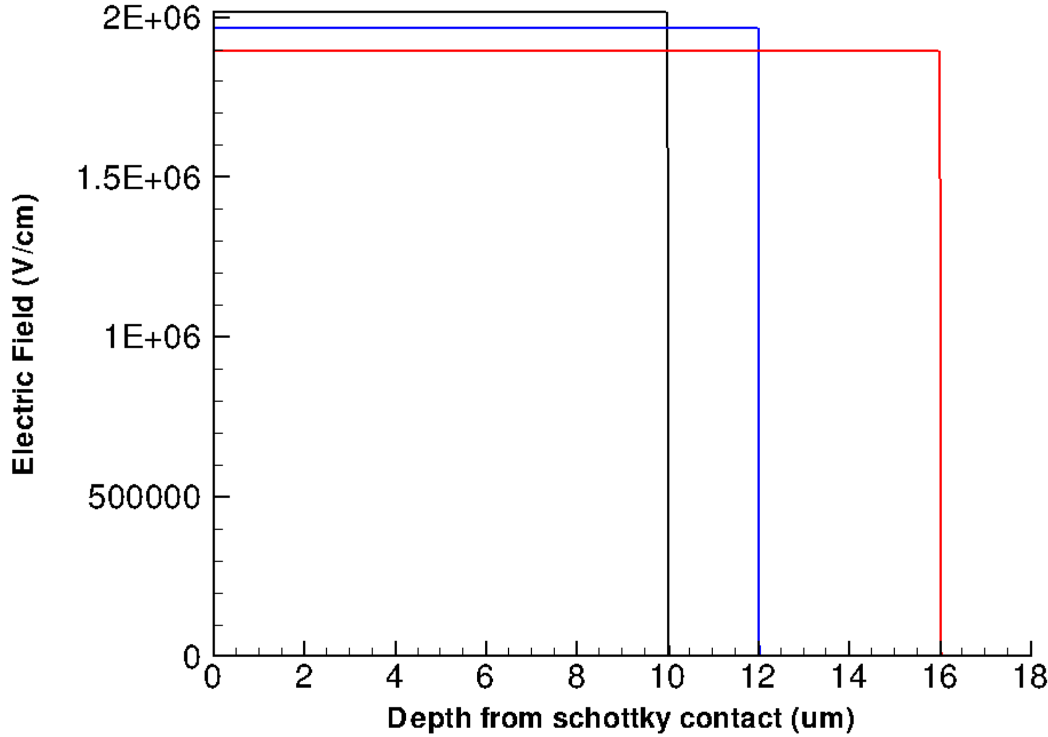

Figure 4-14: Simulated electric field distribution profiles in the diamond m-i-p+ diode with Au Schottky contact at breakdown for drift length of 10 µm, 12 µm, and 16 µm.

In contrast to the simulated electric field distribution in diamond SBD in Figure 3-13, the electric field distribution in diamond m-i-p+ diode is quite uniform in the drift region because of the absence of dopant in the drift region (i- layer). Consequently, the simulated diamond m-i-p+ diode can support higher breakdown voltage (~2000 V) compared to the diamond SBD (~1755 V in Table 3-2) for the same drift length of 10 µm.

Furthermore, breakdown characteristics of diamond m-i-p+ diodes with Au Schottky contact, 18 µm drift length, and without edge termination structure have been experimentally measured and reported [14, 84]. The measurements results for two diode samples using gold point contact immersed in liquid dielectric are shown in Figure 4-15.

In addition, measurements at different surface locations on the same diode sample resulted in breakdown voltage in range of 950 V- 1.7 kV. This shows spatial variations on the diamond's surface and device's quality. At small reverse bias less than 800 V, the measured leakage current is quite low (in the order of 10^{-7} to 10^{-5} A/cm^2).

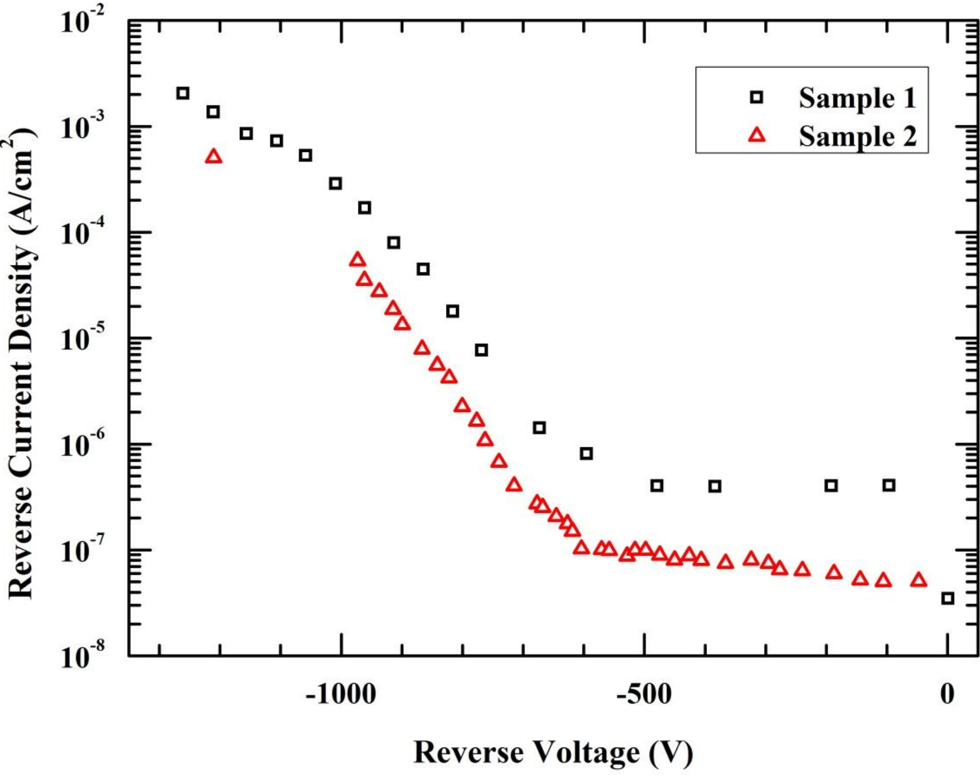

Figure 4-15: Measured reverse bias $I-V$ characteristics of Au diamond m-i-p+ diodes gold point contact in the liquid dielectric [14, 84].

Assuming uniform electric field in the drift region (using 2 dimensional device approximation), the electric field at breakdown is roughly 0.53 MV/cm- 0.94 MV/cm. This value is much lower than the normally quoted breakdown electric field of diamond (10- 20 MV/cm). In addition to device's quality, defects, and leakage path in metal-diamond interface, the low breakdown is mostly caused by the lack of edge termination structure.

At this point, it does not make any sense to compare the reverse bias simulations results and measurements results because the simulated diode has ideal metal-diamond interface with parallel plate structure.

4.4.2 Diamond Schottky barrier diode

Figure 4-16 shows the simulations results of the forward $I-V$ characteristics in comparison with the experimental data for the investigated diamond p-/p+ SBD (refer to Figure 4-3) at different temperatures. In the simulations, miniaturized diode area of 3x1 μm^2 was used (as compared to real area of the investigated diamond SBD= 0.97x10^6 μm^2). Therefore, the implemented area factor (real device area/ simulated device area) was 323333.33.

Good matching between the measurements and simulations results were achieved by adjusting the metal work function and total ohmic resistance in the simulations to values indicated in Table 4-2. Adjustments of the parameters are needed due to the same reasons as the parameters adjustments in the simulations of diamond m-i-p+ diode. In this case, the experimental Schottky barrier height for holes has decreased from ideal value of 2.24 eV (using $q\phi_m$ = 4.53 eV) to 1.5 eV (using modified $q\phi_m$ = 5.27 eV) at 298 K. This results in decrease of diode's turn-on voltage as shown in Figure 4-16. From the $\log I-V$ curves, we can observe that better matching with measurements data is obtained at higher temperature, where thermionic current is more dominant.

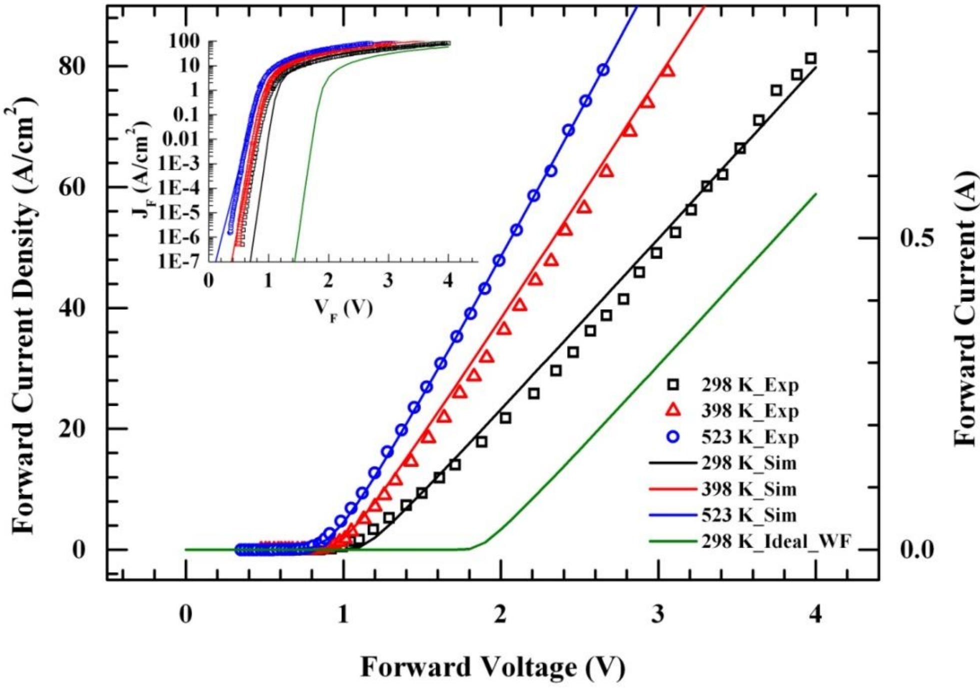

Figure 4-16: Simulation results and experimental data of static forward $I-V$ characteristics of the investigated diamond SBD at 298 K, 398 K, and 523 K. The simulation result using ideal metal work function at 298 K (298K_Ideal_WF curve) is also shown.

Table 4-2: Modified values of parameters used in the simulations of the investigated diamond SBD.

Schottky contact	Metal work function (eV)	Temp (K)	Modified metal work function (eV)	Total ohmic resistance (Ω.µm)
Mo	4.53	298	5.27	350000
		398	5.3	420000
		523	5.2	500000

In contrast with the characteristics of diamond m-i-p+ diode, the investigated diamond SBD displays negative temperature coefficient of resistance, i.e. the on-resistance decreases with the increase of temperature. In the moderately Boron doped p- layer (Boron doping of 10^{16} cm^{-3} in the investigated SBD), decrease in mobility value is countered by the increase in the number of carrier as temperature increases (refer to Figure 3-4 and Figure 3-5), thus lowering the on-resistance of the diode.

Furthermore, the higher Boron doping in p+ region of the diamond SBD ($3x10^{20}$ cm^{-3} compared to $2x10^{19}$ cm^{-3} in diamond m-i-p+ diode) also contributes to the high current density of the diamond SBD. As the Boron doping increased above $3x10^{19}$ cm^{-3}, hopping conduction starts to occur until Boron doping of $3x10^{20}$ cm^{-3}, where metallic conduction starts. In the process, the resistivity of diamond decreases by more than 3 orders of magnitude as shown in Figure 3-1 [70].

The simulated energy band diagram of the diamond SBD at 298 K at thermal equilibrium is shown in Figure 4-17. With the modified metal work function of 5.27 eV, the Schottky barrier height yielded is 1.5 eV. In contrast with diamond m-i-p+ diode, the Fermi level in the p+ region of diamond SBD is lower than the valence band by 0.201 eV because of high Boron doping concentration. Moreover, the depletion layer in the drift region is restricted to small area close to Schottky contact because of the moderate doping in the p- layer. In the region where energy band is flat, $E_F - E_v = 0.3$ eV.

Energy band diagrams of the diamond SBD under small forward bias (before turn-on) and larger forward bias are shown in Figure 4-18 and Figure 4-19. The corresponding distribution of hole density in the diode at thermal equilibrium and under different bias conditions are related to the depletion region in the p- layer as shown in Figure 4-20. The increase of hole density with increase of temperature is also shown in Figure 4-21 for forward bias of 4V.

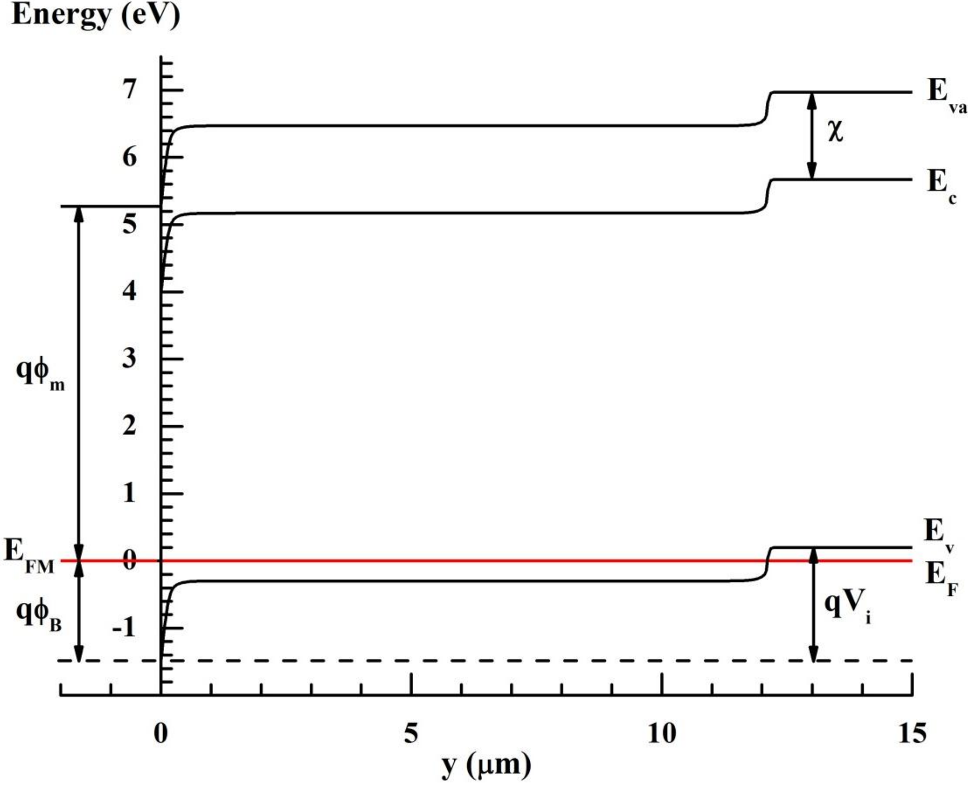

Figure 4-17: Energy band diagram for the diamond SBD at 298 K at equilibrium condition (0V).

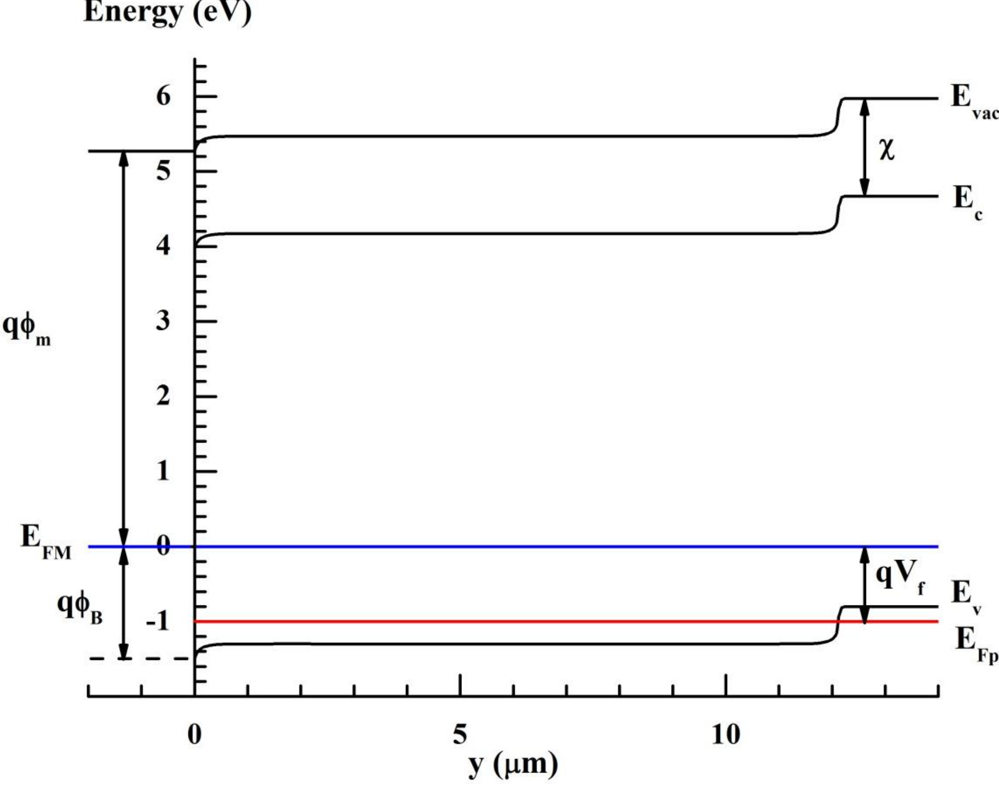

Figure 4-18: Energy band diagram for the diamond SBD 298 K under forward bias V_f of 1 V.

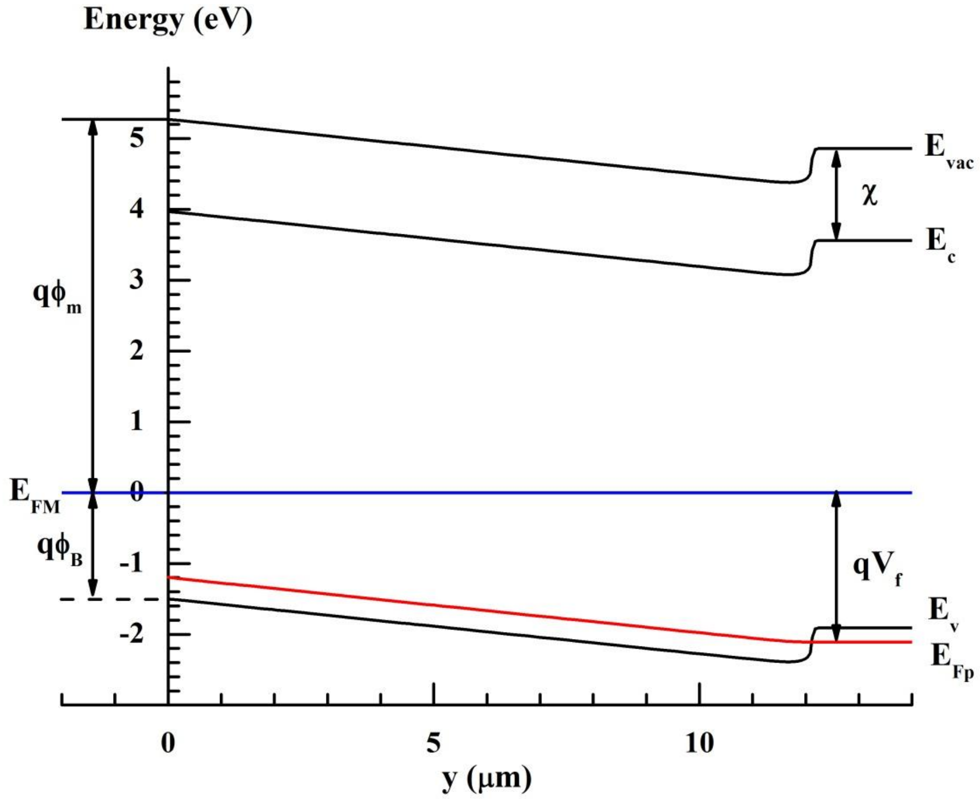

Figure 4-19: Energy band diagram for the diamond SBD 298 K under forward bias V_f of 2.108 V.

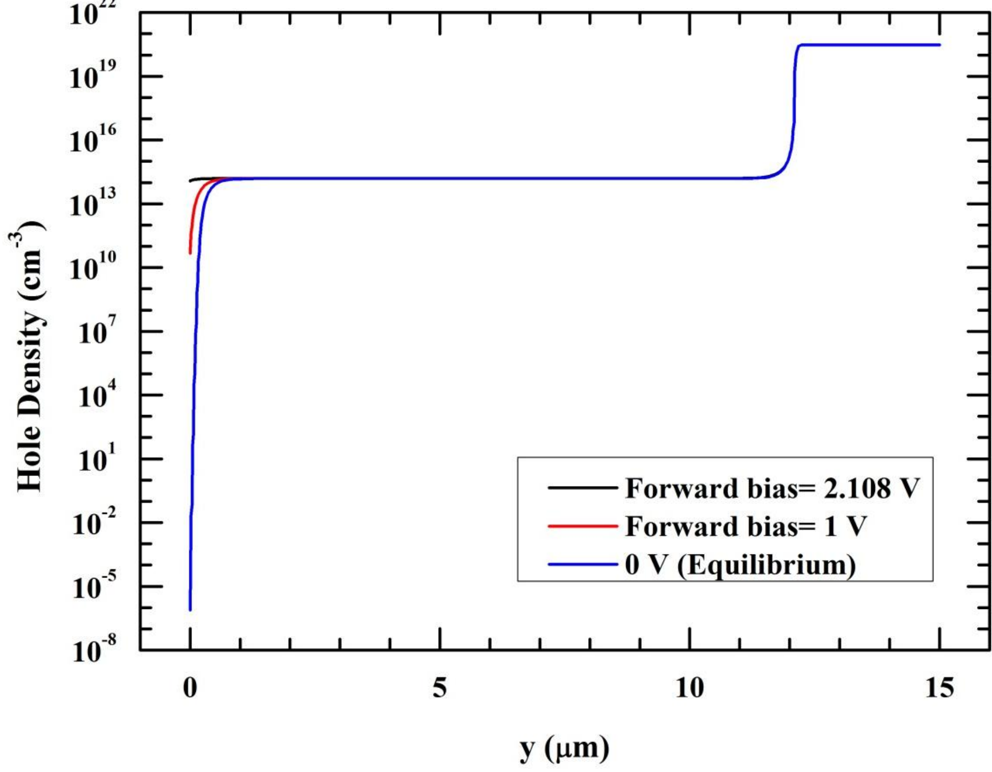

Figure 4-20: The distribution of hole density in the diamond SBD at thermal equilibrium (298 K) and under different bias conditions.

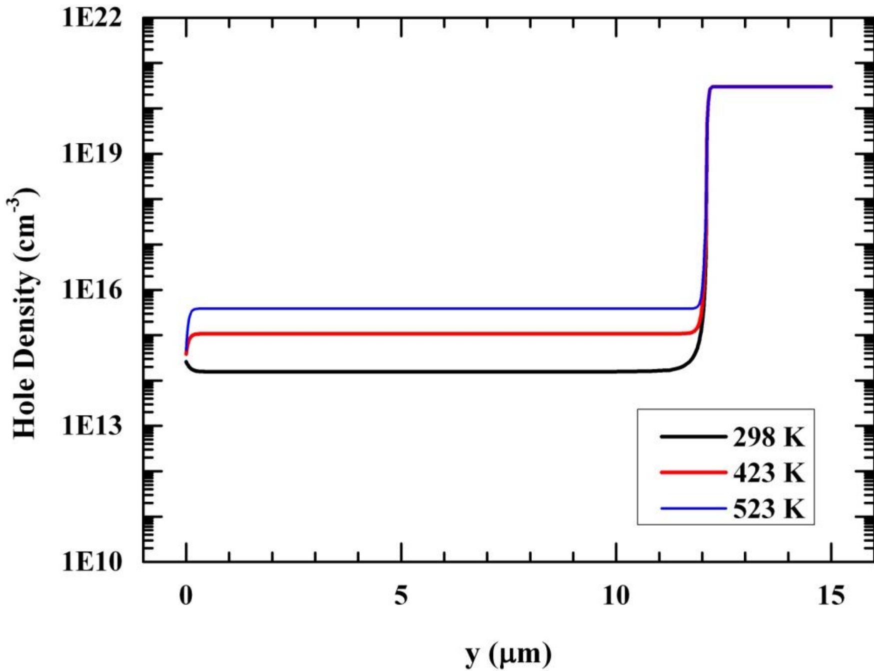

Figure 4-21: The distribution of hole density in the diamond SBD under forward bias of 4 V at different temperatures.

Furthermore, the reverse characteristics of the investigated diamond SBD are far from ideal, with breakdown voltage around 200 V [54]. As no avalanche breakdown is observed, the large leakage current might be caused by flawed Schottky metal- diamond interface, non-uniformities, leakage paths, defects, and low barrier paths.

4.5 Transient characteristics

While there are few experimental works on the transient characteristics of diamond SBD reported in the literature [53, 54, 85], there is no reported study on the transient characteristics of diamond m-i-p+ diode up to this date. In this section, we present analysis, modelling, and simulations of the transient characteristics of the diamond diodes using the double-pulse test method shown in Figure 4-22 [53, 54, 85]. The transient simulations were conducted using TCAD Sentaurus software in the mixed- mode environment to include single-device simulator (for the diamond diode) and circuit simulator [68]. Established models and parameters to fit the static $I-V$ characteristics of the diodes in the previous section were implemented in the single-device simulator.

Firstly, we presented the study of transient characteristics of the investigated diamond SBD by means of simulations and measurements data. Then, TCAD simulation studies on the transient characteristics of diamond m-i-p+ diode were presented.

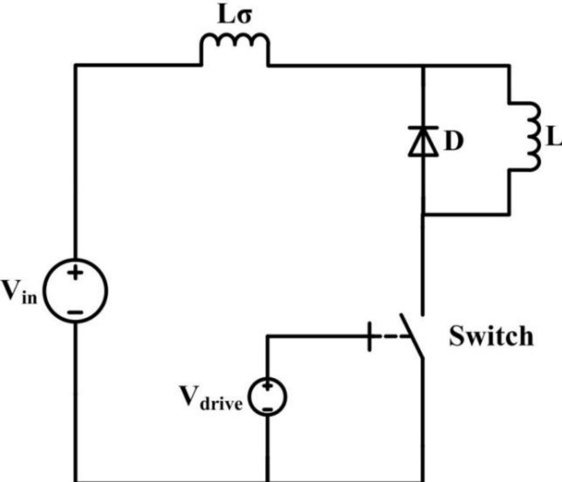

Figure 4-22: Circuit diagram of the double-pulse test-circuit to study the transient characteristics of the diode.

4.5.1 Diamond Schottky barrier diode

Measurements of the turn-off transient characteristics of the investigated diamond SBD (refer to Figure 4-3) were reported by T. Funaki et al. using the double-pulse test method with power MOSFET switch [54]. The measured turn-off transient characteristics with forward conduction current of 0.5 A and reverse blocking voltage of 100V under different turn-off speed di/dt are shown in Figure 4-23. In the measurements, the turn-off speed di/dt was controlled by the value of gate resistance used in the power MOSFET driver. While the measured peak reverse current I_{Rpeak} is higher under higher di/dt, the turn-off time of the diode is smaller, as seen in the faster build-up of diode's voltage dv/dt. The calculated reverse recovery charges ($Q_{rr} = \int I_R.dt$) show very similar value of 5.54 nC and 5.49 nC for different di/dt of 30 A/µs and 50 A/µs respectively [54]. This is reasonable as the amount of charge (hole as majority carrier) that needs to be extracted to support the reverse voltage stays the same regardless of the removal speed.

Figure 4-24 shows the measured turn-off transient characteristics with forward conduction current of 0.4 A and reverse blocking voltage of ~50V under

different temperatures. The measured peaks reverse current I_{Rpeak} increases with higher temperature because the diamond SBD has negative temperature coefficient of resistance. As temperature increases, the hole density increases (refer to Figure 4-21), and so does the amount of charge that needs to be extracted during turn-off. This can be verified from the increase of the calculated recovery charge at higher temperature (3.41 nC at 298 K and 4.24 nC at 523 K) [54].

For measurements under different temperatures, only diamond SBD was subjected to elevated temperature. The circuit parasitic inductance becomes large because of the long wiring used to connect the SBD to the rest of the circuit. This also explains the high ringing oscillation observed in Figure 4-24.

To fit these measurements results, model of power MOSFET switch and circuit parasitic components were incorporated into the simulation circuit set-up as shown in Figure 4-25. The parasitic components are $LPar$, $LDiode$, $LDrain$, and $LSource$. Node 1 is connected to the ohmic contact of the SBD while node 2 is connected to the Schottky contact. The diode was simulated with single-device simulator based on the models and parameters described in previous section.

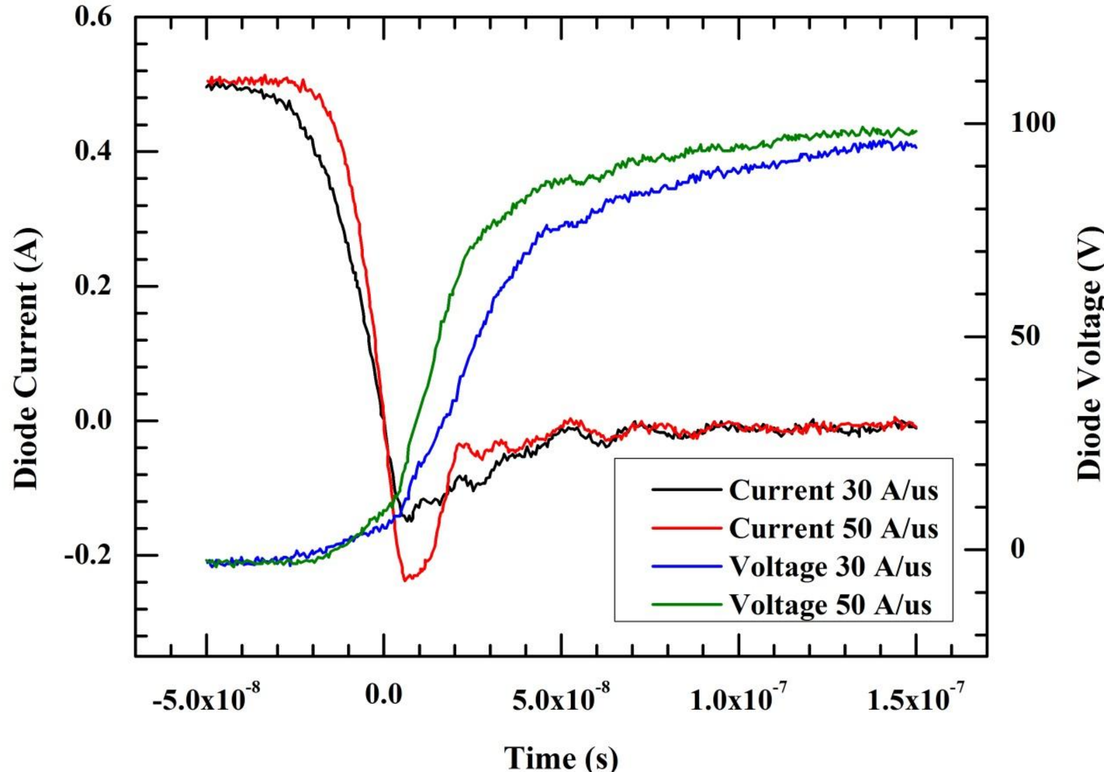

Figure 4-23: Measured turn-off transient characteristics of the investigated SBD at 298 K with 0.5 A forward current and 100 V reverse voltage under different di/dt.

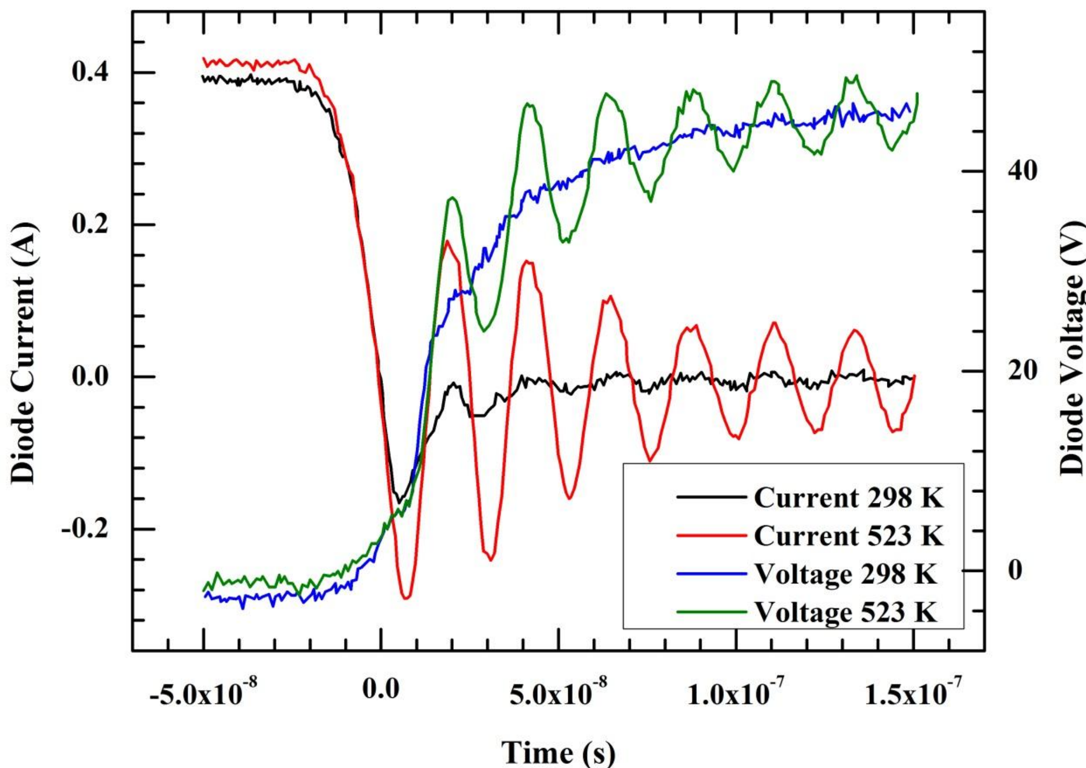

Figure 4-24: Measured turn-off transient characteristics of the investigated SBD with 0.4 A forward current and 50 V reverse voltage at temperature of 298 K and 523 K.

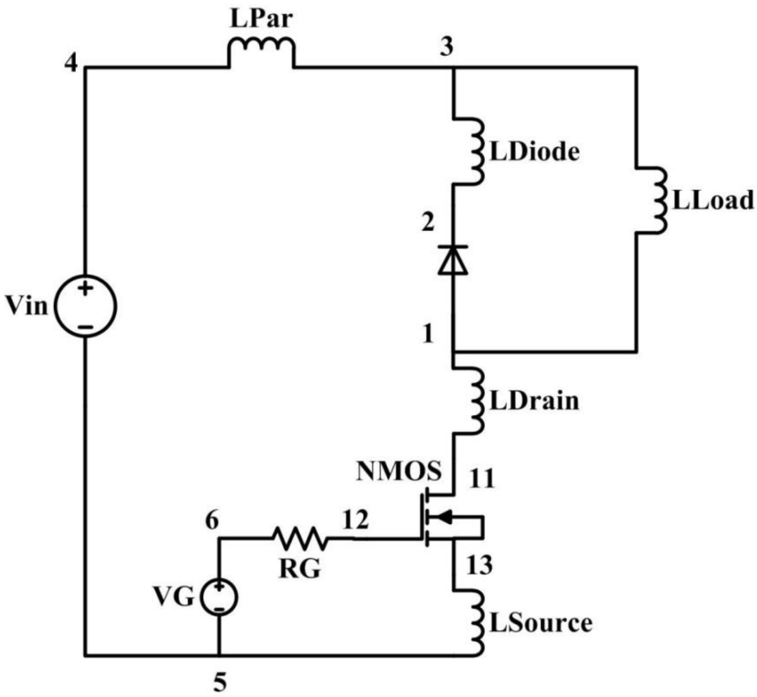

Figure 4-25: Simulated double-pulse test circuit with MOSFET switch and circuit parasitic components.

The power NMOS switch is modelled with sub-circuit SPICE model as shown in Figure 4-26 [86] to produce similar characteristics to the power MOSFET STP4N150. Figure 4-27 and Figure 4-28 show the simulated static characteristics of the power NMOS in comparison with the values in datasheet. Generally good matching between simulations and datasheet results of transfer and output characteristics can be observed.

The value of the gate-drain capacitance (CGD), gate-source capacitance (CGS), and drain-source capacitance (CDS) are 12 pF, 1288 pF, and 108 pF. Parameters of the MOS, DBODY, and other components can be found in APPENDIX C.

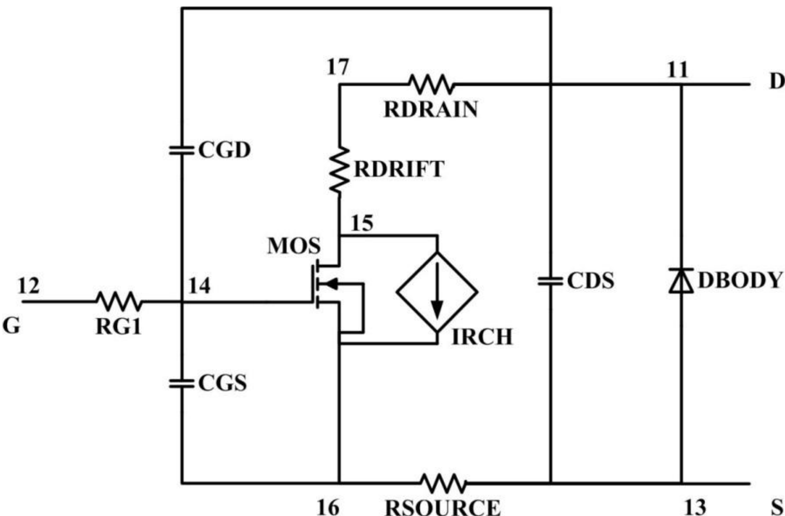

Figure 4-26: Sub-circuit SPICE model of the power NMOS implemented in the simulations.

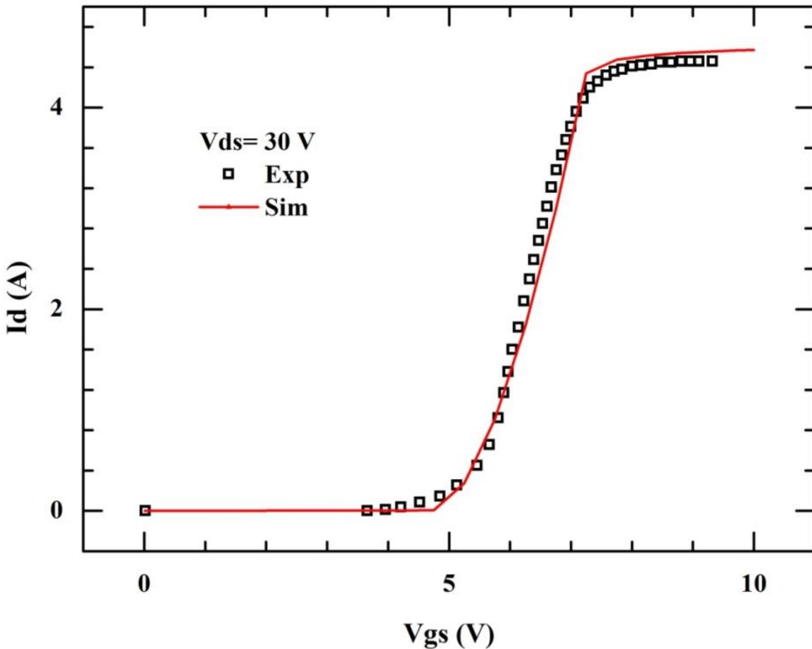

Figure 4-27: Simulated transfer characteristics ($Id - Vgs$) of the power NMOS for different drain-source voltage.

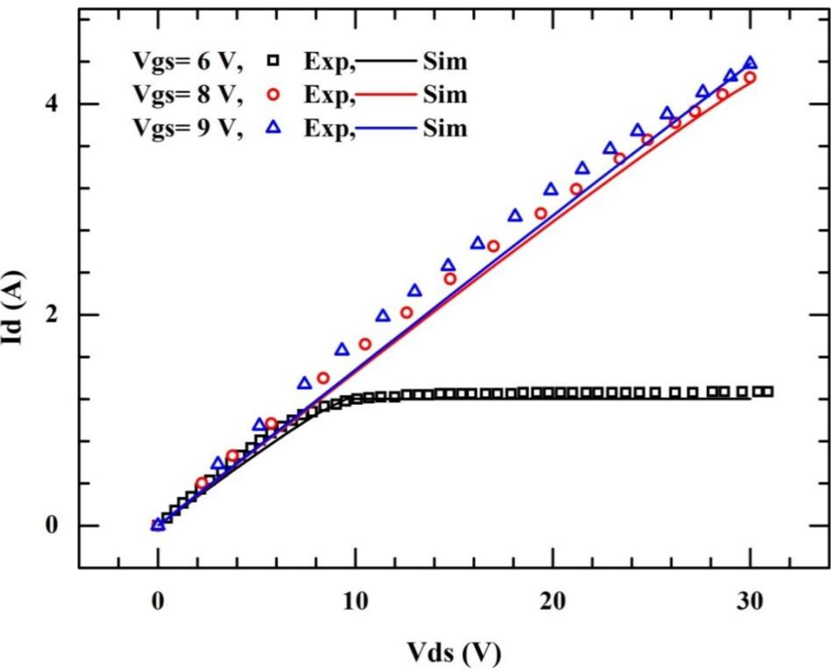

Figure 4-28: Simulated output characteristics ($Id - Vds$) of the power NMOS for different gate-source voltage.

In the simulated circuit (Figure 4-25), the value of $Lload$ used is 5x10^{-4} H while Vin is adjusted to match the blocking voltage for the diode in the measurements. The power NMOS is driven by square wave voltage VG of 10 V.

The turn-off speed di/dt of the diode is controlled by the value of the MOSFET gate resistance RG. During all simulations, the value of $LDiode$, $LDrain$, and $LSource$ are kept at 5x10^{-12} H.

At room temperature

Figure 4-29 shows the simulations results and measurement data (shown as scattered symbol) of the turn-off transient characteristics of the investigated diamond SBD at 298 K with 0.5 A forward current, 100 V reverse voltage, and $di/dt =$ 30 A/µs. In fitting the experimental data, the parameters are adjusted to values indicated in Table 4-3.

Preliminary simulations by using constant value of $CGD = CGD1$ for the power NMOS model shows discrepancies of diode voltage (curve Vdiode_cons) with the measurements data. In real power MOSFET, the values of CGD varies with drain-source voltage Vds. When the MOSFET is on (Vds is low), the capacitance is high. When the MOSFET is off (Vds is high), the capacitance is low because of the larger depletion width.

To simulate this effect, the value of CGD is ramped from initial value $CGD1$ to $CGD2$ at time= $tramp$ during the transient simulations. This step approximation of CGD results in 2 slopes of dv/dt (curve Vdiode_ramp) which better fits the experiment results. This shows the importance of accurate modelling of the switch in the circuit. From Figure 4-29, good matching between the simulated diode current and measurements data can be observed. The voltage of node 1 (SBD's ohmic contact) and node 2 (SBD's Schottky contact) are also shown. Furthermore, the corresponding simulated transient characteristics of the power MOSFET during diode's turn-off are also shown in Figure 4-30.

Table 4-3: Values of parameters used in the transient simulations of diamond SBD at 298 K with 0.5 A forward current and 100 V reverse voltage.

di/dt (A/µs)	$LPar$ (H)	$CGD1$ (pF)	$CGD2$ (pF)	$tramp$ (s)	RG (Ω)
30 (cons_CGD)	50x10^{-8}	35	-	-	80
30 (ramp_CGD)	50x10^{-8}	35	240	0.436x10^{-6}	80
50	50 x10^{-8}	48	800	0.3756 x10^{-6}	35

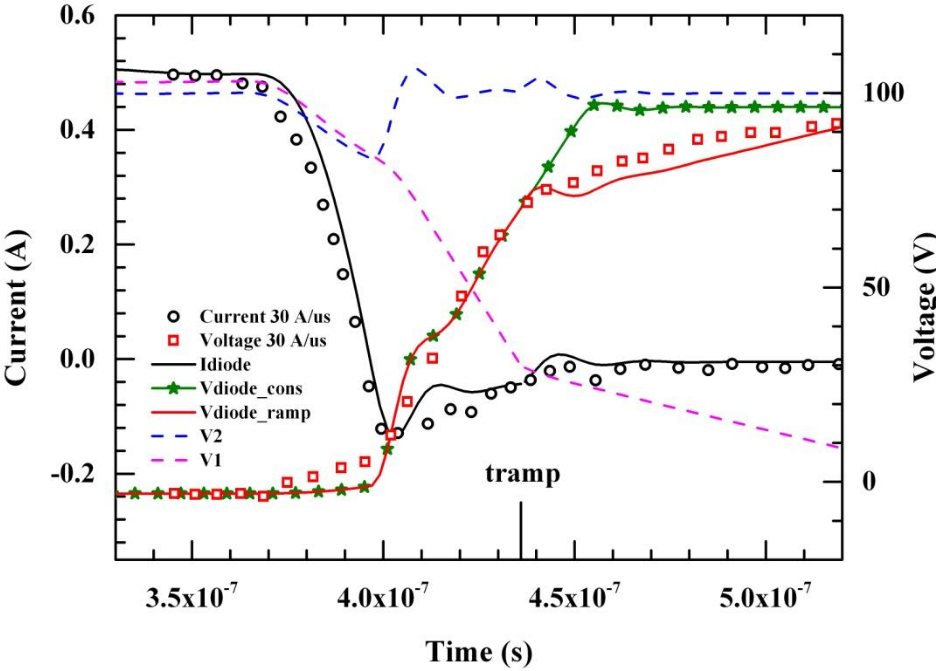

Figure 4-29: Simulation results and measurement data of the turn-off transient characteristics of the investigated SBD at 298 K with 0.5 A forward current, 100 V reverse voltage, and di/dt = 30 A/μs. Variation of diode voltage with different values of MOSFET gate-drain capacitance CGD are shown. The diode's forward voltage drop at 0.5 A forward current is 3 V.

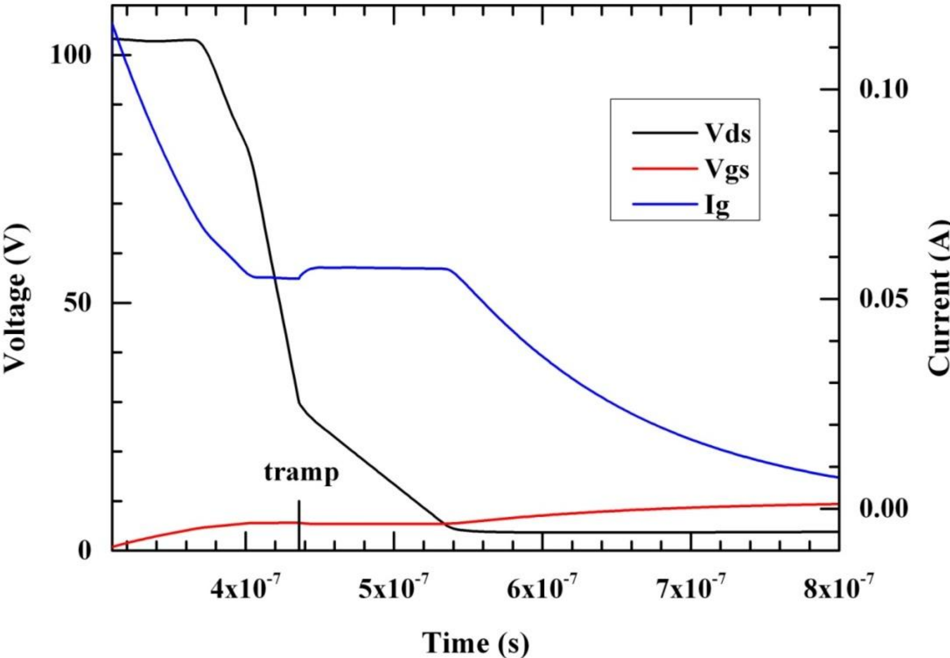

Figure 4-30: Simulated turn-on transient characteristics of the MOSFET at 298 K when the diamond SBD is turned-off with di/dt = 30 A/μs.

Figure 4-31 shows the simulation results and measurements data of turn-off transient characteristics of the investigated diamond SBD with di/dt = 50 A/μs at

the same conditions (298 K for 0.5 A forward current, 100 V reverse voltage). By using 2 values of CGD (refer to Table 4-3), generally good matching with measurements data can be observed.

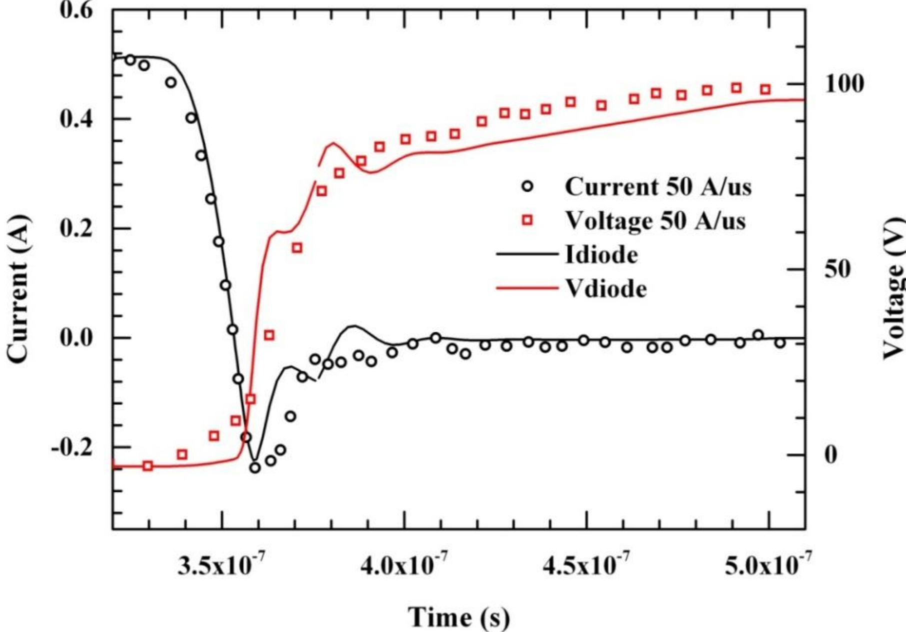

Figure 4-31: Simulation results and measurement data of the turn-off transient characteristics of the investigated SBD at 298 K with 0.5 A forward current, 100 V reverse voltage, and di/dt = 50 A/μs.

At elevated temperatures

In the transient simulations at elevated temperature, the value of $LPar$ was set at 1x10^{-6} H to simulate the large inductance of the long wiring used in the experimental set-up. Furthermore, the value of CGD is ramped twice from $CGD1$ to $CGD2$ at time= $tramp1$ and then to $CGD3$ at time= $tramp2$ to further smooth the simulated dv/dt. Comparisons of the simulation results and measurements data with 0.4 A forward current, 50 V reverse voltage, and $di/dt \sim$ 40 A/μs at 298 K are shown in Figure 4-32. The corresponding parameters used in the simulations are listed in Table 4-4. While good agreement with measurements data can be observed in general, the simulated SBD's voltage shows large overshoot due to the swing of voltage in node 2 (V2). This happens because of the increase in the value of $LPar$.

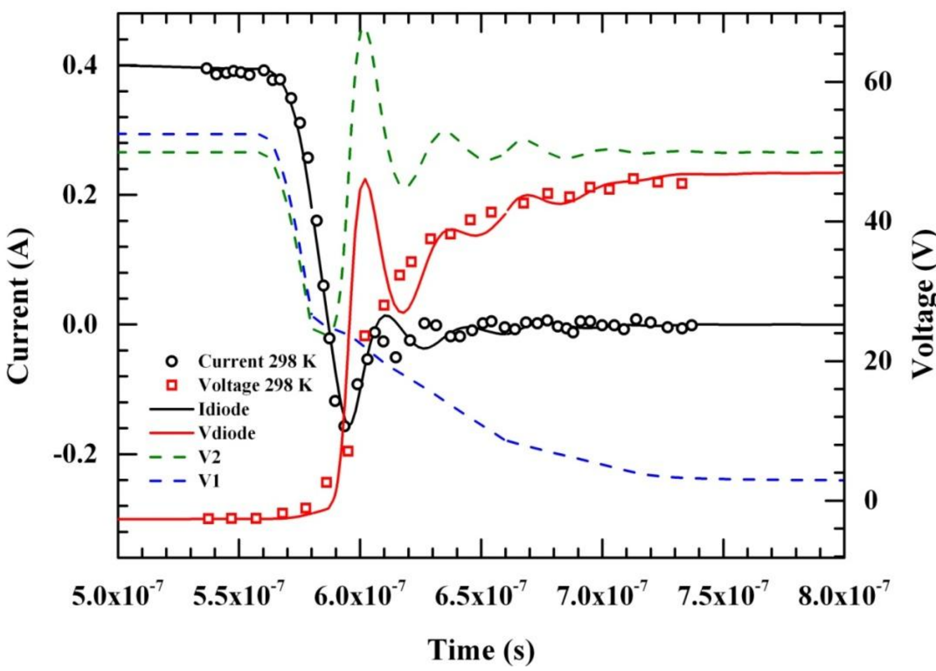

Figure 4-32: Simulation results and measurement data of the turn-off transient characteristics of the investigated SBD at 298 K with 0.4 A forward current and 50 V reverse voltage.

Table 4-4: Values of parameters used in the transient simulations of diamond SBD with 0.4 A forward current and 50 V reverse voltage for elevated temperature set-up.

Temperature (K)	$CGD1$ (pF)	$CGD2$ (pF)	$CGD3$ (pF)	$tramp1$ (s)	$tramp2$ (s)	RG (Ω)
298	12	300	800	0.58e-6	0.66e-6	69.5
523	30	500	1500	0.518e-6	0.533e-6	9.5

Comparisons of simulation results (based on parameters in Table 4-4) and measurements data at 523 K are shown in Figure 4-33. The corresponding simulated voltage of node 1 and 2 are shown in Figure 4-34. The simulated SBD's voltage also exhibits large overshoot due to large swing of voltage in node 2. To improve the simulations results, the increase of parasitic inductance should be distributed as parasitic inductor connected to the Schottky contact and ohmic contact of the SBD, instead of increasing $LPar$ only.

Furthermore, the simulation results shown in Figure 4-32 and Figure 4-33 cannot reproduce the same ringing oscillations (frequency and amplitude) found in the measurements data. More accurate modeling of the circuit parasitic components and the switch is needed for better fitting.

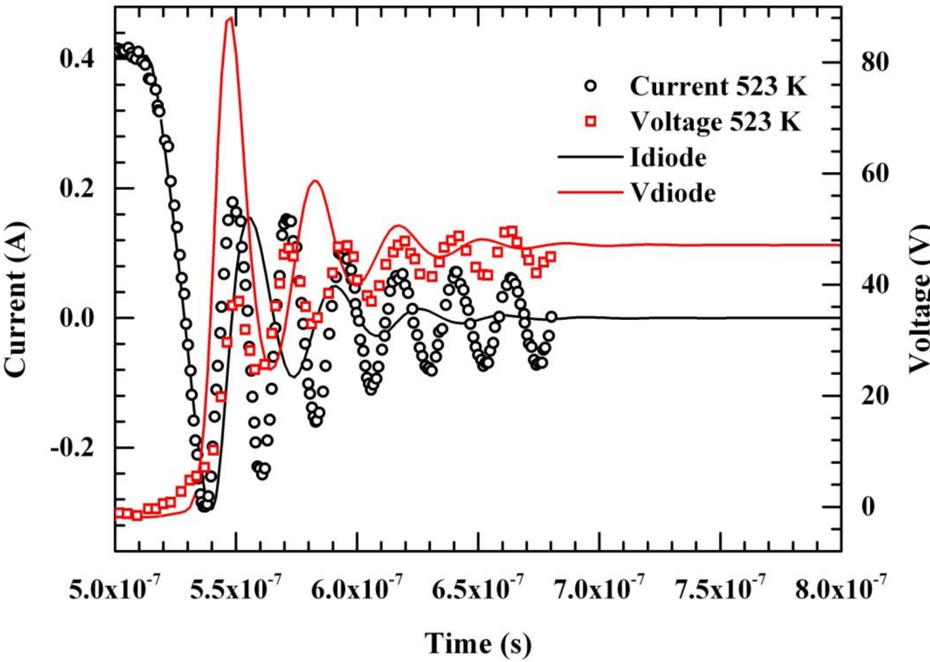

Figure 4-33: Simulation results and measurement data of the turn-off transient characteristics of the investigated SBD at 523 K with 0.4 A forward current and 50 V reverse voltage.

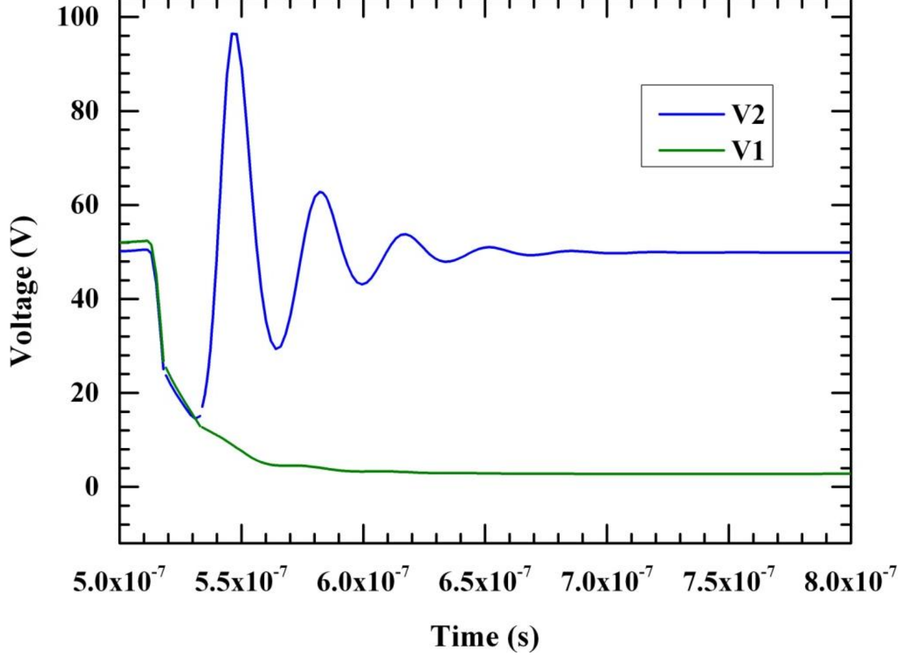

Figure 4-34: The simulated voltage in node 1 and 2 during the turn-off transient simulation of the investigated SBD at 523 K with 0.4 A forward current and 50 V reverse voltage.

4.5.2 Diamond metal-intrinsic-p+ diode

As there is no measurement on the transient characteristics of diamond m-i-p+ diode reported up to this date, we conducted the transient study solely based on the

TCAD simulations. We presented and compared the transient simulations using different circuit parasitic components and different switch models, i.e. ideal switch model [52] and power NMOS model.

BASED ON IDEAL SWITCH MODEL

Transient simulations for the diamond m-i-p+ diode were conducted using the circuit in Figure 4-22 with ideal voltage sources for V_{in} and V_{drive}, ideal inductor for load inductor (L) and stray inductance (L_{σ}), and ideal switch with on-resistance of 10 Ω and off-resistance of 10^{12} Ω. Diode D was simulated with single-device simulator based on the established models and parameters that have been calibrated to match the static forward $I-V$ characteristics of the investigated diamond m-i-p+ diode samples, i.e. Al and Au diamond m-i-p+ diode with 10 µm drift length (elaborated in section 4.4.1).

The diodes' cross-sectional area is scaled up to support forward current of 0.1 A with reasonable forward voltage drops as shown in Table 4-5 (verified with static and transient simulation results). During the simulations, the values of L and L_{σ} were kept at 0.5 mH and 1 µH respectively, while V_{in} and switch on-time duration were varied to control the turn-off speed (di/dt) and the forward current magnitude respectively.

Table 4-5: Diodes' characteristics implemented in the transient simulations.

Schottky contact	Scaled cross-sectional Area (cm^2)	Temp (K)	Forward voltage drop at 0.1 A current (V)
Al	0.0166	300	2.559
Au	0.04	300	3.104
		400	3.082
		507	3.485

At room temperature

Turn-off transient simulations at 300 K were conducted for the diamond m-i-p+ diode with Al contact. To verify the majority carrier conduction of the diode, peak reverse current (I_{Rpeak}) dependency to forward current (I_F) was investigated.

During the simulations, reverse voltage (V_{in}) was maintained at 50 V, while I_F was varied around 0.1 A. The simulations results shown in Figure 4-35 display fast switching behaviour with I_{Rpeak} that is independent of I_F. This suggests that no minority carriers are involved in the conduction process and the reverse-current is mainly due to displacement current. The value of di/dt in this circuit set-up is dependent on the circuit inductive components and the value of V_{in} [53].

Furthermore, reverse current dependency to the reverse voltage was studied by maintaining same forward current I_F at around 0.1 A while varying V_{in}. Figure 4-36 shows the simulations results for this set-up at 300 K. It can be seen that I_{Rpeak} varied with the applied reverse voltage V_{in}, which is caused by different extracted charge for different reverse voltage.

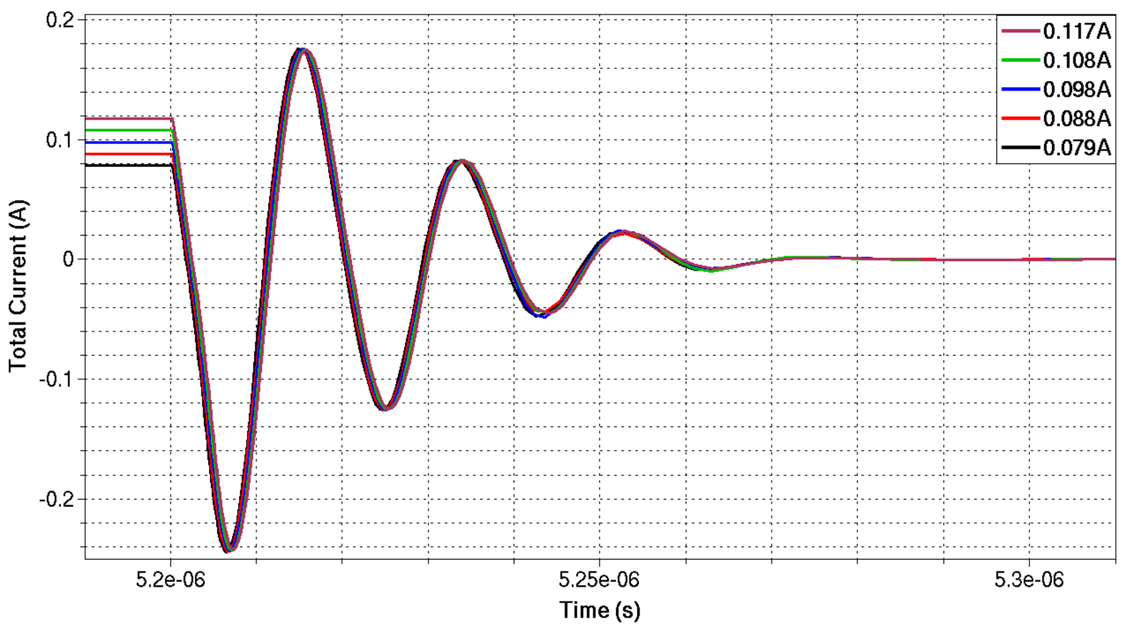

Figure 4-35: Simulated turn-off transient characteristics of Al diamond m-i-p+ diode with different forward current under reverse voltage of 50 V at 300 K.

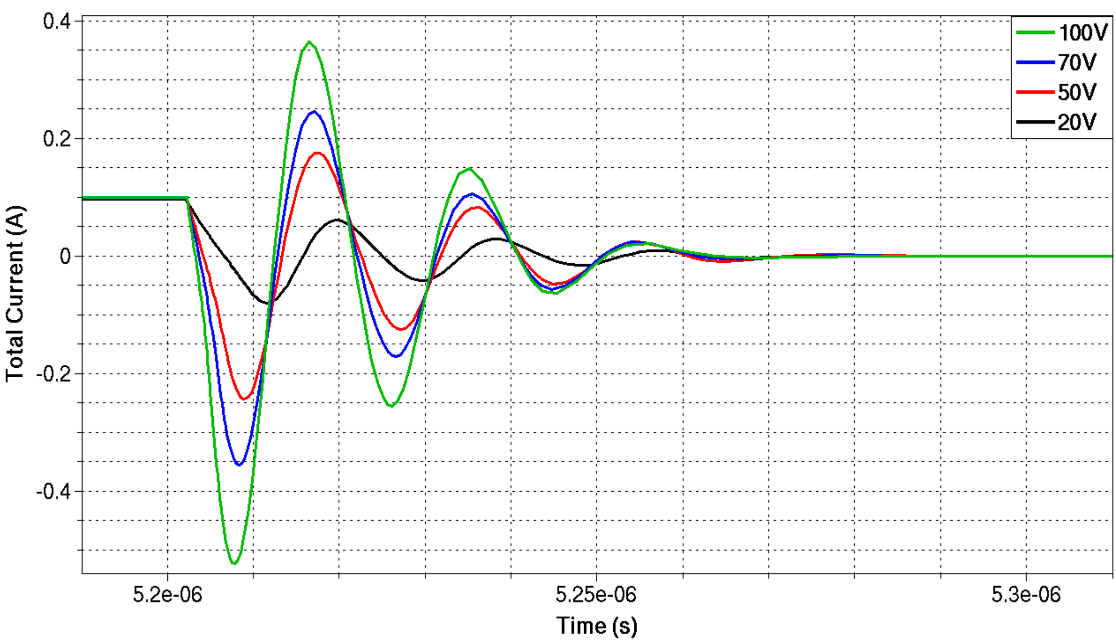

Figure 4-36: Simulated turn-off transient characteristics of Al diamond m-i-p+ diode with 0.1 A forward current under different reverse voltage at 300 K.

Due to difficulties in obtaining the diodes samples, there is no measurement on the switching characteristics of diamond m-i-p+ diodes conducted. Therefore, the simulations results in Figure 4-35 and Figure 4-36 are compared with the measurements on diamond Schottky barrier diodes reported in [53, 85] for comparative evaluations. This is rational because both diodes have the same basic structures of unipolar Schottky diode. Even though they have different dimensions, contact materials, and doping concentration, they should demonstrate similar switching behaviours under certain conditions.

We found qualitative agreements between the simulations and experiments results for the peak reverse current dependency on the forward current and reverse voltage, which are the actual characteristics of unipolar diode. Ringing oscillations observed both in simulation and experiment results are caused by interactions between circuit inductance and terminal capacitance (depletion capacitance) of the diode. While the oscillation frequency is constant with variation of forward current (refer to Figure 4-35), it varies with variation of reverse voltage (refer to Figure 4-36) because the depletion capacitance of the diode only varies with the reverse voltage.

At elevated temperatures

Turn-off transient simulations at elevated temperatures were conducted for the diamond m-i-p+ diode with Au Schottky contact and drift length of 10 µm because its static characteristics at elevated temperatures have been measured and fitted with the simulations results (refer to Figure 4-8). The established models and parameters to match those static $I-V$ characteristics at different temperatures were implemented in the transient simulations for diode D with scaled area stated in Table 4-5. Figure 4-37 shows the transient simulations results at temperature of 300 K, 400 K, and 507 K with reverse voltage V_{in} and forward current I_F maintained at 50 V and 0.1 A.

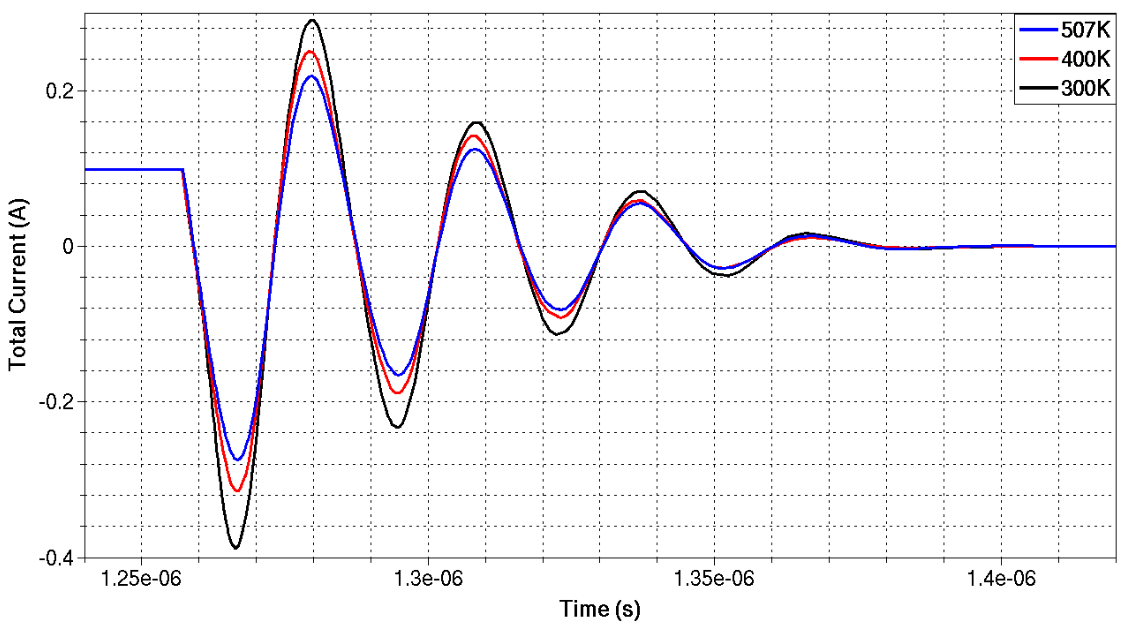

Figure 4-37: Simulated turn-off transient characteristics of Au diamond m-i-p+ diode with forward current of 0.1 A under reverse voltage of 50 V at 300 K, 400 K, and 507 K.

It can be observed that I_{Rpeak} decreases with increasing temperature for diamond m-i-p+ diode. This is reasonable since diamond m-i-p+ diode has positive temperature coefficient of resistance. This analysis is in line with the experiment results for diamond SBD reported in [54], where I_{Rpeak} increases with increasing temperature due to the negative temperature coefficient of resistance of the experimental diamond SBD. While decrease of I_{Rpeak} at high temperature can be advantageous, the forward voltage drop in the diode increases. Therefore, careful

device design to optimize the trade-off between on-state and switching losses is crucial.

While the simulated turn-off transient characteristics of diamond m-i-p+ diodes in Figure 4-35, Figure 4-36, and Figure 4-37 show certain behaviours of unipolar diode, the peak reverse current I_{Rpeak} values is much larger than expected values and experiment results for diamond SBD. This might be cause by the use of ideal switch model, inaccurate modelling of circuit's parasitic components, and inaccurate intrinsic parameters of the diode (such as doping profiles, trap profiles, deep levels, etc.) [87, 88].

BASED ON POWER NMOS MODEL

Transient simulations of the diamond m-i-p+ diode using power NMOS model were conducted based on the double pulse test circuit in Figure 4-25 to include the parasitic components. Sub-circuit SPICE model with ramped CGD model and parameters elaborated in Section 4.5.1 were implemented. The simulated diode was Al diamond m-i-p+ diode with 10 µm drift length. The diode's cross sectional area was scaled up to 0.0097 cm^2 (the same area as the investigated diamond p-/p+ SBD in section 4.5.1).

Figure 4-38 shows the simulation results of the turn-off transient characteristics of the investigated Al diamond m-i-p+ diode at 298 K with 0.5 A forward current, 100 V reverse voltage. In the simulation, the same test conditions as those for transient simulations of diamond SBD in section 4.5.1. were used: $LPar$ =50x10^{-8} H, $CGD1$ = 35 pF, $CGD2$ = 240 pF, $tramp$ = 0.436x10^{-6} s, RG = 80 Ω.

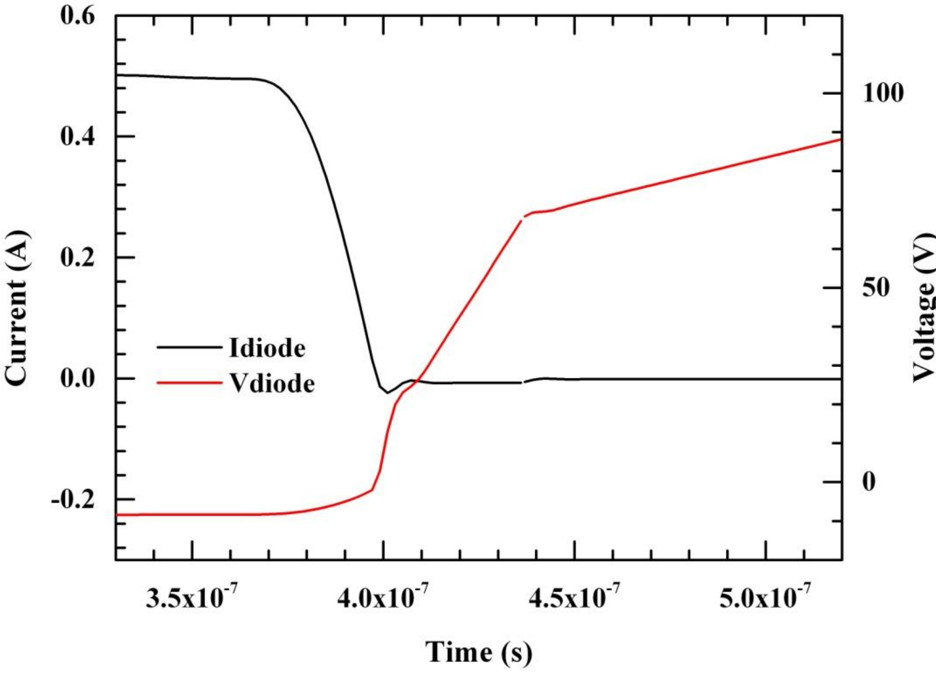

Figure 4-38: Simulation results of the turn-off transient characteristics of the investigated diamond m-i-p+ diode with Al Schottky contact (area of 0.0097 cm^2) at 298 K with 0.5 A forward current, 100 V reverse voltage. The diode's forward voltage drop at 0.5 A forward current is 8.5 V.

The results shown in Figure 4-38 display very small peak reverse current compared to that of diamond SBD (Figure 4-29) due to the low holes concentration in the drift region of diamond m-i-p+ diode. Although diamond m-i-p+ diode shows high on-state/conduction losses (due to high voltage drop), it has very low switching losses which makes it suitable for high switching frequency applications. Therefore, the doping concentration in the drift region of diamond Schottky diode should be carefully designed based on the intended applications for optimal performances.

Furthermore, the simulated turn-off transient characteristics of diamond m-i-p+ diode in Figure 4-38 that uses power NMOS model and takes the circuit parasitic components into account exhibits very different behaviour from simulation results that uses ideal switch model. This shows the importance of accurate modelling of the switch and circuit parasitic components in the simulations to yield reliable results.

4.6 Conclusions

The electrical characteristics of diamond m-i-p+ diode and typical p-/p+ diamond SBD have been compared and investigated by means of experimental data and numerical simulations. Good correlations between the simulations results and experiments results for static forward $I-V$ characteristics of both diodes have been achieved by applying suitable physics models and parameters (elaborated in Chapter 3) in the intimate contact diode model. In contrast with the behaviour of diamond m-i-p+ diodes, the diamond SBD displays negative temperature coefficients of resistance due to the incomplete ionization phenomena.

The turn-off transient characteristics of both diodes have been investigated using the double-pulse test method. For the investigated diamond SBD, generally good matching between simulation results and measurements data can be achieved by taking into account the circuit parasitic components and by implementing sub-circuit SPICE model to simulate the power MOSFET.

On the other hand, study on the transient characteristics of diamond m-i-p+ diode was conducted solely based on TCAD simulations since there is no reported transient measurement up to this date. While simulation results using ideal switch show qualitative agreement with the behaviour of unipolar diode, the peak reverse current is larger than expectation. More realistic simulations by incorporating the circuit parasitic components and power MOSFET models show that the peak reverse current of the diamond m-i-p+ diode during transient turn-off is even smaller than that of diamond SBD. This demonstrate the importance of accurate modelling of the switch and circuit parasitic components in the transient simulations to yield reliable results.

Furthermore, while the ideal intimate contact diode model has shown overall good matches with experiment results, it does not take into account the non-ideal properties of the experimental diodes such as Fermi level pinning, defects, traps, nonhomogeneous metal-diamond interface, etc. which cause deviations of Schottky barrier heights from their ideal values. Analysis of these non-ideal behaviours is presented in the next chapter.

5 CHARACTERIZATIONS OF VERTICAL MO/DIAMOND SCHOTTKY BARRIER DIODE FROM NON-IDEAL *I-V* AND *C-V* MEASUREMENTS BASED ON THE MIS MODEL

5.1 Introduction

Characteristics of practical diodes depart from the ideal rectifier characteristics which might be caused by non-ideal metal-semiconductor interface in practical devices such as defects, inhomogeneity, interfacial layer and interfacial states charges, traps, edge leakage, etc. Consequently, Schottky barrier height dependence on metal work function becomes weaker and its value is dependent on the applied bias (as indicated by their ideality factor) [89].

Rectifying contact in diamond SBDs has been realized by Schottky contact on Oxygen terminated diamond surface due to its chemical stability [22]. However, the nature of metal-semiconductor interface is poorly understood. Schottky barrier height dependence on metal work function is unclear and highly dependent on the fabrication process, especially surface preparations [22]. Oxygen surface treatments such as plasma oxidation, thermal oxidation, and wet-chemical oxidation might result in interfacial layer, surface oxidized layer, and highly disordered surface defect layer [90-92].

Owing to the importance of contact characteristics to the device's performances, many theoretical models to explain Schottky metal-semiconductor interface have been presented in the literature in the past few decades [93]. Examples are metal-interfacial layer-semiconductor (MIS) model that relies on the existence of thin interfacial layer with interface states charges, metal-induced-gap-states (MIGS) model, defect-induced-gap-states (DIGS) model, bond-polarization (BP) model [94], etc. Despite the long research history, there is no model that is unanimously agreed so far. Studies that focus on metal-diamond interface

employing electrical and optical characterization using different Schottky metals were also reported in recent years [43, 91, 92, 95-97].

In this study, we presented and analysed the measurements results of several experimental vertical diamond SBDs with Molybdenum Schottky contact with different specifications. The Mo/diamond SBDs were fabricated on the Oxygen terminated single-crystal diamond substrates with field plate termination structure using Al_2O_3 as the field oxide.

As simple intimate contact diode model is not sufficient to explain the non-ideal behaviours of our experimental SBDs, we presented the analysis of the SBD based on the MIS model by using the current- voltage ($I-V$) and capacitance-voltage ($C-V$) measurements results. The MIS model is applied to account for the surface oxidized layer and the Fermi level pinning at the Schottky metal-diamond interface. We also presented the determination of interfacial layer thickness and interface states energy distribution.

5.2 Investigated vertical Mo/diamond Schottky barrier diodes

5.2.1 Fabrication process

As part of our collaborative work with AIST Japan, vertical Mo/diamond SBDs with field plate termination structure as shown in Figure 5-1 had been fabricated.

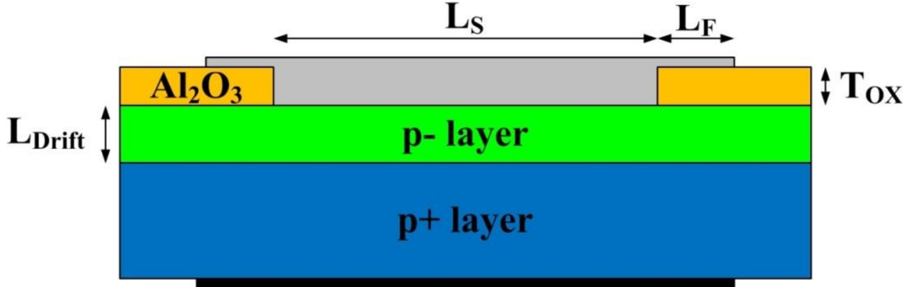

Figure 5-1: Structure of the experimental vertical Mo/diamond SBD with field plate termination structure.

Initially, p- drift layer of thickness L_{Drift} was deposited by Microwave Plasma Chemical Vapour Deposition (MPCVD) technique on the heavily Boron doped HPHT (001) IIb single crystal diamond substrate with thickness > 300 µm and Boron concentration> 10^{20} cm^{-3}. The source of Boron doping was Trimethylboron

(TMB) diluted by Hydrogen. Oxygen was introduced to control the concentration in the p- drift layer. Afterwards, the substrate was chemically cleaned using acid wash. Ti (30 nm)/Pt (30 nm)/Au (100 nm) ohmic contact was formed on the backside of the substrate by electron beam deposition, followed by annealing at 420^0 C.

The Al_2O_3 field plate insulator with thickness T_{OX} and length L_F was formed by utilizing photolithography with lift-off technique and RF sputtering. The p- layer surface is then oxidized with Oxygen plasma and treated with UV/Ozone to increase the Oxygen coverage. Finally, several Schottky contacts of Mo (30 nm)/Au (200 nm) with square shape and rounded corners of area ~ L_S x L_S were formed by photolithography with lift-off technique and RF sputtering.

In the study, two diamond wafers, i.e. R100230-03 and R100230-17 were fabricated with different specifications as indicated in Table 5-1. On each wafers, several SBDs with different sizes of Schottky contacts and field plate lengths as indicated in Table 5-2 were formed. The top views of both dies with various Schottky contacts configurations are shown in Figure 5-2 and Figure 5-3. Some defects on the experimental SBDs can be obviously observed in both figures.

Furthermore, the measurements of SBD's $I-V$ and $C-V$ characteristics were carried out using Agilent B1505A Power Device Analyzer/ Curve Tracer.

Table 5-1: Specifications of the fabricated diamond wafers.

	Doping of p- layer (cm^{-3})	L_{Drift} (μm)	T_{OX} (μm)
Wafer R100230-03	~$9.29x10^{14}$	10	1.2
Wafer R100230-17	~$1.029x10^{16}$	11	1.9

Table 5-2: Specifications of the diamond SBDs fabricated on each wafers.

	L_F (μm)	L_S (μm)	Schottky contact area (cm^2)
A1000	50	1000	$9.9x10^{-3}$
B200	50	200	$3.96x10^{-4}$
C100	25	100	$9.9x10^{-5}$
D80	35	80	$6.336x10^{-5}$
E50	50	50	$2.475x10^{-5}$
F30	60	30	$8.91x10^{-6}$

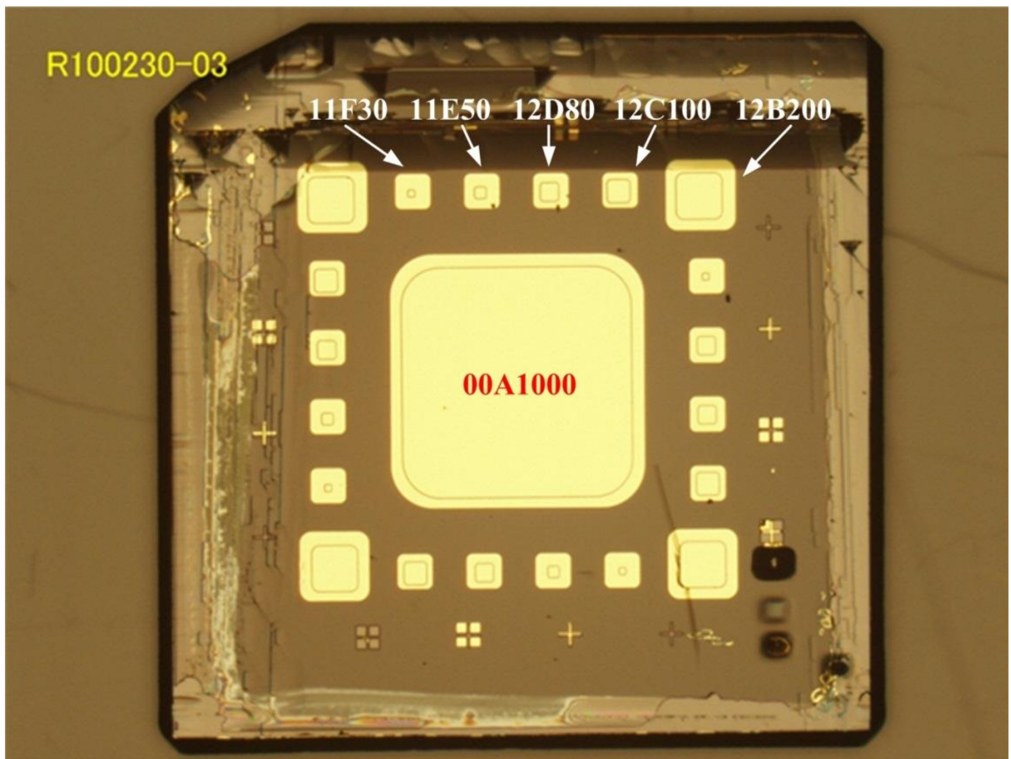

Figure 5-2: The top view of R100230-03 die with SBDs of different sizes and field plate lengths.

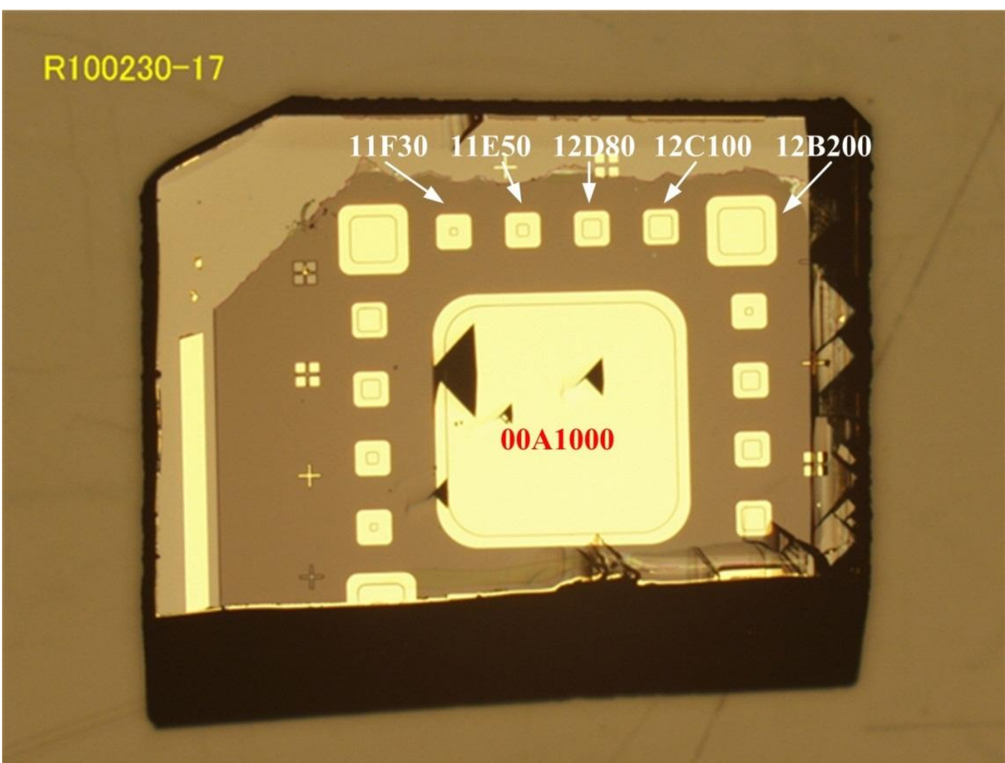

Figure 5-3: The top view of R100230-17 die with SBDs of different sizes and field plate lengths.

5.2.2 Experimental results and discussions

Measurements on wafer R100230-03

The forward bias $I-V$ measurements results for vertical Mo/diamond SBDs, i.e. 11F30, 11E50, 12D80, 12C100, 12B200, and 00A1000 (refer to Figure 5-2) fabricated on wafer R100230-03 at temperatures of 298 K, 423 K, and 523 K are shown in Figure 5-4, Figure 5-5, and Figure 5-6. Their corresponding reverse bias $I-V$ measurements results are shown in Figure 5-7, Figure 5-8, and Figure 5-9.

From the forward bias log-scale curves, we can observe multiple barriers for SBD 00A1000, 12D80, and 11E50 which form low barrier leakage paths, especially for 11E50 and 12D80. This might be caused by defects as black spots are apparent on these SBDs as shown in Figure 5-2. Furthermore, SBD with large contact size such as 00A1000 are prone to poor reverse bias performance due to incorporation of defects and non-uniformities in the metal-diamond interface. As a result, the breakdown voltages achieved by these SBDs are quite low as seen in the reverse $I-V$ measurements results.

Non-uniformities in the contact formations can also be observed from the forward current density curves, where larger SBDs has higher current density (especially for SBD 00A1000). The high turn-on voltage ~3 V observed also suggests increase in the Schottky barrier height from ideal values of 2.24 eV.

Among all the SBDs on wafer R100230-03, the best performing SBDs are 11F30, 12 C100, and 12B200 with high breakdown voltages more than 1500 V. Forward bias $I-V$ measurements for SBD 11E50 at elevated temperatures of 423 K and 523 K might be somewhat erroneous as the low voltage leakage current (observed in $I-V$ measurements at 298 K) vanishes. In addition, sudden increase in the reverse current of SBD 11F30 at reverse bias around 1300 V at 298 K and 523 K might also be caused by erroneous measurements.

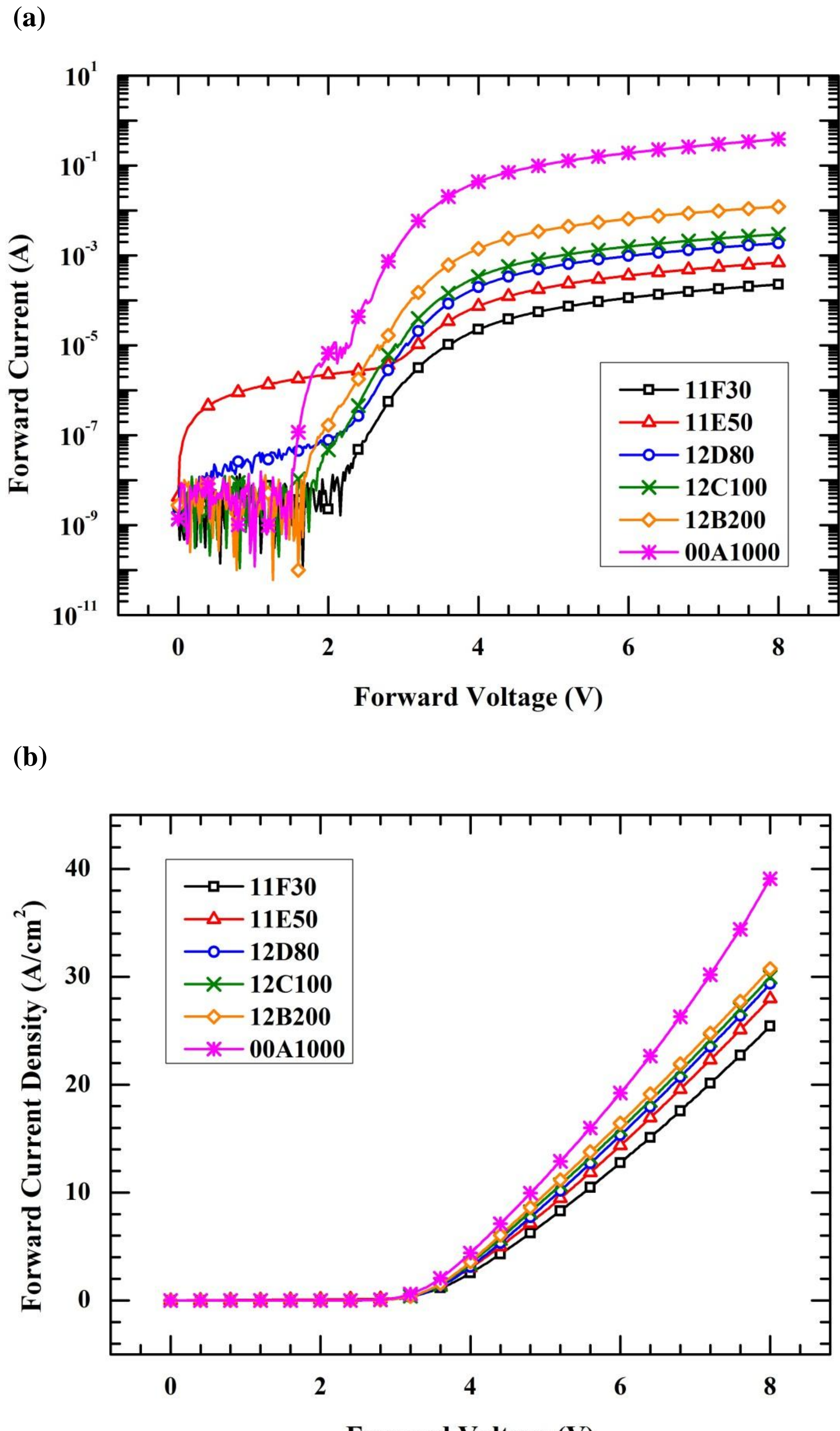

Figure 5-4: The measured forward bias $I-V$ characteristics of the Mo/diamond SBDs on R100230-03 wafer at 298 K in terms of: (a) total current and (b) current density.

(a)

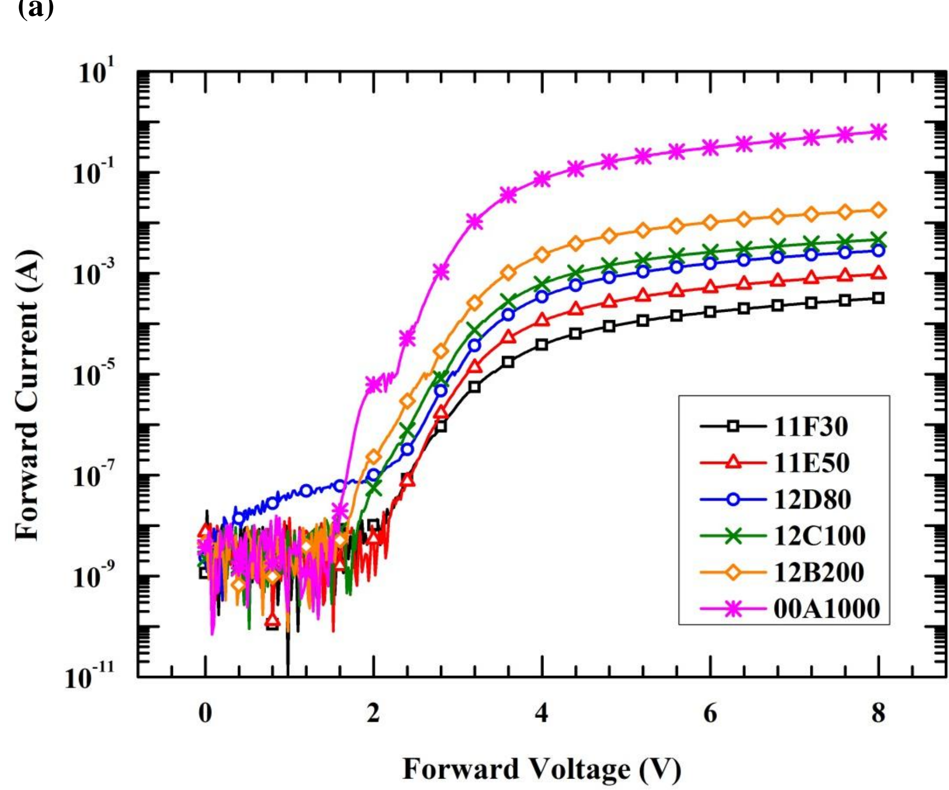

(b)

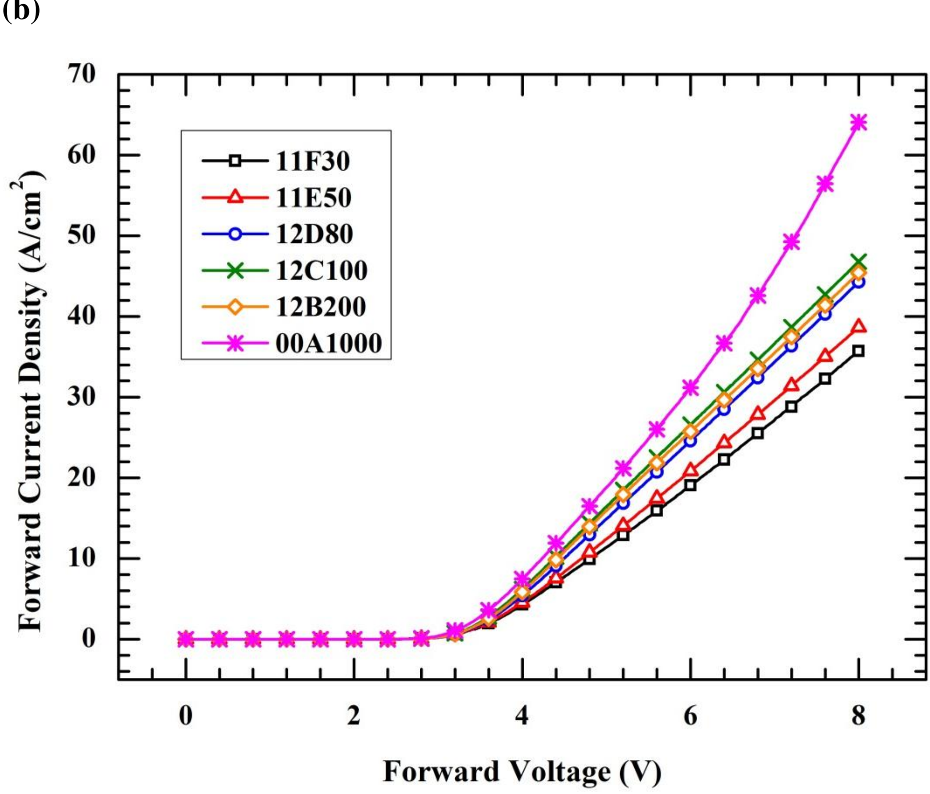

Figure 5-5: The measured forward bias $I-V$ characteristics of the Mo/diamond SBDs on R100230-03 wafer at 423 K in terms of: (a) total current and (b) current density.

(a)

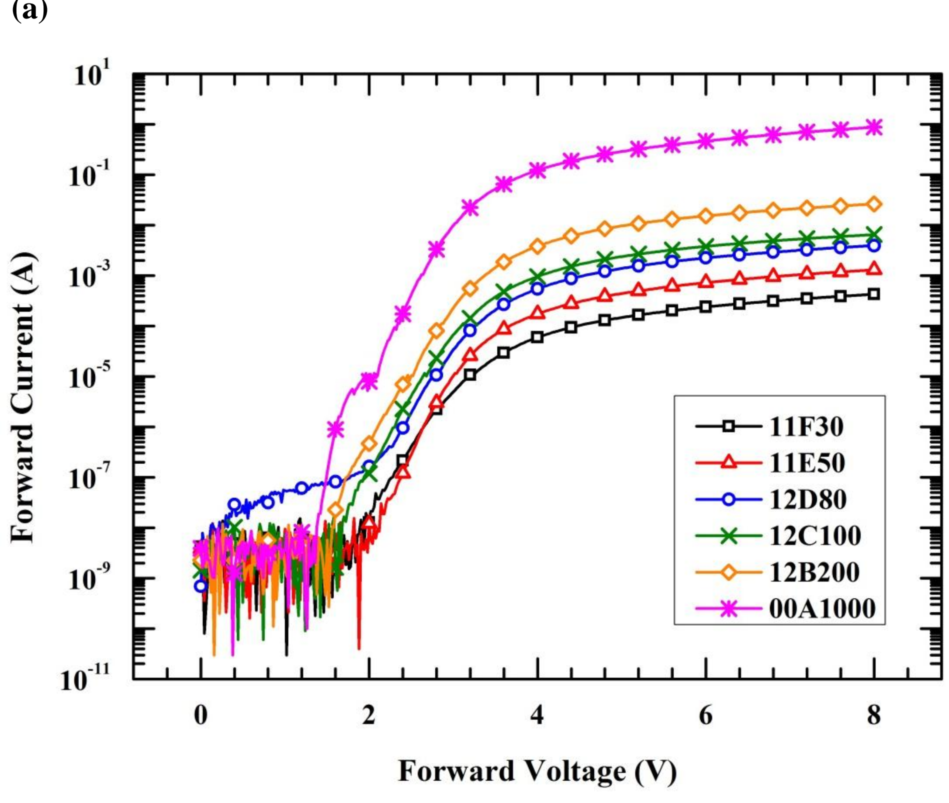

(b)

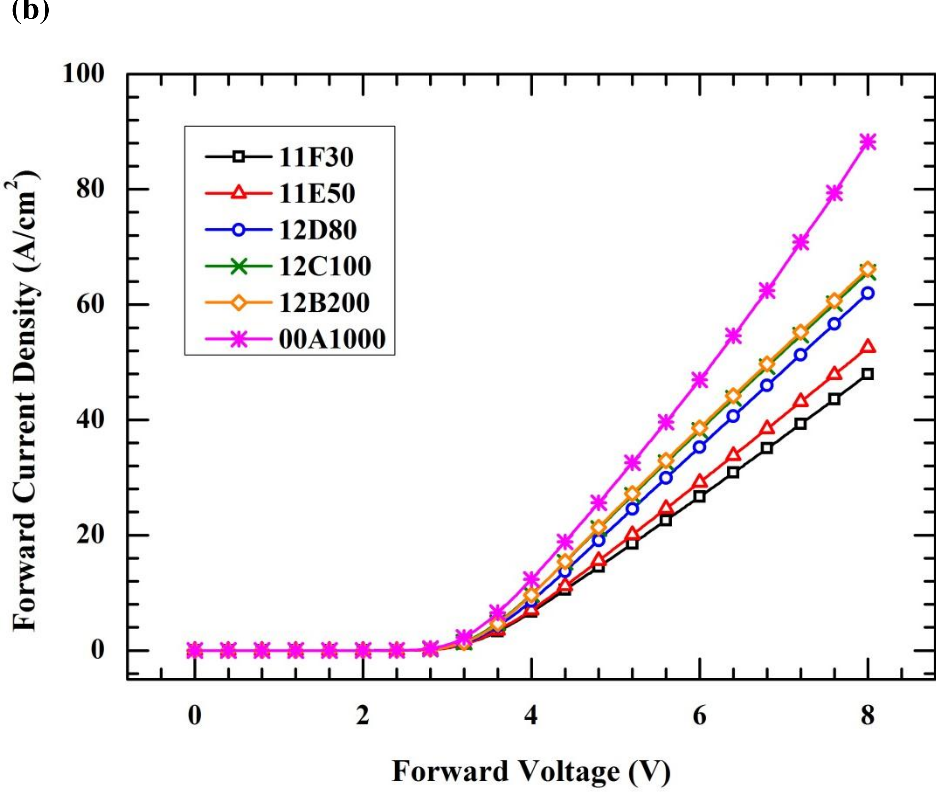

Figure 5-6: The measured forward bias $I-V$ characteristics of the Mo/diamond SBDs on R100230-03 wafer at 523 K in terms of: (a) total current and (b) current density.

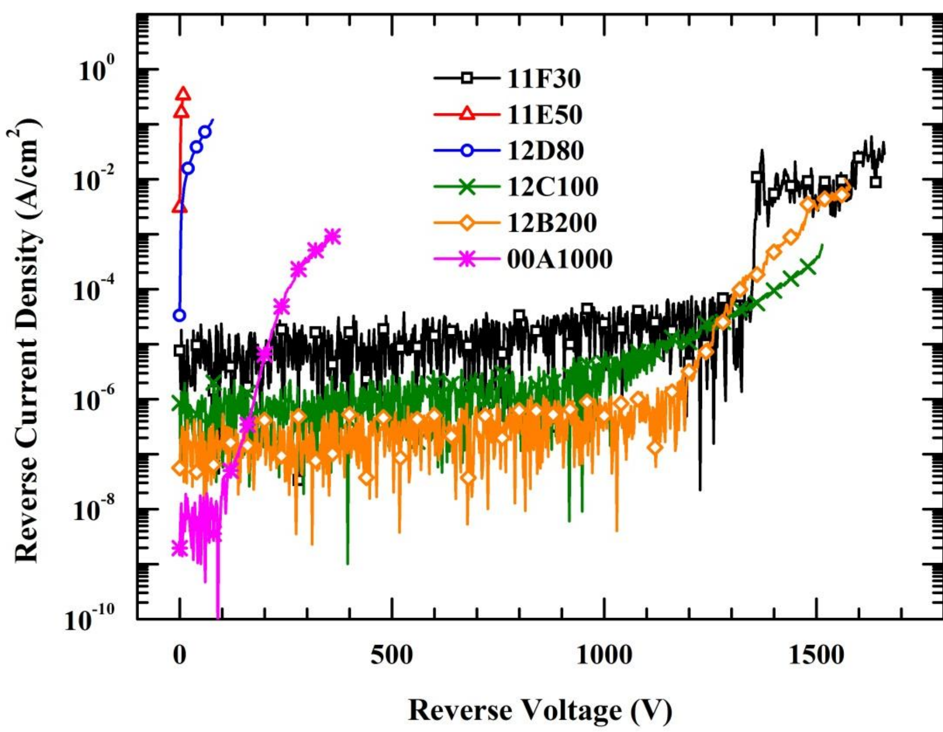

Figure 5-7: The measured reverse bias $I-V$ characteristics of the Mo/diamond SBDs on R100230-03 wafer at 298 K.

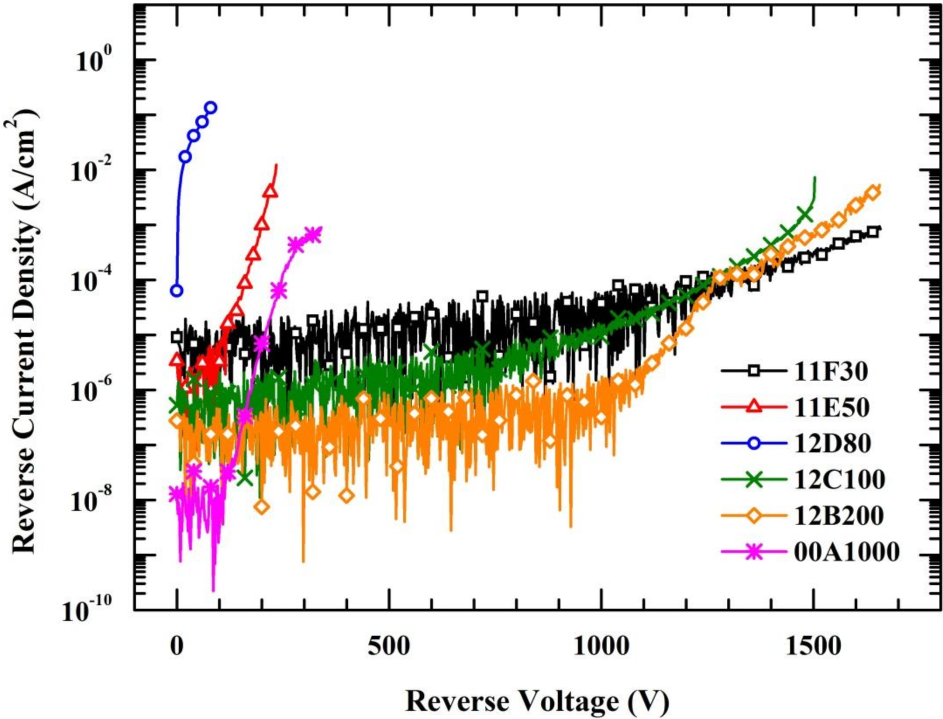

Figure 5-8: The measured reverse bias $I-V$ characteristics of the Mo/diamond SBDs on R100230-03 wafer at 423 K.

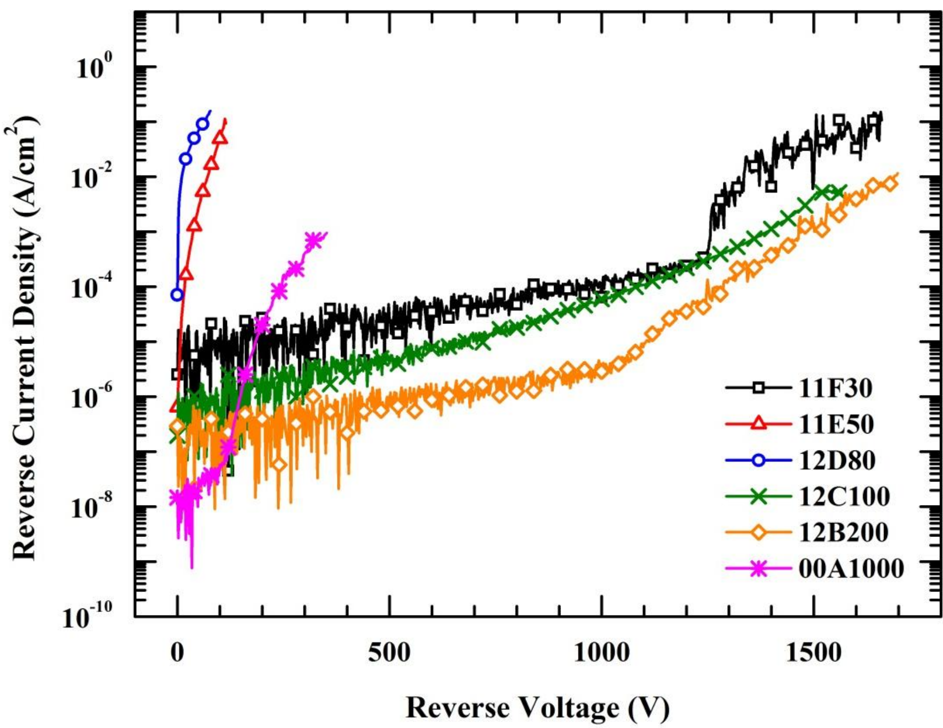

Figure 5-9: The measured reverse bias $I-V$ characteristics of the Mo/diamond SBDs on R100230-03 wafer at 523 K.

Measurements on wafer R100230-17

The forward bias $I-V$ measurements results for different vertical Mo/diamond SBDs fabricated on wafer R100230-17 at temperatures of 298 K, 423 K, and 523 K are shown in Figure 5-10, Figure 5-11, and Figure 5-12. During the measurements, the forward current was limited to 1 A which results in flat curve for SBD 00A1000.

In general, the fabricated SBDs on this wafer have better forward bias characteristics compared to those fabricated on wafer R100230-03. The extracted turn-on voltages of the SBDs are around 2 V (close to ideal barrier height of 2.24 eV), except for SBD 00A1000. As commonly found in large contact size diode, SBD 00A1000 has multiple barriers formation, including low barrier paths. Defective regions on SBD 00A1000 is quite apparent in Figure 5-3.

In contrast with the SBDs on wafer R100230-03, more thermionic emission dominant behaviour can be observed in these SBDs (from the larger slope of the log-scale curves at around 2 V). This behaviour can be verified with more convergence of forward current density curves as temperature increases.

Furthermore, the corresponding reverse bias $I-V$ measurements results for the SBDs on wafer R100230-17 are shown in Figure 5-13, Figure 5-14, and Figure 5-15. The best performing SBDs are 11E50 and 12B200 with breakdown voltage ~900V. In addition to crystal quality, the variations of breakdown voltages among SBDs on wafer R100230-03 and R100230-17 are also influenced by the thickness of field oxide for the edge termination structure. Further analysis on the influences of SBD's geometry is elaborated in Chapter 7.

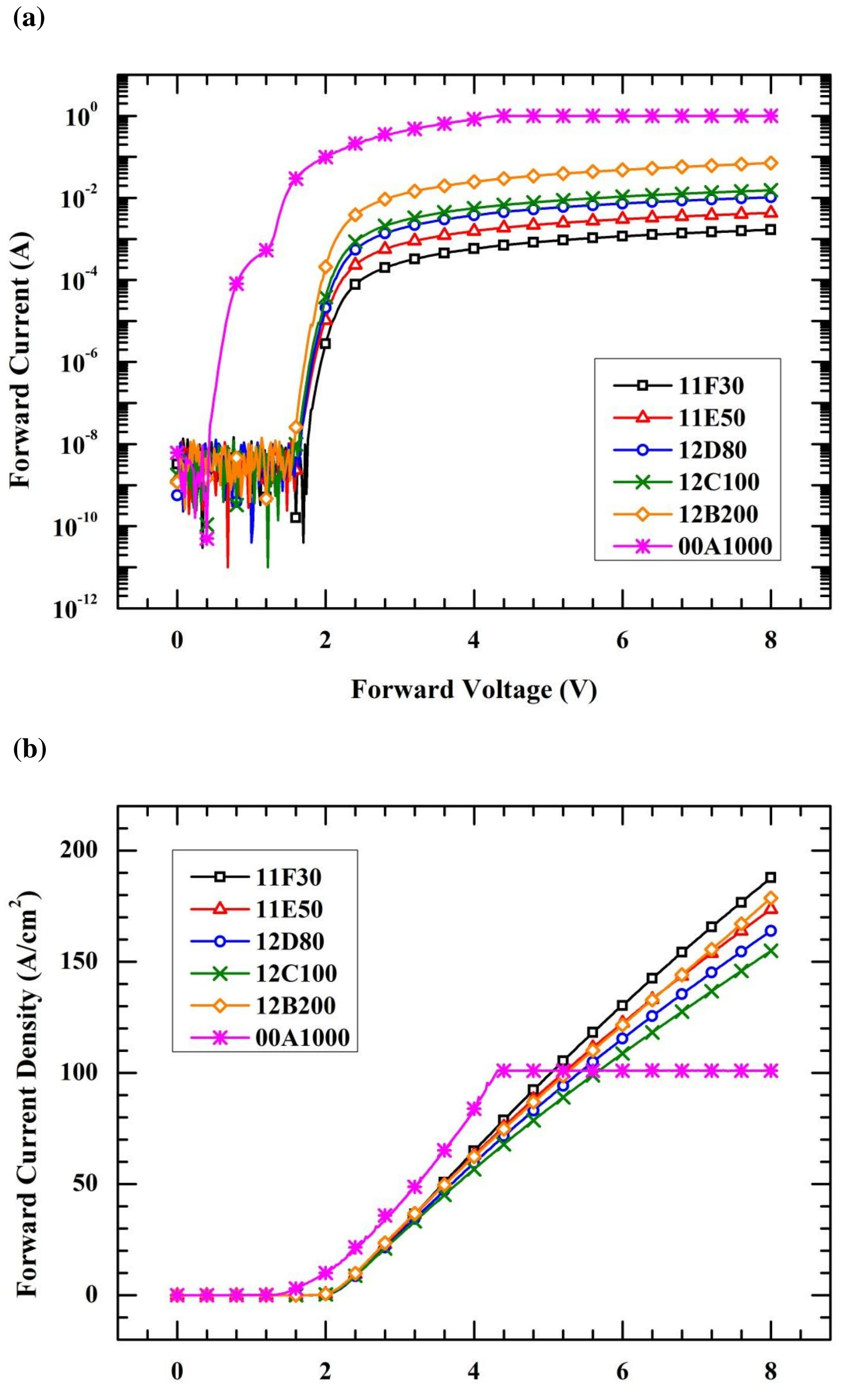

Figure 5-10: The measured forward bias $I-V$ characteristics of the Mo/diamond SBDs on R100230-17 wafer at 298 K in terms of: (a) total current and (b) current density.

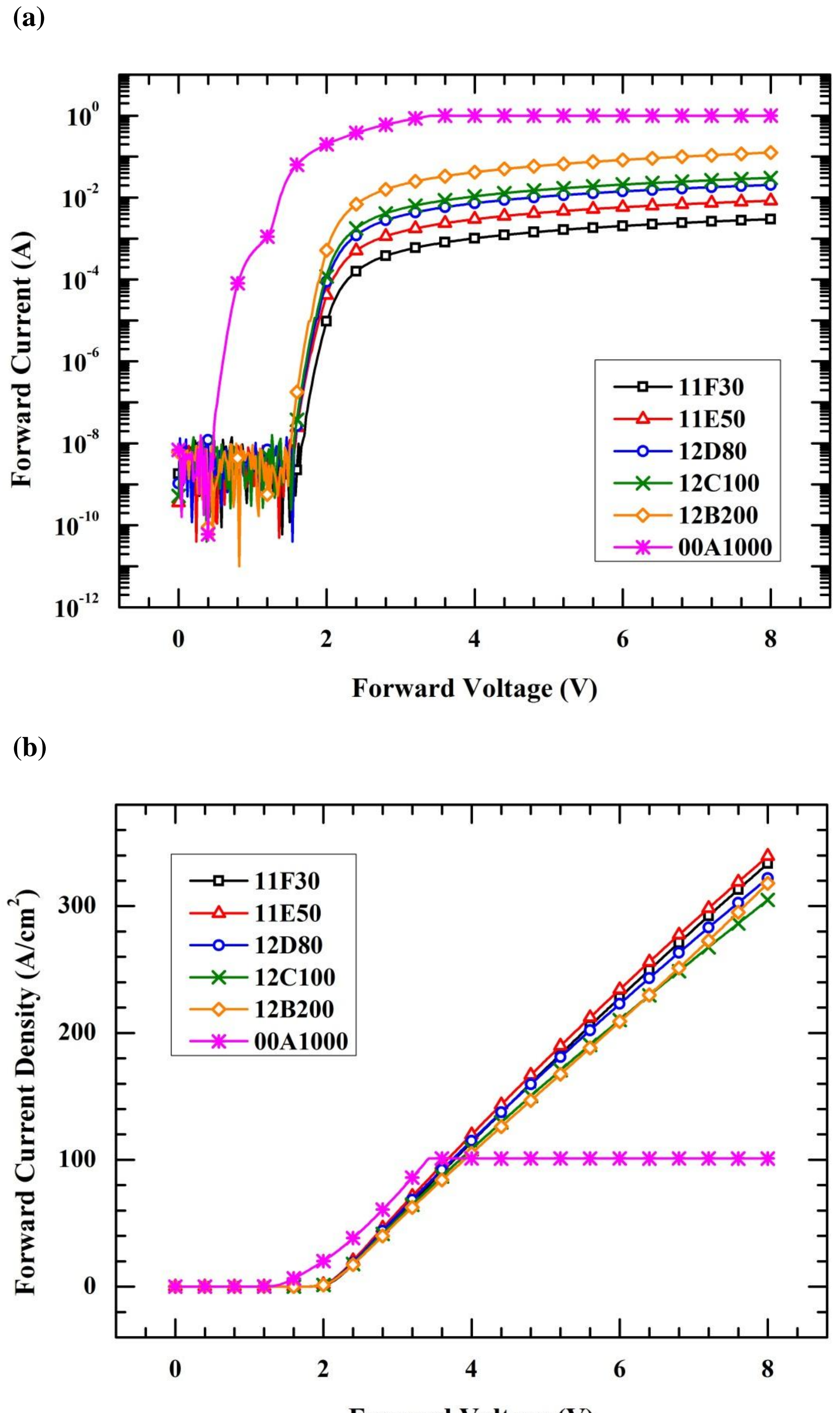

Figure 5-11: The measured forward bias $I-V$ characteristics of the Mo/diamond SBDs on R100230-17 wafer at 423 K in terms of: (a) total current and (b) current density.

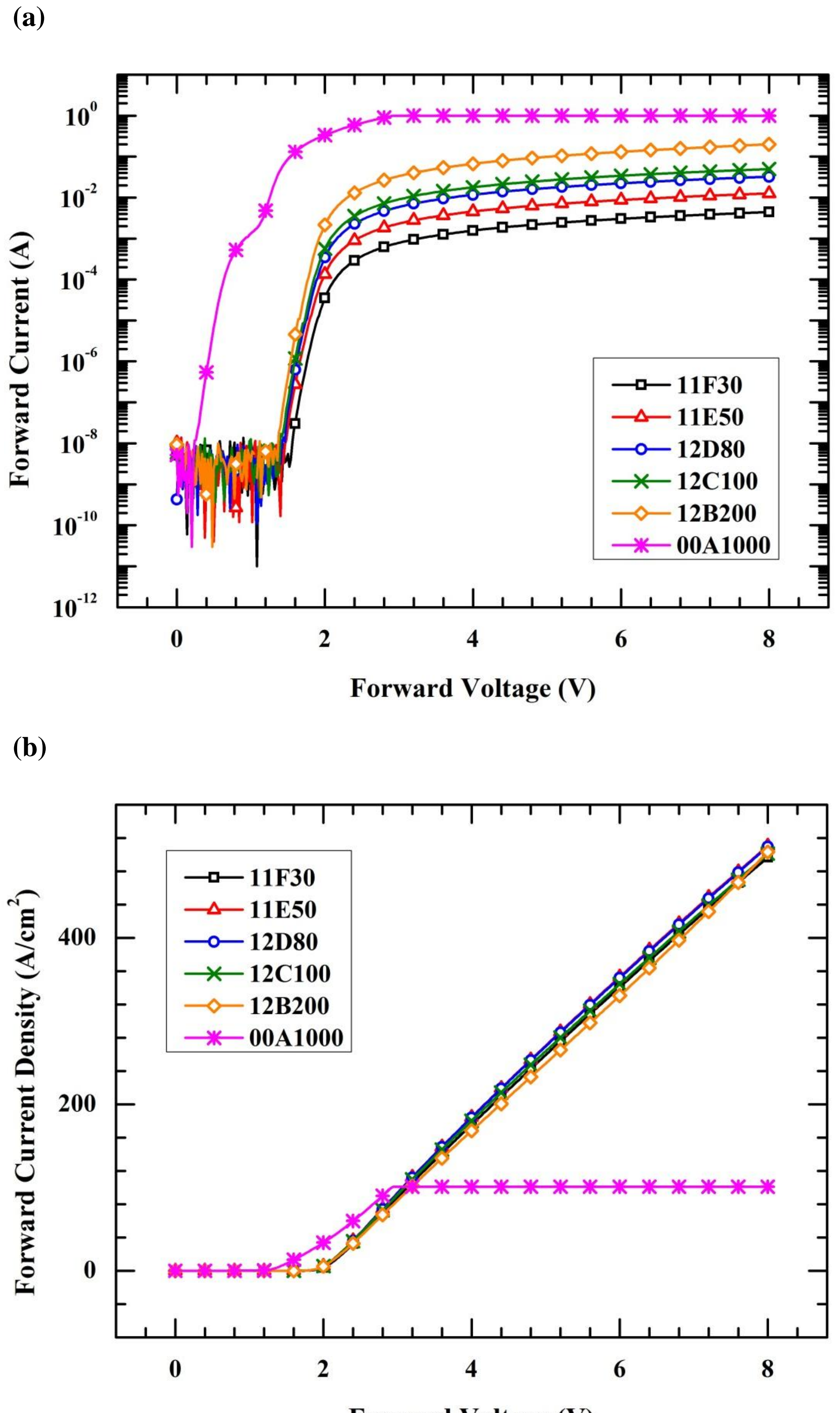

Figure 5-12: The measured forward bias $I-V$ characteristics of the Mo/diamond SBDs on R100230-17 wafer at 523 K in terms of: (a) total current and (b) current density.

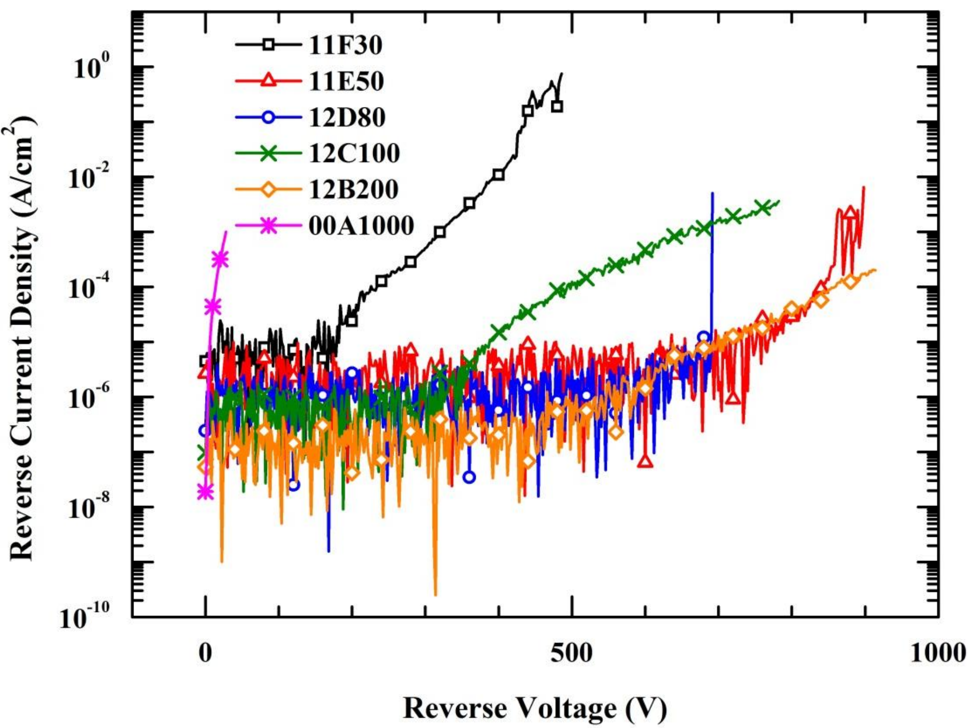

Figure 5-13: The measured reverse bias $I-V$ characteristics of the Mo/diamond SBDs on R100230-17 wafer at 298 K.

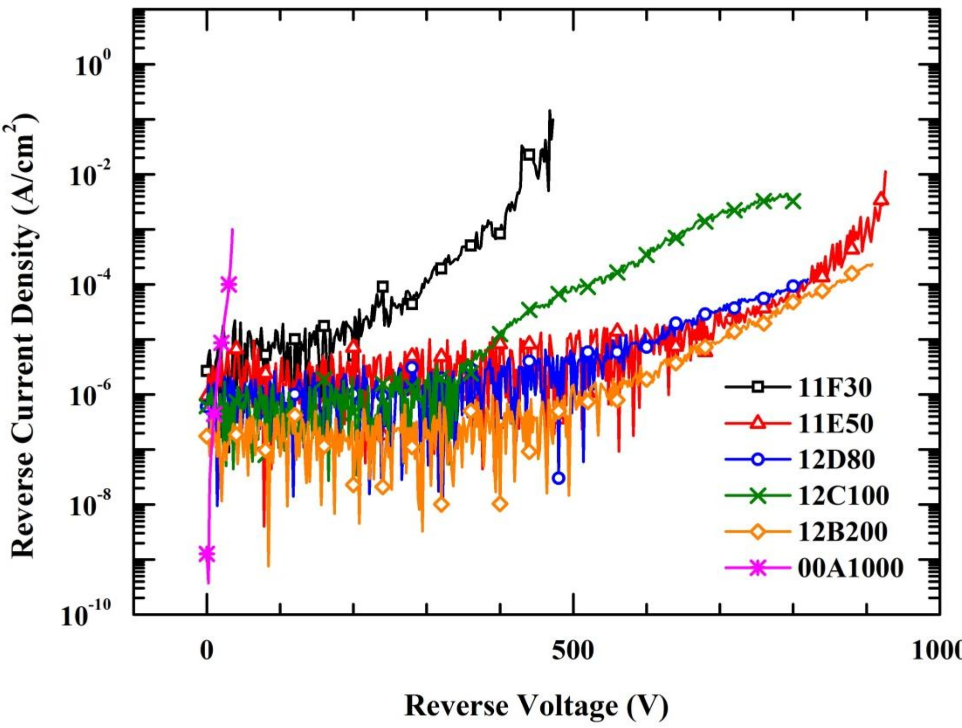

Figure 5-14: The measured reverse bias $I-V$ characteristics of the Mo/diamond SBDs on R100230-17 wafer at 423 K.

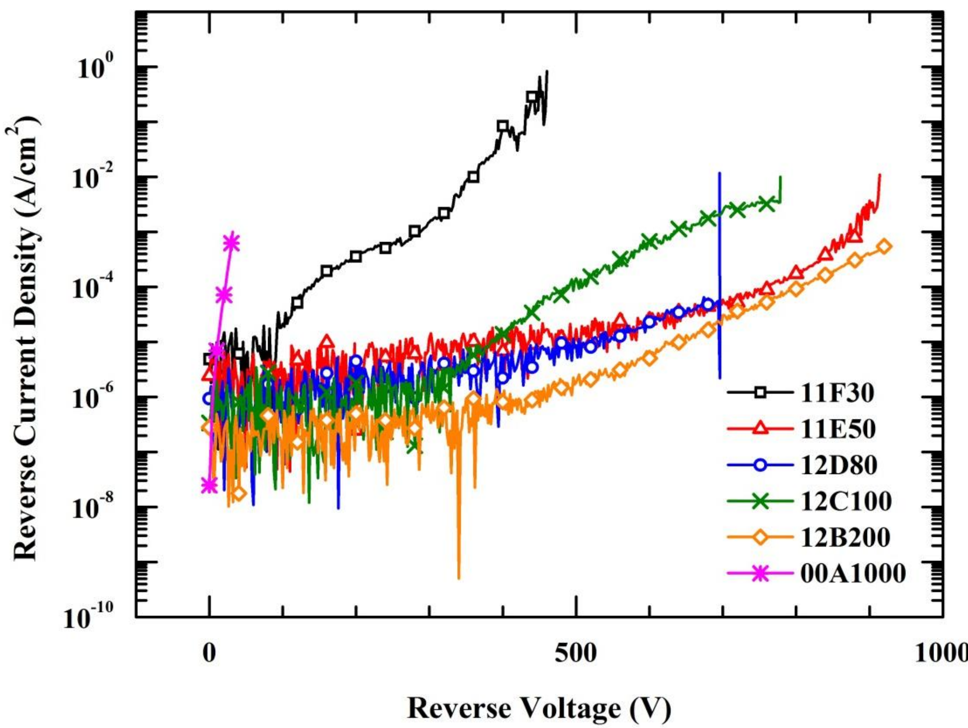

Figure 5-15: The measured reverse bias $I-V$ characteristics of the Mo/diamond SBDs on R100230-17 wafer at 523 K.

From the measurements results, it can be seen that the experimental Mo/diamond SBDs show non-ideal behaviours such as multiple barrier formation, Fermi level pinning that causes changes in the Schottky barrier height and turn-on voltage, leakage paths, etc. As these imperfections at the metal-diamond interface cannot be explained with simple intimate contact diode model, we presented analysis based on the MIS model in the following sections.

5.3 Theoretical background of the MIS model

5.3.1 Expression of barrier height and surface potential

The energy band diagram of a p-type MIS device under thermal equilibrium and under small forward bias is shown in Figure 5-16 (a) and Figure 5-16 (b), where E_g is the band gap of the semiconductor, $q\phi_m$ is the metal work function, $q\chi$ is the electron affinity of the semiconductor, V_p is the potential difference between Fermi level and the valence band level in neutral region, ψ_S is the surface or diffusion potential, δ is the thickness of the interfacial layer, Δ is the potential

drop across interfacial layer, V is the forward bias, $q\phi_B$ is the effective barrier height, $q\phi_{B0}$ is the barrier height at zero bias, and $q\phi_0$ is the neutrality level of the interface states [89]. Interface states above ϕ_0 are acceptor like (negative when filled, neutral when empty). Below ϕ_0, interface states are donor like (neutral when filled, positive when empty).

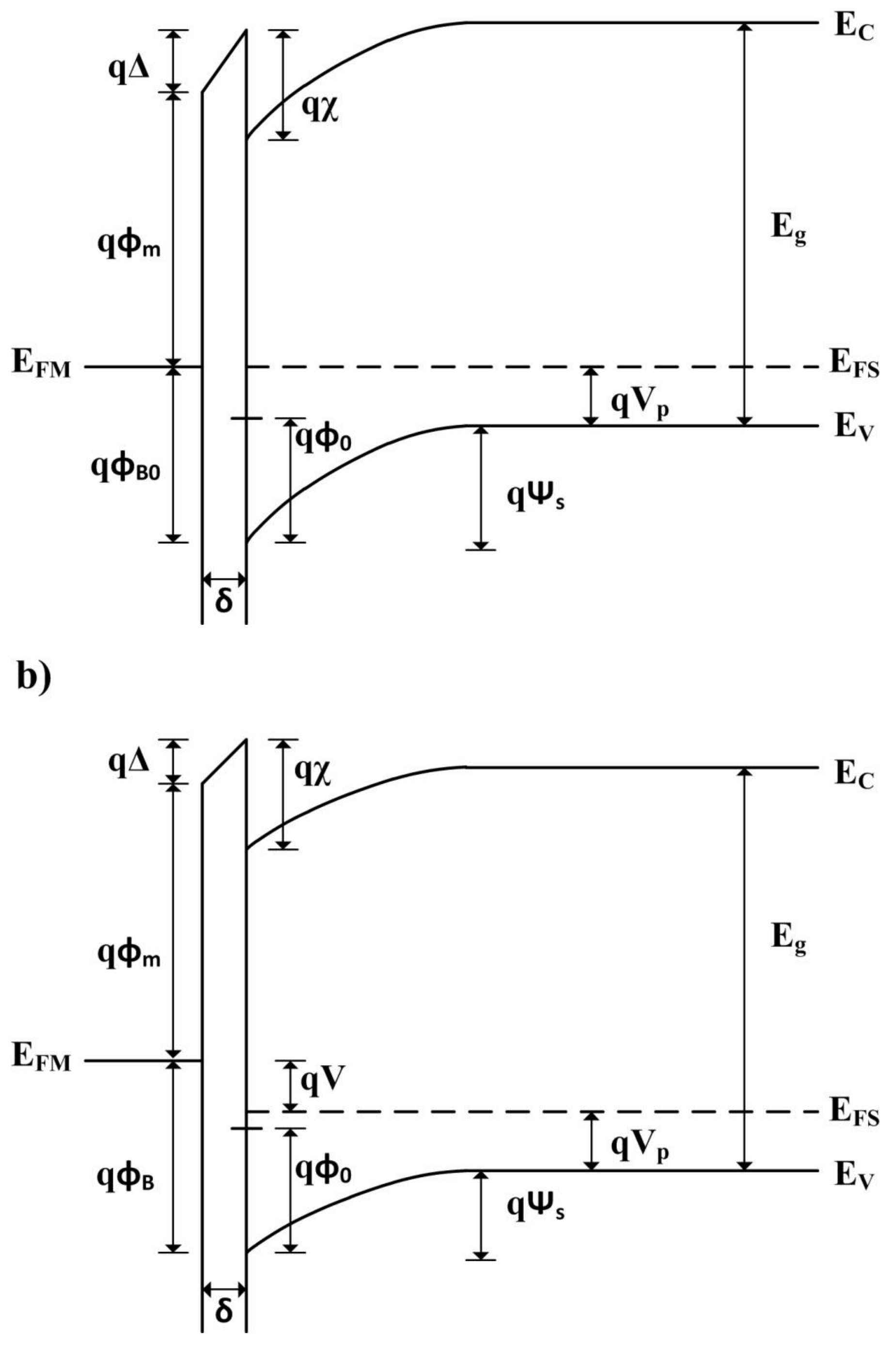

Figure 5-16: Energy band diagram of the metal-interfacial layer-semiconductor (MIS) structure under zero bias (a) and under applied forward bias (b).

Fonash [98], Chattopadhyay [99], and Turut [100] have elaborated the expressions for surface potential and barrier height of MIS structure. From the energy band diagram, we have

$$\Delta = \left[\frac{E_g}{q} + \chi - \psi_s(V) - V_p - V - \phi_m \right] \tag{5.1}$$

and from Gauss's law:

$$\Delta = -\frac{\delta}{\varepsilon_i}\left[Q_{sc}(V) + Q_{it}(V) + Q_f \right] \tag{5.2}$$

where ε_i is the permittivity of the interfacial layer, $Q_{sc}(V)$ is the space charge density (C/cm^2) in the semiconductor depletion layer, $Q_{it}(V)$ is the interface state charge density (C/cm^2) in semiconductor interface, and Q_f is the positive fixed surface charge (C/cm^2) on semiconductor surface. $Q_{sc}(V)$ can be related to the surface potential approximately by [89, 98]

$$Q_{sc}(V) = -\left[2q\varepsilon_s N_A \left(\psi_s(V) - V_2 \right) \right]^{1/2} \tag{5.3}$$

where N_A is the acceptor doping concentration (cm^{-3}) in the semiconductor, ε_S is the permittivity of the semiconductor, and V_2 is the correction factor due to the transition region ($V_2 = 0$ for depletion approximation). In our calculation, we approximate V_2 with kT/q [89] and ignore image force lowering.

Assuming uniform distribution of interface states and fixed charge, $Q_{it}(V)$ and Q_f are given by

$$Q_{it}(V) = -qD_{it}\left[q\psi_s(V) + qV_p - q\phi_0 \right] \tag{5.4}$$

$$Q_f = qN_f \tag{5.5}$$

where D_{it} is the density of acceptor like interface states (states/cm^{2}eV) and N_f is the density of positive fixed surface charge (cm^{-2}). Assuming $N_f = 0$, then solving Eq. (5.1), (5.2), (5.3), (5.4), (5.5) yields:

$$\begin{aligned}\psi_s(V) &= c_2(E_g/q+\chi-\phi_m)+(1-c_2)\phi_0-c_2V-V_p+(c_1c_2^2)/2 \\ &-(1/2)[4c_1c_2^2(c_2(E_g/q+\chi-\phi_m)+(1-c_2)\phi_0-c_2V-V_p)+c_1^2c_2^4-4c_1c_2^2V_2]^{(1/2)}\end{aligned} \tag{5.6}$$

with

$$c_1 = \frac{2q\varepsilon_s N_A \delta^2}{\varepsilon_i^2} \tag{5.7}$$

$$c_2 = \frac{\varepsilon_i}{\varepsilon_i + q^2\delta D_{it}} \tag{5.8}$$

For lowly doped semiconductor and low bias, $\psi_S(V)$ can be approximated to

$$\psi_s(V) \approx c_2\left(\frac{E_g}{q}+\chi-\phi_m\right)+(1-c_2)\phi_0-c_2V-V_p \tag{5.9}$$

From Figure 5-16 (b), the expression for effective barrier height dependent of bias voltage is given by [101]

$$\phi_B(V) = V + V_p + \psi_s(V) \tag{5.10}$$

Substituting Eq. (5.9) to Eq. (5.10), we have

$$\phi_B(V) = c_2\left(\frac{E_g}{q}+\chi-\phi_m\right)+(1-c_2)\phi_0+(1-c_2)V \tag{5.11}$$

It is worth to note that for uniform distribution of interface state density D_{it}, values of c_2 is constant while $\phi_B(V)$ and $\psi_S(V)$ vary linearly with bias voltage. Expression of ϕ_B by Eq. (5.10) and (5.11) is different from those in [99, 102], i.e. $\phi_B = c_2(E_g/q+\chi-\phi_m)+(1-c_2)\phi_0$ which is valid only for zero bias.

5.3.2 Current- voltage ($I-V$) characteristics

Following [103], the expression of thermionic emission current is given by

$$I = I_0 exp\left(\frac{qV}{nkT}\right)\left[1-exp\left(-\frac{qV}{kT}\right)\right] \tag{5.12}$$

with n as the ideality factor and I_0 as the saturation current given by

$$I_0 = AA^*T^2\exp\left(-\frac{q\phi_{B0}}{kT}\right) \tag{5.13}$$

A is the diode area, A^* is the effective Richardson constant given by $A^* = 2\pi q m^* k^2 / h^3 =$ 96 A/cm^2.K^2 [96] with $m^* = m_{h,dos} = 0.8 m_0$ [22], and ϕ_{B0} is the mean Schottky barrier height at equilibrium (zero bias).

For non- uniform distribution of interface state density, ideality factor is bias dependence and given by

$$n(V) = \frac{q}{kT}\frac{d(V)}{d(\ln I)} = \frac{1}{1-\beta(V)} \tag{5.14}$$

where $\beta_n(V)$ describes the dependence of effective barrier height on bias voltage.

$$\beta_n(V) = \frac{d\phi_B}{dV} \tag{5.15}$$

Therefore, effective barrier height dependent on bias is

$$\phi_B(V) = \phi_{B0} + \beta_n(V)V = \phi_{B0} + \left(1 - \frac{1}{n(V)}\right)V \tag{5.16}$$

For thick interfacial layer where interface states are in equilibrium with semiconductor [103, 104], $n(V)$ can be expressed as

$$n(V) = 1 + \frac{\delta}{\varepsilon_i}\left[\frac{\varepsilon_s}{W(V)} + qD_{it}(V)\right] \tag{5.17}$$

where $W(V)$ is the semiconductor depletion layer width given by

$$W(V) = \left[\frac{2\varepsilon_s}{qN_A}\left(\psi_s(V) - V_2\right)\right]^{1/2} \tag{5.18}$$

Substituting Eq. (5.8) to (5.17), we have

$$n(V) = \frac{1}{c_2(V)} + \frac{\delta}{\varepsilon_i}\frac{\varepsilon_s}{W(V)} \tag{5.19}$$

Since ε_i and ε_S are normally of almost the same order of magnitude, and δ $<< W(V)$, we can approximate

$$n(V) \approx 1/c_2(V) \tag{5.20}$$

By comparing Eq. (5.11) and (5.16), we can reproduce Eq. (5.20) and barrier height at zero bias.

$$\phi_{B0} = c_2\left(\frac{E_g}{q} + \chi - \phi_m\right) + \left(1 - c_2\right)\phi_0 \tag{5.21}$$

which shows the consistency of the analysis. Relationship of interface states energy level $E_{SS}(V)$ with bias voltage in p-type semiconductor is given by [105]

$$E_{ss}\left(V\right) - E_V = q(\phi_B(V) - V) \tag{5.22}$$

5.3.3 Capacitance- voltage ($C-V$) characteristics

At low frequency, capacitance of a MIS diode with interface states is the contribution of interface state capacitance C_{it} in parallel with space charge capacitance C_{sc}, and in series with interfacial layer capacitance C_i as given by [98, 103]

$$\frac{1}{C_{LF}} = \frac{1}{C_i} + \frac{1}{C_{sc} + C_{it}} \tag{5.23}$$

where

$$C_{it} = A\frac{dQ_{it}}{d\psi_s} \approx AqD_{it} \tag{5.24}$$

$$C_i = \frac{\varepsilon_i A}{\delta} \tag{5.25}$$

$$C_{sc} = A\frac{dQ_{sc}}{d\psi_s} = \frac{\varepsilon_s A}{W} \tag{5.26}$$

At high frequency where interface states cannot follow the AC signal, $C_{it} = 0$. The total capacitance becomes

$$\frac{1}{C_{HF}} = \frac{1}{C_i} + \frac{1}{C_{sc}} \tag{5.27}$$

Considering $\delta << W(V)$, $C_i >> C_{SC}$, using Eq. (5.27) and by substituting Eq. (5.3) and (5.10) to Eq. (5.26), we have

$$C_{HF} \approx C_{sc} = \left(\frac{q\varepsilon_s N_A \mathrm{A}^2}{2\psi\left(\Psi_s\left(V\right) - V_2\right)}\right)^{1/2} = \left[\frac{q\varepsilon_s N_A \mathrm{A}^2}{2\left(\phi_B\left(V\right) - V - V_p - V_2\right)}\right]^{1/2} \tag{5.28}$$

By substituting Eq. (5.11) to (5.28) and differentiating it, the value of c_2 can be extracted from the slope of the reverse $C^{-2} - V$ curve.

$$c_2 = \frac{q\varepsilon_s N_A A^2 \left[\frac{d\left(C^{-2}\right)}{dV}\right]}{2} \tag{5.29}$$

Note that for uniform distribution of interface state density, value of c_2 is constant, i.e. $C^{-2}-V$ curve is linear. Depletion layer capacitance can also be expressed as [106]

$$C^{-2} = \frac{2\left(V_0 - V\right)}{q\varepsilon_s N_A A^2} \tag{5.30}$$

where V_0 is the intercept voltage at which extrapolated $C^{-2}-V$ plot intercepts V axis (C^{-2}= 0). Zero bias Schottky barrier height ϕ_{B0} can be calculated using the measured zero bias capacitance C_0 and $V = 0$ in Eq. (5.28) and (5.30).

$$\phi_{B0} = \frac{q\varepsilon_s N_A \mathrm{A}^2 C_0^{-2}}{2} + V_p + V_2 = V_0 + V_p + V_2 \tag{5.31}$$

This is in agreement with the result in [102, 105].

5.4 Characterizations from *I-V* and *C-V* measurements

In this section, we demonstrate the application of the MIS model in analysing the characteristics of experimental Mo/diamond SBD 12B200 fabricated on wafer R100230-17. Figure 5-17 shows the measured forward bias $I-V$ characteristics of the investigated Mo/diamond SBD 12B200 for temperature of 298 K, 423 K, and 523 K. From the inset, we can see that the turn-on voltage is around 2 V. Considering the effect of series resistance R_S and for $V > 3kT/q$, Eq. (5.12) can be modified to

$$I = I_0 exp\left(\frac{q\left(V - IR_s\right)}{nkT}\right) \tag{5.32}$$

with I_0 given by Eq. (5.13). Curve fitting of the measured forward bias $I-V$ characteristics based on Eq. (5.32) were conducted in MATLAB Curve Fitting Toolbox (with 95% confidence bounds) to yield the mean values of n, ϕ_{B0}, and R_S for each temperature. Their values are shown in Table 5-3, indexed with ($I-V$).

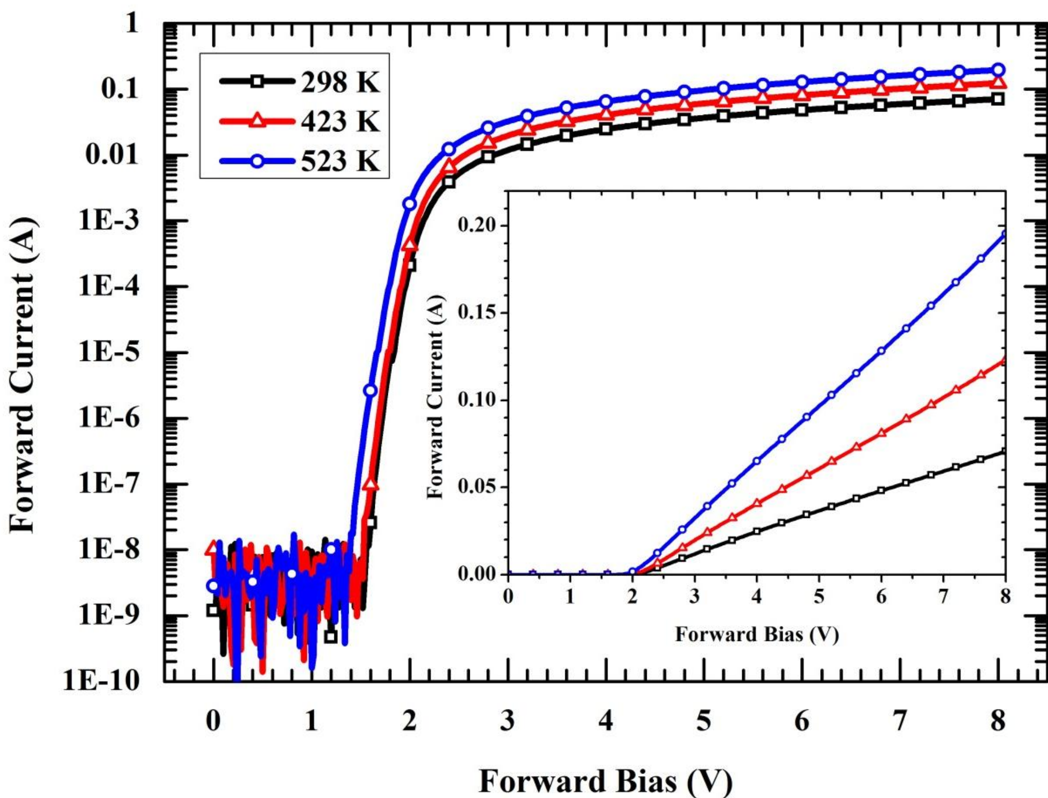

Figure 5-17: Measured forward bias $I-V$ characteristics of the experimental Mo/diamond SBD 12B200 on wafer R100230-17 at different temperatures.

Table 5-3: Temperature dependent values of various parameters extracted from forward I-V characteristics of the experimental Mo/diamond SBD 12B200 on wafer R100230-17.

T (K)	$n(I-V)$	$n(dV/d\ln I)$	$\phi_{B0}(I-V)$ (eV)	$\phi_{B0}(H(I))$ (eV)	$R_S\ (I-V)$ (Ω)	$R_S\ (dV/d\ln I)$ (Ω)	$R_S\ (H(I))$ (Ω)
298	1.3	1.285	1.872	1.875	82.4	86.72	82.82
423	1.15	1.207	2.276	2.185	47.48	47.22	47.54
523	1.03	1.087	2.547	2.441	30.26	29.82	30.26

We also evaluate these parameters using method developed by Cheung and Cheung [107] as follows.

$$\frac{d(V)}{d(\ln I)} = R_s I + \frac{nkT}{q} \quad (5.33)$$

$$H(I) = V - \frac{nkT}{q}\ln\frac{I}{AA^*T^2} \quad (5.34)$$

$$H(I) = R_s I + n\phi_{B0} \quad (5.35)$$

By plotting $d(V)/d(\ln I) vs I$, values of R_S and n are evaluated using Eq. (5.33). This value of n is then used in Eq. (5.34) to compute $H(I)$. Plot of

$H(I) vs I$ provides the determination of ϕ_{B0} and the verification of the extracted R_S based on Eq. (5.35). Associated plots of $d(V)/d(\ln I)$ and $H(I)$ of our SBD are shown in Figure 5-18 (a) and Figure 5-18 (b) with their fitting curves for different temperatures. The extracted values of n, ϕ_{B0}, and R_S are shown in Table 5-3, indexed with ($d(V)/d(\ln I)$) and ($H(I)$) respectively.

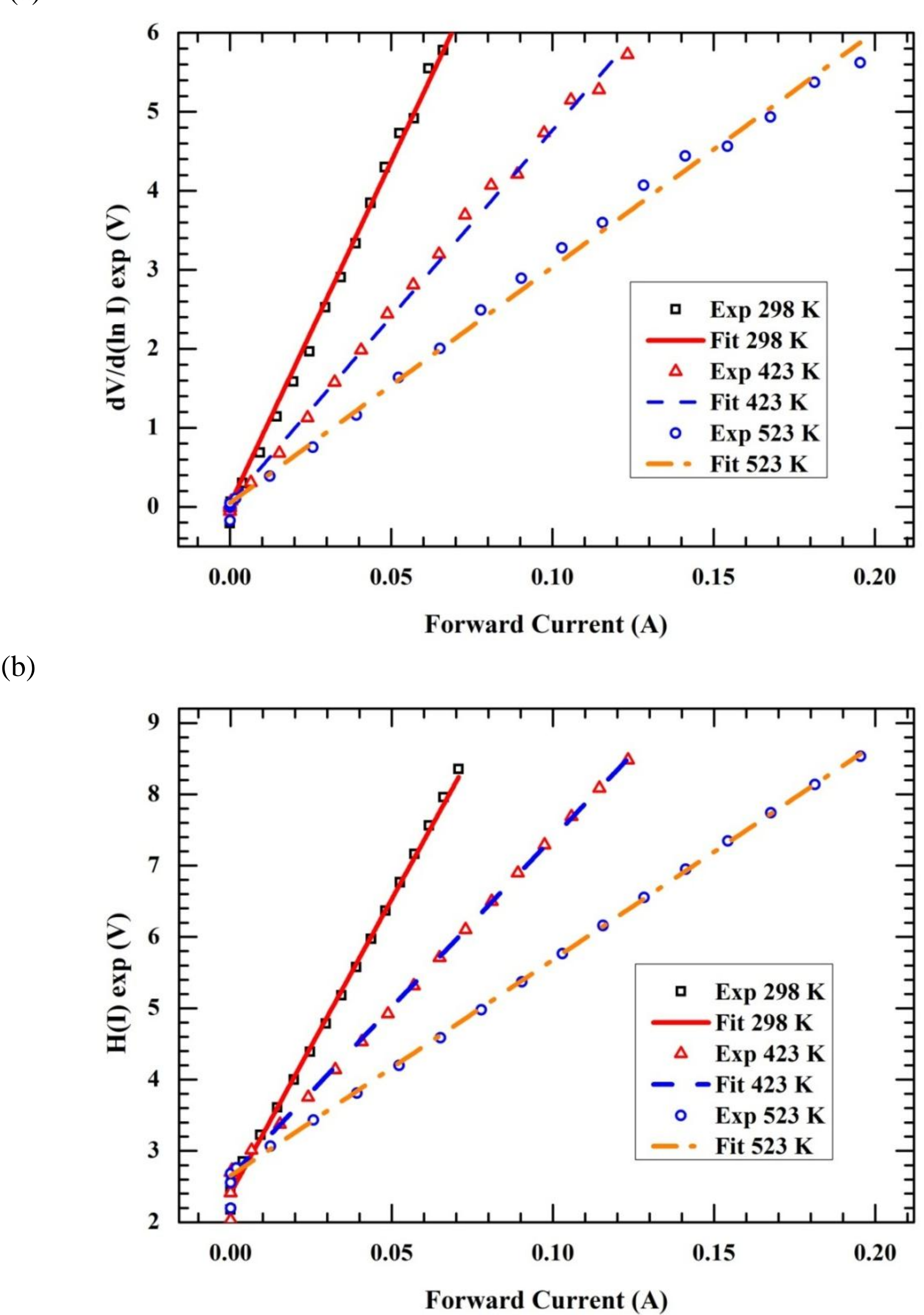

Figure 5-18: The experimental and fitting curves of $d(V)/d(\ln I) vs I$ plots in (a) and $H(I) vs I$ plots in (b) of the experimental Mo/diamond SBD 12B200 on wafer R100230-17 at different temperatures.

The extracted parameters' values from both methods show good agreement. The extracted series resistance $R_S(I-V)$ ranges from 11.98 mΩ.cm^2 at 523 K to 32.63 mΩ.cm^2 at 298 K. It is found from $I-V$ characterization that the extracted ϕ_{B0} deviates from ideal intimate Schottky barrier height of 2.24 eV ($q\chi$ = 1.3 eV, $q\phi_m$ = 4.53 eV). We attributed this Fermi level pinning to interfacial layer and interface states charges between Schottky metal and diamond.

From Table 5-3, we can observe that value of n decreases while value of ϕ_{B0} increases with increasing temperature. Decrease in the value of n means that the current transport becomes closer to ideal thermionic emission current (n = 1). This is reasonable as more thermal energy is available to the carrier for thermionic emission process at high temperature.

Figure 5-19 and Figure 5-20 show respectively the measured reverse bias $C-V$ and $C^{-2}-V$ characteristics at 50 kHz and temperature of 298 K. Most of the interface states charges cannot follow the AC signal at this high frequency.

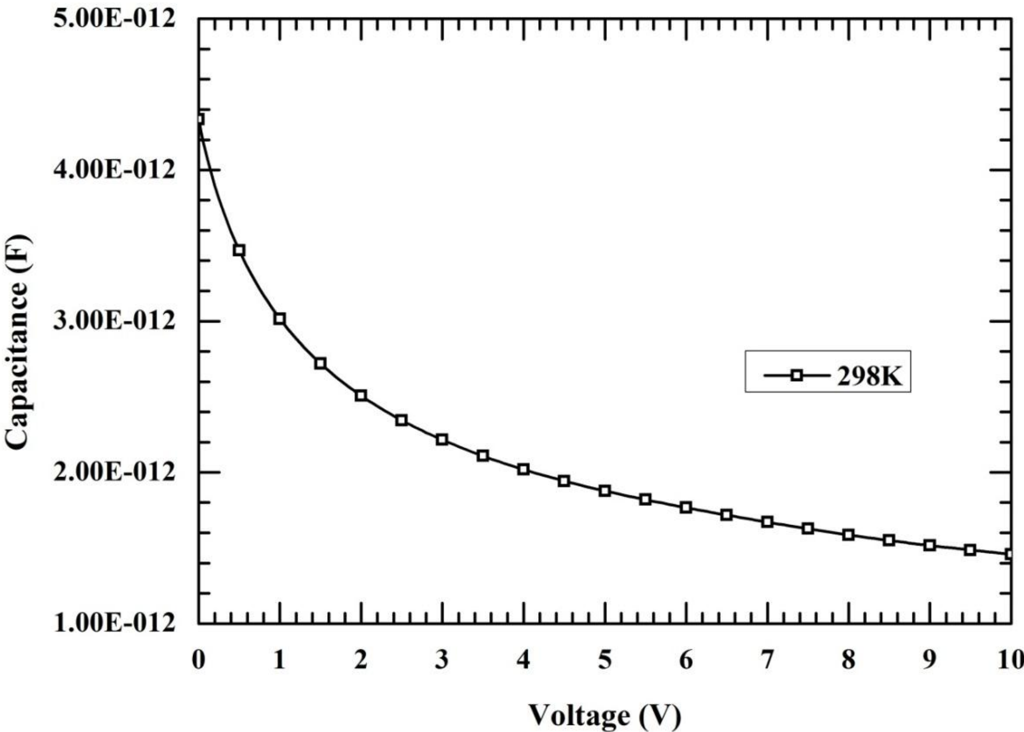

Figure 5-19: The reverse bias $C-V$ characteristics of the experimental Mo/diamond SBD 12B200 on wafer R100230-17 measured at 50 kHz at 298 K.

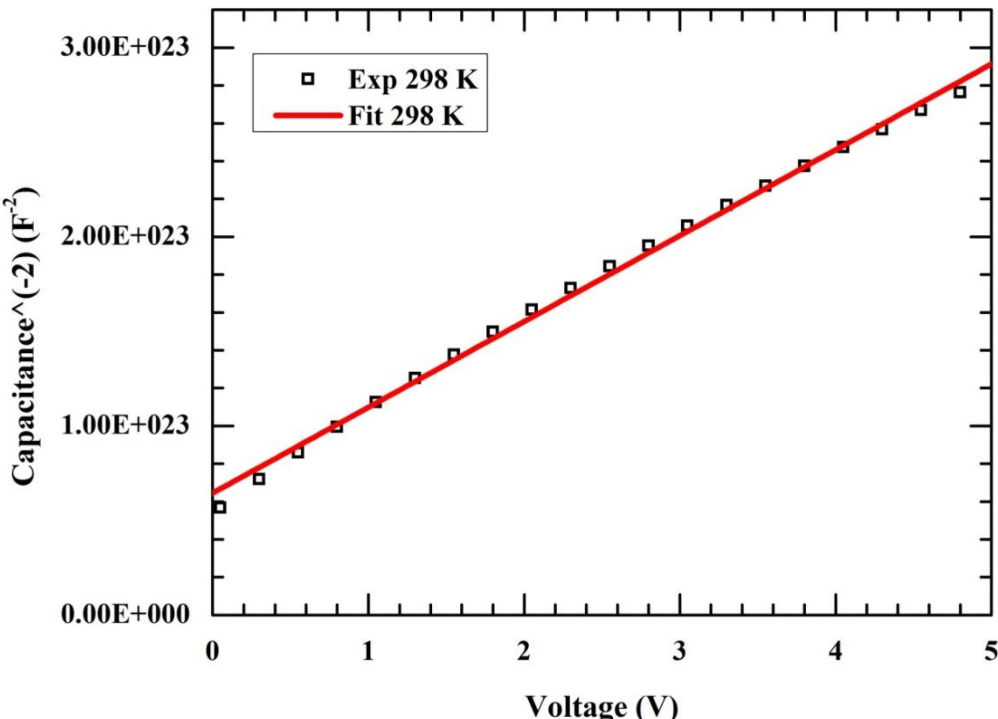

Figure 5-20: The measured reverse bias $C^{-2}-V$ characteristics the experimental Mo/diamond SBD 12B200 on wafer R100230-17 and the linear fitting curve measured at 50 kHz at 298 K.

From the reverse $C^{-2}-V$ characteristics, the zero bias capacitance C_0^{-2} is found to be 5.3239x10^{22} F^{-2}. By fitting linear curve to $C^{-2}-V$ characteristics as shown Figure 5-20 and extrapolating it to the x- axis, we extracted the intercept voltage V_0 = 1.4193 V and slope $d\left(C^{-2}\right)/dV = 4.539$x10^{22} F^{-2}.V^{-1}.

By substituting the values of C_0^{-2}, V_0, and V = 0 into Eq. (5.30), N_A is calculated to be 4.2053x10^{15} cm^{-3}. The extracted N_A value is lower than the Boron doping concentration in the drift region (1.029x10^{16} cm^{-3}). This is attributed to the incomplete ionization phenomena because the Boron dopant in diamond material has high activation energy of ~0.37 eV [22]. The extracted N_A = 4.2053x10^{15} cm^{-3} from $C^{-2}-V$ characteristics using Eq. (5.30) is actually an effective carrier density. It is a good approximation to majority carrier density p [69]. We can approximate $N_A^- \approx p$ by utilizing the charge neutrality condition in Eq. (3.10) as an approximation, assuming no acceptor compensation (N_D^+ = 0), and negligible minority carrier density ($n \approx 0$).

To extract the Schottky barrier height from $C^{-2}-V$ characteristics using Eq. (5.31), value of V_p must be evaluated by considering incomplete ionization phenomena. Assuming $N_D = 0$ and using $N_A^- \approx 4.2053\text{x}10^{15}$ cm^{-3}, $V_p = E_F / q$ = 0.3971 eV is evaluated using Eq. (3.1), (3.2), and (3.3). Finally, substituting values of V_0, V_p, and $V_2 = kT/q$ in Eq. (5.31) results in ϕ_{B0} = 1.8421 eV. This value of Schottky barrier height extracted from reverse $C^{-2}-V$ characteristics at 298 K is in good agreement with value extracted from the forward bias $I-V$ characteristics.

To estimate the thickness of interfacial layer δ, we used the classical C_{max} technique where the interfacial layer capacitance C_i is approximated as maximum capacitance of the device biased in accumulation [108]. While this method gives crude approximation to δ, it provides simple and fast determination. The measured $C_i \approx C_{max}$ in the fabricated Mo/diamond SBD is 2.03x10^{-9} F. Using Eq. (5.25), we get δ / ε_i = 0.1727 nm. This value is close to the calculated effective dipole length for diamond (δ / ε_i = 0.142 nm) based on MIGS theory [109]. Using ε_i = 2 [109], value of δ in the fabricated SBD is approximated to be 0.284 nm.

At this moment, no direct measurement is conducted to investigate the nature of the interfacial layer in the investigated Mo/diamond SBD. Oxidative treatments for surface termination of diamond can induce thin layer of SiO_x which might be originated from the UV/Ozone apparatus. Work by [92] also indicated occurrence of highly disordered surface defect film with thickness less than 1 nm on single crystal Boron doped diamond caused by Oxygen plasma treatment. Another possible origin of the interfacial layer is oxidization or nitrization of Schottky metal, resulting in thin MoO_x or MoN_x layer.

Furthermore, ϕ_{B0} = 1.872 eV is used in Eq. (5.12) and (5.13) to extract bias dependent $n(V)$ and subsequently bias dependent $\phi_B(V)$ using Eq. (5.16) from the measured forward bias $I-V$ characteristics (with correction for series resistance using R_S = 82.4 Ω). We can then determine $\psi_S(V)$ and $W(V)$ using Eq. (5.10) and (5.18). The evaluated $W(V)$ is shown in Figure 5-21.

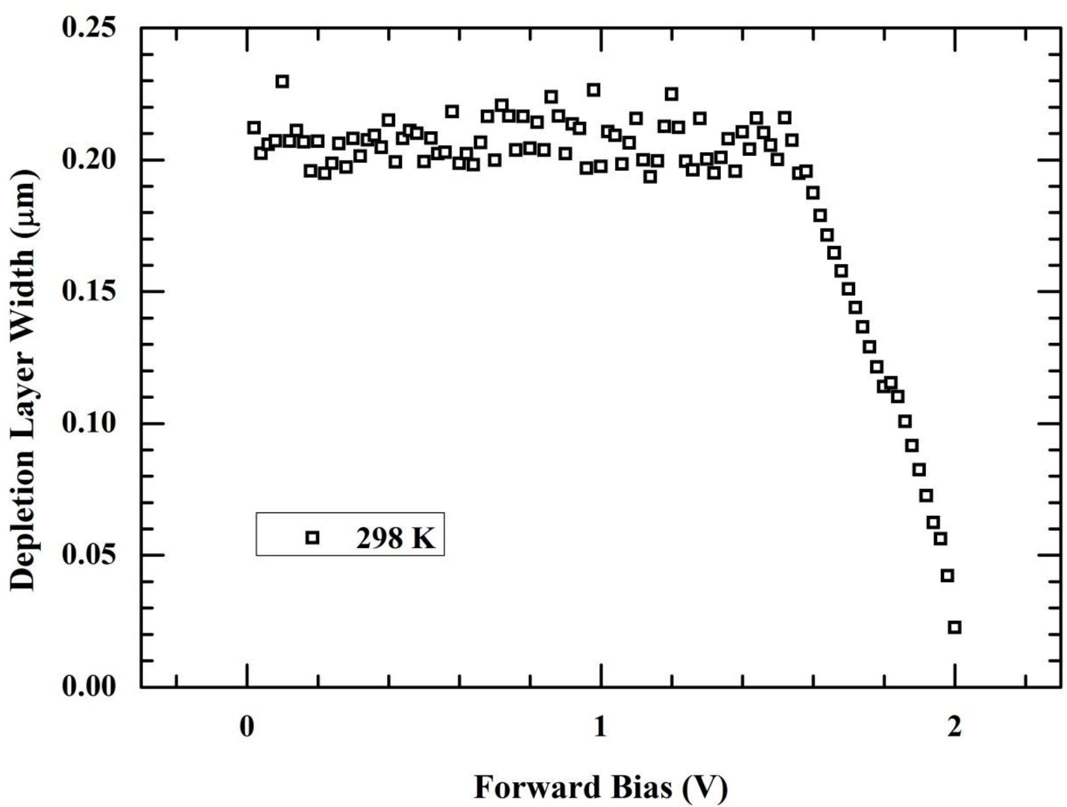

Figure 5-21: Variation of depletion layer width with forward bias of the experimental Mo/diamond SBD 12B200 on wafer R100230-17 at 298 K.

Note that $W(V)$ curve at voltage range of 0- 1.5 V is scattered because the forward current in this voltage range is below the sensitivity of measurement equipment (refer to Figure 5-17). Width of depletion layer $W(V)$ decreases rapidly when the bias is approaching 2 V as the diode starts to turn-on.

In the determination of the interface states energy distribution $D_{it}(E_{SS}-E_V)$, we employed extracted values of δ = 0.248 nm, ε_i = 2, bias dependent $n(V)$, $W(V)$, and $\phi_B(V)$ in Eq. (5.17) and (5.22). The extracted energy distribution profile of the interface state densities $D_{it}(E_{SS}-E_V)$ is shown in Figure 5-22. The D_{it} is quite uniformly distributed and the values are in the order of 10^{13} $eV^{-1}.cm^{-2}$.

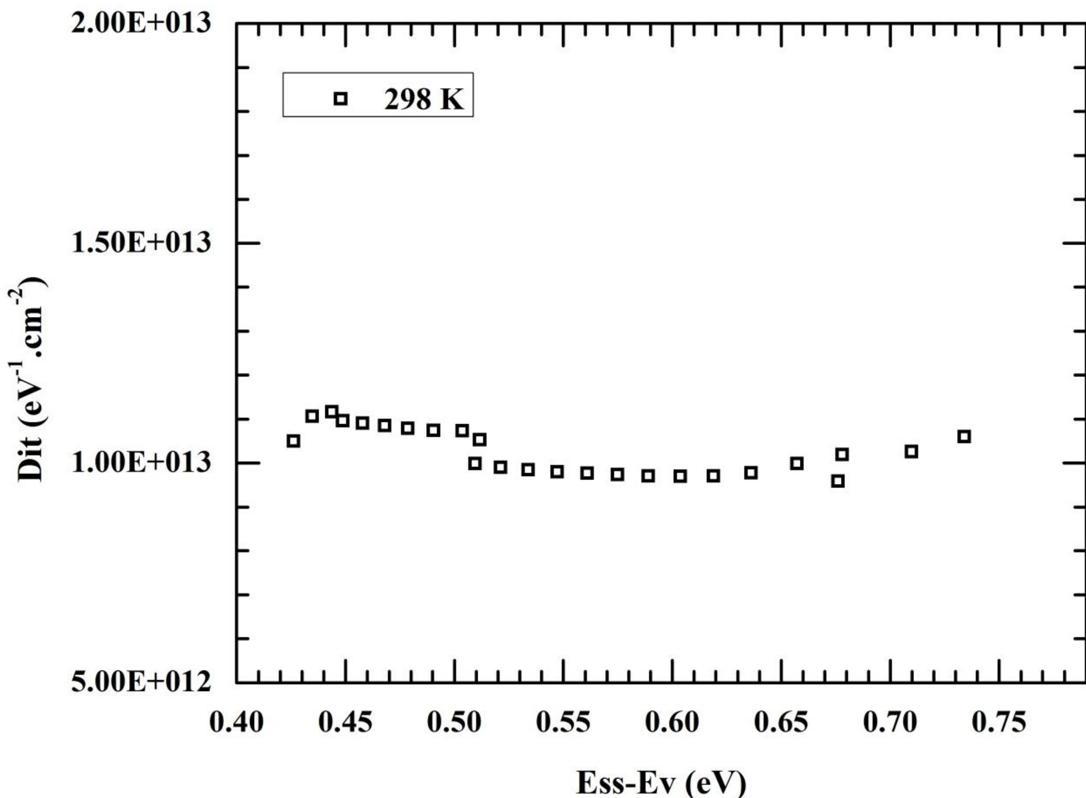

Figure 5-22: Energy distribution of the interface state density of the experimental Mo/diamond SBD 12B200 on wafer R100230-17 at 298 K.

5.5 Conclusions

We have presented the measurements results and investigations of the vertical Mo/diamond SBDs fabricated on different diamond substrates with different contacts sizes and field plate termination lengths. High forward current density up to 100 A/cm^2 at ~5 V and breakdown voltage up to 1700 V was achieved in the experimental SBDs. Furthermore, non-ideal behaviours such as multiple barrier formations, low barrier leakage current paths, and Fermi level pinning were found in the experimental SBDs.

Characterizations from the $I-V$ measurements for one of the experimental SBDs (12B200) at temperatures of 298 K, 423 K, and 523 K by curve fitting and Cheung and Cheung's method showed that ideality factor decreases while Schottky barrier height increases with increasing temperature. At 298 K, diode's ideality factor, Schottky barrier height, and on-resistance are 1.3, 1.872 eV, and 32.63 mΩ.cm^2 respectively. The value of barrier height was verified with the extraction

from reverse $C^{-2}-V$ characteristic and was found to deviate from ideal diode's barrier height of 2.24 eV. Such non-ideal behaviour (Fermi level pinning) is attributed to the existence of thin interfacial layer and interface states charges at the Schottky metal-diamond interface. They might be originated from Oxygen surface treatment on the diamond's surface during fabrication process.

We then presented analysis of the investigated SBD using MIS theory to explain the Fermi level pinning. From the forward bias maximum capacitance, the thickness of interfacial layer is approximated to be 0.248 nm. Determination of the interface states charge density from measured forward bias $I-V$ characteristics reveals uniform distribution of interface states charges with value around 10^{13} $eV^{-1}.cm^{-2}$. Further studies on the nature of the interfacial layer and interface states and their relationship with surface treatments are needed to improve the interface quality and fabrication techniques of the Schottky contact for diamond electronic devices.

6 MODELLING AND SIMULATIONS OF NON-IDEAL CHARACTERISTICS OF VERTICAL MO/DIAMOND SCHOTTKY BARRIER DIODE BASED ON THE MIS MODEL

6.1 Introduction

Given the importance of modelling and simulation tools in analysis, understanding, and design of diamond devices, it is crucial to develop accurate model in simulating the behaviour of diamond devices. However, the reported works on simulations of diamond SBDs up to this date are based on the ideal intimate contact diode model [52, 64-66, 110]. Even though simple, it is not suitable to simulate the non-ideal characteristics of diamond SBD.

The simplified intimate contact diode model has several disadvantages as observed in Chapter 4. It can only simulate the diode's forward $I-V$ characteristics with limited success, i.e. the Schottky barrier height needs to be readjusted for each temperature to simulate the effect of Fermi level pinning at the Schottky metal-diamond interface. Furthermore, the simulated reverse bias characteristics cannot match the experimental results.

In this chapter, we performed a rigorous approach to the modelling and simulations of non-ideal characteristics of experimental vertical Mo/diamond SBD by utilizing MIS model elaborated in Chapter 5. Measurements and characterization of SBD's behaviours at different temperatures were presented. The simulations were performed using finite element TCAD Sentaurus software. We present the determination of unknown parameters (related to interfacial layer and interface states charges) by using the characterization results with the aid of the simulations results to obtain best fitting of measured forward and reverse bias characteristics simultaneously at different temperatures ($I-V-T$ characteristics). Moreover, the effects of interfacial layer on the SBD's forward and reverse bias performances

were investigated by comparing numerical simulations results with experiment results. In the end, the distributions of electric field in the devices were also analyzed and discussed.

6.2 Diode under investigation

The diode under investigation is SBD 11F30 fabricated on wafer R100230-03 (refer to Figure 5-2). As mentioned earlier in Chapter 5, the SBDs on wafer R100230-03 display characteristics that deviate far from ideal, as compared to SBDs on wafer R100230-17. This is further illustrated in Figure 6-1, where the $I-V$ characteristics of SBDs 11F30 on wafer R100230-03 and R100230-17 are compared with simulation results for SBD 11F30 based on ideal intimate contact model. It should be noted that difference in the forward current of both SBDs is caused by difference in their drift doping concentration.

The increase in the Schottky barrier height and the small slope dI/dV around the turn-on voltage observed in experimental SBD 11F30 on wafer R100230-03 cannot be explained with pure thermionic emission and Schottky barrier lowering alone.

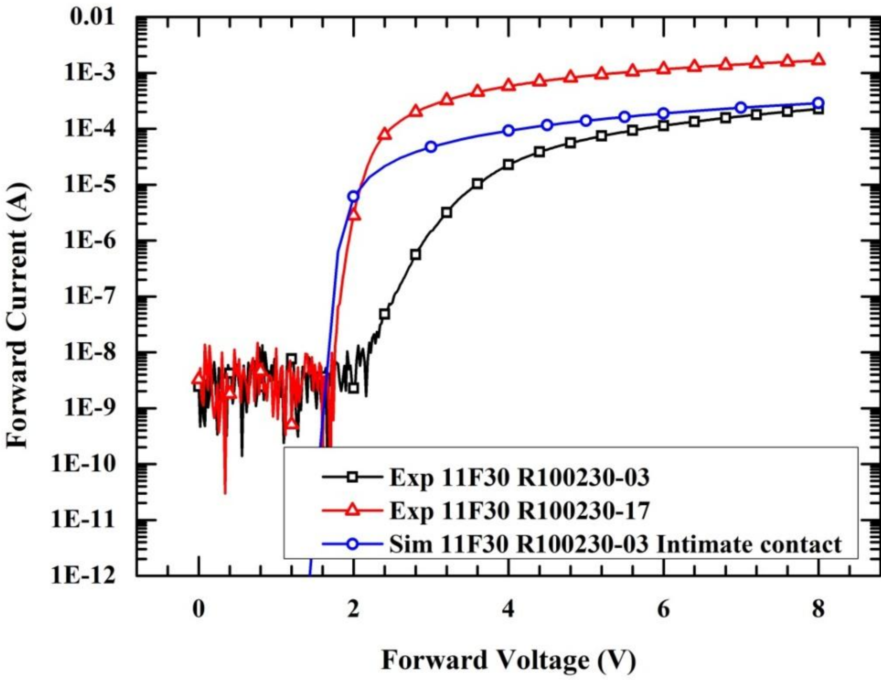

Figure 6-1: Comparison of measured forward bias $I-V$ characteristics of SBDs 11F30 fabricated on wafer R100230-03 and R100230-17 with simulation results of SBD 11F30 on R100230-03 using intimate contact diode model.

6.3 Experiment results and characterizations

The measured forward bias $I-V$ characteristics of the investigated SBD 11F30 at temperature of 298 K, 423 K, and 523 K are shown in Figure 6-2 (a). It can be observed that the turn-on voltage of this SBD is quite high (around 3 Volt) compared to that of intimate contact diode (~2 V). Figure 6-2 (b) shows the measured reverse bias $I-V$ characteristics of the investigated SBD at different temperatures. We can observe higher leakage current at higher temperature.

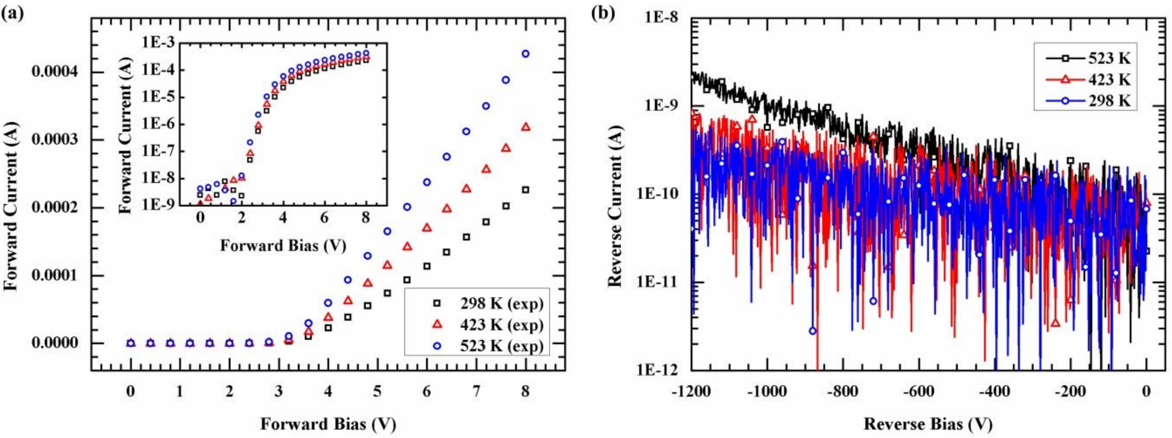

Figure 6-2: Measured $I-V$ characteristics of the experimental Mo/diamond SBD 11F30 on wafer R100230-03 at different temperatures: (a) forward bias and (b) reverse bias.

We then extracted the values of the ideality factor n, the Schottky barrier height ϕ_{B0}, and the series resistance R_S by curve fitting the measured forward bias $I-V$ characteristics using Eq. (5.32) and (5.13). Figure 6-3, Figure 6-4, and Figure 6-5 show the fitting of $V-\log I$ curves at temperature of 298 K, 423 K, and 523 K by using MATLAB Curve Fitting Toolbox with 95% confidence bounds. The extracted values are shown in Table 6-1 for each temperature.

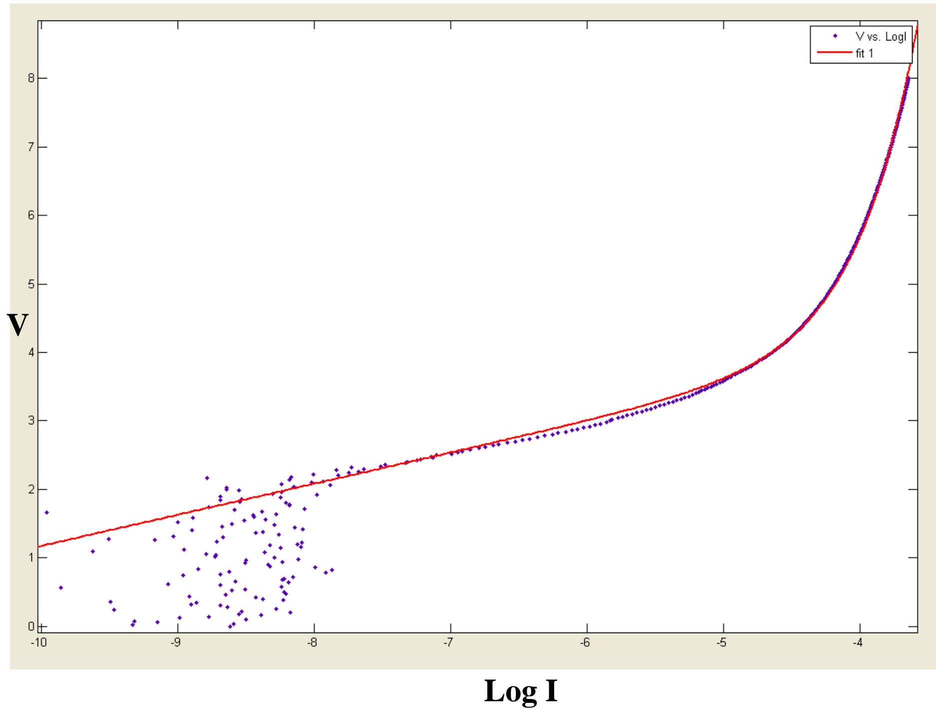

Figure 6-3: Fitting of $V - \log I$ curve at temperature of 298 K in MATLAB Curve Fitting Toolbox with 95% confidence bounds.

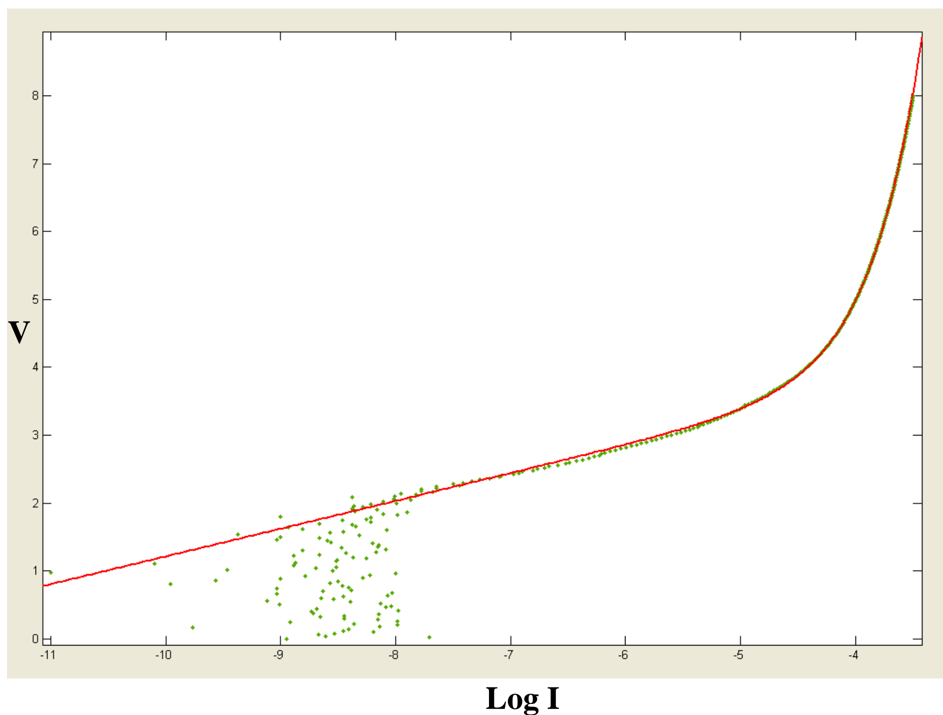

Figure 6-4: Fitting of $V - \log I$ curve at temperature of 423 K in MATLAB Curve Fitting Toolbox with 95% confidence bounds.

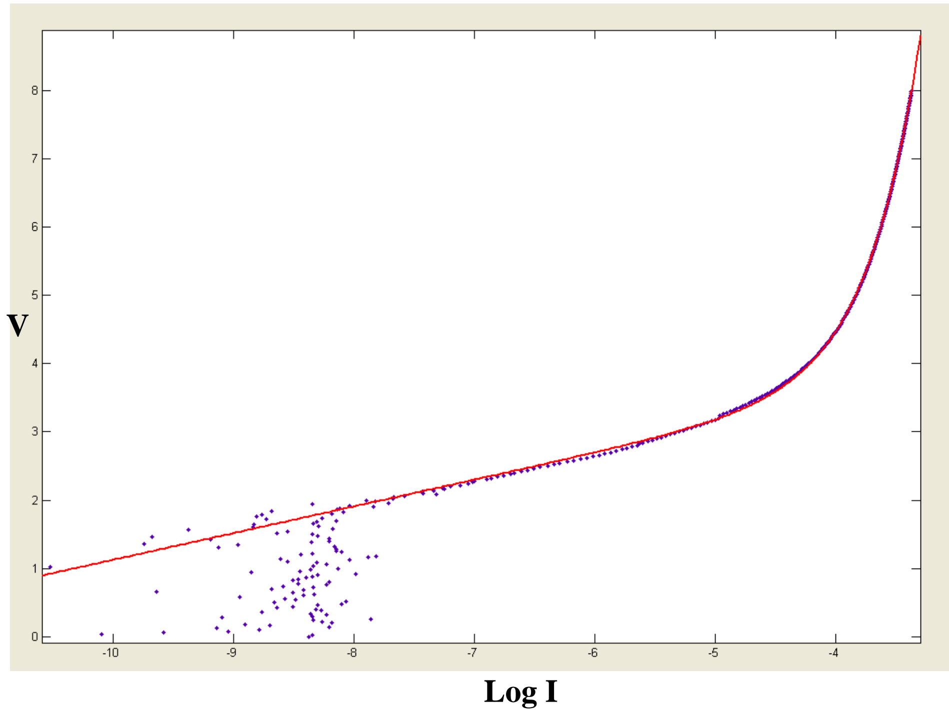

Figure 6-5: Fitting of $V - \log I$ curve at temperature of 523 K in MATLAB Curve Fitting Toolbox with 95% confidence bounds.

Table 6-1: Temperature dependent values of various parameters extracted from forward bias $I - V$ characteristics of the experimental Mo/diamond SBD 11F30 on wafer R100230-03.

T (K)	n	$q\phi_{B0}$ (eV)	R_S (Ω)	$R_{on}S$ (mΩ.cm^2)
298	7.677	0.8554	17850	159.04
423	4.872	1.272	13100	116.72
523	3.766	1.582	10040	89.46

High values of the extracted specific on-resistance $R_{on}S$ (89.46~159.04 mΩ.cm^2) is caused by the low doping concentration in the p- region and the contribution from the parasitic resistance. High values of n suggest the departure of diode's current transport from pure thermionic emission characteristics. Deviation of the extracted ϕ_{B0} from the barrier height of ideal intimate Schottky contact $q\phi_{B0}=$ 2.24 eV (assuming $\chi=$ 1.3 eV and $q\phi_m=$ 4.53 eV) and increased in the turn-on voltage indicates Fermi level pinning at Schottky metal-diamond interface.

Compared to the Mo/diamond SBD 12B200 on wafer R100230-17 investigated in Chapter 5 and the previously reported SBD (n~1.02, $q\phi_{B0}$~2.1 eV) in [36], the investigated SBD in this study is far from ideal. We attributed these

non-ideal behaviours to the existence of interfacial layer and interface states charges at Schottky metal-diamond interface which form Metal-interfacial layer-semiconductor (MIS) structure. As elaborated in Chapter 5, oxidative treatments to terminate diamond's surface can induce surface oxidized layer and highly disordered surface defect layer [90-92]. Oxidation or Nitrization of Schottky metal might also form thin MoOx or MoNx layer.

As no direct observations on the nature of interfacial layer were carried out at this moment, we relied on numerical simulations using TCAD Sentaurus software and characterizations results from measured $I-V$ characteristics in determining the values of unknown parameters. Through extensive simulations, the thickness of the interfacial layer δ is found to be approximately 2.5 nm to best fit the measured forward bias $I-V$ characteristics at different temperature (shown in Figure 6-10). The simulations and fitting process are described in Section 6.4. This thick interfacial layer can be justified given the very high extracted ideality factor n.

In the determination of interface states charges density, we followed the method elaborated in Chapter 5 [111]. Considering the effect of incomplete ionization given by Eq. (3.1), (3.2), and (3.3), and coupled with charge neutrality condition, electron and hole concentration given by Eq. (3.10), (3.4), and (3.5), we can approximate the value of the Fermi level E_F and ionized acceptor concentration N_A^-. The calculated values of g_A, $E_F - E_V$, and N_A^- at different temperatures are shown in Table 6-2. These values were also verified with the simulations results by TCAD Sentaurus software. In the calculations, we assume no acceptor compensation ($N_D = N_D^+ = 0$).

Table 6-2: Calculated temperature dependent values of degeneracy factor, Fermi level, and ionized acceptor concentration.

T (K)	g_A	$E_F - E_V$ (eV)	N_A^- (cm^{-3})
298	5.583	0.3323	4.273x10^{13}
423	5.697	0.4130	3.614x10^{14}
523	5.751	0.4951	6.996x10^{14}

From the measured forward bias $I-V$ characteristics, we extracted the values of bias dependent ideality factor $n(V)$ using Eq. (5.32) and (5.13), with values of

ϕ_{B0} and R_S in Table 6-1. The bias dependent effective barrier height $\phi_B(V)$ and the surface potential $\psi_S(V)$ can then be calculated using Eq. (5.16) and (5.10).

With the calculated $\phi_B(V)$ and $\psi_S(V)$, we evaluated the width of depletion region $W(V)$ and subsequently the interface states energy distribution $D_{it}(E_{SS}-E_V)$ (states/cm^2.eV) by using Eq. (5.18), (5.17), and (5.22) (following the steps elaborated in Chapter 5). Using $\delta = 2.5$ nm (established by the simulations) and $\varepsilon_i = 2\ \varepsilon_0$ [109], the extracted $D_{it}(E_{SS}-E_V)$ of the investigated SBD at different temperatures are shown in Figure 6-6. Their values are in the same order (~10^{13} eV^{-1}.cm^{-2}) as the extracted interface states charges density of the investigated Mo/diamond SBD on R100230-17 substrate [111] (refer to Chapter 5). They are quite uniformly distributed and decreasing with increasing temperature.

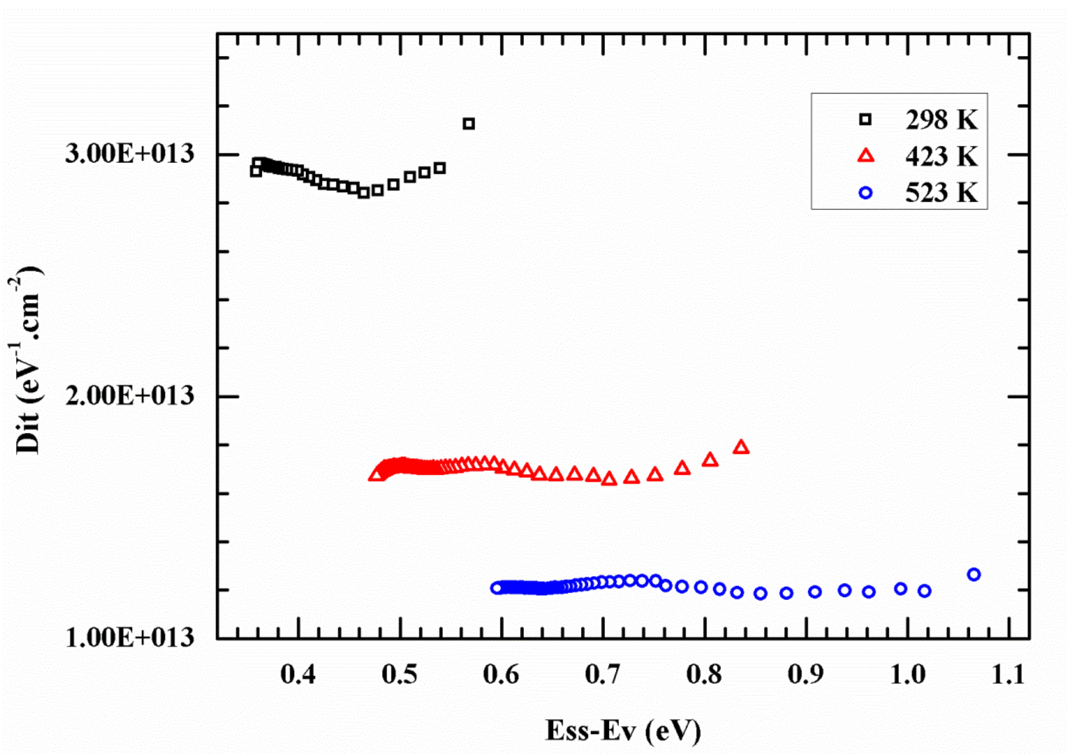

Figure 6-6: Energy distribution profile of the interface states density of the experimental Mo/diamond SBD 11F30 on wafer R100230-03 at different temperatures.

6.4 Modelling and simulations

Modelling and simulations of the investigated SBD 11F30 on wafer R100230-03 were carried out in TCAD Sentaurus software using the two dimensional MIS structure as shown in Figure 6-7. The p- drift region has Boron doping of 9.29×10^{14} cm^{-3} and thickness of 10 μm. The p+ region has high Boron doping of 1.82×10^{20} cm^{-3}. To save computational time and effort, the thickness of the simulated p+ region is reduced to 3 μm and only half of the symmetrical device was simulated. The simulated Schottky electrode's area is 15 μm^2, resulting in area factor of 59.4 compared to the actual electrode's area. The total parasitic resistance of the substrates and the contacts are lumped and simulated as the resistance of ohmic contact $R_{parasitic}$ that is adjustable and varies with temperature.

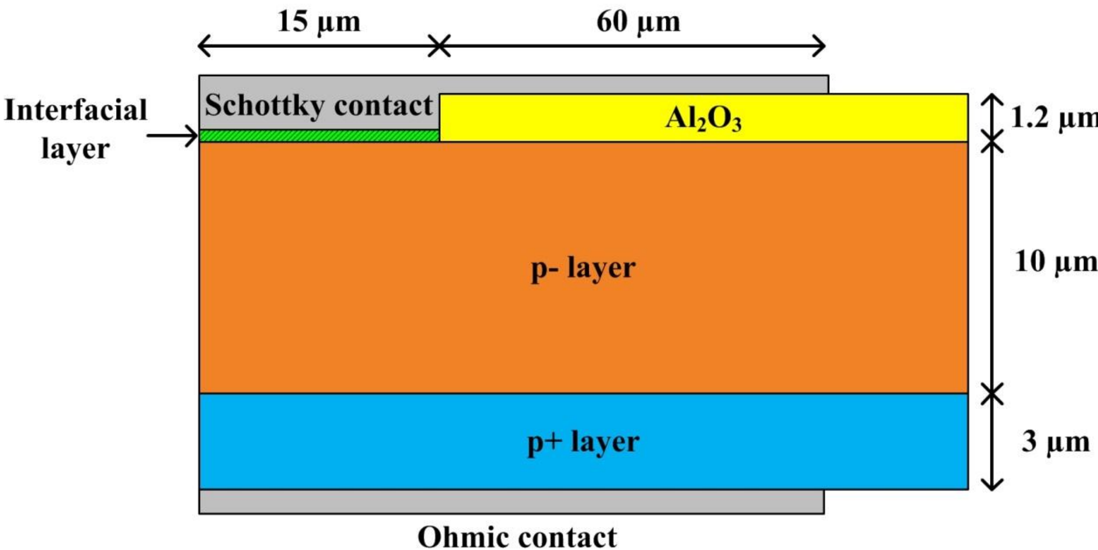

Figure 6-7: The simulated two dimensional MIS device structure implemented in TCAD Sentaurus software.

In the simulations, the Schottky metal used is Molybdenum with metal work function $q\phi_m$ of 4.53 eV. Al_2O_3 with dielectric constant of 9, band gap of 8.8 eV, electron affinity of 1 eV [112, 113], and thickness of 1.2 μm is used as the field plate oxide. The diamond is Oxygen terminated with electron affinity χ of 1.3 eV.

Interfacial layer with dielectric constant of 2 and electron affinity of 0.9 eV is inserted between the Molybdenum metal and diamond. Through numerous simulations, the thickness of interfacial layer is determined to be ~2.5 nm to fit the

forward bias $I-V$ characteristics. The band gap of the interfacial layer E_{gi} is kept as an adjustable parameter in fitting the forward and reverse bias $I-V-T$ characteristics.

Furthermore, acceptor-like interface state charges located at interfacial layer-diamond interface are implemented as acceptor traps in the TCAD Sentaurus software [68]. The trap's capture cross sections for electron and hole are set at 10^{-10} cm^2 and 10^{-12} cm^2 respectively. As the initial guesses, the implemented distribution profiles of these traps in the simulations follow the extracted profiles of $D_{it}(E_{SS}-E_V)$ shown in Figure 6-6. Later on, their distribution profiles are varied accordingly to fit the forward and reverse bias $I-V-T$ characteristics.

In the simulations, various physics models and parameters that are described in Chapter 3 were implemented, except for the incomplete ionization model due to uncertainty in the impact ionization coefficients values.

For the current transport through any arbitrary barrier shape between the Molybdenum and diamond (through the interfacial layer), we implemented Nonlocal tunneling model with Wentzel-Kramers-Brillouin (WKB) approximation for the computation of tunneling probability [68, 114]. The Nonlocal tunneling model computes tunneling current based on the band edge profile along the entire path between the points where tunneling occurs. Details of the Nonlocal tunneling model implemented in the simulations can be found in [68].

The main adjustable parameters for the Nonlocal tunneling model are the scaling factors (g_c, g_v) and the electron and hole tunneling masses (m_c, m_v). Increasing the scaling factors increases tunneling current, while increasing the tunneling masses decreases the tunneling current significantly. In addition, the interface state charges density D_{it} and the properties of interfacial layer that determine the barrier shape (such as the thickness, band gap, and the electron affinity) also have significant impact to the $I-V$ characteristics of the SBD. Larger interfacial layer band gap E_{gi} increases the barrier height for holes, and thus reducing the current.

Variations in the simulated forward and reverse $I-V$ characteristics of the SBD with respect to changes in these parameters are shown in Figure 6-8 and Figure 6-9. The parameters used in Reference curve ($m_v = 0.5m_e$, $g_v = 0.66$, $D_{it} =$

2.7x10^{13} eV^{-1}.cm^{-2}, E_{gi} =7.3 eV, δ = 2.5 nm) are used as standard parameters set for the other comparative curves, except for the stated change. From the figures, it can be observed that changes in g_v result in linear changes for both forward and reverse $I-V$; while changes in other parameters influence the $I-V$ characteristics in non-linear ways.

(a)

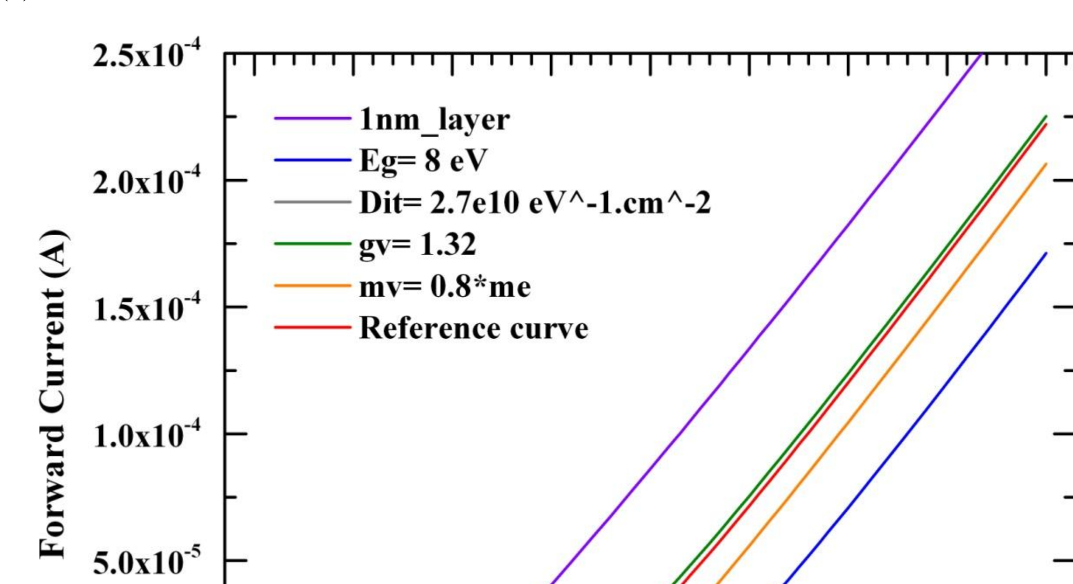

(b)

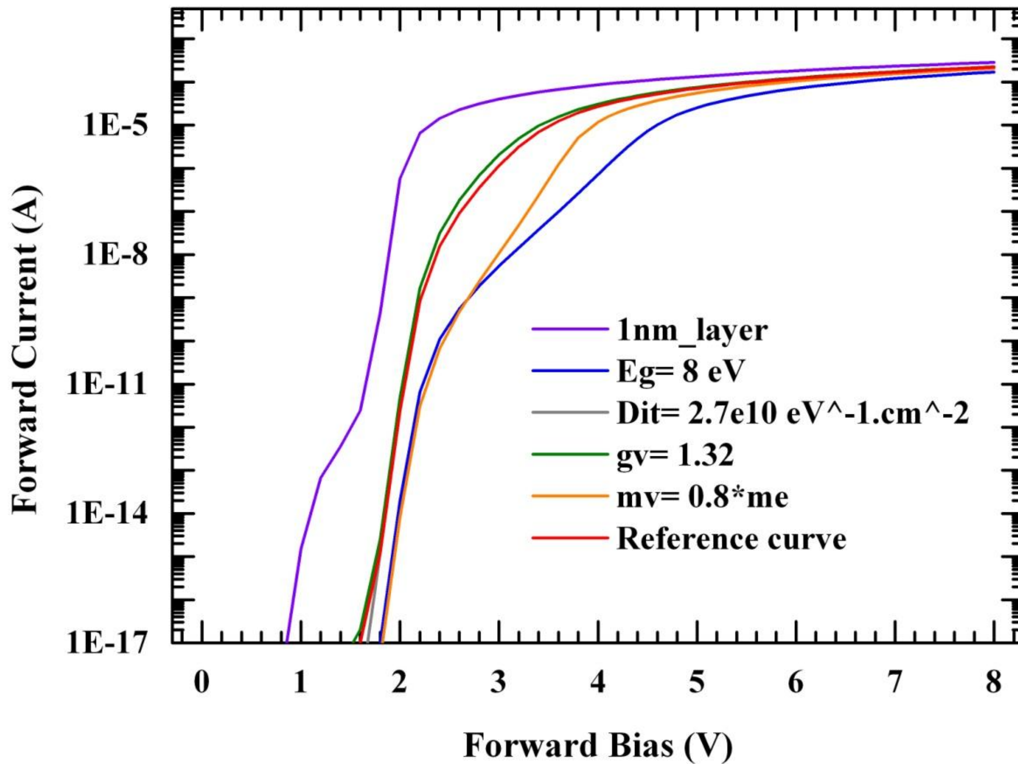

Figure 6-8: Variations in the simulated forward $I-V$ characteristics with respect to changes in parameters for Nonlocal tunnelling and interfacial layer in linear (a) and log scale (b).

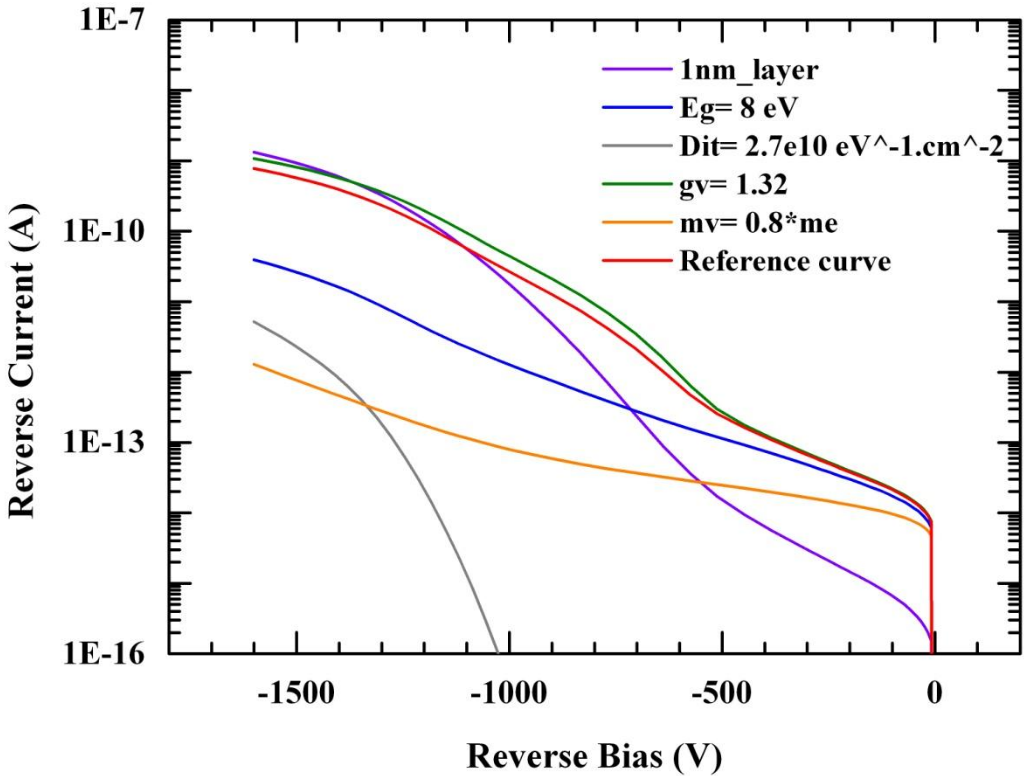

Figure 6-9: Variations in the simulated reverse $I-V$ characteristics with respect to changes in parameters for Nonlocal tunnelling and interfacial layer.

Through numerous simulations, the values of the adjustable parameters to best fit the measured forward and reverse bias $I-V-T$ simultaneously were determined. In the simulations, temperature independent parameters such as E_{gi}, g_c, g_v, m_c, m_v are fixed at 7.3 eV, 2.1, 0.66, 0.5m_e, and 0.5m_e to obtain the best fitting. Good matching between the measurements and simulations results of SBD's forward bias $I-V-T$ can be seen in Figure 6-10 (a). The comparisons between the measured reverse bias $I-V-T$ of the investigated SBD and the simulations results are shown in Figure 6-10 (b). In general, correlation between experimental data and simulations results can be observed, except for small reverse current (at low temperature and low reverse bias) where much scattering occurs due to the noise and sensitivity limit of the measurement equipment.

(a)

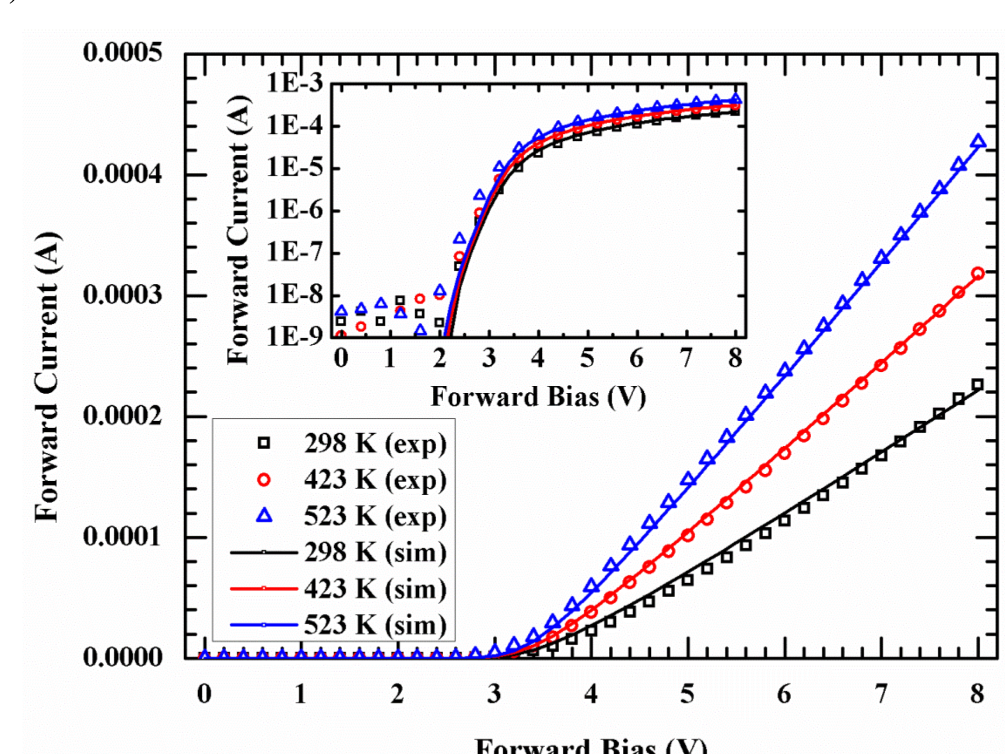

(b)

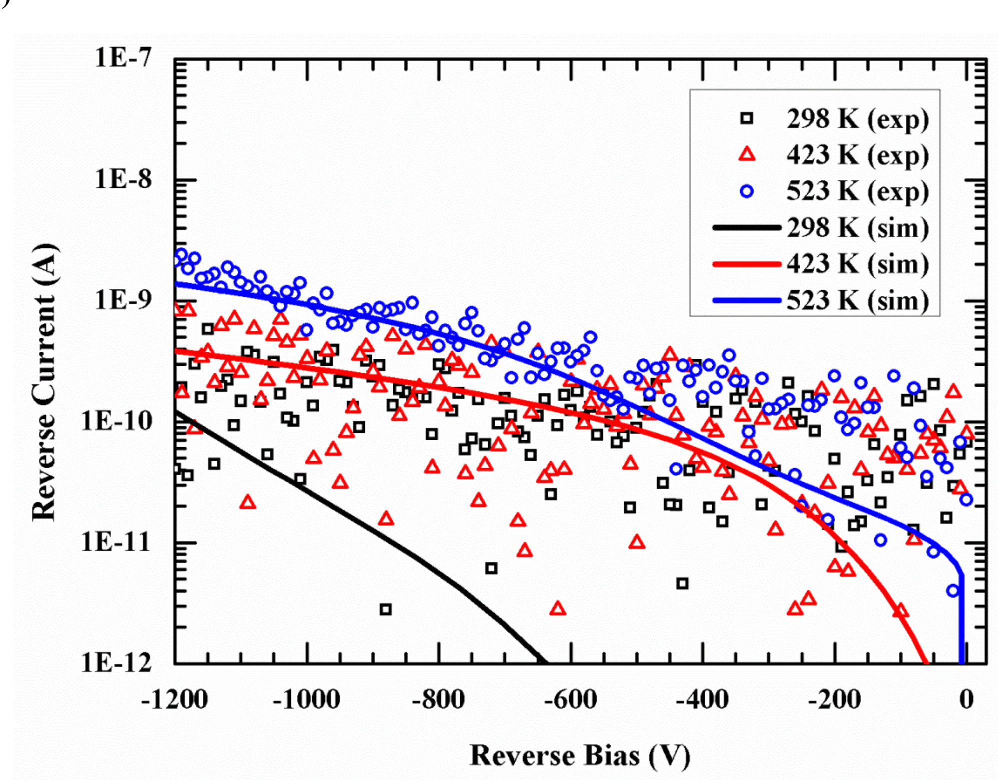

Figure 6-10: Simulation and experiment results of (a) forward bias and (b) reverse bias $I-V$ characteristics of the experimental Mo/diamond SBD 11F30 on wafer R100230-03 at different temperatures.

To fit the slope of forward bias $I-V-T$ curves at high forward bias, $R_{parasitic}$ values in the 2-D simulations are adjusted to the values shown in Table 6-3. Their absolute series resistance values are shown as R_{series} correspondingly. The values of R_{series} are smaller compared to the extracted R_S in Table 6-1 for each temperature because of the resistance of the p- region which can be approximated as $R_{p-} \approx R_S - R_{series}$. As expected, R_{p-} is decreasing with increasing temperature which results in the negative temperature coefficient of resistance (higher current at higher temperature) for this investigated SBD.

In fitting the the measured reverse bias $I-V-T$ curves, acceptor traps density and their energy distributions are adjusted to values shown in Table 6-3, while maintaining the same values for the other parameters. The acceptor traps are uniformly distributed (with density given by D_{it}) from $E_{SS} - E_V$ = 5.47 eV (the conduction band) to $E_{SS} - E_V = E_{Dit}$. They seem to be in agreement with the extracted values of $D_{it}(E_{SS} - E_V)$ shown in Figure 6-6, i.e. the D_{it} values are similar and decreasing with increasing temperature.

Table 6-3: Values of temperature dependent parameters used in the simulations.

T (K)	D_{it} (eV^{-1}.cm^{-2})	E_{Dit} (eV)	$R_{parasitic}$ (Ω.μm)	R_{series} (Ω)	R_{p-} (Ω)
298	2.7x10^{13}	4.85	705920	11884	5966
423	1.4x10^{13}	4.83	675000	11363.64	1736.36
523	1.3x10^{13}	4.74	516780	8700	1340

The simulated energy band diagram for the investigated SBD based on MIS model at thermal equilibrium (0 V) and at 298 K is shown in Figure 6-11. From the zoom-in figure, high barrier for holes can be observed at -0.0025 μm < y < 0 μm due to the large band gap of the interfacial layer. The corresponding energy band diagrams under forward bias of 3 V (around the turn-on voltage) and 5 V are shown in Figure 6-12 and Figure 6-13. With the increase of forward bias, effective barrier height for holes (travelling from the p- layer to Schottky metal) is decreasing. The opposite can be observed in the energy band diagram under reverse bias of 4 V shown in Figure 6-14. Figure 6-15 shows the corresponding distributions of hole density in the device under different bias conditions. It can be observed that at 0 V,

the hole density in the depletion region near Schottky contact (at y= 0 μm) is very low. During reverse bias operation, the depletion region grows to support the reverse voltage, as evident in the decrease of hole density. On the other hand, hole density increases during forward bias operation due to injection of holes from p+ region.

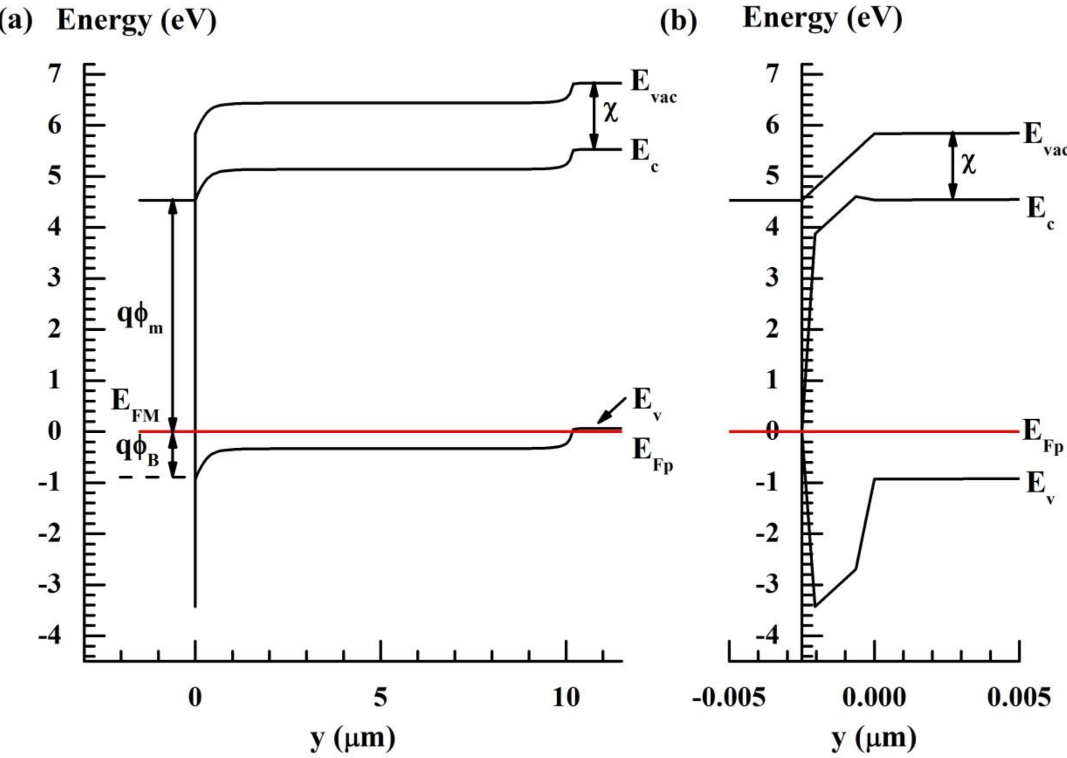

Figure 6-11: Energy band diagram for the investigated SBD based on MIS model at 298 K at equilibrium condition (0V). The zoom-in figure at the metal-diamond interface is given in (b).

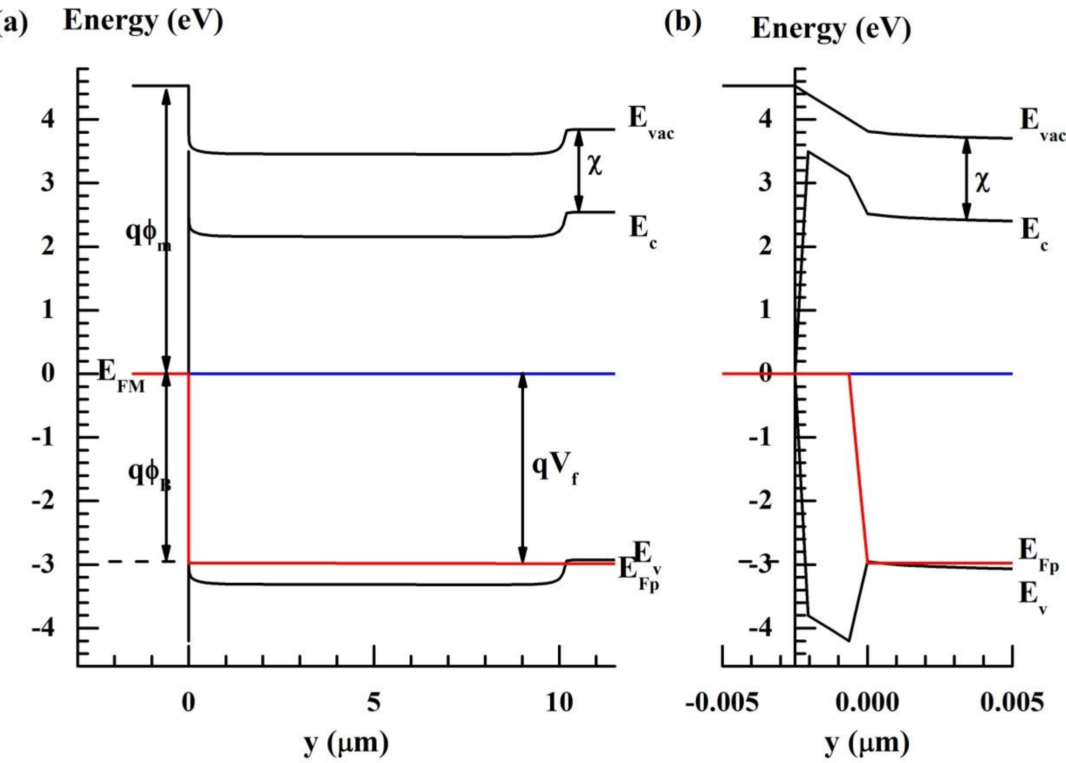

Figure 6-12: Energy band diagram for the investigated SBD based on MIS model at 298 K under forward bias V_f 3 V. The zoom-in figure at the metal-diamond interface is given in (b).

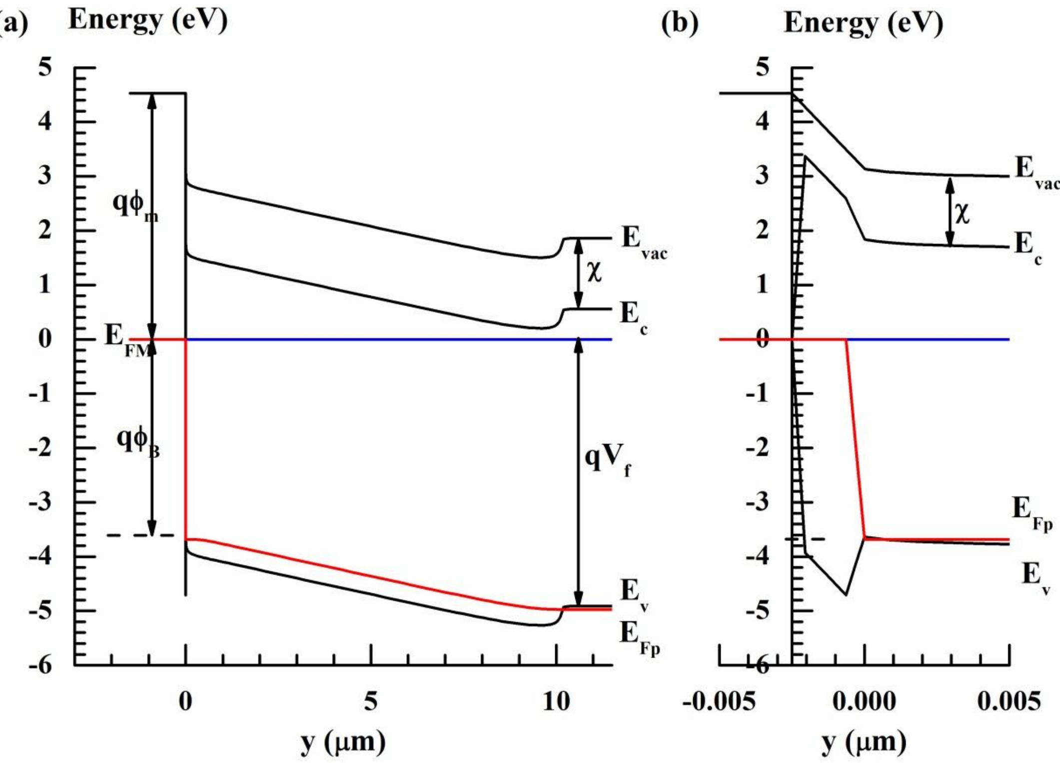

Figure 6-13: Energy band diagram for the investigated SBD based on MIS model at 298 K under forward bias V_f 5 V. The zoom-in figure at the metal-diamond interface is given in (b).

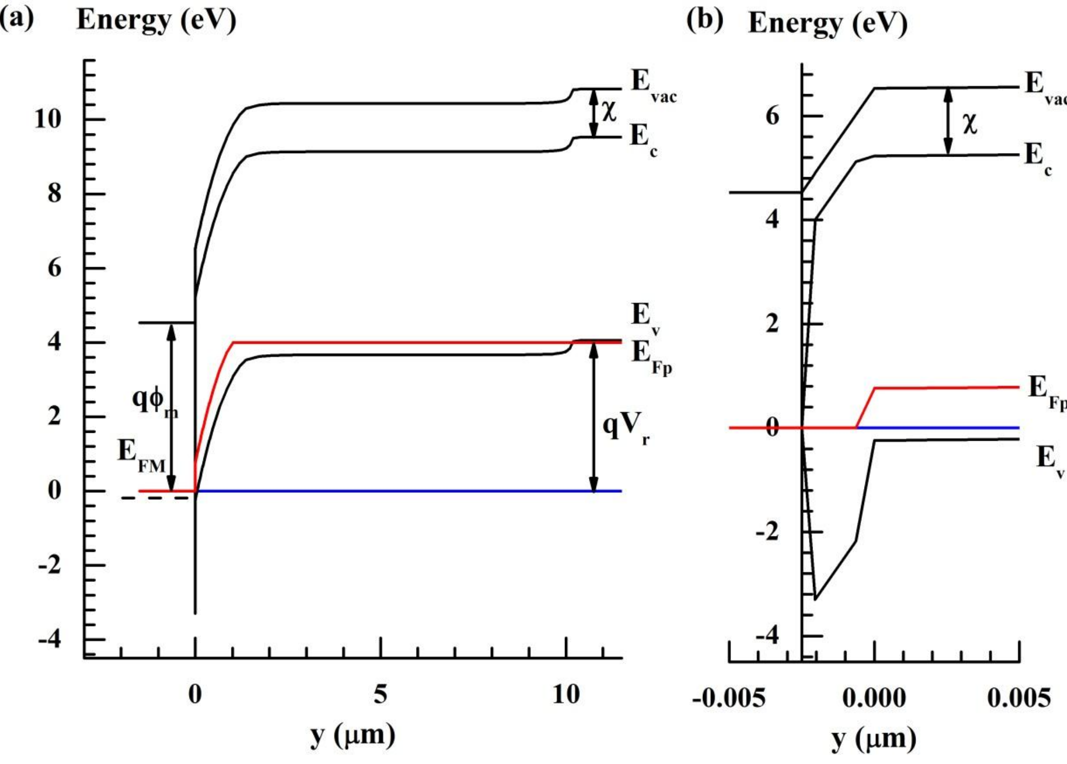

Figure 6-14: Energy band diagram for the investigated SBD based on MIS model at 298 K under reverse bias V_r 4 V. The zoom-in figure at the metal-diamond interface is given in (b).

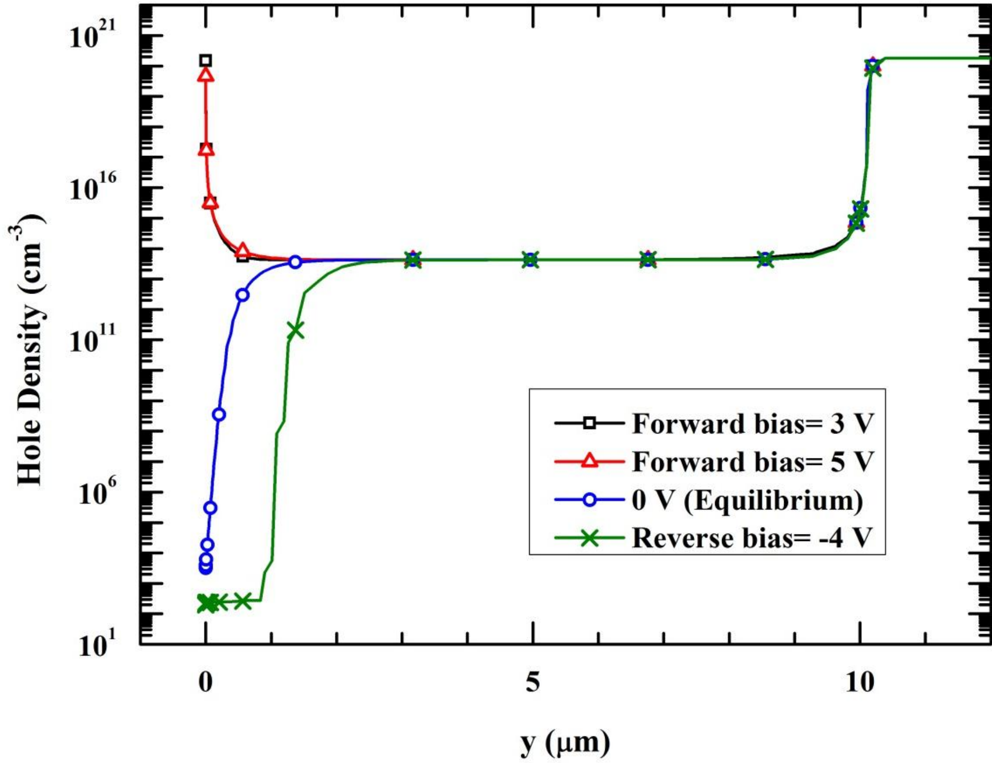

Figure 6-15: Simulated distribution of hole density in the MIS structure at thermal equilibrium and under different bias condition.

The implemented MIS model in this simulations work exhibits improvements over the simplified intimate contact SBD model (refer to Chapter 4). The simplified SBD model does not simulate Fermi level pinning at the Schottky metal-diamond interface. Consequently, Schottky barrier height needs to be readjusted at each temperature to match the measured forward bias $I-V$ curves. Moreover, reverse bias simulations using the simplified SBD model have not been successful in matching the measured leakage current.

On the other hand, the MIS model employed in this study is able to simulate Fermi level pinning at the interface by taking into account the effects of interfacial layer and interface states charges. As a result, the MIS model is able to fit the forward and reverse bias $I-V$ curves at different temperatures simultaneously.

6.5 Effects of the interfacial layer and interface states charges on diamond Schottky barrier diode

To investigate the significance of the interfacial layer and interface states charges that produce non-ideal behaviours (found in the experimental SBDs on wafer R100230-03), we performed simulations of a Mo/diamond SBD with identical bulk properties as the investigated SBD, but with ideal intimate contact (ideal barrier height $q\phi_{B0}$ = 2.24 eV). By comparing its characteristics with those of the investigated SBD, we can observe the resulting deviations.

Figure 6-16 shows the simulated forward bias $I-V$ characteristics of the ideal intimate contact SBD in comparison with the measurements data of the investigated SBD. The SBD with intimate Schottky contact exhibits lower turn-on voltage by more than 1 V. Thus, at the same forward bias, SBD with intimate Schottky contact has higher current carrying capability compared to the investigated SBD (with interfacial layer and interface states charges at the interface).

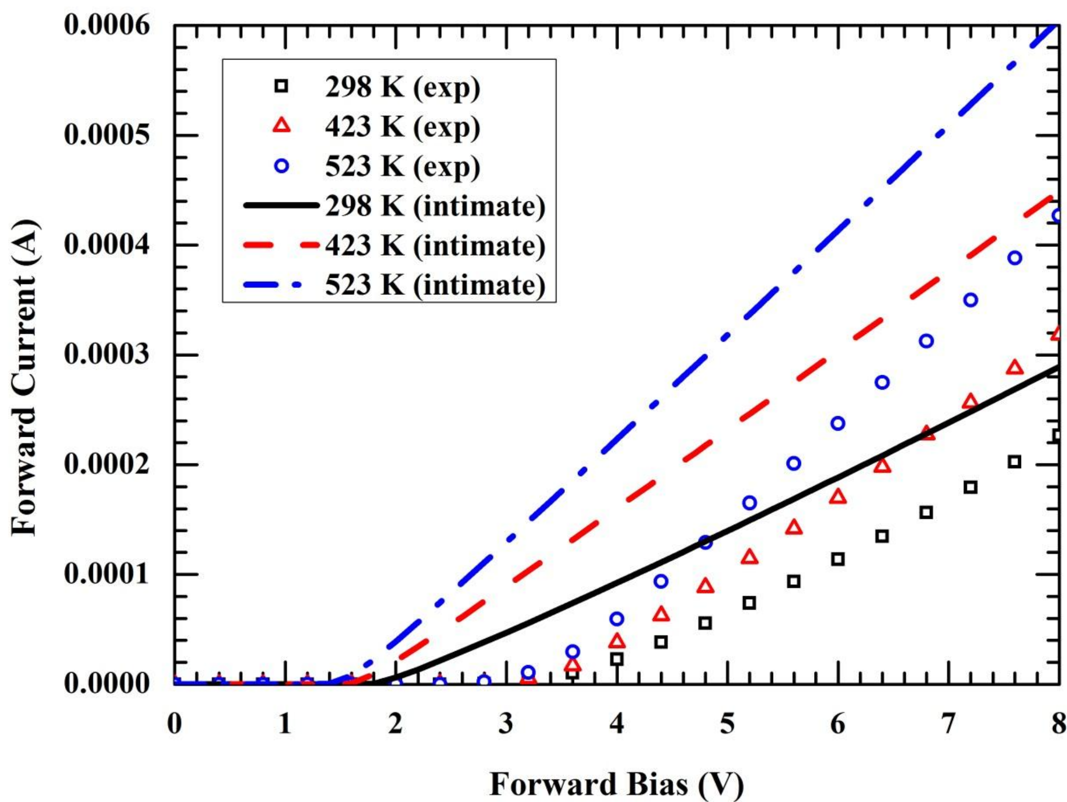

Figure 6-16: Comparison between simulated forward bias $I-V$ characteristics of the SBD with ideal intimate Schottky contact and experiment results.

To investigate the effect of interfacial layer on the SBD's reverse bias performances, we carried out reverse bias simulations in TCAD Sentaurus software for (1) Mo/diamond SBD without interfacial layer (intimate contact SBD) and (2) the investigated Mo/diamond SBD (utilizing the established MIS model and parameters: 2.5 nm thick interfacial layer, interface states charges distribution based on values in Table 6-3, etc.).

Distributions of the simulated electric field E_f in the investigated SBD (MIS structure) at reverse bias of 1300 V at 298 K are shown in Figure 6-17. Peak electric field E_f occurs at point A (at the corner of the Schottky contact) and point B (at metal-oxide interface at the end of metal plate extension). High peak E_f of ~11.8 MV/cm in the interfacial layer can be observed at point A.

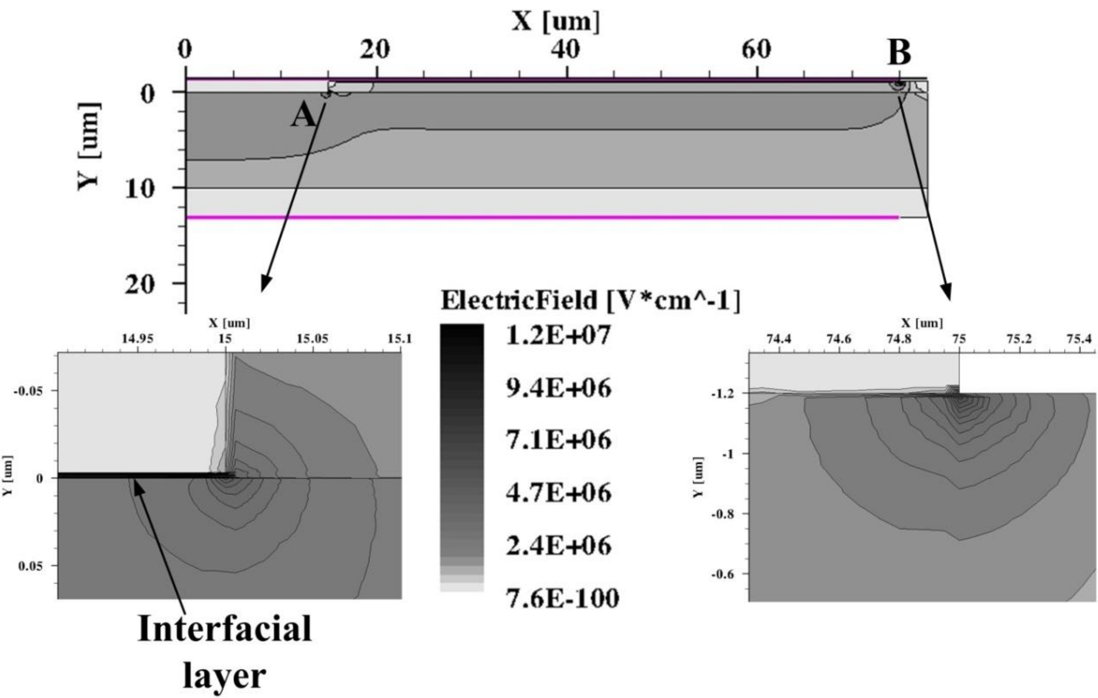

Figure 6-17: Distribution of simulated electric field in the investigated Mo/diamond SBD with interfacial layer and interface state charges (MIS model) at reverse bias of 1300 V at 298 K.

Distributions of E_f along the horizontal line y= 0 μm (in the diamond region and in the interfacial layer) and along the vertical line x= 0 μm in the MIS diode are shown in Figure 6-18. In addition, distributions of E_f in the SBD with intimate contact are also presented for comparisons.

From Figure 6-18 (a), we can observe peak E_f at x= 15 μm which corresponds to the peak E_f at the corner of the Schottky contact (point A). While the peak E_f in diamond material for MIS diode (~4.8 MV/cm) is smaller than that in the intimate contact SBD (~11.3 MV/cm), peak E_f in the interfacial layer reaches high value of 11.8 MV/cm (shown as blue colored dash line in Figure 6-18 (a)). It can be observed that the E_f distributions in both diodes are similar, except for the peak E_f at point A and the E_f in the interfacial layer.

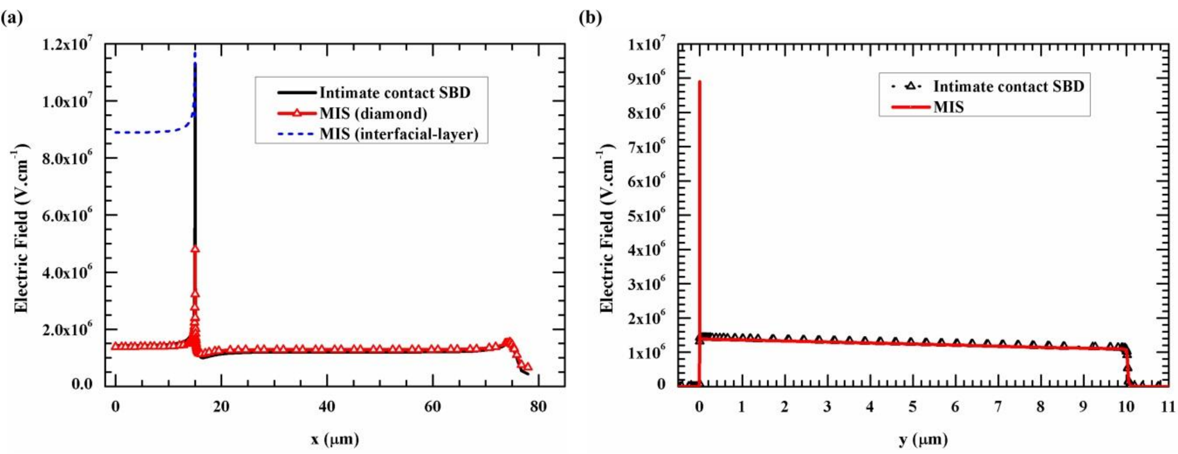

Figure 6-18: Simulated electric field distribution in MIS diode structure and intimate contact SBD structure at reverse bias of 1300 V and at 298 K along the horizontal line y= 0 µm (a) and vertical line x= 0 µm (b).

Away from point A and towards the center of Schottky contact, the E_f in the interfacial layer remains at high value of ~9 MV/cm as shown in Figure 6-18 (a) and (b). This presents the possibility of SBD's premature breakdown due to breakdown of the interfacial layer. Thus, unintentional interfacial layer in the metal-diamond interface is not desirable. It changes the turn-on voltage of the SBD and presents the risk of premature breakdown during the reverse bias operations. In order to enhance the SBD's performance and reliability, careful design and control of metal-diamond interface is a must.

6.6 Conclusions

We have demonstrated rigorous modelling and simulations of non-ideal characteristics of a vertical Mo/diamond SBD by utilizing the MIS model. The experimental Mo/diamond SBD was characterized based on the combination of measurements and finite element simulation results (using TCAD Sentaurus software) to extract the distributions of interface states charges density. In the simulations, Nonlocal tunnelling model with WKB approximation was implemented to simulate the current transport through arbitrary Schottky barrier shape (across the interfacial layer).

Compared to the typically employed simplified intimate contact diode model, the MIS model with interface states charges is able to simulate Fermi level pinning effect at the interface. The best fitting of simulation results to the measured forward and reverse bias $I-V$ simultaneously at different temperatures yielded interfacial

layer thickness of 2.5 nm and band gap of 7.3 eV, hole tunnelling mass of $0.5\,m_0$, and interface states charges density (acceptor traps) of $1.3\text{x}10^{13}$ - $2.7\text{x}10^{13}$ $\text{eV}^{-1}.\text{cm}^{-2}$.

We also found out that existence of this unintentional interfacial layer at the metal-diamond interface is not desirable. It reduces the forward current carrying capability of the diode and increases the risk of premature breakdown during reverse bias operation because of the high electric field in the interfacial layer.

Furthermore, the MIS model can be expanded for nonhomogeneous contact cases by taking into account inhomogeneity of metal-diamond interface such as spatial variations in the interfacial layer thickness and the interface states charges density.

However, interface issue in the device is a complex problem. In order to fabricate high performance diamond Schottky barrier diode, more studies on the interface control including the effects of different surface treatments on the nature of metal-diamond interface need to be investigated.

7 TERMINATION STRUCTURES FOR DIAMOND SCHOTTKY BARRIER DIODE

7.1 Introduction

Diamond diodes are expected to withstand high reverse voltage with thin drift region due to the high breakdown electric field of diamond material (10-20 MV/cm). In order to achieve high voltage diamond Schottky barrier diodes, it is important to improve the quality of synthetic single crystal diamond and the metal contact-diamond interface. Furthermore, design and optimization of the edge termination structure plays crucial role to maximize the breakdown voltage capability of the diode.

Because of the high ionization energy of n-type dopant in diamond, termination techniques that require n-type diamond region such as junction termination are not applicable at this moment. Instead, termination techniques that utilize field plate extension such as field plate termination, three step termination, and ramp oxide termination have been developed [63]. High k dielectric oxide and semi- resistive materials have also been employed recently in order to prevent breakdown in the field oxide [67, 115, 116].

In this work, we propose planar mesa termination structure [117] for p-type diamond SBD to improve the trade-off between forward and reverse bias characteristics. Design and optimizations are carried out by simulations in finite element physics-based TCAD Sentaurus software. High k dielectric Al_2O_3 is used as the field oxide in this simulation study. The electrical performances of the planar mesa termination structure have been investigated and compared with those of the field plate termination structure.

7.2 Termination structures for diamond Schottky barrier diode

In any practical diode devices, any metallic contact has to terminate at a certain point on the device. The early SBD was fabricated without any special

termination structure as shown in Figure 7-1 [8]. While the fabrication process for this structure is very simple, it suffers from the low breakdown voltage due to the electric field enhancement at the abrupt edge of Schottky contact termination. To prevent premature breakdown, other more sophisticated termination structures are needed to redistribute the electric field more uniformly.

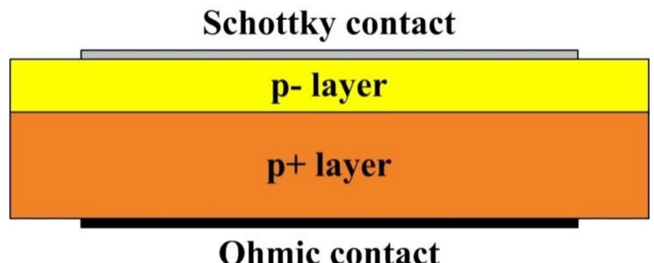

Figure 7-1: Schottky barrier diode structure without termination structure.

The most common termination structure considered for the diamond SBD currently is the field plate termination, as shown in Figure 7-2. Although this structure is able to increase the breakdown voltage of the diode, the peak electric field still occurs at the edge of Schottky metal-semiconductor interface. This can cause Schottky barrier lowering and consequently an increase in the leakage current. At high reverse bias, the leakage current is further increased due to the multiplication effects [8] which can lead to breakdown at small area under the edge of Schottky contact.

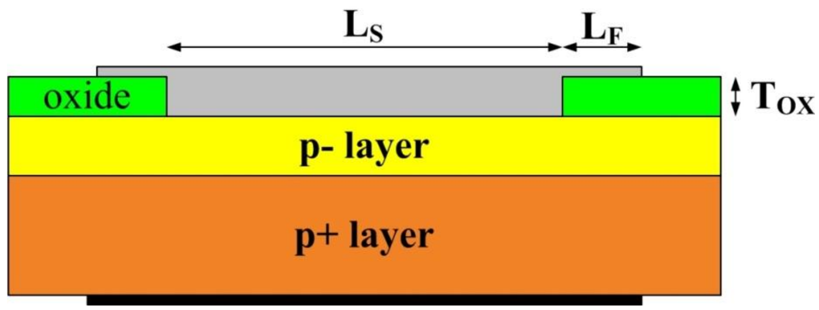

Figure 7-2: Schottky barrier diode with field plate type of termination structure.

In this work, we propose the planar mesa termination structure to improve the performances of diamond SBD. This structure has the potential to reduce the peak electric field at the Schottky metal-diamond interface. Applications of this structure

in conventional silicon SBD have demonstrated vast improvement in the reverse bias performance with minimal effect on the forward bias performance [69, 117].

The proposed planar mesa termination structure for diamond SBD is shown in Figure 7-3. The mesa region is surrounded by an oxide layer to reduce the electric field crowding at the corner of the Schottky contact. This mesa structure can be obtained by Inductively Coupled Plasma (ICP) etching technique using O_2 and CF_4 reactant gases [36, 61]. Possible process flow for the fabrication is shown in Figure 7-4. In this process, the center area for the Schottky contact is firstly masked. Then, ICP process is carried out to selectively etch the p- region at the edge of the device. Next, oxide is deposited to fill the trench region created by the etching process, followed by Schottky contact metallization.

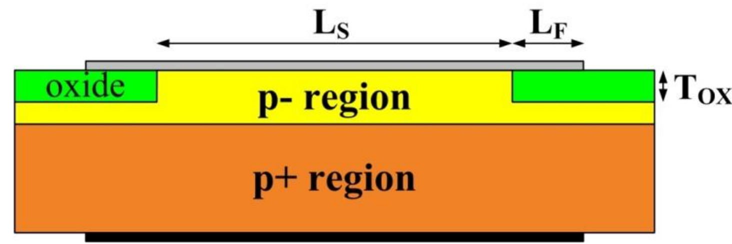

Figure 7-3: Schottky barrier diode with planar mesa type of termination structure.

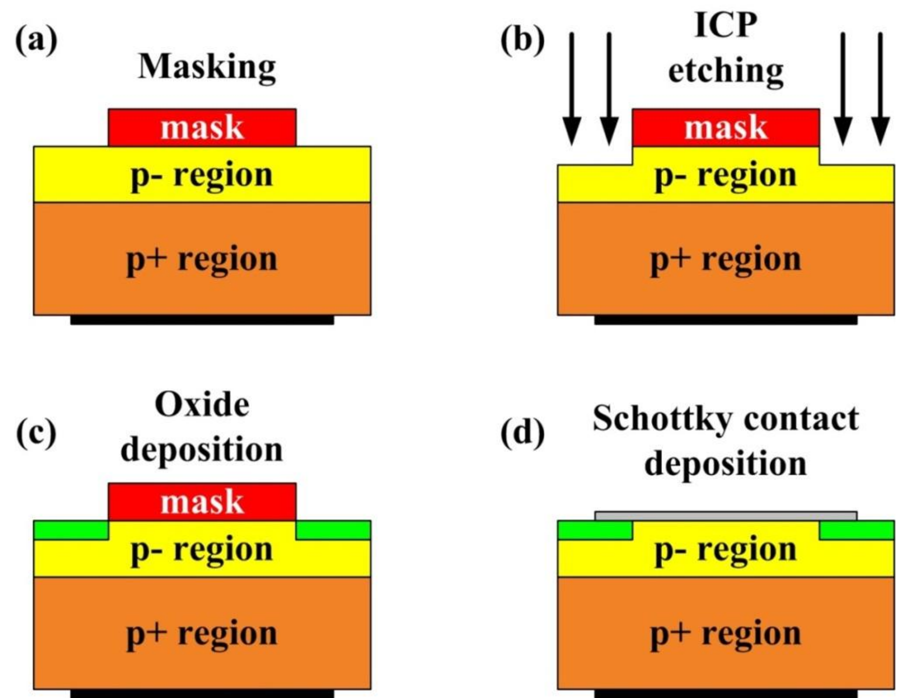

Figure 7-4: Process flow for fabrication of planar mesa termination for diamond SBD. (a) Masking of p- region at center area for Schottky contact. (b) Selective ICP etching to create diamond mesa structure. (c) Oxide deposition to fill in the trench region for termination purposes. (d) Schottky contact metallization.

7.3 Performances comparisons- Simulation studies

In order to investigate the performances of planar mesa termination structure in comparison with the field plate termination structure for diamond SBD, we performed two dimensional numerical simulation studies using TCAD Sentaurus software. Except for the termination structure, all of the simulated SBDs have identical properties. The p+ region is 20 μm thick and it has high Boron doping of 10^{20} cm^{-3}. The p- drift region has Boron doping of $5x10^{15}$ cm^{-3} and thickness of 10 μm. The diamond is Oxygen terminated with electron affinity of 1.3 eV. The Schottky metal work function is fixed at 4.27 eV to yield Schottky barrier height of 2.5 eV. In both termination structures, the width of the Schottky contact L_S is selected as 30 μm and high k dielectric Al_2O_3 with dielectric constant k of 8.7 [66] is used as the oxide layer.

In the simulations, we applied various physics models and parameters as elaborated in Chapter 3. The impact ionization coefficients used are the values suggested by S. J. Rashid et al [64]. While the simulated breakdown voltage will be lower than what can be achieved in single crystal diamond material, these values serve as references in comparing the performances of different edge termination structures. Moreover, we did not consider non-ideal factors such as defects, imperfect metal-diamond interface, etc. in these simulation studies.

For the sake of completeness, breakdown simulations of diamond SBD without termination structure were carried out and presented. The non-terminated diamond SBD yields low breakdown voltage of 250 V because of high peak electric field at the corner of Schottky contact as shown in Figure 7-5. This underlines the importance of edge termination structure to redistribute and reduce peak electric field and to increase the diode’s breakdown voltage capability.

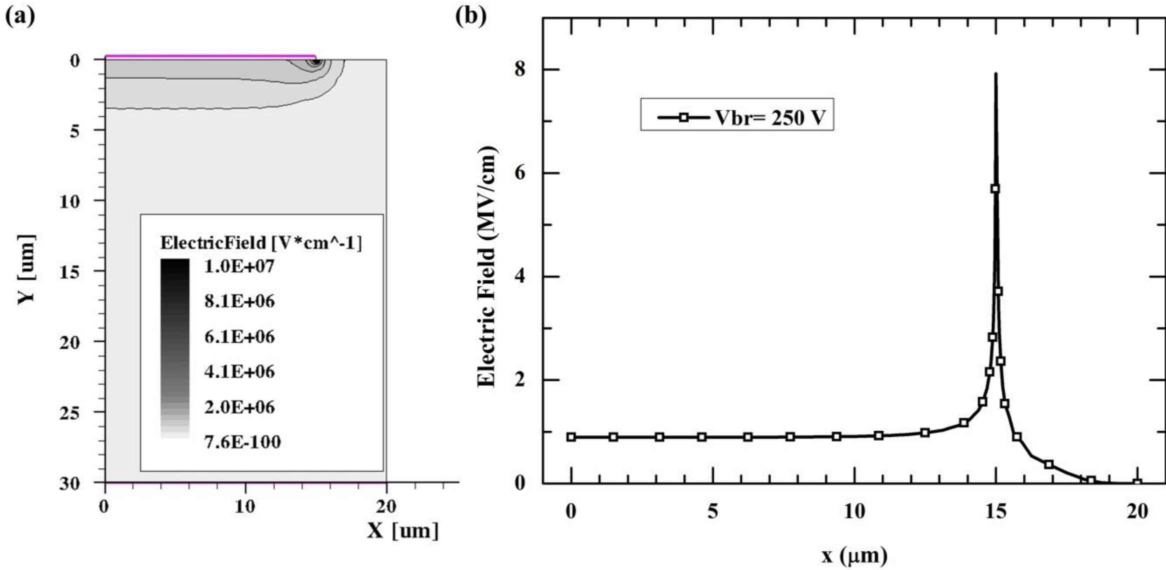

Figure 7-5: Distribution of electric field in the non-terminated diamond SBD at reverse bias of 250 V: (a) In the half of symmetrical device and (b) along the metal-diamond interface.

In comparing the performances of the planar mesa and the field plate termination structure, design and optimizations were firstly conducted. To find the optimum devices' geometry for high breakdown voltage applications, we varied the values of metal plate extension length L_F and the oxide thickness T_{OX} for both termination structures (refers to Figure 7-2 and Figure 7-3) throughout the simulations.

Variations of the simulated breakdown voltage V_{Br} for different L_F and T_{OX} for the field plate terminated diamond SBD are shown in Figure 7-6 (a). While longer L_F can result in higher V_{Br}, this effect starts to saturate for $L_F > 15$ µm. We can also see that small variations in T_{OX} affect the V_{Br} significantly. Experimentally, the significance of T_{OX} can be observed from the reverse bias measurements of SBDs on wafer R100230-03 and R100230-17 (refer to Chapter 5). Maximum V_{Br} of ~1700 V is achieved by SBDs on wafer R100230-03 with $T_{OX} =$ 1.2 µm, as compared to maximum V_{Br} of ~900 V for SBDs on wafer R100230-17 with $T_{OX} = 1.9$ µm.

From Figure 7-6 (a), it can be observed that optimum geometry for field plate terminated SBD (with $L_F = 15$ µm and $T_{OX} = 1$ µm) exhibits V_{Br} of 1480 V (using the incomplete ionization coefficients by S. J. Rashid et al). Figure 7-6 (b) shows

the distribution of current density in the device at breakdown. The breakdown mainly occurs at the small region at the corner of Schottky contact due to high electric field.

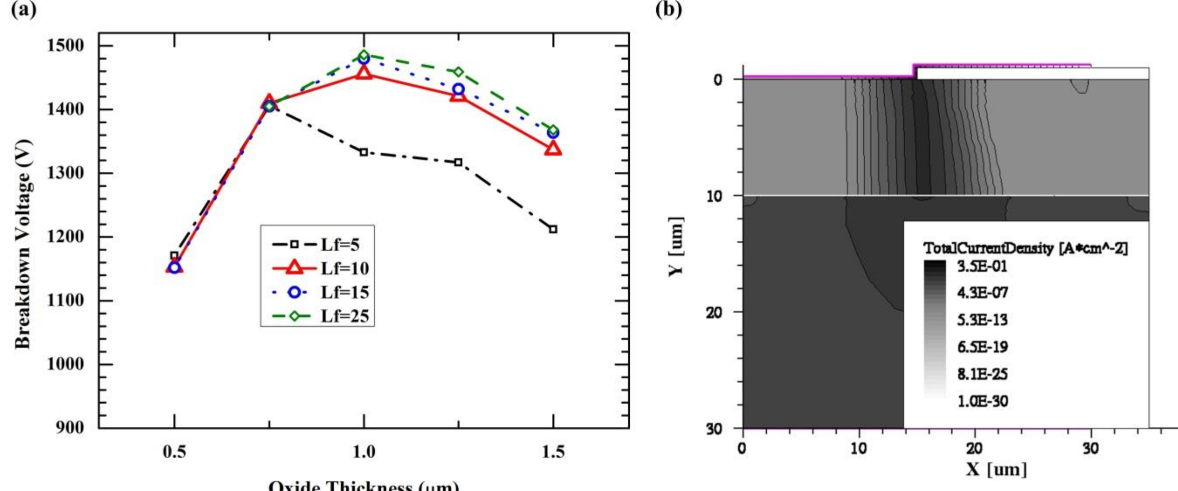

Figure 7-6: (a) Variations of simulated breakdown voltage for different field plate length L_F and oxide thickness T_{OX} for field plate terminated diamond SBD. (b) Distribution of reverse current density in the field plate terminated diamond SBD at 1480 V.

The distributions of electric field at breakdown in this structure are shown in Figure 7-7 (a) and (b). Peak electric field can be observed at 2 points, i. e. E_f = 5.76 MV/cm at the corner of Schottky contact (x= 15 µm, y= 0 µm) and E_f = 9.38 MV/cm in the oxide layer at the end of field plate termination (x= 30 µm, y= -1 µm). As the peak E_f in the oxide layer is lower than the Al_2O_3's breakdown electric field (10 MV/cm) [118, 119], no oxide breakdown occurs in the optimum field plate terminated SBD.

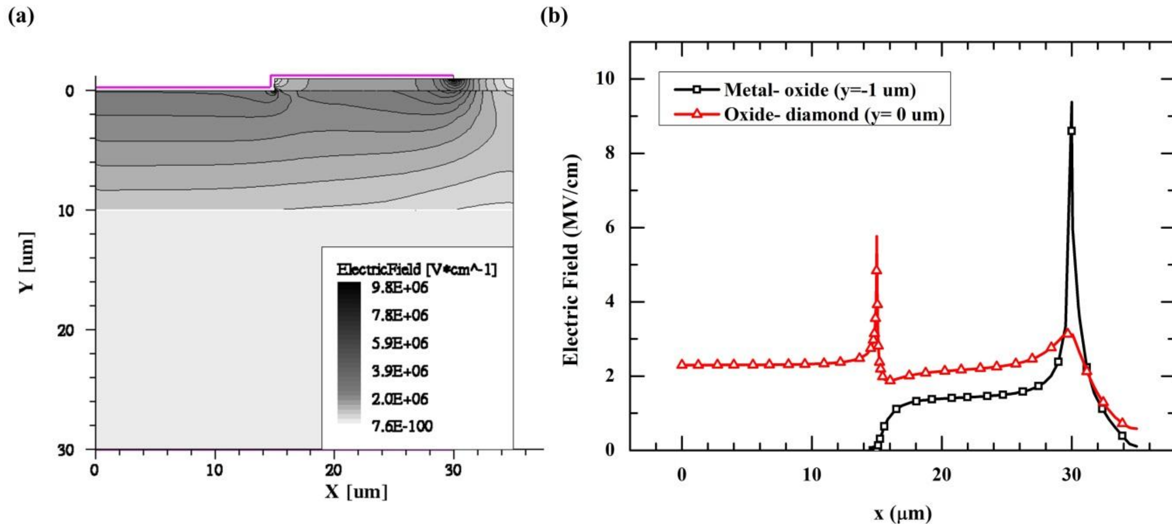

Figure 7-7: Distribution of electric field in the field plate terminated diamond SBD at 1480 V: (a) In the half of symmetrical device and (b) along the line y= 0 μm (oxide- diamond) and y= -1 μm (metal- oxide).

For the planar mesa terminated diamond SBD, variations of the simulated breakdown voltage V_{Br} for different L_F and T_{OX} are shown in Figure 7-8 (a). Increasing L_F and T_{OX} up to certain values can increase the V_{Br} significantly. The optimum geometry for planar mesa terminated SBD can be realized with L_F = 5 μm and T_{OX} = 2 μm. Without considering the oxide breakdown, this structure is able to achieve V_{Br} of 1751 V. From the distribution of current density in the device at breakdown (shown in Figure 7-8 (b)), we can observe that breakdown occurs at large area (bulk diamond) under the Schottky contact.

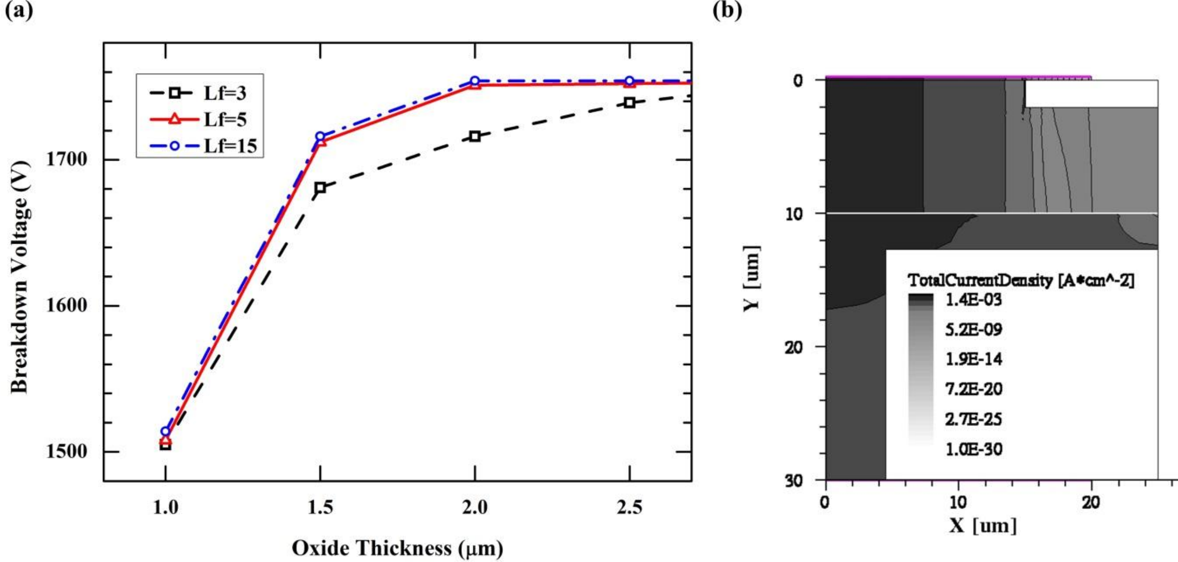

Figure 7-8: (a) Variations of simulated breakdown voltage for different field plate length L_F and oxide thickness T_{OX} for planar mesa terminated diamond SBD. (b) Distribution of reverse current density in the planar mesa terminated diamond SBD at 1751 V.

The electric field distributions in the device at 1751 V are shown in Figure 7-9 (a) and (b). In this structure, the electric field is distributed almost uniformly under the Schottky contact (channel area) and the peak E_f occurs only at 1 point, i. e. E_f = 11.41 MV/cm in the oxide region at the end of metal plate extension (x= 20 μm, y= 0 μm). This prevents the Schottky barrier lowering and the breakdown due to electric field crowding at the Schottky contact. However, peak E_f = 11.41 MV/cm in the oxide is beyond the breakdown electric field of Al_2O_3. By limiting the peak E_f in the oxide to 10 MV/cm to prevent Al_2O_3 breakdown, the optimum planar mesa terminated SBD yields V_{Br} = 1440 V. The distribution of electric field in the device at reverse bias of 1440 V along the line y= 0 μm is shown in Figure 7-9 (b), with the peak E_f = 9.84 MV/cm (at x= 20 μm, y= 0 μm).

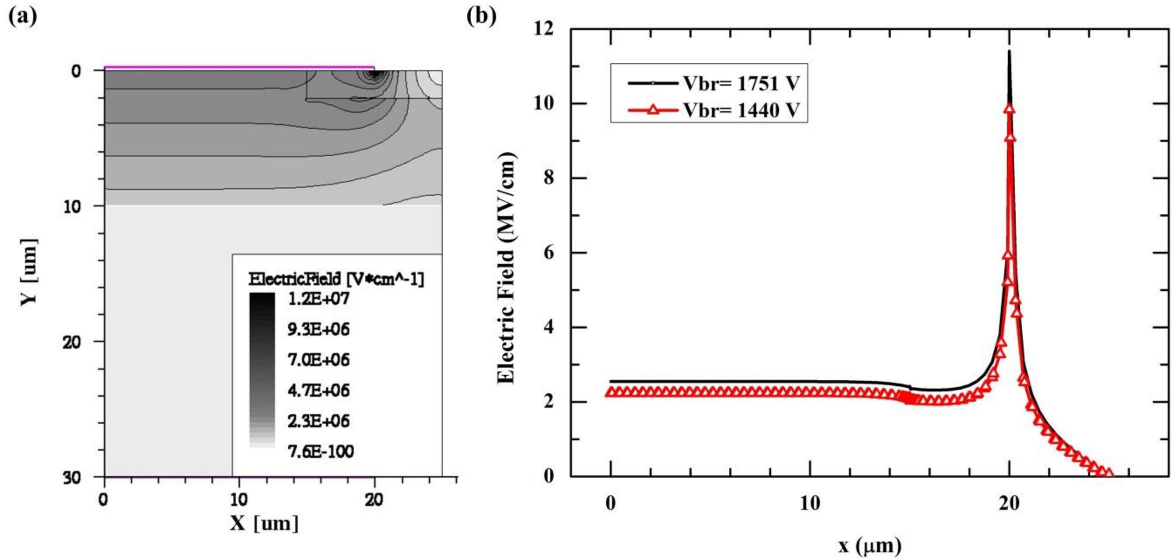

Figure 7-9: Distribution of electric field in the planar mesa terminated SBD: (a) At 1751 V in the half of the symmetrical device. (b) At 1751 V and at 1440 V along the line y= 0 μm.

By comparing the optimum geometry of the field plate termination and the planar mesa termination structure for diamond SBD, it is clear that the later consumes less area due to shorter metal plate extension required. Therefore, for the same total device's area, the planar mesa terminated SBD can be designed with bigger Schottky contact area which increases its current carrying capability.

To compare the forward $I-V$ characteristics of both termination structures, we simulated the SBDs with circular contact occupying the same total device's area (total device's diameter of 230 μm) as shown in Figure 7-10 based on optimum structure design.

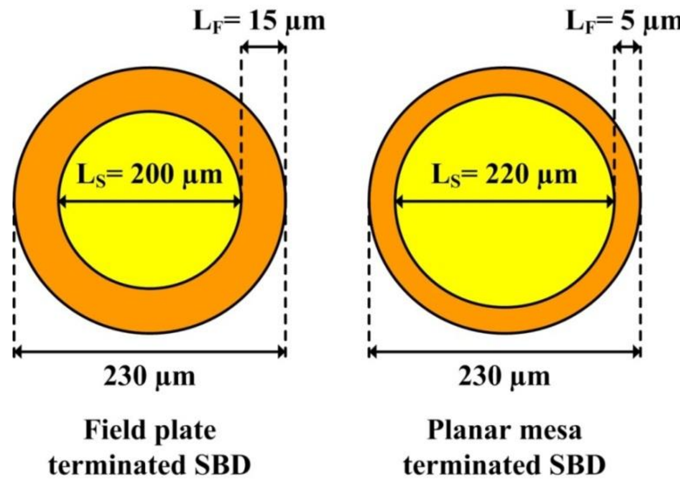

Figure 7-10: Top view schematic diagram of optimum field plate terminated SBD and planar mesa terminated SBD occupying the same total device's area (diameter of 230 μm). L_S and L_F are the diameter of Schottky contact and length of metal plate extension in the corresponding structures.

The Schottky contact area in the planar mesa terminated SBD (L_S = 220 µm, Schottky contact area= 91.49% of total device's area) is 1.21 times bigger than the Schottky contact area in the field plate terminated SBD (L_S = 200 µm, Schottky contact area= 75.61% of total device's area). The applied parasitic resistance on both devices is 8 mΩ.cm^2 [61]. The simulated forward $I-V$ characteristics for both structures are shown in Figure 7-11 (a) and (b). Even though planar mesa terminated SBD has slightly lower forward current density compared to that of field plate terminated SBD, it has higher total forward current (lower on-resistance) due to larger Schottky contact area.

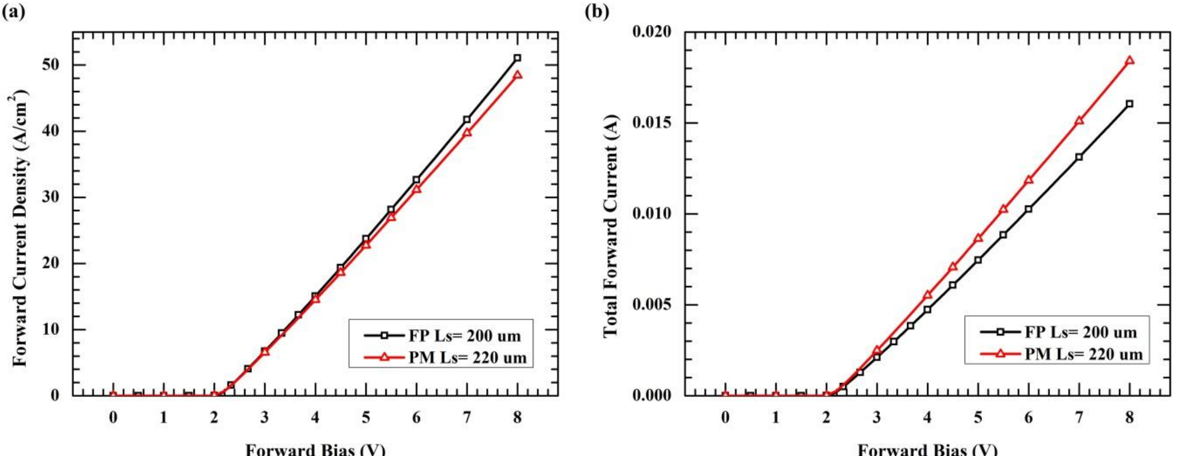

Figure 7-11: Simulated forward $I-V$ characteristics of the field plate terminated (FP) and planar mesa terminated (PM) diamond SBD with the same total device's area (diameter of 230 µm): (a) Comparison of forward current density. (b) Comparison of total forward current.

Table 7-1 summarizes the performances comparisons between the optimum field plate terminated SBD and the optimum planar mesa terminated SBD.

Table 7-1: Performances comparisons between optimum field plate and planar mesa termination structure for diamond Schottky barrier diode.

Termination structure	Optimum geometry		V_{Br} considering Al_2O_3 breakdown (V)	V_{Br} without considering oxide breakdown (V)	Forward $I-V$ for total device's diameter of 230 µm (refer to Figure 7-11)	
	L_F (µm)	T_{OX} (µm)			Current density at 5 V (A/cm^2)	Total current at 5 V (A)
Field plate	15	1	1480	1480	23.73	0.00746
Planar mesa	5	2	1440	1751	22.74	0.00864

With the usage of Al_2O_3 as the oxide layer (considering breakdown in Al_2O_3), the planar mesa terminated SBD yields slightly lower V_{Br} and forward current density compared to the field plate terminated SBD. However, it requires shorter metal plate extension for the termination structure. Therefore, it can accommodate larger Schottky contact for the same total device's area which results in higher total forward current.

From Table 7-1, we can also observe that the reverse bias performances of the planar mesa terminated SBD is limited by the breakdown of Al_2O_3 layer. Unlike field plate terminated SBD, V_{Br} of planar mesa terminated SBD can be increased further to 1751 V if breakdown does not occurs in oxide layer. This can only be realized by replacing Al_2O_3 with suitable high k material that can support sufficient electric field.

Moreover, it is worthy to point out that the impact ionization coefficients used in these simulations (suggested by S. J. Rashid et al.) underestimate the real capability of diamond (breakdown electric field of 10- 20 MV/cm). By applying other coefficients' values such as $\alpha_n = \alpha_p = 5.48\text{x}10^6 exp\left(-8\text{x}10^7 / E_f\right)$ (mentioned in Chapter 3) for a test case, the optimum planar mesa terminated SBD yields simulated V_{Br} of 9190 V. At breakdown, the peak E_f in the Al_2O_3 region at the end of metal plate extension (x= 20 μm, y= 0 μm) reaches high value of 48.15 MV/cm. This value is about 4 times of the maximum E_f in the diamond (~12 MV/cm under Schottky contact) and well beyond the capability of Al_2O_3.

Therefore, to fully realize the potential of diamond power devices, we need to utilize material with higher dielectric constant and sufficient breakdown electric field to prevent the oxide breakdown. Development of such material for diamond SBD can gain insights from research on high k materials to replace SiO_2 in Complementary Metal Oxide Semiconductor (CMOS) technology. In addition, high k materials are also being developed for applications in diamond FETs (Field Effect Transistors). Some of the high k materials of interest for the applications in diamond devices are Ta_2O_5 (k~ 16- 29) [120], $SrTiO_3$ [121], PZT [122-125], Yb_2O_3 (k~ 15) , HfO_2 (k~ 25) , TiO_2 (k~ 80- 95), ZrO_2 (k~ 29), etc. [119, 126].

7.4 Conclusions

In conclusion, we have presented the planar mesa termination structure for high voltage diamond Schottky barrier diode. Analysis, design, and optimization are carried out using simulations in TCAD Sentaurus software. The performances of the planar mesa terminated SBD are compared with those of the field plate terminated SBD. In both termination structures, Al_2O_3 is used as the field oxide. Through many simulations, we found out that the optimum geometry of planar mesa termination structure requires shorter metal plate extension (less area consumption for termination structure) compared to the field plate termination structure. For the same total device's area, the planar mesa terminated SBD can be designed with larger Schottky contact which increases its current carrying capability.

Using Al_2O_3 as the field oxide, the optimum field plate terminated SBD and the optimum planar mesa terminated SBD yield breakdown voltage of 1480 V and 1440 V respectively. In the field plate terminated SBD, breakdown occurs at small area at the corner of Schottky contact due to high peak electric field (without breakdown in Al_2O_3 layer). On the contrary, premature breakdown in the planar mesa terminated SBD at 1440 V is caused by the breakdown of Al_2O_3 layer (at electric field of 10 MV/cm). Although the planar mesa termination structure is able to reduce the electric field crowding at the Schottky contact, the peak electric field inside the oxide is around 4 times of maximum electric field in the diamond. Assuming that oxide breakdown does not occur, the breakdown voltage of the planar mesa terminated SBD can further be increased to 1751 V where breakdown occurs in the bulk diamond (under the Schottky contact).

Therefore, special attentions must be paid on the choice of the field oxide to prevent the oxide breakdown. With the right choice of field oxide material, the planar mesa termination structure can realize high breakdown voltage diamond SBD. Further studies on the development and integration of alternative high k materials suitable for diamond devices are crucial to fully realize the potential of diamond material.

8 CONCLUSIONS AND RECOMMENDATIONS

In this chapter, we present the conclusions of our research and recommendation for future works.

8.1 Conclusions

The goal of this research has been to contribute towards the understanding, development, and uses of diamond SBD for power electronics applications. State of the art of diamond SBD technology and their challenges have been reviewed. The importance of modelling and simulations approach as a low cost and effective method to study, analyse, design, and optimize the diamond devices was highlighted. Throughout this research, finite element physics based TCAD Sentaurus software from Synopsys has been employed to simulate various diamond diodes. Various physics models and parameters suitable for numerical implementation of diamond material have been elaborated and discussed.

The performances of diamond m-i-p+ diode and diamond SBD have been investigated and compared. Numerical simulations of the diodes based on the ideal intimate contact diode model were demonstrated. While good match to the measured forward $I-V$ characteristics can be achieved, the ideal intimate contact diode model is not able to simulate Fermi level pinning at the metal-diamond interface. Thus, the metal work function needs to be readjusted in the simulations to match diodes' turn-on voltages at different temperatures.

Furthermore, the turn-off transient characteristics of the diamond diodes have been studied. Transient simulations in the mixed-mode environment were conducted using double pulse test circuit to match the experiment results. While transient simulations results using ideal switch displayed characteristics of a unipolar diode, the peak reverse current was larger than expected. In order to match the measured transient characteristics of diamond SBD, SPICE sub-circuit model of power MOSFET switch was employed. Good correlation between simulations and experiments results at different temperature indicates the importance of modelling switch and circuit parasitic components accurately.

Throughout this research, several vertical diamond SBDs with different sizes of Molybdenum Schottky contact and field plate termination with high k dielectric Al_2O_3 have been fabricated on different diamond wafers (p- and p+ layer stack). Forward and reverse bias $I-V$ measurements results of the diamond SBDs indicated various deviations from the ideal characteristics, such as variations in the Schottky barrier heights (and turn-on voltages), multiple barriers formations, large leakage current, etc.

To develop more accurate model of the metal-diamond interface, we analysed the non-ideal characteristics of the SBD based on MIS model. This model attributes the non-ideal characteristics to the existence of thin interfacial layer and interface states charges at the Schottky metal-diamond interface. Oxygen surface treatments on the diamond's surface during fabrication process have been reported to induce interfacial layer, surface oxidized layer, and highly disordered surface defect layer. The characterizations and parameters extraction from the $I-V$ and $C-V$ measurements results revealed interface states charges density of around 10^{13} $eV^{-1}.cm^{-2}$.

Moreover, we successfully implemented the MIS model analysis to characterize and simulate another experimental Mo/diamond SBD with characteristics far from ideal (ideality factor of 3.77- 7.68). Combination of the characterization results and extensive simulations to best fit the measured forward and reverse bias $I-V-T$ yielded interfacial layer thickness of 2.5 nm and band gap of 7.3 eV, hole tunnelling mass of $0.5\,m_0$, and interface states charges density of $1.3x10^{13}$- $2.7x10^{13}$ $eV^{-1}.cm^{-2}$. Our simulations study also pointed out the undesirable effects of this unintentional interfacial layer as it increases the SBD's turn-on voltage and presents the risk of premature breakdown due to high electric field in the interfacial layer.

To improve the trade-off between the forward and the reverse bias performances, we proposed the planar mesa structure with high k dielectric Al_2O_3 for the edge termination of diamond SBD. The performances of the planar mesa terminated SBD are evaluated and compared with those of the field plate terminated SBD. Design optimizations for both structures have been carried out using TCAD Sentaurus software to find the optimal geometry for high voltage diamond power SBD.

We found out that the breakdown capability of the field plate terminated SBD is limited by the field plate structure itself (due to the high electric field at the corner of Schottky contact). In contrast, the reverse bias operation of the planar mesa terminated SBD is limited by the breakdown of Al_2O_3. With the right alternative high k materials, the planar mesa terminated SBD can realize higher breakdown voltage with shorter metal plate extension. Consequently, the planar mesa terminated SBD offers higher total forward current for the same device's cross sectional area.

8.2 Recommendations

Diamond technology for power electronics devices is still in the infancy stage and there are many areas to be studied. Based on our research, several recommendations for future works are given below.

- Design of diamond Schottky barrier diode

To realize the full potential of diamond materials for high voltage high power devices, special attention must be paid on the design of the diode structure and the choice of the high k materials for the field oxide in addition to the improvement of the diamond crystal quality. Our numerical simulations studies in Chapter 7 have shown the potential of planar mesa termination structure for diamond SBD. Naturally, the next step will be the fabrication of this structure to study and verify its properties experimentally.

Furthermore, the peak electric field in the field oxide like Al_2O_3 has been shown to reach value of several times of that in the diamond. This limits the reverse bias performance due to the premature breakdown of oxide. Thus, several high k materials such as Ta_2O_5, $SrTiO_3$, and PZT, etc. have been explored for applications in diamond devices.

While many other alternative high k materials are available, selection of suitable high k material is not straightforward as the breakdown electric field is inversely related to the dielectric constant k. Other issues such as the band-offset, interface quality, leakage current, fabrication process, and reliability issues, etc. require further investigations.

At the same time, other approaches to the design of diamond SBD can be explored, such as termination structure with semi-resistive materials at the peripheral to smooth the distribution of electric field in the device.

- Characterizations, modelling, and simulations

Precise modelling and simulation tools plays important roles in the design of diamond power devices, i.e. in the optimization of the trade-off between forward and reverse bias performance and the trade-off between static and switching performance.

More detailed model needs to be developed to take into account varieties of non-ideal factors such as non-uniformity in the doping concentration, traps profile and carrier lifetime, spatial variations in the Schottky barrier height, etc. Other models to describe the metal-diamond interface can be explored, such as MIGS, DIGS, and BP model. As device's interface has significant effect to the device's behaviours, mechanisms of Fermi level pinning at the metal-diamond interface need to be found out. More importantly, the effects of different diamond surface treatments to the nature of metal-diamond interface needs to be investigated to improve the interface quality and fabrication techniques of the Schottky contact for diamond electronic devices. Interface engineering might hold the key to the development of diamond devices.

In order to verify the transient simulations results of diamond m-i-p+ diode, experimental studies on the switching characteristics of diamond m-i-p+ diode need to be carried out. Accurate modelling of the switch and circuit parasitic components should be incorporated in the simulations to match the experiment results quantitatively.

For the estimation of breakdown voltage of diamond devices, accurate measurements of the impact ionization coefficients values in synthetic single crystal diamond at different temperatures are required. As elaborated in Chapter 3, the existing impact ionization coefficients in the literature underestimates the capability of diamond material.

LIST OF PUBLICATIONS

Journals

1. A. Nawawi, K. J. Tseng, Rusli, G. A. J. Amaratunga, H. Umezawa, and S. Shikata, "Characterization of vertical Mo/diamond Schottky barrier diode from non-ideal I–V and C–V measurements based on MIS model," *Diamond and Related Materials,* vol. 35, pp. 1-6, 2013.
2. A. Nawawi, K. J. Tseng, Rusli, G. A. J. Amaratunga, H. Umezawa, and S. Shikata, "Design and Optimization of Planar Mesa Termination for Diamond Schottky Barrier Diodes," *Diamond and Related Materials, ,* vol. 36, pp. 51-57, 2013.
3. A. Nawawi, K. J. Tseng, Rusli, G. A. J. Amaratunga, H. Umezawa, and S. Shikata, "Modeling and simulation of non-ideal characteristics of vertical Mo/diamond Schottky barrier diode based on MIS model," *Transactions of Material Research Society of Japan,* 2013. Manuscript submitted for publication.

Conferences

1. A. Nawawi, T. K. Jet, Rusli, and G. A. J. Amaratunga, "Switching Characteristics of Diamond-based m-i-p plus Diodes in Power Electronic Applications," *2011 IEEE Energy Conversion Congress and Exposition (ECCE),* pp. 2676-2680, 2011.
2. A. Nawawi, K. J. Tseng, Rusli, G. A. J. Amaratunga, H. Umezawa, and S. Shikata, "Device fabrication and modeling of high temperature, high power diamond vertical Schottky barrier diode," in *International Union of Materials Research Societies- International Conference on Electronic Materials 2012 (IUMRS-ICEM 2012)*, Yokohama, Japan, 2012. Presentation.

3. A. Nawawi, K. J. Tseng, Rusli, G. A. J. Amaratunga, H. Umezawa, and S. Shikata, "Modeling and Simulation Study of Fabricated Diamond Pseudo-vertical Schottky Barrier Diode " in *New Diamond and Nanocarbon Conference 2013 (NDNC 2013)*, Singapore, 2013. Poster.
4. A. Nawawi, K. J. Tseng, Rusli, G. A. J. Amaratunga, H. Umezawa, and S. Shikata, " Field plate termination structure with alternative high-k materials for high voltage diamond Schottky barrier diode- simulation study" in *International Conference on Diamond and Carbon Materials 2013 (ICDCM 2013)*, Riva del Garda, Italy, September 2013. Presentation.
5. A. Nawawi, K. J. Tseng, Rusli, G. A. J. Amaratunga, H. Umezawa, and S. Shikata, “Static and Transient Performance Comparisons between Diamond p+/p- Diode and m-i-p+ (Metal-Intrinsic-p+) Diode”, in *Solid State Devices and Materials 2014*, Tsukuba, Japan, September 2014. Submitted.

BIBLIOGRAPHY

[1] M. Willander, M. Friesel, Q. U. Wahab, and B. Straumal, "Silicon carbide and diamond for high temperature device applications," *Journal of Materials Science-Materials in Electronics,* vol. 17, pp. 1-25, Jan 2006.

[2] T. Ericsen, "Future navy application of wide bandgap power semiconductor devices," *Proceedings of the IEEE,* vol. 90, pp. 1077-1082, Jun 2002.

[3] L. M. Tolbert, B. Ozpineci, S. K. Islam, and M. S. Chinthavali, "Wide bandgap semiconductors for utility applications," *Power and Energy Systems, Proceedings,* pp. 317-321, 2003.

[4] B. Ozpineci and L. Tolbert, "Comparison of wide-bandgap semiconductors for power electronics applications," U. S. D. o. Energy, Ed., ed, 2004.

[5] J. Isberg, J. Hammersberg, E. Johansson, T. Wikstrom, D. J. Twitchen, A. J. Whitehead, *et al.*, "High carrier mobility in single-crystal plasma-deposited diamond," *Science,* vol. 297, pp. 1670-1672, Sep 6 2002.

[6] R. J. Trew, J. B. Yan, and P. M. Mock, "The Potential of Diamond and SiC Electronic Devices for Microwave and Millimeter-Wave Power Applications," *Proceedings of the IEEE,* vol. 79, pp. 598-620, May 1991.

[7] B. Zhao, H. Qin, J. Wen, and Y. Yan, "Characteristics, applications and challenges of SiC power devices for future power electronic system," in *Power Electronics and Motion Control Conference (IPEMC), 2012 7th International*, 2012, pp. 23-29.

[8] B. J. Baliga, *Silicon carbide power devices*. Singapore ; Hackensack, NJ: World Scientific, 2005.

[9] B. J. Baliga, "Trends in power semiconductor devices," *IEEE Transactions on Electron Devices,* vol. 43, pp. 1717-1731, Oct 1996.

[10] B. J. Baliga, "The future of power semiconductor device technology," *Proceedings of the IEEE,* vol. 89, pp. 822-832, Jun 2001.

[11] N. Kaminski, "State of the Art and the Future of Wide Band-Gap Devices," *Epe: 2009 13th European Conference on Power Electronics and Applications, Vols 1-9,* pp. 5936-5944, 2009.

[12] P. Friedrichs, "SiC power devices-lessons learned and prospects after 10 years of commercial availability."

[13] J. L. Hudgins, G. S. Simin, E. Santi, and M. A. Khan, "An assessment of wide bandgap semiconductors for power devices," *IEEE Transactions on Power Electronics,* vol. 18, pp. 907-914, May 2003.

[14] S. J. Rashid, "High Voltage Packaging Technology for Wide Bandgap Power Semiconductor Devices," Doctor of Philosophy, University of Cambridge, United Kingdom, 2008.

[15] A. Kumta, "Development of process technology for fabrication of 4H-SiC silicon carbide schottky barrier diodes," Doctor of Philosophy, Nanyang Technological University, Singapore, 2009.

[16] J. Millan, "Wide band-gap power semiconductor devices," *IET Circuits Devices & Systems,* vol. 1, pp. 372-379, Oct 2007.

[17] J. Millan, P. Godignon, and A. Perez-Tomas, "Wide Band Gap Semiconductor Devices for Power Electronics," *Automatika: Journal for*

Control, Measurement, Electronics, Computing & Communications, vol. 53, pp. 107-116, Apr-Jun 2012.

[18] J. C. Zolper, "A review of junction field effect transistors for high-temperature and high-power electronics," *Solid-State Electronics,* vol. 42, pp. 2153-2156, Dec 1998.

[19] A. R. Powell and L. B. Rowland, "SiC materials - Progress, status, and potential roadblocks," *Proceedings of the IEEE,* vol. 90, pp. 942-955, Jun 2002.

[20] M. Pomorski, E. Berdermann, W. de Boer, A. Furgeri, C. Sander, J. Morse*, et al.*, "Charge transport properties of single crystal CVD-diamond particle detectors," *Diamond and Related Materials,* vol. 16, pp. 1066-1069, Apr-Jul 2007.

[21] R. S. Balmer, J. R. Brandon, S. L. Clewes, H. K. Dhillon, J. M. Dodson, I. Friel*, et al.*, "Chemical vapour deposition synthetic diamond: materials, technology and applications," *Journal of Physics-Condensed Matter,* vol. 21, Sep 9 2009.

[22] R. S. Sussmann, *CVD diamond for electronic devices and sensors*. Chichester, U.K.: J. Wiley, 2009.

[23] J. W. Palmour, "Energy efficient wide bandgap devices," *IEEE Compound Semiconductor Integrated Circuit Symposium - 2006 IEEE Csic Symposium, Technical Digest 2006,* pp. 4-7, 2006.

[24] C. M. Breeding and J. E. Shigley, "The" Type" Classification System of Diamonds and Its Importance in Gemology," *Gems & Gemology,* vol. 45, pp. 96-111, 2009.

[25] G. Janssen, W. Vollenberg, L. J. Giling, W. J. P. van Enckevort, J. J. D. Schaminée, and M. Seal, "Rapid growth of single-crystal diamond on diamond substrates," *Surface and Coatings Technology,* vol. 47, pp. 113-126, 1991.

[26] P. N. Volpe, P. Muret, J. Pernot, F. Omnes, T. Teraji, Y. Koide*, et al.*, "Extreme dielectric strength in boron doped homoepitaxial diamond," *Applied Physics Letters,* vol. 97, Nov 29 2010.

[27] P. N. Volpe, P. Muret, J. Pernot, F. Omnes, T. Teraji, F. Jomard*, et al.*, "High breakdown voltage Schottky diodes synthesized on p-type CVD diamond layer," *Physica Status Solidi a-Applications and Materials Science,* vol. 207, pp. 2088-2092, Sep 2010.

[28] Y. Gurbuz, W. P. Kang, J. L. Davidson, D. V. Kerns, and Q. Zhou, "PECVD diamond-based high performance power diodes," *IEEE Transactions on Power Electronics,* vol. 20, pp. 1-10, Jan 2005.

[29] C. R. Miskys, J. A. Garrido, C. E. Nebel, M. Hermann, O. Ambacher, M. Eickhoff*, et al.*, "AlN/diamond heterojunction diodes," *Applied Physics Letters,* vol. 82, pp. 290-292, Jan 13 2003.

[30] T. Zimmermann, M. Kubovic, A. Denisenko, K. Janischowsky, O. A. Williams, D. M. Gruen*, et al.*, "Ultra-nano-crystalline/single crystal diamond heterostructure diode," *Diamond and Related Materials,* vol. 14, pp. 416-420, Mar-Jul 2005.

[31] E. Kohn, A. Denisenko, M. Kubovic, T. Zimmermann, O. A. Williams, and D. M. Gruen, "A new diamond based heterostructure diode," *Semiconductor Science and Technology,* vol. 21, pp. L32-L35, Apr 2006.

[32] A. M. Rodrigues, "Two levels of the Schottky barrier in CVD diamond/silicon heterojunctions at low temperature," *Diamond and Related Materials,* vol. 16, pp. 1029-1032, Apr-Jul 2007.

[33] W. Cheng-Xin, G. Chun-Xiao, Z. Tie-Chen, L. Hong-Wu, L. Xun, H. Yong-Hao*, et al.*, "Preparation of pn Junction Diode by B-Doped Diamond Film Grown on Si-Doped c-BN," *Chinese physics letters,* vol. 19, p. 1513, 2002.

[34] C. X. Wang, T. C. Zhang, H. W. Liu, C. X. Gao, and G. T. Zou, "Heterojunction diodes made from B-doped diamond grown heteroepitaxially on Si-doped c-BN," *Journal of Physics-Condensed Matter,* vol. 14, pp. 10989-10993, Nov 11 2002.

[35] J. Achard, F. Silva, R. Issaoui, O. Brinza, A. Tallaire, H. Schneider*, et al.*, "Thick boron doped diamond single crystals for high power electronics," *Diamond and Related Materials,* vol. 20, pp. 145-152, Feb 2011.

[36] R. Kumaresan, H. Umezawa, N. Tatsumi, K. Ikeda, and S. Shikata, "Device processing, fabrication and analysis of diamond pseudo-vertical Schottky barrier diodes with low leak current and high blocking voltage," *Diamond and Related Materials,* vol. 18, pp. 299-302, Feb-Mar 2009.

[37] H. Umezawa, N. Tokuda, M. Ogura, S.-G. Ri, and S.-i. Shikata, "Characterization of leakage current on diamond Schottky barrier diodes using thermionic-field emission modeling," *Diamond and Related Materials,* vol. 15, pp. 1949-1953, 2006.

[38] R. Kumaresan, H. Umezawa, and S. Shikata, "Parasitic resistance analysis of pseudovertical structure diamond Schottky barrier diode," *Physica Status Solidi a-Applications and Materials Science,* vol. 207, pp. 1997-2001, Aug 2010.

[39] H. Umezawa, M. Nagase, Y. Kato, and S. Shikata, "High temperature application of diamond power device," *Diamond and Related Materials,* vol. 24, pp. 201-205, Apr 2012.

[40] H. Umezawa, K. Ikeda, R. Kumaresan, N. Tatsumi, and S. Shikata, "Increase in Reverse Operation Limit by Barrier Height Control of Diamond Schottky Barrier Diode," *IEEE Electron Device Letters,* vol. 30, pp. 960-962, Sep 2009.

[41] M. Brezeanu, T. Butler, N. Rupesinghe, S. J. Rashid, M. Avram, G. A. J. Amaratunga*, et al.*, "Single crystal diamond M-i-P diodes for power electronics," *IET Circuits Devices & Systems,* vol. 1, pp. 380-386, Oct 2007.

[42] M. Suzuki, H. Yoshida, N. Sakuma, T. Ono, T. Sakai, and S. Koizumi, "Electrical characterization of phosphorus-doped n-type homoepitaxial diamond layers by Schottky barrier diodes," *Applied Physics Letters,* vol. 84, pp. 2349-2351, 2004.

[43] M. Suzuki, S. Koizumi, M. Katagiri, T. Ono, N. Sakuma, H. Yoshida*, et al.*, "Electrical characteristics of n-type diamond Schottky diodes and metal/diamond interfaces," *Physica Status Solidi a-Applications and Materials Science,* vol. 203, pp. 3128-3135, Sep 2006.

[44] T. Makino, S. Tanimoto, H. Kato, N. Tokuda, M. Ogura, D. Takeuchi*, et al.*, "Diamond Schottky p–n diode with high forward current density," *physica status solidi (a),* vol. 206, pp. 2086-2090, 2009.

[45] M. Kubovic, H. El-Haj, J. E. Butler, and E. Kohn, "Diamond merged diode," *Diamond and Related Materials,* vol. 16, pp. 1033-1037, Apr-Jul 2007.

[46] K. Oyama, S. G. Ri, H. Kato, M. Ogura, T. Makino, D. Takeuchi*, et al.*, "High performance of diamond p^+-i-n^+ junction diode fabricated using

heavily doped p^+ and n^+ layers," *Applied Physics Letters,* vol. 94, pp. 152109-152109, 2009.

[47] S Kono and S. Koizumi, "Images and Energy Distributions of Electrons Emitted from a Diamond pn-Junction Diode," *e-Journal of Surface Science and Nanotechnology,* vol. 7, pp. 660-664, 2009.

[48] A. Tajani, C. Tavares, M. Wade, C. Baron, E. Gheeraert, E. Bustarret*, et al.*, "Homoepitaxial {111}-oriented diamond pn junctions grown on B-doped Ib synthetic diamond," *physica status solidi (a),* vol. 201, pp. 2462-2466, 2004.

[49] J. E. Butler, M. W. Geis, K. E. Krohn, J. Lawless, S. Deneault, T. M. Lyszczarz*, et al.*, "Exceptionally high voltage Schottky diamond diodes and low boron doping," *Semiconductor Science and Technology,* vol. 18, pp. S67-S71, Mar 2003.

[50] A. Vescan, I. Daumiller, P. Gluche, W. Ebert, and E. Kohn, "1000^0C operation of diamond Schottky diode," in *Device Research Conference Digest, 1997. 5th*, 1997, pp. 40-41.

[51] A. Vescan, I. Daumiller, P. Gluche, W. Ebert, and E. Kohn, "Very high temperature operation of diamond Schottky diode," *IEEE Electron Device Letters,* vol. 18, pp. 556-558, Nov 1997.

[52] A. Nawawi, T. K. Jet, Rusli, and G. A. J. Amaratunga, "Switching Characteristics of Diamond-based m-i-p plus Diodes in Power Electronic Applications," *2011 IEEE Energy Conversion Congress and Exposition (ECCE),* pp. 2676-2680, 2011.

[53] T. Funaki, K. Kodama, H. Umezawa, and S. Shikata, "Characterization of fast switching capability for Diamond Schottky barrier diode," *Silicon Carbide and Related Materials 2010,* vol. 679-680, pp. 820-823, 2011.

[54] T. Funaki, M. Hirano, H. Umezawa, and S. Shikata, "High temperature switching operation of a power diamond Schottky barrier diode," *IEICE Electronics Express,* vol. 9, pp. 1835-1841, 2012.

[55] K. Ikeda, H. Umezawa, K. Ramanujam, and S. Shikata, "Thermally Stable Schottky Barrier Diode by Ru/Diamond," *Applied Physics Express,* vol. 2, Jan 2009.

[56] H. Umezawa, K. Ikeda, N. Tatsumi, K. Ramanujam, and S. Shikata, "Device scaling of pseudo-vertical diamond power Schottky barrier diodes," *Diamond and Related Materials,* vol. 18, pp. 1196-1199, Sep 2009.

[57] H. Umezawa, T. Saito, N. Tokuda, M. Ogura, S. G. Ri, H. Yoshikawa*, et al.*, "Leakage current analysis of diamond Schottky barrier diode," *Applied Physics Letters,* vol. 90, Feb 12 2007.

[58] A. Vescan, W. Ebert, T. Borst, and E. Kohn, "I/V Characteristics of Epitaxial Schottky Au Barrier Diode on P(+) Diamond Substrate," *Diamond and Related Materials,* vol. 4, pp. 661-665, May 1 1995.

[59] S. J. Rashid, F. Udrea, D. J. Twitchen, R. S. Balmer, and G. A. J. Amaratunga, "High Conductivity d-Doped Single Crystal Diamond Schottky m-i-p^+ Diodes," in *Power Semiconductor Devices and IC's, 2008. ISPSD '08. 20th International Symposium on*, 2008, pp. 249-252.

[60] H. Umezawa, Y. Mokuno, H. Yamada, A. Chayahara, and S. Shikata, "Characterization of Schottky barrier diodes on a 0.5-inch single-crystalline CVD diamond wafer," *Diamond and Related Materials,* vol. 19, pp. 208-212, Feb-Mar 2010.

[61] R. Kumaresan, H. Umezawa, and S. Shikata, "Vertical structure Schottky barrier diode fabrication using insulating diamond substrate," *Diamond and Related Materials,* vol. 19, pp. 1324-1329, Oct 2010.

[62] A. Aleksov, M. Kubovic, N. Kaeb, U. Spitzberg, A. Bergmaier, G. Dollinger*, et al.*, "Diamond field effect transistors - concepts and challenges," *Diamond and Related Materials,* vol. 12, pp. 391-398, Mar-Jul 2003.

[63] M. Brezeanu, M. Avram, S. J. Rashid, G. A. J. Amaratunga, T. Butler, N. L. Rupesinghe*, et al.*, "Termination structures for diamond Schottky barrier diodes," *Proceedings of the 18th International Symposium on Power Semiconductor Devices & Ics,* pp. 73-76, 2006.

[64] S. J. Rashid, A. Tajani, D. J. Twitchen, L. Coulbeck, F. Udrea, T. Butler*, et al.*, "Numerical Parameterization of Chemical-Vapor-Deposited (CVD) Single-Crystal Diamond for Device Simulation and Analysis," *IEEE Transactions on Electron Devices,* vol. 55, pp. 2744-2756, Oct 2008.

[65] S. Kone, H. Ding, H. Schneider, K. Isoird, and G. Civrac, "High performances CVD diamond Schottky barrier diode - Simulation and carrying out," *Epe: 2009 13th European Conference on Power Electronics and Applications, Vols 1-9,* pp. 5137-5144, 2009.

[66] K. Ikeda, H. Umezawa, and S. Shikata, "Edge termination techniques for p-type diamond Schottky barrier diodes," *Diamond and Related Materials,* vol. 17, pp. 809-812, Apr-May 2008.

[67] F. Thion, K. Isoird, D. Planson, M. L. Locatelli, and H. Ding, "Simulation and design of junction termination structures for diamond Schottky diodes," *Diamond and Related Materials,* vol. 20, pp. 729-732, May-Jun 2011.

[68] "Sentaurus Device User Guide D-2010.03," Synopsys2010.

[69] S. M. Sze, *Physics of semiconductor devices*, 2nd ed. New York: Wiley, 1981.

[70] C. Nebel and M. Stutzmann, "Transport properties of diamond: carrier mobility and resistivity," *EMIS Datareviews Series,* vol. 26, pp. 40-52, 2002.

[71] M. Werner, R. Job, A. Zaitzev, W. R. Fahrner, W. Seifert, C. Johnston*, et al.*, "The relationship between resistivity and boron doping concentration of single and polycrystalline diamond," *Physica Status Solidi a-Applied Research,* vol. 154, pp. 385-393, Mar 1996.

[72] F. Fontaine, "Calculation of the hole concentration in boron-doped diamond," *Journal of Applied Physics,* vol. 85, pp. 1409-1422, Feb 1 1999.

[73] J. Isberg, A. Lindblom, A. Tajani, and D. Twitchen, "Temperature dependence of hole drift mobility in high-purity single-crystal CVD diamond," *Physica Status Solidi a-Applications and Materials Science,* vol. 202, pp. 2194-2198, Sep 2005.

[74] T. H. Borst and O. Weis, "Electrical Characterization of Homoepitaxial Diamond Films Doped with B, P, Li and Na during Crystal-Growth," *Diamond and Related Materials,* vol. 4, pp. 948-953, May 15 1995.

[75] K. Somogyi, "Classical approximations for ionised impurity scattering applied to diamond monocrystals," *Diamond and Related Materials,* vol. 11, pp. 686-691, Mar-Jun 2002.

[76] T. Watanabe, T. Teraji, T. Ito, Y. Kamakura, and K. Taniguchi, "Monte Carlo simulations of electron transport properties of diamond in high electric

fields using full band structure," *Journal of Applied Physics,* vol. 95, pp. 4866-4874, May 1 2004.

[77] M. Brezeanu, "Daimond Schottky Barrier Diodes," Doctor of Philosophy, Department of Engineering, University of Cambridge, United Kingdom, 2008.

[78] J. Isberg, M. Gabrysch, A. Tajani, and D. Twitchen, "High-Field Electrical Transport in Single Crystal CVD Diamond Diodes," *Advances in Science and Technology,* vol. 48, pp. 73-76, 2006.

[79] "Inspect User Guide D-2010.03," Synopsys2010.

[80] H. Umezawa and S. Shikata, "Diamond High-Temperature Power Devices," *2009 21st International Symposium on Power Semiconductor Devices & Ics,* pp. 259-262, 2009.

[81] C. A. Klein and R. Desalvo, "Thresholds for Dielectric-Breakdown in Laser-Irradiated Diamond," *Applied Physics Letters,* vol. 63, pp. 1895-1897, Oct 4 1993.

[82] P. Liu, R. Yen, and N. Bloembergen, "Dielectric-Breakdown Threshold, 2-Photon Absorption, and Other Optical Damage Mechanisms in Diamond," *IEEE Journal of Quantum Electronics,* vol. 14, pp. 574-576, 1978.

[83] C. Raynaud, D. Tournier, H. Morel, and D. Planson, "Comparison of high voltage and high temperature performances of wide bandgap semiconductors for vertical power devices," *Diamond and Related Materials,* vol. 19, pp. 1-6, 2010.

[84] S. J. Rashid, L. Coulbeck, A. Tajani, M. Brezeanu, A. Garraway, T. Butler*, et al.*, "Numerical and experimental analysis of single crystal diamond Schottky barrier diodes," *Proceedings of the 17th International Symposium on Power Semiconductor Devices & Ics,* pp. 315-318, 2005.

[85] K. Kodama, T. Funak, H. Umezawa, and S. Shikata, "Switching characteristics of a diamond Schottky barrier diode," *IEICE Electronics Express,* vol. 7, pp. 1246-1251, Sep 10 2010.

[86] M. Hasanuzzaman, S. K. Islam, L. M. Tolbert, and B. Ozpineci, "Design, modeling, testing, and spice parameter extraction of DIMOS transistor in 4H-silicon carbide," *International journal of high speed electronics and systems,* vol. 16, pp. 733-746, 2006.

[87] M. Bellini and J. Vobecky, "TCAD simulations of irradiated power diodes over a wide temperature range," in *Simulation of Semiconductor Processes and Devices (SISPAD), 2011 International Conference on*, 2011, pp. 183-186.

[88] F. Cappelluti, F. Bonani, M. Furno, G. Ghione, R. Carta, L. Bellemo*, et al.*, "Physics-based mixed-mode reverse recovery modeling and optimization of SiPIN and MPS fast recovery diodes," *Microelectronics Journal,* vol. 37, pp. 190-196, Mar 2006.

[89] E. H. Rhoderick and R. H. Williams, *Metal-semiconductor contacts*, 2nd ed. Oxford, England: Clarendon Press, 1988.

[90] P. Gonon, A. Deneuville, E. Gheeraert, F. Fontaine, and F. Lenormand, "Metal/Insulator/Semiconductor Tunnel-Diodes Formed by the Oxidation of Polycrystalline Diamond Films," *Journal of Applied Physics,* vol. 76, pp. 3929-3931, Sep 15 1994.

[91] C. Pietzka, A. Denisenko, A. Romanyuk, P. J. Schafer, L. A. Kibler, J. Scharpf*, et al.*, "Electronic surface barrier properties of boron-doped

diamond oxidized by plasma treatment," *Diamond and Related Materials,* vol. 19, pp. 213-216, Feb-Mar 2010.

[92] J. Scharpf, A. Denisenko, C. Pietzka, and E. Kohn, "Effect of surface defects by RF oxygen plasma on the electrical properties of thin boron-doped diamond layers in electrolyte," *Diamond and Related Materials,* vol. 20, pp. 1250-1254, Aug 2011.

[93] H. Hasegawa and M. Akazawa, "Interface models and processing technologies for surface passivation and interface control in III–V semiconductor nanoelectronics," *Applied Surface Science,* vol. 254, pp. 8005-8015, 2008.

[94] K. Sarpatwari, "Toward understanding the electrical properties of metal semiconductor Schottky contacts: The effects of barrier inhomogeneities and geometry in bulk and nanoscale structures," Doctor of Philosophy, Engineering Science and Mechanics, The Pennsylvania State University, 2009.

[95] S. Majdi, M. Gabrysch, R. Balmer, D. Twitchen, and J. Isberg, "Characterization by Internal Photoemission Spectroscopy of Single-Crystal CVD Diamond Schottky Barrier Diodes," *Journal of Electronic Materials,* vol. 39, pp. 1203-1208, Aug 2010.

[96] M. Wade, P. Muret, F. Omnes, and A. Deneuville, "Technology and electrical properties of ohmic contacts and Schottky diodes on homoepitaxial layers grown on (100) diamond surfaces," *Diamond and Related Materials,* vol. 15, pp. 614-617, Apr-Aug 2006.

[97] J. Alvarez, F. Houze, J. P. Kleider, M. Y. Liao, and Y. Koide, "Electrical characterization of Schottky diodes based on boron doped homoepitaxial diamond films by conducting probe atomic force microscopy," *Superlattices and Microstructures,* vol. 40, pp. 343-349, Oct-Dec 2006.

[98] S. J. Fonash, "A Reevaluation of the Meaning of Capacitance Plots for Schottky-Barrier-Type Diodes," *Journal of Applied Physics,* vol. 54, pp. 1966-1975, 1983.

[99] P. Chattopadhyay and A. N. Daw, "On the Current Transport Mechanism in a Metal-Insulator Semiconductor (Mis) Diode," *Solid-State Electronics,* vol. 29, pp. 555-560, May 1986.

[100] A. Turut, N. Yalcin, and M. Saglam, "Parameter Extraction from Nonideal C-V Characteristics of a Schottky Diode with and without Interfacial Layer," *Solid-State Electronics,* vol. 35, pp. 835-841, Jun 1992.

[101] S. Chattopadhyay, L. K. Bera, S. K. Ray, P. K. Bose, and C. K. Maiti, "Extraction of interface state density of Pt/p-strained-Si Schottky diode," *Thin Solid Films,* vol. 335, pp. 142-145, Dec 14 1998.

[102] A. Turut, M. Saglam, H. Efeoglu, N. Yalcin, M. Yildirim, and B. Abay, "Interpreting the Nonideal Reverse Bias C-V Characteristics and Importance of the Dependence of Schottky-Barrier Height on Applied Voltage," *Physica B,* vol. 205, pp. 41-50, Jan 1995.

[103] A. Turut and M. Saglam, "Determination of the Density of Si-Metal Interface States and Excess Capacitance Caused by Them," *Physica B,* vol. 179, pp. 285-294, Aug 1992.

[104] H. C. Card and Rhoderic.Eh, "Studies of Tunnel Mos Diodes .1. Interface Effects in Silicon Schottky Diodes," *Journal of Physics D-Applied Physics,* vol. 4, pp. 1589-&, 1971.

[105] S. Altindal, S. Karadeniz, N. Tugluoglu, and A. Tataroglu, "The role of interface states and series resistance on the I-V and C-V characteristics in Al/SnO2/p-Si Schottky diodes," *Solid-State Electronics,* vol. 47, pp. 1847-1854, Oct 2003.

[106] S. Zeyrek, S. Altindal, H. Yuzer, and M. M. Bulbul, "Current transport mechanism in Al/Si3N4/p-Si (MIS) Schottky barrier diodes at low temperatures," *Applied Surface Science,* vol. 252, pp. 2999-3010, Feb 15 2006.

[107] S. K. Cheung and N. W. Cheung, "Extraction of Schottky Diode Parameters from Forward Current-Voltage Characteristics," *Applied Physics Letters,* vol. 49, pp. 85-87, Jul 14 1986.

[108] E. Vincent, G. Ghibaudo, G. Morin, and C. Papadas, "On the oxide thickness extraction in deep-submicron technologies," *1997 IEEE International Conference on Microelectronic Test Structures - Proceedings,* pp. 105-110, 1997.

[109] W. Monch, "Barrier heights of real Schottky contacts explained by metal-induced gap states and lateral inhomogeneities," *Journal of Vacuum Science & Technology B,* vol. 17, pp. 1867-1876, Jul-Aug 1999.

[110] S. J. Rashid, A. Tajani, L. Coulbeck, M. Brezeanu, A. Garraway, T. Butler, *et al.*, "Modelling of single-crystal diamond Schottky diodes for high-voltage applications," *Diamond and Related Materials,* vol. 15, pp. 317-323, Feb-Mar 2006.

[111] A. Nawawi, K. J. Tseng, Rusli, G. A. J. Amaratunga, H. Umezawa, and S. Shikata, "Characterization of vertical Mo/diamond Schottky barrier diode from non-ideal I–V and C–V measurements based on MIS model," *Diamond and Related Materials,* vol. 35, pp. 1-6, 2013.

[112] Y. C. Yeo, T. J. King, and C. M. Hu, "Metal-dielectric band alignment and its implications for metal gate complementary metal-oxide-semiconductor technology," *Journal of Applied Physics,* vol. 92, pp. 7266-7271, Dec 15 2002.

[113] J. Robertson, "Band offsets of wide-band-gap oxides and implications for future electronic devices," *Journal of Vacuum Science & Technology B,* vol. 18, pp. 1785-1791, May-Jun 2000.

[114] A. Hermle, G. Letay, S. P. Philipps, and A. W. Bett, "Numerical simulation of tunnel diodes for multi-junction solar cells," *Progress in Photovoltaics,* vol. 16, pp. 409-418, Aug 2008.

[115] K. Ikeda, H. Umezawa, N. Tatsumi, K. Ramanujam, and S. Shikata, "Fabrication of a field plate structure for diamond Schottky barrier diodes," *Diamond and Related Materials,* vol. 18, pp. 292-295, Feb-Mar 2009.

[116] M. Brezeanu, T. Butler, N. L. Rupesinghe, G. A. J. Amaratunga, S. J. Rashid, F. Udrea*, et al.*, "Ramp oxide termination structure using high-k dielectrics for high voltage diamond Schottky diodes," *Diamond and Related Materials,* vol. 16, pp. 1020-1024, Apr-Jul 2007.

[117] N. G. Anantha and K. G. Ashar, "Planar Mesa Schottky Barrier Diode," *Ibm Journal of Research and Development,* vol. 15, pp. 442-445, 1971.

[118] H. C. Lin, P. D. Ye, and G. D. Wilk, "Leakage current and breakdown electric-field studies on ultrathin atomic-layer-deposited Al2O3 on GaAs," *Applied Physics Letters,* vol. 87, Oct 31 2005.

[119] J. W. McPherson, J. Kim, A. Shanware, H. Mogul, and J. Rodriguez, "Trends in the ultimate breakdown strength of high dielectric-constant

materials," *IEEE Transactions on Electron Devices,* vol. 50, pp. 1771-1778, Aug 2003.
[120] S. H. Cheng, L. W. Sang, M. Y. Liao, J. W. Liu, M. Imura, H. D. Li, *et al.*, "Integration of high-dielectric constant Ta2O5 oxides on diamond for power devices," *Applied Physics Letters,* vol. 101, Dec 3 2012.
[121] G. C. Chen, M. Y. Liao, M. Imura, K. Nakajima, Y. Sugimoto, and Y. Koide, "Fabrication and electrical properties of SrTiO3/diamond junctions," *Diamond and Related Materials,* vol. 19, pp. 319-323, Apr 2010.
[122] M. Y. Liao, K. Nakajima, M. Imura, and Y. Koide, "Improved ferroelectric properties of Pb(Zr-0.52,Ti-0.48)O-3 thin film on single crystal diamond using CaF2 layer," *Applied Physics Letters,* vol. 96, Jan 4 2010.
[123] M. Liao, M. Imura, X. Fang, K. Nakajima, G. Chen, and Y. Koide, "Integration of ($PbZr_{0.52}Ti_{0.48}O_3$) on single crystal diamond as metal-ferroelectric-insulator-semiconductor capacitor," *Applied Physics Letters,* vol. 94, pp. 242901-3, 2009.
[124] M. Chandran, B. Tiwari, C. R. Kumaran, S. K. Samji, S. S. Bhattacharya, and M. S. R. Rao, "Integration of perovskite PZT thin films on diamond substrate without buffer layer," *Journal of Physics D-Applied Physics,* vol. 45, May 23 2012.
[125] M. Liao, Y. Gotoh, H. Tsuji, K. Nakajima, M. Imura, and Y. Koide, "Piezoelectric $Pb(Zr_{0.52}Ti_{0.48})O_3$ thin films on single crystal diamond: Structural, electrical, dielectric, and field-effect-transistor properties," *Journal of Applied Physics,* vol. 107, pp. 024101-6, 2010.
[126] J. Robertson, "High dielectric constant gate oxides for metal oxide Si transistors," *Reports on Progress in Physics,* vol. 69, pp. 327-396, Feb 2006.
[127] (30 June). *TCAD Central*. Available: http://www.tcadcentral.com/index.php/Software
[128] S. Li and S. Li, *3D TCAD Simulation for Semiconductor Processes, Devices and Optoelectronics*: Springer, 2012.
[129] (30 June). *Technology CAD*. Available: http://en.wikipedia.org/wiki/Technology_CAD
[130] R. Minixhofer, "Integrating Technology Simulation into the Semiconductor Manufacturing Environment," Doctor of Philosophy, Vienna University of Technology, Austria, 2006.
[131] "Sentaurus Structure Editor User Guide D-2010.03," Synopsys2010.

APPENDICES

APPENDIX A: TCAD SENTAURUS SIMULATION SOFTWARE

Technology computer aided design (TCAD) is simulation software that computes the behaviour of semiconductor devices based on fundamental semiconductor physics models such as current continuity and Poisson equations by using finite element approach (triangular meshes with box discretization method is implemented).

TCAD software package normally includes simulation tools for process simulator (e.g. Sentaurus Process, TSUPREME4, and ATHENA), device simulator (Sentaurus Device, MEDICI, ATLAS, and DESSIS), Graphical User Interface (GUI), and the plotting tools [128]. Process simulator models and simulates the fabrication process of semiconductor devices. The results can then be inputted into device simulator to simulate the characteristics (electrical, thermal, optical, and even mechanical properties) of the devices. While several TCAD providers are available in the market such as Crosslight, Cogenda, Global TCAD Solutions, GSS, the main competitors are Synopsys (owns 80% of the market share) and Silvaco [130].

Throughout our study, all semiconductor simulations had been carried out using general purpose TCAD Sentaurus simulator from Synopsys. While this software does not particularly take diamond devices into considerations, we can incorporate various materials (and their properties) and physics models into the simulations. Furthermore, simulations of other wide band gap devices such as Silicon Carbide power devices had been successfully demonstrated.

Besides the Sentaurus Process simulator, TCAD Sentaurus provides another alternative simulator in the device creation, i.e. Sentaurus Structure Editor (SSE) [131]. SSE lets user create complex device structure in 2-dimensional (2D) or 3-dimensional (3D) without difficulties in going through the process simulation. Device geometry, doping and refinement, and meshing specifications are declared in the SSE command file (sde_dvs.cmd). As the fabrication process of diamond

devices has not yet been established well, we utilized SSE in creating the diamond devices for our simulations work.

Further on, simulations of the electrical characteristics of the diamond devices were performed by using Sentaurus Device (SDevice) simulator. It is a multi-dimensional simulator that is capable of devices' electro-thermal simulations, including static and transient, mixed-mode environment, and circuit (several physical devices combined in a circuit) simulations as indicated in Figure A-1 [68].

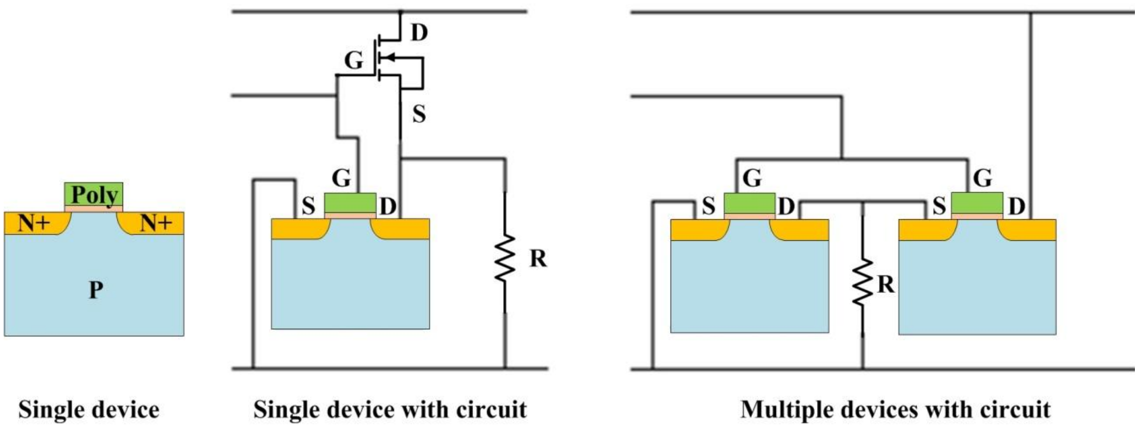

Figure A-1: Types of simulations that can be performed in TCAD Sentaurus Device simulator.

Besides the file containing device's structure, doping, and meshing information (SSE output file), SDevice takes additional input files, i.e. the command file (sdevice_des.cmd) and the parameter file (sdevice.par). The command file contains details of the applied physics models and biasing conditions, while the parameter file contains the parameters for the applied physics models and the materials' properties.

In summary, a complete flow of device simulation starting from device creation is shown in the Figure A-2 [68].

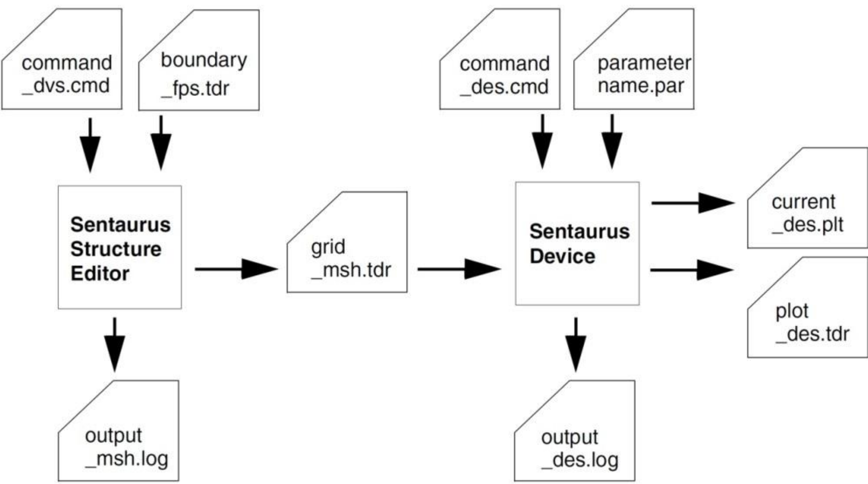

Figure A-2: A typical complete flow of device simulation in TCAD Sentaurus simulator.

The output of SDevice can contain a lot more information besides current and voltage, e.g. electric field, energy bands level, carrier density, carrier velocity, etc. They can be plotted by using visualization tools provided from Synopsys, such as Inspect (for _des.plt file) and Tecplot (for _dest.tdr file)

APPENDIX B: PARAMETER FILE IN TCAD SENTAURUS DEVICE SIMULATIONS

Parameter file contains the parameters of materials and physics models that are implemented in the simulations. As parameter file is quite similar for most simulations, only one sample of the parameter files is presented in this appendix, i.e. sdevice.par in the static simulations of diamond Schottky barrier diode with edge termination structure discussed in Chapter 7.

```
Material = "Metal"{
      Bandgap {
      Work function = @Work function@
      }
}

Material = "Oxide" {
Epsilon
{ *  Ratio of the permittivities of material and vacuum

  * epsilon() = epsilon
      epsilon     = @Dielectric@    # [1]
}
```

```
Bandgap
{
      Chi0= 1
      Eg0= 8.8
}
}

Material = "Diamond" {

      Epsilon
      { * Ratio of the permittivities of material and vacuum
      * epsilon() = epsilon
            epsilon = 5.7
      }

#-----------------------------------------------------------------
---------
      RefractiveIndex
      { * Optical Refractive Index
      *refractiveindex() = refractiveindex*(1+alpha*(T-Tpar))
            refractiveindex = 2.684
            alpha = 4.04e-06 #[1/K]
            Tpar = 3.0000e+02 #[K]
      }

#-----------------------------------------------------------------
---------
      Kappa
      { * Lattice thermal conductivity

      * Formula = 1
      * kappa() = kappa+kappa_b*T+kappa_c*T^2
            kappa = 24 #[W/(K cm)]
            kappa_b = 0.0000e+00 #[W/(K^2 cm)]
            kappa_c = 0.0000e+00 #[W/(K^3 cm)]
      }

#-----------------------------------------------------------------
---------
      Ionization
      { * Incomplete ionization parameter


            E_B_0 = 0.37 #[eV]
            alpha_B = 4.1000e-08 #[eV cm]
            g_B = @g@
            Xsec_B = 1.0000e-12 #[cm^2/sec]

            # NDopant and PDopant are generic dopant supported
by Sentaurus Device

            E_NDopant_0 = 0.1 #[eV]
            alpha_NDopant = 3.1000e-08 #[eV cm]
            g_NDopant = 2
            Xsec_NDopant = 1.0000e-12 #[cm^2/sec]

            E_PDopant_0 = 0.2 #[eV]
            alpha_PDopant = 3.1000e-08 #[eV cm]
```

```
          g_PDopant = 4
          Xsec_PDopant = 1.0000e-12 #[cm^2/sec]

          NdCrit = 1.0000e+18 #[cm-3]
          NaCrit = 3.0000e+19 #[cm-3]

     }

#-----------------------------------------------------------------
---------
     Bandgap
     { * Lattice temperature-dependence of the band gap (Band
gap and electron affinity model)
          Chi0 = 1.3 #[eV]
          Bgn2Chi = 0.5
          Eg0 = 5.47 #[eV]
          dEg0(Bennett) = 0.0000e+00 #[eV]
              dEg0(Slotboom) = 0.0000e+00 #[eV]
          dEg0(OldSlotboom) = 0.0000e+00 #[eV]
          dEg0(delAlamo) = 0.0000e+00 #[eV]
          alpha = 0 #[eV K^-1]
          beta = 0.0000e+00 #[K]
          Tpar = 0.0000e+00 #[K]
     }

#-----------------------------------------------------------------
---------
     * All the bandgap narrowing model below use default
parameters for Silicon

     BennettWilson
     { * Bandgap Narrowing for Bennett-Wilson Model
          Ebgn = 6.8400e-03 #[eV]
          Nref = 3.1620e+18 #[cm^-3]
     }

     Slotboom
     { * Bandgap Narrowing for Slotboom Model
          Ebgn = 6.9200e-03 #[eV]
          Nref = 1.3000e+17 #[cm^-3]
     }

     OldSlotboom
     { * Bandgap Narrowing for OldSlotboom Model
          Ebgn = 9.0000e-03 #[eV]
          Nref = 1.0000e+17 #[cm^-3]
     }

     delAlamo
     { * Bandgap Narrowing for del Alamo Model
          Ebgn = 18.7000e-03 #[eV]
          Nref = 7.0000e+17 #[cm^-3]
     }

#-----------------------------------------------------------------
---------
```

```
eDOSmass
      { * Temperature dependent DOS effective mass of electrons,
computed as a function of Nc(300K)
            Formula = 2
            Nc300 = 1.0516e+19 #[cm^-3]
      }

      hDOSmass
      { * Temperature dependent DOS effective mass of electrons,
computed as a function of Nv(300K)
            Formula = 2
            Nv300 = 1.7956e+19 #[cm^-3]
      }

#-----------------------------------------------------------------
---------

      ConstantMobility:
      { * Temperature dependence mobility
            mumax = 4500, 3800 #[cm^2/Vs]
            Exponent = 3.0, 3.0
      }

      DopingDependence:
      { * Doping dependence mobility model (due to charged
impurity ions)
            Formula = 1, 1 # Masetti Formula for electrons and
hole [1, 1] is set to be default formula for diamond material
            mumin1 = 20, 103 #[cm^2/Vs]
            mumin2 = 0.0000e+00, 70 #[cm^2/Vs]
            mu1 = 0.0000e+00, 48.5 #[cm^2/Vs]
            Pc = 0.0000e+00, 0.0000e+00 #[cm^3]
            Cr = 4.5000e+17, 1.0000e+14 #[cm^3]
            Cs = 3.4300e+20, 5.6000e+14 #[cm^3]
            alpha = 0.45, 0.57
            beta = 2, 10
      }

#-----------------------------------------------------------------
---------
      UniBoDopingDependence:
      {
      *Parameters of electron are default values used in
Arsenide doped Silicon. This is acceptable approximations as the
main carrier in the simulated p-type diamond devices is hole.
      *Parameters of hole are values for diamond

            #if@< Temperature <= 325 >@
            mumax = 1.4410e+3, 3.4450e+3 #[cm^2/(Vs)]
            Exponent = 2.4500e+00, 1.5000e+00 #[1]
            mumin2 = 132, 55 #[cm^2/(Vs)]

            #if@< Temperature > 325 >@
            mumax = 1.4410e+3, 4.1000e+3 #[cm^2/(Vs)]
            Exponent = 2.4500e+00, 3.2000e+00 #[1]
            mumin2 = 132, 70 #[cm^2/(Vs)]
```

```
            Exponent2 = -0.1100e+00, 0.0000e+00 #[1]
            mumin1 = 55, 0 #[cm^2/(Vs)]
            mumin1_exp = 0.6, 0 #[1]
            mumin2_exp = 1.3, -2.5 #[1]
            mu1 = 42.4, 0 #[cm^2/(Vs)]
            mu1_exp = 0.5, 0 #[1]
            mu2 = 73.5, 0 #[cm^2/(Vs)]
            mu2_exp = 1.25, 0 #[1]
            Cr = 8.9000e+16, 1.0000e+30 #[cm^-3]
            Cr_exp = 3.65, 0 #[1]
            Cr2 = 1.2200e+17, 1.1200e+14 #[cm^-3]
            Cr2_exp = 2.6500, 2.5890 #[1]
            Cs = 2.9000e+20, 1.0000e+30 #[cm^-3]
            Cs_exp = 0, 0 #[1]
            Cs2 = 7.0000e+20, 1.0000e+30 #[cm^-3]
            alpha = 0.6800, 1.0000 #[1]
            beta = 0.7200, 0.5890 #[1]
      }

#-----------------------------------------------------------------
---------
      HighFieldDependence:
      {

      * Extended Canali Model
            * Setting alpha = 0 brings the model back to
Caughey-Thomas model
            alpha = 0, 0
            beta0 = 2, 2
            betaexp = 0.0000e+00, 0.0000e+0
            * Smoothing parameter is using default value
            K_dT = 0.2, 0.2

      * Transferred Electron Model
            * Default parameters value are used
            E0_TrEf = 4.0000e+03, 4.0000e+03 #[V/cm]
            Ksmooth_trEf = 1, 1


      * Velocity Saturation Model for electron and hole
(temperature dependence)
            Vsat_formula = 1, 1
            vsat0 = 2.0000e+07, 2.0000e+07 #[cm/s]
            vsatexp = 0.5, 0.5
      }

#-----------------------------------------------------------------
---------
      PooleFrenkel
      { * Poole-Frenkel trap model
            epsPF =  5.7, 5.7
      }

      vanOverstraetendeMan
      { * Avalanche Generation Model

            a(low) = @An@, @Ap@ #[1/cm]
            a(high) = @An@, @Ap@ #[1/cm]
```

```
            b(low) = @Bn@, @Bp@ #[V/cm]
            b(high) = @Bn@, @Bp@ #[V/cm]
            E0 = 4.0000e+05, 4.0000e+05 #[V/cm]
            hbarOmega = 1.0000e+03, 1.0000e+03 #[eV]
      }

      Scharfetter
      { * SRH doping dependence model
            taumin = 0.0000e+00, 0.0000e+00 #[s]
            taumax = 1.0000e-05, 3.0000e-06 #[s]
            Nref = 1.0000e+16, 1.0000e+16 #[cm^-3]
            gamma = 1, 1
            Talpha = -1.5000e+00, -1.5000e+00
            Tcoeff = 2.55, 2.55
            Etrap = 0.0000e+00 #[eV]
      }

      Auger
      { A= 5e-31, 9.9e-32
        B= 0, 0
        C= 0, 0
      }

MaterialInterface = "Metal/Diamond" {
      ThermionicEmission {
      A = @a@, @a@    # [1]
      B = 4, 4    # [1]
      C = 1, 1    # [1]
      }

      BarrierLowering {
      a1= 1.589e-5
      p1= 0.5
      p1_eq= 0.5
      a2= 0
      p2= 1
      p2_eq = 1
      }

      BarrierTunneling {
      g= 2.1e-5, 0.66e-5
      mt= 0.5, 0.5
      }
}

BarrierTunneling "NLM" {
      g= 2.1e-5, 0.66e-5
      mt= 0.5, 0.5
}
```

APPENDIX C: COMMAND FILES FOR SIMULATIONS OF TRANSIENT CHARACTERISTICS OF DIAMOND SBD IN TCAD SENTAURUS SOFTWARE

The command files for the simulations of transient characteristics of diamond SBD (in Chapter 4) are presented, i.e. command file for device creation (sde_dvs.cmd), command file for the static simulations (sdevice_des.cmd), and command file for the transient simulations (transient_des.cmd).

Sde_dvs.cmd

```
; =================== Outer Boundary Creation
=========================
(sdegeo:set-default-boolean "BAB")
;---Diamond Regions

(sdegeo:create-rectangle
      (position 0.0 0.0 0.0) (position @HalfLs@ (+ @LDrift@
@LSub@) 0.0)
 "Diamond" "DriftSubRegion" )

(sdegeo:create-rectangle
      (position (/ (- @HalfLs@ @HalfLs@) 2) 0.0 0.0) (position
(+ (/ (- @HalfLs@ @HalfLs@) 2) @HalfLs@) -0.05 0.0)
 "Metal" "SchottkyMetal" )

; =================== Contact Definition Placement
=========================
(sdegeo:define-contact-set "top_schottky" 4.0 (color:rgb 1.0 0.0
0.0) "##")
(sdegeo:define-contact-set "bot_ohmic"    4.0 (color:rgb 1.0 0.0
0.0) "##")


(sdegeo:define-2d-contact (find-edge-id (position  (/ @HalfLs@
2) -0.05 0.0)) "top_schottky")
(sdegeo:define-2d-contact (find-edge-id (position  (/ @HalfLs@
2) (+ @LDrift@ @LSub@) 0.0)) "bot_ohmic")

; =================== Constant and Analytical Profiles
=========================
;---Definitions
(sdedr:define-constant-profile "Drift_Dop_Defn"
"BoronActiveConcentration" @DriftDoping@ )
(sdedr:define-constant-profile "Sub_Dop_Defn"
"BoronActiveConcentration" @SubDoping@ )

;---Windows
(sdedr:define-refeval-window "Drift_Win"
 "Rectangle"  (position 0 0 0) (position @HalfLs@ @LDrift@ 0.0))
```

```
(sdedr:define-refeval-window "Sub_Win"
"Rectangle"  (position 0 (+ @LDrift@ 0.2) 0) (position @HalfLs@
(+ @LDrift@ @LSub@) 0.0))

 ;---Placement
(sdedr:define-constant-profile-placement "Drift_Place"
"Drift_Dop_Defn" "Drift_Win")
(sdedr:define-constant-profile-placement "Sub_Place"
"Sub_Dop_Defn" "Sub_Win")

(sdedr:define-refinement-window "Sub_Drift_Line" "Line"
 (position 0.0  (+ @LDrift@ 0.2) 0.0)
 (position @HalfLs@ (+ @LDrift@ 0.2) 0.0) )
(sdedr:define-gaussian-profile "Impl.Substrate"
 "BoronActiveConcentration"
 "PeakPos" 0.0  "PeakVal" @SubDoping@
 "ValueAtDepth" @DriftDoping@  "Depth" 0.2
 "Erf"  "Length" 0.01)
(sdedr:define-analytical-profile-placement "Impl.Substrate"
 "Impl.Substrate" "Sub_Drift_Line" "Negative" "NoReplace"
"Eval")

; =================== Refinements  =========================

;---Definitions
(sdedr:define-refinement-size "Global_Ref_Defn"
  1 1 0.0
  0.9 0.7 0.0 )
(sdedr:define-refinement-size "Drift_Ref_Defn"
  1 0.8 0.0
  0.9 0.5 0.0 )
(sdedr:define-multibox-size   "Multi_Box_Defn"
  1.0 0.3   0.0
  1.0 0.1 0.0
  1.0 1.4   1.0)
(sdedr:define-refinement-size "Interface_Ref_Defn"
  1 0.05 0.0
  0.7 0.03 0.0 )
   (sdedr:define-refinement-size "Top_Ref_Defn"
  1 0.05 0.0
  0.5 0.03 0.0 )

;---Windows
(sdedr:define-refinement-window  "Global_Win"
 "Rectangle"  (position 0.0 0.0 0.0) (position @HalfLs@ (+
@LDrift@ @LSub@) 0.0) )
(sdedr:define-refinement-window  "Drift_Win"
 "Rectangle" (position 0.0 0.0 0.0) (position @HalfLs@ @LDrift@
0.0) )
(sdedr:define-refinement-window  "Top_Win"
 "Rectangle" (position 0.0 0.0 0.0) (position @HalfLs@ 0.5 0.0)
)

(sdedr:define-refinement-window  "Multi_Box_Win"
 "Rectangle" (position 0.0 0.0 0.0) (position @HalfLs@ 5.0 0.0)
)

(sdedr:define-refinement-window  "Interface_Win"
```

```
 "Rectangle" (position 0.0 (- @LDrift@ 0.15) 0.0) (position
@HalfLs@ (+ @LDrift@ 0.15) 0.0) )

;---Placement
(sdedr:define-refinement-placement "Global_Ref_Place"
"Global_Ref_Defn" "Global_Win" )
(sdedr:define-refinement-placement "Drift_Ref_Place"
"Drift_Ref_Defn"    "Drift_Win" )
(sdedr:define-multibox-placement   "Multi_Box_Place"
"Multi_Box_Defn"  "Multi_Box_Win")
(sdedr:define-refinement-placement "Top_Place" "Top_Ref_Defn"
"Top_Win" )
(sdedr:define-refinement-placement "Interface_Place"
"Interface_Ref_Defn" "Interface_Win" )

;----------------------------------------------------------------
-------
; Saving BND file
(sdeio:save-tdr-bnd (get-body-list) "@tdrboundary/o@")

; Save CMD file
(sdedr:write-cmd-file "@commands/o@")

; Build Mesh
(system:command "snmesh n@node@_msh")

(exit)
```

Sdevice_des.cmd

```
Electrode {
#if @<[string compare SIM "IV"] == 0>@
   { Name="bot_ohmic" Voltage= 0.0 Resist= @Rparasitic@}
#else
   { Name="bot_ohmic" Voltage= 0.0 Resist= 1e13 }
#endif
   { Name="top_schottky" Voltage= 0.0 }
}

File {
   Grid= "@tdr@"
   Plot= "@tdrdat@"
   Plot= "@tdr@"
   Current= "@plot@"
   Output= "@log@"
   Parameter= "@parameter@"

}

Physics {

   AreaFactor= @AF@
   Fermi
   Recombination (
      SRH(DopingDependence)
      Auger
      #if @<[string compare An "0"] == 1>@
      eAvalanche (vanOverstraeten)
```

```
      #endif

      hAvalanche (vanOverstraeten)
   )
#if @<[string compare SIM "Breakdown"] == 0>@
   OptBeam(
      WaveInt= @WaveInt@    # [1/cm/s]
      SemAbs= 1e0     # [1/cm]
      SemSurf= -0.1    # [cm]
      SemWindow= ( 0.0 50.e-4 ) # [cm]
   )
#endif

   IncompleteIonization
   eBarrierTunneling "NLM"
   hBarrierTunneling "NLM"


   hMobility (
      - ConstantMobility
      IncompleteIonization
      DopingDependence(UniBo)
      HighFieldSaturation
   )
   eMobility (
      ConstantMobility
      DopingDependence(Masetti)
      HighFieldSaturation
   )


   EffectiveIntrinsicDensity(NoBandGapNarrowing)
   Temperature= @Temperature@
}




Physics (MaterialInterface= "Metal/Diamond") {
   Schottky
   BarrierLowering
   hThermionic
   eThermionic
   Recombination(
      eBarrierTunneling
      hBarrierTunneling)
   Temperature= @Temperature@
}

Plot {
   eDensity hDensity
   eCurrent hCurrent
   ElectricField
   eQuasiFermiEnergy hQuasiFermiEnergy
   Potential Doping SpaceCharge
   SRH
   AvalancheGeneration
   eAvalanche hAvalanche
```

```
   eMobility hMobility
   eVelocity hVelocity
   ConductionBandEnergy ValenceBandEnergy BandGap
   Current
   BoronMinusConcentration
   BoronConcentration
   BoronActiveConcentration
   hDriftVelocity
   IntrinsicDensity
   TotalRecombination
   ConductionCurrent
   DeepLevels
   DisplacementCurrent
   Nonlocal
   eBarrierTunneling
   hBarrierTunneling
   eTrappedCharge
   hTrappedCharge
   eInterfaceTrappedCharge
   hInterfaceTrappedCharge
}

Math (MaterialInterface= "Metal/Diamond") {
   Nonlocal (
      Length= 7e-8
      Permeation= 7e-8
      Digits= 7
      EnergyResolution= 0.001
   )
}


Math {
   Nonlocal "NLM" (
      MaterialInterface= "Metal/Diamond"
      Length= 7e-8
      Digits= 7
      EnergyResolution= 0.001
   )

   Extrapolate
   Digits= @Digits@
   ExtendedPrecision (@Extended@)
   RHSmax= 1e30
   RHSmin= 1e-30
   RHSFactor= 1e120
   ErrEff(electron)= 1e-27
   ErrEff(hole)= 1e-27
   Notdamped= 20
   Iterations= 15
   RecBoxIntegr
   CNormPrint
   CDensityMin= 1e-25
   ExitOnFailure
}
Solve {

   Poisson
```

```
#if @<[string compare Damping "ILS"] == 0>@
   Coupled(Iterations= 300 Method= ILS){ Poisson Hole }
   Coupled(Iterations= 300 Method= UMF){ Poisson Hole Electron}
#else
   Coupled(Iterations= 300 LineSearchDamping= @Damping@){
Poisson Hole }
   Coupled(Iterations= 300 LineSearchDamping= @Damping@){
Poisson Hole Electron}
#endif

   Quasistationary (
      DoZero
            InitialStep= 2e-3 Minstep= 1e-5 MaxStep= 0.1
            Goal{Name="bot_ohmic" Voltage= 0}
      ) {
            Coupled { Poisson Hole Electron }
      }

#if @<[string compare SIM "Breakdown"] == 0>@

    NewCurrentFile= "BV_"
    Quasistationary (
       Initialstep= 2.5e-5 Increment= 1.4 Decrement= 2
       Maxstep= 0.075 Minstep= 1.e-10
       Goal { Name="bot_ohmic" Voltage= @Goal@ }
       Plot { range = (0 1) Intervals=5}
       )

       { Coupled { Poisson Hole Electron }
       CurrentPlot( Time= ( Range= (0.00 0.05) Intervals= 10;
                    Range= (0.05 0.20) Intervals= 10;
                    Range= (0.2 0.6) Intervals= 10;
                    Range= (0.6 1.00) Intervals= 20))
       }
#endif

#if @<[string compare SIM "IV"] == 0>@

   NewCurrentFile= "IV_"
   Quasistationary (
      Initialstep= 1e-2 Increment= 1.4
      Maxstep= 0.05 Minstep= 1.e-8
      Goal { Name="bot_ohmic" Voltage= @Goal@ }
      Plot {Range = (0 1) Intervals= 8}
      )
      { Coupled { Poisson Hole Electron}
      CurrentPlot ( Time= (Range= (0.00 0.50) Intervals= 20;
                    Range= (0.50 0.75) Intervals= 20;
      Range= (0.75 1.00) Intervals= 10))}

#endif

}
```

Transient_des.cmd

```
Device Diamond_Schottky_Diode {
```

```
*-----------------------------------------------------------------
-------*
File {
   #Grid= "/home/arie/STDB/HTswitch/DiaSBDSwitch/n1235_msh.tdr"
   Grid= "@tdr@"
   Parameters= "@parameter@"
   Plot= "@tdrdat@"
   Plot= "@tdr@"
   Current= "@plot@"
}
Electrode {
   { Name="bot_ohmic" Voltage= 0.0 Resist= @Rparasitic@}
   { Name="top_schottky" Voltage= 0.0 }
}
Physics {

   AreaFactor= @AF@
   Fermi
   Recombination (
      SRH(DopingDependence)
      Auger
   )
#if @<[string compare SIM "Breakdown"] == 0>@
   OptBeam(
      WaveInt= @WaveInt@    # [1/cm/s]
      SemAbs= 1e0      # [1/cm]
      SemSurf= -0.1    # [cm]
      SemWindow= ( 0.0 50.e-4 ) # [cm]
   )
#endif

   IncompleteIonization
   eBarrierTunneling "NLM"
   hBarrierTunneling "NLM"

   hMobility (
      - ConstantMobility
      IncompleteIonization
      DopingDependence(UniBo)
      HighFieldSaturation
      #Default is using Canali Model
   )
   eMobility (
      DopingDependence(Masetti)
      HighFieldSaturation
   )

   EffectiveIntrinsicDensity(NoBandGapNarrowing)
   Temperature= @Temperature@
}

Physics (MaterialInterface= "Metal/Diamond") {
   Schottky
   BarrierLowering
   hThermionic
   eThermionic
   Recombination(
      eBarrierTunneling
```

```
      hBarrierTunneling)
   Temperature= @Temperature@
}
*------------------------------------------------------------------
-------*
}
File {
   Output= "@log@"
   SPICEPath =
"/home/arie/STDB/HTswitch/28May2013/Switching7Summary/SPICE"
}
Plot {
   eDensity hDensity
   eCurrent hCurrent
   ElectricField
   eQuasiFermiEnergy hQuasiFermiEnergy
   Potential Doping SpaceCharge
   SRH
   AvalancheGeneration
   eAvalanche hAvalanche
   eMobility hMobility
   eVelocity hVelocity
   ConductionBandEnergy ValenceBandEnergy BandGap
   Current
   BoronMinusConcentration
   BoronConcentration
   BoronActiveConcentration
   hDriftVelocity
   IntrinsicDensity
   TotalRecombination
   ConductionCurrent
   DeepLevels
   DisplacementCurrent
   Nonlocal
   eBarrierTunneling
   hBarrierTunneling
}
Math (MaterialInterface= "Metal/Diamond") {
   Nonlocal (
      Length= 7e-8
      Permeation= 7e-8
      Digits= 7
      EnergyResolution= 0.001
   )
}
Math {
    Nonlocal "NLM" (
      MaterialInterface= "Metal/Diamond"
      Length= 7e-8
      Digits= 7
      EnergyResolution= 0.001
   )
   Extrapolate
   Digits= @Digits@
   ExtendedPrecision (@Extended@)
   RHSmax= 1e30
   RHSmin= 1e-30
   RHSFactor= 1e120
```

```
   ErrEff(electron)= 1e-27
   ErrEff(hole)= 1e-27
   Notdamped= 20
   Iterations= 50
   RecBoxIntegr
   CNormPrint
   ExitOnFailure
   Transient= BE
   CDensityMin= 1e-25
   NoAutomaticCircuitContact
   NoCheckTransientError
}
System {

   DIMOS2 MOS (15 14 16 16){l= 8e-4 w= 1.55e-4}
   DMOD1 DBODY (13 11)
   Capacitor_pset CGS (14 16) {capacitance= @CGS@} #1288e-12
   Capacitor_pset CGD (14 11) {capacitance= @CGD1@} #12e-12
   Capacitor_pset CDS (11 13) {capacitance= @CDS@} #108e-12
   Resistor_pset RDRIFT (15 17) {resistance= 6.25}
   Resistor_pset RDRAIN (11 17) {resistance= 0.1}
   Resistor_pset RSOURCE (13 16) {resistance= 0.1}
   Resistor_pset RG (12 14) {resistance= 1e-6}
   VCCS_pset GIRCH (15 16 12 13) {gain= 0.001}


   Diamond_Schottky_Diode SBD (bot_ohmic=1 top_schottky=2)
   Inductor_pset LLoad (3 1) {inductance= @LLoad@}
   Inductor_pset LDiode (3 2) {inductance= @LDiode@}
   Inductor_pset LPar (4 3) {inductance= @LPar@}
   Inductor_pset LDrain (1 11) {inductance= @LDrain@}
   Inductor_pset LSource (13 5) {inductance= @LSource@}
   Resistor_pset Rg (6 12) {resistance= @Rg@}
   Vsource_pset Vin (4 5) { dc= @Vin@ }
   Vsource_pset VG  (6 5) { pwl= (0 0 @ts1@ @VG1@ @ts2@ @VG2@ 1
@VG2@)}

   Initialize (LLoad.branch = @Forward_Current@)
   Initialize (LDiode.branch = @Forward_Current@)
   Initialize (3= @Vin@)

   Set (4=@Vin@)
Plot "n@node@_1" (time() v(1) v(2) v(3) v(4) v(5) v(6) v(11)
v(12) v(13) v(14) v(15) v(16) v(17) i(RG 12) i(Vin 4) i(LDiode
3) i(LLoad 1) i(LPar 3) i(LDrain 11) i(LSource 5) )

}
Solve {
   Coupled {Poisson}
   Coupled { SBD.Poisson Contact }
   Coupled { SBD.Poisson Contact SBD.Hole SBD.Electron}
SBD.Hole SBD.Electron }
Circuit }
   Quasistationary (
      InitialStep= 1e-3 Increment= 2
      MinStep= 1e-7 MaxStep= 0.05
      Goal { Parameter= LLoad.ic Value= @Forward_Current@ }
   ){ Coupled { Poisson hole electron contact } }
```

```
   NewCurrentPrefix="TRANSIENT1"

   Transient (
      InitialTime= 0 FinalTime= @tramp@
      InitialStep= 1e-9 Increment= 2 Decrement= 1.5
      MinStep= 1e-25 MaxStep= 2e-9
      TurningPoints ( (@ts1@ 5e-9) (@ts2@ 1e-10) )
   ){ Coupled { Poisson hole electron contact circuit }}

   NewCurrentPrefix="RAMPING"
      Quasistationary (
      InitialStep= 1e-3 Increment= 2
      MinStep= 1e-7 MaxStep= 0.05
      Goal { Parameter= CGD.capacitance Value= @CGD2@ }
   ){ Coupled { Poisson hole electron contact } }

   NewCurrentPrefix="TRANSIENT2"
      Transient (
      InitialTime= @tramp@ FinalTime= @tf@
      InitialStep= 1e-9 Increment= 2 Decrement= 1.5
      MinStep= 1e-25 MaxStep= 2e-9
      ){ Coupled { Poisson hole electron contact circuit }}
   }
```

Furthermore, the parameter files of the SPICE model for MOSFET DMOS2 and diode DMOD1 are given below.

```
PSET DMOD1
  DEVICE Diode
  PARAMETERS
    is = 1e-16
    rs= 70
    cjo= 407e-12
END PSET

PSET DIMOS2
  DEVICE Mos2
  PARAMETERS

    // level = 2
    nmos = 1
    pmos = 0
      vto = 4.7
      kp = 10
      tox = 1e-7
      lambda = 0.0005
      gamma = 0
      nfs = 0
      rsh = 0
      uo= 600
      phi = 0.7
      rs = 0
      is= 1e-14
      vmax=0.86e5
END PSET
```

APPENDIX D: COMMAND FILES FOR SIMULATIONS OF DIAMOND SBD WITH INTERFACIAL LAYER IN TCAD SENTAURUS SOFTWARE

The command files that were implemented in the simulations of non-ideal diamond SBD with interfacial layer and interface states charges (in Chapter 6) are presented, i.e. file for the device creation (sde_dvs.cmd) and for the device simulations (sdevice_des.cmd). Structure of the simulated SBD with interfacial layer and its parameters are shown below.

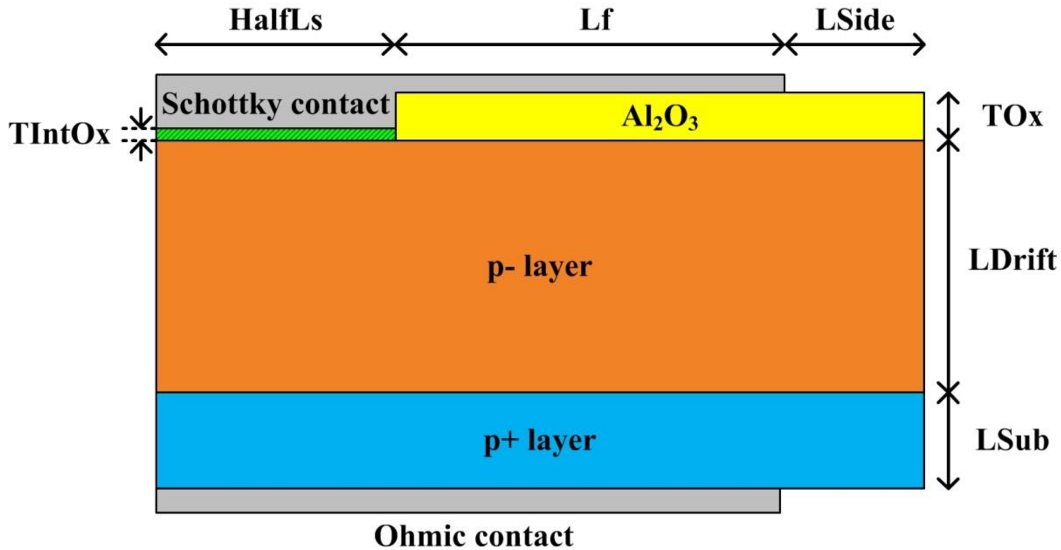

sde_dvs.cmd

```
; ==================== Outer Boundary Creation
==========================
(sdegeo:set-default-boolean "BAB")
;---Diamond Regions

(sdegeo:create-rectangle
      (position 0.0 0.0 0.0) (position (+ (+ @HalfLs@ @Lf@)
@LSide@) (+ @LDrift@ @LSub@) 0.0)
 "Diamond" "DriftSubRegion" )

;---- Oxide Regions
(sdegeo:create-rectangle
  (position @HalfLs@ (- 0 @TOx@) 0.0) (position (+ (+ @HalfLs@
@Lf@) @LSide@) 0 0.0)
  "Oxide" "Ox_Region" )

;---- InterfacialOxide Regions
```

```
(sdegeo:create-rectangle
  (position 0 (- 0 @TIntOx@) 0.0) (position @HalfLs@ 0 0.0)
  "InterfacialOxide" "Interface_Layer_Region" )

;---- Metal Regions
(sdegeo:create-polygon   (list (position 0 (- (- 0 @TOx@) 0.3)
0) (position (+ @HalfLs@ @Lf@) (- (- 0 @TOx@) 0.3) 0) (position
(+ @HalfLs@ @Lf@) (- 0 @TOx@) 0)
      (position @HalfLs@ (- 0 @TOx@) 0) (position @HalfLs@ (- 0
@TIntOx@) 0) (position 0 (- 0 @TIntOx@) 0) (position 0 (- (- 0
@TOx@) 0.3) 0))"Molybdenum" "SchottkyMetal" )

; =================== Contact Definition Placement
=========================
(sdegeo:define-contact-set "top_schottky" 4.0 (color:rgb 1.0 0.0
0.0) "##")
(sdegeo:define-contact-set "bot_ohmic"    4.0 (color:rgb 1.0 0.0
0.0) "##")

(sdegeo:insert-vertex (position (+ @HalfLs@ @Lf@) (+ @LDrift@
@LSub@) 0.0))

(sdegeo:define-2d-contact (find-edge-id (position  2.0 (- (- 0
@TOx@) 0.3) 0.0)) "top_schottky")
(sdegeo:define-2d-contact (find-edge-id (position  2 (+ @LDrift@
@LSub@) 0.0)) "bot_ohmic")

; =================== Constant and Analytical Profiles
=========================

;---Definitions
(sdedr:define-constant-profile "Drift_Dop_Defn"
"BoronActiveConcentration" @DriftDoping@ )
(sdedr:define-constant-profile "Sub_Dop_Defn"
"BoronActiveConcentration" @SubDoping@ )

;---Windows
(sdedr:define-refeval-window "Drift_Win"
 "Rectangle"  (position 0 0 0) (position (+ (+ @HalfLs@ @Lf@)
@LSide@) (+ @LDrift@ 0.2) 0.0))
(sdedr:define-refeval-window "Sub_Win"
"Rectangle"  (position 0 (+ @LDrift@ 0.2) 0) (position (+ (+
@HalfLs@ @Lf@) @LSide@) (+ @LDrift@ @LSub@) 0.0))

 ;---Placement
(sdedr:define-constant-profile-placement "Drift_Place"
"Drift_Dop_Defn" "Drift_Win")
(sdedr:define-constant-profile-placement "Sub_Place"
"Sub_Dop_Defn" "Sub_Win")

(sdedr:define-refinement-window "Sub_Drift_Line" "Line"
 (position 0.0  (+ @LDrift@ 0.2) 0.0)
 (position (+ (+ @HalfLs@ @Lf@) @LSide@) (+ @LDrift@ 0.2) 0.0) )
(sdedr:define-gaussian-profile "Impl.Substrate"
 "BoronActiveConcentration"
 "PeakPos" 0.0  "PeakVal" 1e20
 "ValueAtDepth" 1e17  "Depth" 0.2
 "Erf"  "Length" 0.01)
```

```
(sdedr:define-analytical-profile-placement "Impl.Substrate"
 "Impl.Substrate" "Sub_Drift_Line" "Negative" "NoReplace"
"Eval")

; =================== Refinements  =========================

;---Definitions
(sdedr:define-refinement-size "Global_Ref_Defn"
  4.0 3.0 0.0
  3.0 1.0 0.0 )
(sdedr:define-refinement-size "Drift_Ref_Defn"
  2.0 0.8 0.0
  0.1 0.1 0.0 )
(sdedr:define-multibox-size   "Multi_Box_Defn"
  1.0 0.4   0.0
  0.1 0.001 0.0
  1.0 1.4   1.0)
(sdedr:define-refinement-size "Ox_Dia_Ref_Defn"
  0.1 0.01  0.0
  0.04 0.008 0.0 )
(sdedr:define-refinement-size "Ox_Ref_Defn"
  2 0.5  0.0
  0.2 0.2 0.0 )
(sdedr:define-refinement-size "Ox2_Ref_Defn"
  0.3 0.075  0.0
  0.2 0.0375 0.0 )
(sdedr:define-refinement-size "Cont_Ref_Defn"
  0.0015 0.0015 0.0
  0.001 0.001 0.0 )
(sdedr:define-refinement-size "Interface_Ref_Defn"
  0.025 0.0005 0.0
  0.02 0.0003 0.0 )
(sdedr:define-refinement-size "Cont2_Ref_Defn"
  0.10 0.10 0.0
  0.04 0.04 0.0 )
(sdedr:define-refinement-size "Implant_Ref_Defn"
  0.2 0.2 0.0
  0.08 0.08 0.0 )

;---Windows
(sdedr:define-refinement-window  "Global_Win"
 "Rectangle"  (position 0.0 (- (- 0 @TOx@) 0.3) 0.0) (position
(+ (+ @HalfLs@ @Lf@) @LSide@) (+ @LDrift@ @LSub@) 0.0) )
(sdedr:define-refinement-window  "Drift_Win"
 "Rectangle" (position 0.0 0.0 0.0) (position (+ (+ @HalfLs@
@Lf@) @LSide@) 10.0 0.0) )
(sdedr:define-refinement-window  "Ox_Dia_Win1"
 "Rectangle" (position 0.0 -0.04 0.0) (position (+ @HalfLs@ 2)
0.04 0.0) )
#(sdedr:define-refinement-window  "Ox_Dia_Win2"
# "Rectangle" (position @HalfLs@ 1.46 0.0) (position (+ (+
@HalfLs@ @Lf@) 5).0 1.54 0.0) )
(sdedr:define-refinement-window  "Ox_Win"
 "Rectangle" (position @HalfLs@ (- 0 @TOx@) 0.0) (position (+ (+
@HalfLs@ @Lf@) @LSide@) 0 0.0) )
(sdedr:define-refinement-window  "Multi_Box_Win"
 "Rectangle" (position 0.0 0.0 0.0) (position (+ @HalfLs@ 5) 8
0.0) )
```

```
(sdedr:define-refinement-window  "Ox_Win_Middle"
 "Rectangle" (position @HalfLs@ -0.5 0.0) (position (+ @HalfLs@
1) 0 0.0) )
(sdedr:define-refinement-window  "Ox_Win_Right"
 "Rectangle" (position (- (+ @HalfLs@ @Lf@) 0.5) (- 0 @TOx@)
0.0) (position (+ (+ @HalfLs@ @Lf@) 0.5) 0.5 0.0) )


(sdedr:define-refinement-window  "Cont_Region_Win_Right"
 "Rectangle" (position (- @HalfLs@ 0.05) -0.01 0.0) (position (+
@HalfLs@ 0.05) 0.02 0.0) )

(sdedr:define-refinement-window  "Cont2_Region_Win_Right"
 "Rectangle" (position (- (+ @HalfLs@ @Lf@) 0.5) 0 0.0)
(position (+ (+ @HalfLs@ @Lf@) 0.5) 0.5 0.0) )
(sdedr:define-refinement-window  "Interface_Region_Win"
 "Rectangle" (position (- @HalfLs@ 0.5) (- 0 @TIntOx@) 0.0)
(position (+ @HalfLs@ 0.5) 0 0.0) )

;---Placement
(sdedr:define-refinement-placement "Global_Ref_Place"
"Global_Ref_Defn" "Global_Win" )
(sdedr:define-refinement-placement "Drift_Ref_Place"
"Drift_Ref_Defn"    "Drift_Win" )
#(sdedr:define-refinement-placement "Ox_Dia_Ref_Place1"
"Ox_Dia_Ref_Defn"  "Ox_Dia_Win1" )
#(sdedr:define-refinement-placement "Ox_Dia_Ref_Place2"
"Ox_Dia_Ref_Defn"  "Ox_Dia_Win2" )
(sdedr:define-refinement-placement "Ox_Ref_Place"
"Ox_Ref_Defn"     "Ox_Win" )
(sdedr:define-refinement-placement "Ox_Middle_Ref_Place"
"Ox2_Ref_Defn"     "Ox_Win_Middle" )
(sdedr:define-refinement-placement "Ox_Right_Ref_Place"
"Ox2_Ref_Defn"     "Ox_Win_Right" )
(sdedr:define-multibox-placement   "Multi_Box_Place"
"Multi_Box_Defn"  "Multi_Box_Win")

(sdedr:define-refinement-placement "Interface_Ref_Place"
  "Interface_Ref_Defn" "Interface_Region_Win" )

(sdeaxisaligned:set-parameters "yCuts"
   (list
         (- @LDrift@ 0.01) @LDrift@ (+ @LDrift@ 0.01)
   )
)
;----------------------------------------------------------------
-------
; Saving BND file
(sdeio:save-tdr-bnd (get-body-list) "@tdrboundary/o@")

; Save CMD file
(sdedr:write-cmd-file "@commands/o@")

; Build Mesh
(system:command "snmesh n@node@_msh")
```

sdevice_des.cmd

```
Electrode {
#if @<[string compare SIM "IV"] == 0>@
   { Name="bot_ohmic" Voltage= 0.0 Resist= @Rparasitic@}
#else
   { Name="bot_ohmic" Voltage= 0.0 Resist= 1e13 }
#endif
   { Name="top_schottky" Voltage= 0.0 }
}

File {
   Grid= "@tdr@"
   Plot= "@tdrdat@"
   Plot= "@tdr@"
   Current= "@plot@"
   Output= "@log@"
   Parameter= "@parameter@"
}

Physics {

   AreaFactor= @AF@
   Recombination (
      SRH(DopingDependence)
      Auger
   )

   IncompleteIonization

   #if @<[string compare Band2Band "yes"] == 0>@
   eBarrierTunneling "NLMInterface" (Band2Band = Simple TwoBand)
   hBarrierTunneling "NLMInterface" (Band2Band = Simple TwoBand)
   #endif
   #if @<[string compare Band2Band "no"] == 0>@
   eBarrierTunneling "NLMInterface"
   hBarrierTunneling "NLMInterface"
   #endif

   hMobility (
      - ConstantMobility

      DopingDependence(UniBo)
      HighFieldSaturation *Default is using Canali Model
   )
   eMobility (
      ConstantMobility
      DopingDependence(Masetti)
      HighFieldSaturation
   )

   EffectiveIntrinsicDensity(NoBandGapNarrowing NoFermi)
   Temperature= @Temperature@
}

Physics (MaterialInterface= "InterfacialOxide/Diamond") {
   BarrierLowering
   eThermionic
   hThermionic
   #if @<[string compare SurfaceSRH "yes"] == 0>@
```

```
   Recombination (surfaceSRH)
   #endif
   Temperature= @Temperature@
   Traps(
         (Acceptor Uniform fromCondBand
          Conc= @TrapConc@ EnergyMid= @ATrapEnergyMid@
EnergySig= @ATrapEnergySigma@
          eJfactor= 0 hJfactor= 0
          #Constant cross section
          eXsection= @eX@ hXsection= @hX@
         )
         #if @<[string compare DTrap "yes"] == 0>@
         (Donor Uniform fromCondBand
               Conc= @TrapConc@ EnergyMid= @DTrapEnergySigma@
EnergySig= @DTrapEnergySigma@
          eJfactor= 0 hJfactor= 0
          #Constant cross section
          eXsection= @eX@ hXsection= @hX@
         )
         #endif
   )
}

Plot {
   eDensity hDensity
   eCurrent hCurrent
   eDirectTunneling hDirectTunneling
   ElectricField
   eQuasiFermiEnergy hQuasiFermiEnergy
   Potential Doping SpaceCharge
   SRH
   AvalancheGeneration
   eAvalanche hAvalanche
   eMobility hMobility
   eVelocity hVelocity
   ConductionBandEnergy ValenceBandEnergy BandGap
   Current
   BoronMinusConcentration
   BoronConcentration
   BoronActiveConcentration
   UserSpeciesConcentration
   UserSpeciesIncompleteConcentration
   hDriftVelocity
   IntrinsicDensity
   TotalRecombination
   ConductionCurrent
   DeepLevels
   DisplacementCurrent
   Nonlocal
   eBarrierTunneling
   hBarrierTunneling
}

Math {
   Nonlocal "NLMInterface" (
      RegionInterface= "SchottkyMetal/Interface_Layer_Region"
      Length= @Length@
      Digits= 4
```

```
      EnergyResolution= 1e-4
   )

   ConstRefPot= 0
   Extrapolate
   Digits= 5
   ExtendedPrecision (80)
   Error (Electron) = 1e-15
   Error (Hole) = 1e-15
   Notdamped= 50
   Iterations= 20
   RecBoxIntegr
   CDensityMin= 1e-30
   CNormPrint
}

Solve {
   Poisson
   Coupled(Iterations= 100 ){ Poisson Hole }
   Coupled(Iterations= 100 ){ Poisson Hole Electron}
   Quasistationary (
      DoZero
            InitialStep= 2e-3 Minstep= 1e-5 MaxStep= 0.1
            Goal{Name="bot_ohmic" Voltage= 0}
      ) {
            Coupled { Poisson Hole Electron}
      }
 #if @<[string compare SIM "Breakdown"] == 0>@

    NewCurrentFile= "BV_"
    Quasistationary (
       Initialstep= 1e-4 Increment= 1.4 Decrement= 2
       Maxstep= 0.075 Minstep= 1.e-10
       Goal { Name="bot_ohmic" Voltage= @Goal@ }
       Plot { range = (0 1) Intervals=5}
       )

       { Coupled { Poisson Hole Electron}
       CurrentPlot( Time= ( Range= (0.00 0.05) Intervals= 10;
                      Range= (0.05 0.20) Intervals= 10;
                      Range= (0.2 0.6) Intervals= 10;
                      Range= (0.6 1.00) Intervals= 20))
       }
#endif

#if @<[string compare SIM "IV"] == 0>@
   NewCurrentFile= "IV_"
   Quasistationary (
      Initialstep= 1e-2 Increment= 1.4
      Maxstep= 0.05 Minstep= 1.e-15
      Goal { Name="bot_ohmic" Voltage= @Goal@ }
      Plot {Range = (0 1) Intervals= 8}
      )
      { Coupled { Poisson Hole Electron}
      CurrentPlot ( Time= (Range= (0.00 0.50) Intervals= 20;
                      Range= (0.50 0.75) Intervals= 20;
      Range= (0.75 1.00) Intervals= 10))}
   #endif}
```

APPENDIX E: COMMAND FILES FOR SIMULATIONS OF DIAMOND SBD WITH EDGE TERMINATION STRUCTURE IN TCAD SENTAURUS SOFTWARE

The command files for the device creation (sde_dvs.cmd) and device simulations (sdevice_des.cmd) that are implemented in the simulations of diamond SBD with edge termination structure (in Chapter 7) are presented. The structure of the simulated SBD with either field plate or planar mesa termination structure (depending on the values of Toxo and Toxi) and its parameters are shown below. In the simulations, LSide is maintained at 5 µm.

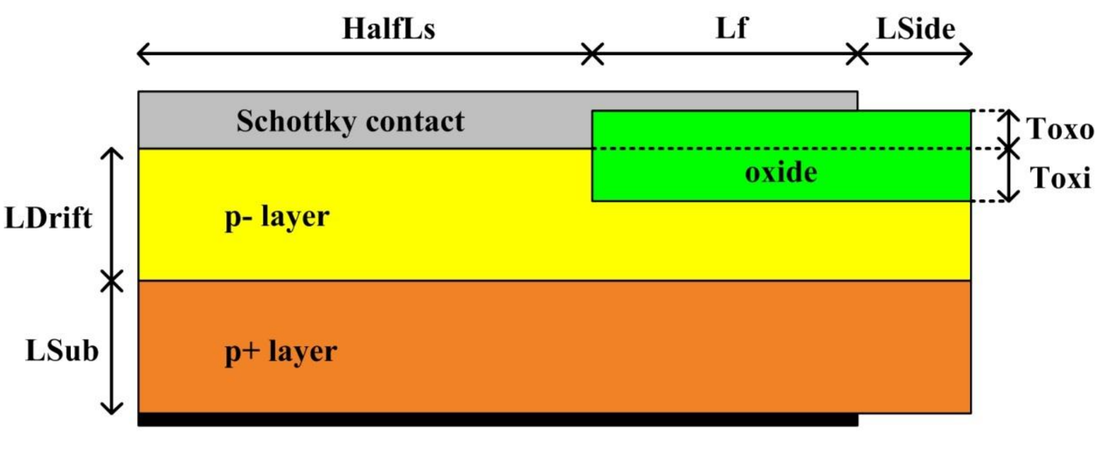

sde_dvs.cmd

```
; =================== Outer Boundary Creation
=========================
(sdegeo:set-default-boolean "BAB")
;---Diamond Regions

(sdegeo:create-polygon (list (position 0.0 0.0 0.0) (position
@HalfLs@ 0 0.0)
      (position @HalfLs@ @Toxi@ 0.0) (position (+ 5 ( + @HalfLs@
@Lf@)) @Toxi@ 0.0)
      (position (+ 5 ( + @HalfLs@ @Lf@)) (+ @LDrift@ @LSub@)
0.0) (position 0 (+ @LDrift@ @LSub@) 0.0)
      (position 0.0 0.0 0.0)
      )
 "Diamond" "DriftSubRegion" )

;---- Oxide Regions
(sdegeo:create-rectangle
```

```
  (position @HalfLs@ (- 0 @Toxo@) 0.0) (position (+ 5 ( +
@HalfLs@ @Lf@)) @Toxi@ 0.0)
  "Oxide" "Ox_Region" )

;---- Metal Regions
(sdegeo:create-polygon   (list (position 0 -0.3 0) (position (-
@HalfLs@ 0.3) -0.3 0)
      (position (- @HalfLs@ 0.3) (- 0 (+ 0.3 @Toxo@)) 0)
(position ( + @HalfLs@ @Lf@) (- 0 (+ 0.3 @Toxo@)) 0) (position (
+ @HalfLs@ @Lf@) (- 0 @Toxo@) 0)
      (position @HalfLs@ (- 0 @Toxo@) 0) (position @HalfLs@ 0 0)
(position 0 0 0)
      (position 0 -0.3 0))"Metal" "SchottkyMetal" )

; =================== Contact Definition Placement
=========================
(sdegeo:define-contact-set "top_schottky" 4.0 (color:rgb 1.0 0.0
0.0) "##")
(sdegeo:define-contact-set "bot_ohmic"    4.0 (color:rgb 1.0 0.0
0.0) "##")

 (sdegeo:insert-vertex (position ( + @HalfLs@ @Lf@) (- 0 (+ 0.3
@Toxo@)) 0.0))
(sdegeo:insert-vertex (position @Lo@ (+ @LDrift@ @LSub@) 0.0))
 (sdegeo:define-2d-contact (find-edge-id (position  (/ @HalfLs@
2) -0.3 0)) "top_schottky")
(sdegeo:define-2d-contact (find-edge-id (position  (- @HalfLs@
0.3) (- 0 (+ 0.3 (/ @Toxo@ 2))) 0)) "top_schottky")
(sdegeo:define-2d-contact (find-edge-id (position  (+ @ HalfLs@
(/ @Lf@ 2)) (- 0 (+ 0.3 @Toxo@)) 0.0)) "top_schottky")
 (sdegeo:define-2d-contact (find-edge-id (position  (/ @HalfLs@
2) (+ @LDrift@ @LSub@) 0)) "bot_ohmic")

; =================== Constant and Analytical Profiles
=========================

;---Definitions
(sdedr:define-constant-profile "Drift_Dop_Defn"
"BoronActiveConcentration" @DriftDoping@ )
(sdedr:define-constant-profile "Sub_Dop_Defn"
"BoronActiveConcentration" @SubDoping@ )

;---Windows

(sdedr:define-refeval-window "Drift_Win"
 "Polygon" (list (position 0.0 0.0 0.0) (position @HalfLs@ 0
0.0)
      (position @HalfLs@ @Toxi@ 0.0) (position (+ 5 ( + @HalfLs@
@Lf@)) @Toxi@ 0.0)
      (position (+ 5 ( + @HalfLs@ @Lf@)) @LDrift@ 0.0) (position
0 @LDrift@ 0.0)
      (position 0.0 0.0 0.0)
      ) )

(sdedr:define-refeval-window "Sub_Win"
"Rectangle"  (position 0 @LDrift@ 0) (position (+ 5 ( + @HalfLs@
@Lf@)) (+ @LDrift@ @LSub@) 0.0))
```

```
 ;---Placement
(sdedr:define-constant-profile-placement "Drift_Place"
"Drift_Dop_Defn" "Drift_Win")
(sdedr:define-constant-profile-placement "Sub_Place"
"Sub_Dop_Defn" "Sub_Win")

(sdedr:define-refinement-window "Sub_Drift_Line" "Line"
 (position 0.0  (+ 0.2 @LDrift@) 0.0)
 (position (+ 5 ( + @HalfLs@ @Lf@)) (+ 0.2 @LDrift@) 0.0) )
(sdedr:define-gaussian-profile "Impl.Substrate"
 "BoronActiveConcentration"
 "PeakPos" 0.0  "PeakVal" 1e19
 "ValueAtDepth" 1e17  "Depth" 0.2
 "Erf"  "Length" 0.2)
(sdedr:define-analytical-profile-placement "Impl.Substrate"
 "Impl.Substrate" "Sub_Drift_Line" "Negative" "NoReplace"
"Eval")

; =================== Refinements  =========================

;---Definitions
(sdedr:define-refinement-size "Global_Ref_Defn"
  4.0 3.0 0.0
  3.0 1.0 0.0 )
(sdedr:define-refinement-size "Drift_Ref_Defn"
  0.5 0.5 0.0
  0.1 0.1 0.0 )
(sdedr:define-multibox-size   "Multi_Box_Defn"
  1.0 0.4   0.0
  0.1 0.001 0.0
  1.0 1.4   1.0)
(sdedr:define-refinement-size "Ox_Dia_Ref_Defn"
  1.0 0.01  0.0
  0.5 0.008 0.0 )
(sdedr:define-refinement-size "Ox_Ref_Defn"
  0.6 0.1  0.0
  0.3 0.04 0.0 )
(sdedr:define-refinement-size "Ox2_Ref_Defn"
  0.35 0.075  0.0
  0.3 0.0375 0.0 )
(sdedr:define-refinement-size "Cont_Ref_Defn"
  0.05 0.05 0.0
  0.02 0.02 0.0 )
(sdedr:define-refinement-size "Cont2_Ref_Defn"
  0.10 0.10 0.0
  0.04 0.04 0.0 )
(sdedr:define-refinement-size "Implant_Ref_Defn"
  0.2 0.2 0.0
  0.08 0.08 0.0 )

;---Windows
(sdedr:define-refinement-window  "Global_Win"
 "Rectangle"  (position 0.0 (- 0 (+ 0.3 @Toxo@)) 0.0) (position
(+ 5 ( + @HalfLs@ @Lf@)) (+ @LDrift@ @LSub@) 0.0) )
(sdedr:define-refinement-window  "Drift_Win"
 "Rectangle" (position 0.0 0.0 0.0) (position (+ 5 ( + @HalfLs@
@Lf@)) @LDrift@ 0.0) )
(sdedr:define-refinement-window  "Dia_Metal_Win"
```

```
 "Rectangle" (position 0.0 -0.04 0.0) (position @HalfLs@ 0.04
0.0) )
(sdedr:define-refinement-window  "Ox_Dia_Win"
 "Rectangle" (position @HalfLs@ (- @Toxi@ 0.04) 0.0) (position
(+ 5 ( + @HalfLs@ @Lf@)) (+ @Toxi@ 0.04) 0.0) )
(sdedr:define-refinement-window  "Ox_Win"
 "Rectangle" (position @HalfLs@ (- 0 @Toxo@) 0) (position (+ 5 (
+ @HalfLs@ @Lf@)) @Toxi@ 0.0) )
(sdedr:define-refinement-window  "Multi_Box_Win"
 "Rectangle" (position 0.0 0.0 0.0) (position (+ 5 ( + @HalfLs@
@Lf@)) (+ 2 @Toxi@) 0.0) )
(sdedr:define-refinement-window  "Ox_Win_Middle"
 "Rectangle" (position (- @HalfLs@ 0.2) (- 0 @Toxo@) 0.0)
(position (+ @HalfLs@ 0.2) @Toxi@ 0.0) )
(sdedr:define-refinement-window  "Ox_Win_Right"
 "Rectangle" (position (- ( + @HalfLs@ @Lf@) 0.5) (- 0 @Toxo@)
0.0) (position (+ 0.5 ( + @HalfLs@ @Lf@)) 0 0.0) )

(sdedr:define-refinement-window  "Cont_Region_Win_Right"
 "Rectangle" (position (- @HalfLs@ 0.3) -0.1 0.0) (position (+
@HalfLs@ 0.3) 0.3 0.0) )
(sdedr:define-refinement-window  "Cont2_Region_Win_Right"
 "Rectangle" (position (- ( + @HalfLs@ @Lf@) 0.5) @Toxi@ 0.0)
(position (+ 0.5 ( + @HalfLs@ @Lf@)) (+ 0.2 @Toxi@) 0.0) )
(sdedr:define-refinement-window  "Cont3_Region_Win_Right"
 "Rectangle" (position (- @HalfLs@ 0.2) (- @Toxi@ 0.2) 0.0)
(position (+ @HalfLs@ 0.2) (+ 0.2 @Toxi@) 0.0) )
(sdedr:define-refinement-window  "Cont4_Region_Win_Right"
 "Rectangle" (position (- ( + @HalfLs@ @Lf@) 0.2) (- 0 @Toxo@)
0.0) (position (+ 0.2 ( + @HalfLs@ @Lf@)) (+ 0.2 (- 0 @Toxo@))
0.0) )

;---Placement
(sdedr:define-refinement-placement "Global_Ref_Place"
"Global_Ref_Defn" "Global_Win" )
(sdedr:define-refinement-placement "Drift_Ref_Place"
"Drift_Ref_Defn"    "Drift_Win" )
(sdedr:define-refinement-placement "Ox_Dia_Ref_Place1"
"Ox_Dia_Ref_Defn"  "Dia_Metal_Win" )
(sdedr:define-refinement-placement "Ox_Dia_Ref_Place2"
"Ox_Dia_Ref_Defn"  "Ox_Dia_Win" )
(sdedr:define-refinement-placement "Ox_Middle_Ref_Place"
"Ox2_Ref_Defn"     "Ox_Win_Middle" )
(sdedr:define-refinement-placement "Ox_Right_Ref_Place"
"Ox2_Ref_Defn"     "Ox_Win_Right" )
(sdedr:define-multibox-placement   "Multi_Box_Place"
"Multi_Box_Defn"  "Multi_Box_Win")

(sdedr:define-refinement-placement "Cont_Ref_Place_Right"
"Cont_Ref_Defn" "Cont_Region_Win_Right" )
(sdedr:define-refinement-placement "Cont2_Ref_Place_Right"
"Cont_Ref_Defn" "Cont2_Region_Win_Right" )
(sdedr:define-refinement-placement "Cont3_Ref_Place_Right"
"Cont_Ref_Defn" "Cont3_Region_Win_Right" )

; Resolve the junction
(sdeaxisaligned:set-parameters "yCuts"
   (list
```

```
         (- @LDrift@ 0.01) @LDrift@ (+ 0.01 @LDrift@)
   )
)
;------------------------------------------------------------------
-------
; Saving BND file
(sdeio:save-tdr-bnd (get-body-list) "@tdrboundary/o@")

; Save CMD file
(sdedr:write-cmd-file "@commands/o@")

; Build Mesh
(system:command "snmesh n@node@_msh")
```

sdevice_des.cmd

```
Electrode {
#if @<[string compare SIM "IV"] == 0>@
   { Name="bot_ohmic" Voltage= 0.0 Resist= @Rparasitic@}
#else
   { Name="bot_ohmic" Voltage= 0.0 Resist= 1e13 }
#endif
   { Name="top_schottky" Voltage= 0.0 }
}

File {
   Grid= "@tdr@"
   Plot= "@tdrdat@"
   Plot= "@tdr@"
   Current= "@plot@"
   Output= "@log@"
   Parameter= "@parameter@"
}

Physics {
   AreaFactor= @AF@
   Fermi
   Recombination (
      SRH(DopingDependence)
      Auger
      eAvalanche (vanOverstraeten)
      hAvalanche (vanOverstraeten)
   )
#if @<[string compare SIM "Breakdown"] == 0>@
   OptBeam(
      WaveInt= @WaveInt@     # [1/cm/s]
      SemAbs= 1e0      # [1/cm]
      SemSurf= -0.1     # [cm]
      SemWindow= ( 0.0 50.e-4 ) # [cm]
   )
#endif

   IncompleteIonization
   eBarrierTunneling "NLM" #Electron tunneling
   hBarrierTunneling "NLM" #Hole tunneling
   hMobility (
      - ConstantMobility
```

```
      DopingDependence(UniBo)
      HighFieldSaturation *Default is using Canali Model
   )
   eMobility (
      ConstantMobility
      DopingDependence(Masetti)
      HighFieldSaturation
   )
   EffectiveIntrinsicDensity(NoBandGapNarrowing)
   Temperature= @Temperature@
}

Physics (MaterialInterface= "Metal/Diamond") {
   Schottky
   BarrierLowering
   hThermionic
   eThermionic
   Recombination(
     eBarrierTunneling
     hBarrierTunneling)
   Temperature= @Temperature@
}

Plot {
   eDensity hDensity
   eCurrent hCurrent
   ElectricField
   Potential Doping SpaceCharge
   SRH
   AvalancheGeneration
   eAvalanche hAvalanche
   eMobility hMobility
   eVelocity hVelocity
   ConductionBandEnergy ValenceBandEnergy BandGap
   Current
   BoronMinusConcentration
   BoronConcentration
   BoronActiveConcentration
   hDriftVelocity
   IntrinsicDensity
   TotalRecombination
   ConductionCurrent
   DeepLevels
   DisplacementCurrent
   Nonlocal
   eBarrierTunneling
   hBarrierTunneling
}

Math (MaterialInterface= "Metal/Diamond") {
   Nonlocal (
     Length= 7e-8
     Permeation= 7e-8
     Digits= 7
     EnergyResolution= 0.001
   )
}
```

```
#if @<[string compare Break "on"] == 0>@
Math (Material= "Oxide") {
      BreakCriteria {
            ElectricField (maxval= 1e7)
      }
}
#endif

Math {
   Nonlocal "NLM" (
      MaterialInterface= "Metal/Diamond"
      Length= 7e-8
      Digits= 7
      EnergyResolution= 0.001
   )
   Extrapolate
   Digits= @Digits@
   ExtendedPrecision (@Extended@)
   ExitOnFailure
   RHSmax= 1e30
   RHSmin= 1e-30
   RHSFactor= 1e120
   ErrEff(electron)= 1e-27
   ErrEff(hole)= 1e-27
   Notdamped= 20
   Iterations= 15
   RecBoxIntegr
   CNormPrint
   CDensityMin= 1e-30
}

Solve {

   Poisson
   Coupled(Iterations= 100 LineSearchDamping= @Damping@){
Poisson Hole }
   Coupled(Iterations= 100 LineSearchDamping= @Damping@){
Poisson Hole Electron}

   Quasistationary (
      DoZero
            InitialStep= 2e-3 Minstep= 1e-5 MaxStep= 0.1
            Goal{Name="bot_ohmic" Voltage= 0}
      ) {
            Coupled { Poisson Hole Electron }
      }

#if @<[string compare SIM "Breakdown"] == 0>@
    NewCurrentFile= "BV_"
    Quasistationary (
       Initialstep= 1e-4 Increment= 1.4 Decrement= 2
       Maxstep= 0.075 Minstep= 1.e-10
       Goal { Name="bot_ohmic" Voltage= @Goal@ }
       Plot { range = (0 1) Intervals=5}
       Plot { range =(0.72 0.725) Intervals=1}
       )
       { Coupled { Poisson Hole Electron }
       CurrentPlot( Time= ( Range= (0.00 0.05) Intervals= 10;
```

```
                        Range= (0.05 0.20) Intervals= 10;
                        Range= (0.2 0.6) Intervals= 10;
                        Range= (0.6 1.00) Intervals= 20))
        }
#endif

#if @<[string compare SIM "IV"] == 0>@

   NewCurrentFile= "IV_"
   Quasistationary (
      Initialstep= 1e-2 Increment= 1.4
      Maxstep= 0.05 Minstep= 1.e-8
      Goal { Name="bot_ohmic" Voltage= @Goal@ }
      Plot {Range = (0 1) Intervals= 8}
      )
      { Coupled { Poisson Hole Electron}
      CurrentPlot ( Time= (Range= (0.00 0.50) Intervals= 20;
                        Range= (0.50 0.75) Intervals= 20;
      Range= (0.75 1.00) Intervals= 10))}
#endif
}
```